DISSERTATION

Wet chemical porosification of LTCC substrates for high frequency and catalyst support applications

zur Erlangung des akademischen Grades
Doktor der technischen Wissenschaften (Dr. techn.)

Institut für Sensor- und Aktuatorsysteme
Technische Universität Wien

MSc. Ali Hajian
Matrikelnummer: 1634860

Wien, 2020

Verteidigung: Wien, 27. October 2020

Betreuer: Univ.Prof. Dr. rer. nat. Ulrich Schmid
Technische Universität Wien, Österreich

Gutachter: Prof. Dr. Dominique de Ligny
Friedrich Alexander Universität Erlangen-Nürnberg, Deutschland

Univ.Prof. Dr. Silvan Schmid
Technische Universität Wien, Österreich

II:

SUMMARY

Nowadays, due to the continuously increasing demand for larger bandwidths and data rates, there is a growing interest in the use of microwave and millimetre wave frequencies in various applications such as mobile phones, automotive radar systems, and wireless communication systems. Low-temperature co-fired ceramics (LTCC) which are advanced composites of glass and ceramics sintered at temperatures below 1000 °C, are capable to fulfil these demands. Due to several exceptional features in the field of dielectric and thermomechanical properties, especially high mechanical fracture strength, low weight, high integration level, and compatibility with radio frequency microelectromechanical systems (RF-MEMS) and monolithic microwave integrated circuits (MMICs), LTCC technology has attracted significant attention for the fabrication of high-density multilayer packages. However, advanced designs of micromachined devices operating at high frequencies require substrates with regions of tailored permittivities. Wet chemical etching with an appropriate etching solution under defined conditions leads to channel-like, statistically distributed and interconnected open meso-to macro-pores which cause a reduction in permittivity of commercially available LTCC tapes without the need to alter the tape composition or the firing process.

The main challenges associated with this approach, however, are achieving a high degree of porosification, thus increasing air embedment while keeping the surface as intact as possible. To ensure that the high-frequency devices can work at maximum efficiency, the surface topography of the LTCC needs to be preserved, since a highly destructed surface prohibits further metallization lines. Additionally, by increasing frequencies up to the GHz range, the skin depth, derived for ideally smooth conductor surfaces, decreases to the order of the surface roughness, thus causing a nearly linear increase in conductor loss. Moreover, the etching may lead to other changes in the physical properties of the LTCC, including detrimental effects on mechanical properties. Therefore, this thesis mainly aims towards the introduction of an alternative approach for porosification of the LTCC surface targeting a better surface quality which features a suitable bearing plane for further metallization lines without the need for wire bonding. Therefore, the etching behaviour of commercially available LTCC tapes was investigated with different etching solutions and at different etching conditions, *i.e.*, etchant temperature, pH, and concentration. Remarkable results were obtained under defined conditions where for the first time, a very deep porosification of the whole LTCC substrate while preserving the surface quality and the original substrate thickness could be obtained. Besides, the impact of firing temperature on morphology, phase composition,

as well as porosification was studied. The effective relative permittivity ($\varepsilon_r{}'$) of LTCC substrates at 1 GHz was reduced up to 10.8% when measuring substrates with a thickness of approximately 600 μm and a porosification depth up to 186 μm from each side. The calculated relative permittivity values for the etched layer showed a reduction of up to 22% in comparison to the initial value for the *as-fired* LTCC.

To explore the impact of porosification on the mechanical properties of LTCC substrates their stiffness behaviour after wet-chemical etching was investigated using dynamic-mechanical analysis at temperatures up to 550 °C. Promising results were obtained which demonstrate the applicability of such modified modules even when operated at such high temperatures. Moreover, a miniaturized biaxial bending test called Ball On Three Balls test (B3B) was developed and successfully used for the flexural strength measurement of different LTCC tapes. The developed setup can be used for testing other brittle materials such as pure ceramics.

Finally, the potential of porosified LTCC for green energy production was explored. For this purpose, first porosified Ferro L8 LTCC substrates were impregnated with palladium nanoparticles. The developed catalyst was then successfully tested for hydrogen production from methanol. The obtained results were promising and indicate the potential of porosified LTCC for application in fuel cells and microreactors. However, additional investigations need to be performed to improve the catalyst performance.

KURZFASSUNG

Heutzutage gibt es aufgrund der hohen Nachfrage nach größerer Bandbreite und Datenraten ein wachsendes Interesse an der Nutzung von Mikrowellen- und Millimeterwellenfrequenzen in verschiedenen Anwendungen wie Mobiltelefonen, Kfz-Radarsystemen und drahtloser Kommunikation. Low Temperature Co-fired Ceramics (LTCC), ein robuster Verbundwerkstoff aus Glas und Keramik, der bei Temperaturen unter 1000 °C gesintert wird, ist in der Lage, diese Anforderungen zu erfüllen. Aufgrund mehrerer außergewöhnlicher Eigenschaften im Bereich dielektrischer und thermomechanischer Eigenschaften, insbesondere einer hohen mechanischen Bruchfestigkeit, geringes Gewicht, einem hohen Integrationsgrad, Kompatibilität mit mikroelektromechanischen Hochfrequenzsystemen (RF-MEMS) und monolithischen integrierten Mikrowellenschaltungen (MMICs), hat die LTCC-Technologie bei der Herstellung hochintegrierter Gehäusungen in Mehrlagentechnik große Aufmerksamkeit erregt. Moderne Designs von Hochfrequenzsystemen erfordern jedoch Substrate mit Bereichen, die maßgeschneiderte Permittivitätswerte aufweisen. Ein nasschemischer Ätzprozess mit einer geeigneten Ätzlösung und unter definierten Bedingungen führt zu kanalartigen, statistisch verteilten und miteinander verbundenen offenen Meso- bis Makroporen, die eine lokale Verringerung der Permittivität kommerziell erhältlicher LTCC- Werkstoffe bewirken, ohne ihre Zusammensetzung oder den Sinterprozess verändern zu müssen.

Die größte Herausforderung bei diesem Ansatz besteht jedoch darin, einen hohen Porösiziergrad zu erreichen, um mit diesem Ansatz mehr Luft einschließen zu können und gleichzeitig die Oberfläche so intakt wie möglich zu halten. Damit die Hochfrequenzbauelemente mit maximaler Effizienz arbeiten können, muss die Oberflächentopographie des LTCC-Substrates erhalten bleiben, da eine stark zerstörte Oberfläche keine Metallisierung in diesem Bereich erlaubt. Zusätzlich nimmt durch die Erhöhung der Frequenzen bis in den GHz-Bereich die Eindringtiefe in der Größenordnung der Oberflächenrauhigkeit ab, was zu einem nahezu linearen Anstieg der Leiterverluste führt. Darüber hinaus kann das Ätzen zu weiteren Veränderungen der physikalischen Eigenschaften der LTCC führen, einschließlich nachteiliger Auswirkungen auf die mechanischen Eigenschaften. Deshalb hat diese Dissertation hauptsächlich zum Ziel, nasschemische Ätzparameter zu finden, um selbst auf porösizierten Bereichen eine geeignete Topographie für einen nachfolgenden Metallisierungsschritt zu erhalten.

Für eine systematische Analyse wird der Ätzprozess mit verschiedenen Ätzlösungen und unter verschiedenen Ätzbedingungen, d.h. Ätzmitteltemperatur, pH-Wert und Konzentration an kommerziell erhältlichen LTCC Substraten untersucht. Vielversprechende Ergebnisse wurden unter

definierten Bedingungen erzielt, wobei zum ersten Mal eine sehr tiefe Porösierung des gesamten LTCC-Substrats unter Beibehaltung der Oberflächenqualität und der ursprünglichen Substratdicke erreicht werden konnte. Außerdem wurde der Einfluss der Brenntemperatur auf die Morphologie, die Phasenzusammensetzung sowie das Porösizierverhalten untersucht. Die effektive relative Dielektrizitätskonstante (ε_r´) der LTCC-Substrate wurde bei 1 GHz gemessen, wobei die effektive Dielektrizitätskonstante des gesamten LTCC-Substrats mit einer Dicke von 600 μm und einer maximalen, beidseitigen Porösiziertiefe von 186 μm bis zu 10.8% abnahm. Die berechneten Werte der relativen Dielektrizitätskonstanten im Bereich der geätzten Schicht zeigten eine Verringerung bis zu 22% im Vergleich zum ursprünglichen, gebrannten Zustand.

Zur Untersuchung des Porösiziereinflusses auf die mechanischen Eigenschaften von LTCC-Substraten wurde deren Steifigkeitsverhalten nach nasschemischem Ätzen mittels dynamisch-mechanischer Analyse bei Temperaturen bis 550 °C untersucht. Es wurden vielversprechende Ergebnisse erzielt, die die Anwendbarkeit solcher modifizierter Module auch bei solch hohen Temperaturen zeigen. Darüber hinaus wurde ein miniaturisierter biaxialer Biegeversuch, der sogenannte Ball On Three Balls-Test (B3B), entwickelt und erfolgreich für die Biegefestigkeitsmessung verschiedener LTCC-Substrate eingesetzt. Der entwickelte Aufbau kann auch für die Prüfung anderer spröder Materialien, wie reine Keramiken, verwendet werden.

Schließlich wurde das hohe Potenzial von porösiziertem LTCC für die Erzeugung grüner Energie untersucht. Zu diesem Zweck wurden porösizierte Ferro L8-LTCC-Substrate mit Palladium-Nanopartikeln imprägniert. Der entwickelte Katalysator wurde dann erfolgreich für die Wasserstoffproduktion aus Methanol getestet. Die erzielten Ergebnisse waren vielversprechend und weisen auf das Potenzial von poröser LTCC für die Anwendung in Brennstoffzellen und Mikroreaktoren hin. Es sind jedoch zusätzliche Untersuchungen notwendig, um die Katalysatorleistung weiter zu verbessern.

ACKNOWLEDGEMENTS

First of all, I would like to thank Prof. Ulrich Schmid for giving me the opportunity to do this PhD thesis in his multidisciplinary research group and for his generous support during my research at the *Institute of Sensor and Actuator Systems (ISAS)*. I am grateful that whenever I needed guidance, support, or help his door was open.

Also, thanks go to Prof. Dominique de Ligny and Martin Brehl the project partners from the Institute of Glass and Ceramics at Friedrich–Alexander University Erlangen–Nuremberg for all their support and cooperation during this project.

Moreover, in the course of this research, I got the chance to have fruitful collaborations with brilliant scientists around the world. So, I would like to acknowledge all those who helped me during this project:

Dr. Thomas Konegger for his support in porosimetry tests and the joint supervision of two Bachelor students. I really appreciate the opportunity Thomas gave me to work in his laboratory when there were technical issues with ours at ISAS. (*Institute of Chemical Technologies and Analytics, TU Wien*).

Dr. Christoph and Raffael Rameshan, and Elischa Ellersdorfer for their support with catalyst tests (*Institute of Material Chemistry, TU Wien*).

Dr. Torsten Rabe and Dr. Björn Mieller for their support in dielectric characterisation (*Advanced Technical Ceramics Division, Bundesanstalt für Materialforschung und -prüfung, Germany*).

Prof. Alexander Kromka for his support in XPS and Raman measurements (*Institute of Physics, Czech Academy of Sciences*).

Isabella Lau for her supports in dielectric measurements and scientific discussions (*Institute for Electronics Engineering, Friedrich–Alexander University Erlangen–Nuremberg*).

Dr. Sabine Schwarz and Dr. Michael Stöger-Pollach for their support in TEM analyses (*University Service Centre for Transmission Electron Microscopy, TU Wien*).

Stefan Smetaczek and Dr. Andreas Limbeck for the LA-ICP-MS measurements (*Institute of Chemical*

Technologies and Analytics, Wien).

Dr. Thomas Koch for his support for the mechanical characterisation (*Institute of Materials Science and Technology, TU Wien*).

Dr. Klaudia Hradil and Werner Artner for their help with the XRD measurements (*X-ray Center, TU Wien*).

Moreover, I would like to thank Christopher Zellner, and my great bachelor students Doruk Müftüoglu, Ivan Delic, Konrad Bielecki, for their valuable contributions to this project.

Furthermore, I want to thank my colleagues for the wonderful time, Dr. Michael Schneider for the scientific discussions and helpful advice, and also our administration team especially Martina Bittner, Martina Nuhsbaumer, Sabine Fuchs, and Andreas Astleitner.

I would like to thank the technical supports from all technicians at *ISAS*; Franz Prewein, Micha, Sophia, and Patrick for all their supports in the clean room and technical issues, and Heinz Homolka for his support in the LTCC lab.

Last but not the least, I would like to thank my wife Azam who was always there cheering me up and stood by me through the good times and bad.

This project has been supported by the Austrian Science Fund FWF, No. I 2551-N30.

Table of Contents

SUMMARY iii

KURZFASSUNG v

ACKNOWLEDGEMENTS vii

1. INTRODUCTION 1

1.1. State of the art and motivation 1

1.2. Theory and basics in LTCC technology 2

1.2.1. Inorganic, non-metallic materials 2

1.2.2. LTCC multilayer technology 3

1.2.3. Physical and chemical properties of LTCC materials 9

1.3. Different approaches for the permittivity reduction 12

1.3.1. The state-of-the-art approach for the porosification in one layer 14

1.3.2. Porosity and surface metrology 15

1.3.3. Dissolution of minerals 19

1.4. State-of-the-art in LTCC devices and systems 25

1.5. LTCC technology for green energy production 27

1.5.1. Green energy production 27

1.5.1.1. Significance of catalyst support 28
1.5.1.2. Metallic catalysts 29
1.5.2. LTCC-based microreactors 30

2. EXPERIMENTAL DETAILS **31**

2.1. Materials and technology aspects 31
2.1.1. LTCC materials and etching solutions 31
2.1.2. Etching process 33
2.1.3. Preparation of LTCC samples 35
2.1.4. Experimental setup and measuring method for the catalytic hydrogen production 39
2.1.4.1. Experimental setup 39
2.1.4.2. Measuring method 41
2.2. Characterization 42
2.2.1. Electron microscopy techniques 42
2.2.1.1. Scanning Electron Microscopy 42
2.2.1.2. Three-dimensional SEM imaging 43
2.2.1.3. Transmission electron microscopy 47
2.2.2. Porosimetry 47
2.2.3. White light interferometry 51
2.2.4. X-ray diffractometry 51
2.2.5. Inductively coupled plasma mass/optical emission spectrometry (ICP-MS/OES) 52
2.2.6. Laser ablation (LA) in chemical analysis (LA-ICP-MS) 53
2.2.7. Raman spectroscopy 54
2.2.8. X-ray photoelectron spectroscopy (XPS) 56

2.2.9. Mechanical Characterization 58
2.2.9.1. Three-point bending test 58
2.2.9.2. Ball-on-three-balls (B3B) test 60
2.2.9.3. Determination of characteristic flexural strength 67
2.2.10. Permittivity measurements 68
2.2.11. Design of experiments (DOE) 69
2.2.12. Optical microscopy 69
2.2.13. Gravimetric measurements 69
2.2.14. Geometrical measurements 69

3. POROSIFICATION OF GC LTCC AND FERRO L8 WITH H_3PO_4 71

3.1. Investigation of the porosification of Ferro L8 LTCC with H_3PO_4 72
3.1.1. Morphological and chemical characterization analyses for Ferro L8 LTCC . . 72
3.1.2. Investigation of the etching mechanism (kinetic analysis) for Ferro L8 LTCC 83
3.1.3. Mechanical characterization of the Ferro L8 LTCC substrates by 3-point bending test 86
3.2. Investigation of the etchant pH and concentration on the porosification of GC LTCC 89
3.2.1. Impact of pH value 89
3.2.2. Impact of etchant concentration 99
3.2.3. Permittivity measurements 104

4. ALKALINE SOLUTIONS AS ALTERNATIVE ETCHANTS FOR LTCC POROSIFICATION 106

4.1. Porosification of GC LTCC with KOH 107
4.2. Ferro L8 Porosification with NaOH 116
4.2.1. Morphological and chemical characterization analyses 117
4.2.2. Investigation of the etching mechanism (kinetic analysis) 122

4.2.3. Modelling of etching parameters by DOE 130

5. IMPACT OF FIRING TEMPERATURE ON THE PHASE COMPOSITION AND POROSIFICATION OF LTCC 132

5.1. *In-situ* high-temperature XRD measurements 132

5.2. Morphological and chemical characterization 134

5.3. Etching treatment 144

6. DETERMINATION OF FLEXURAL STRENGTH OF LTCC SUBSTRATES BY BALL ON THREE BALLS METHOD 147

6.1. Sample Preparation 147

6.2. Morphological characterization of *as-fired* tapes 149

6.3. Wet chemical etching of the *as-fired* samples 152

6.4. Determination of characteristic flexural strength by the B3B method 154

7. POROSIFIED LTCC SUBSTRATES FOR GREEN ENERGY PRODUCTION 157

7.1. Sample Preparation 158

7.2. Blank test 159

7.3. Reduction at different temperatures (porosified LTCC) 160

7.4. Comparison of results 165

7.5. Long-term activity measurement 166

8. CONCLUSIONS AND OUTLOOK 167

REFERENCES 171

List of Figures 194

List of Tables 205

Nomenclature **207**

List of Publications **212**

Chapter 1.

INTRODUCTION

1.1. State of the art and motivation

Microwave frequencies were initially utilized mainly for military and space applications. In recent years with the significant and rapid progress in the Internet of Things (IoT), the Tactile Internet (5G technology), sensors technology, intelligent transport systems, and wireless communication, the demand for passive and active microwave components (resistors, capacitors, inductors, filters, antennas, *etc.*) is continuously increased [1–4]. These devices require enhanced integrability, processing speed, and performance, as well as applicability at a higher frequency range. At the same time, the demand for high volume and miniaturized circuit fabrication has led to a major development in integration technologies by moving towards three-dimensional substrate and packaging technologies. Low temperature co-fired ceramics (LTCC) technology is a viable technology to effectively meet these demands [5]. Dielectric properties of LTCC, especially when used in high-frequency electronic modules, are one of the most important factors determining the system performance.

With the increasing frequency bands in use, *e.g.* short-range and long-range automotive radar systems in the 77–79 GHz band, for the integration of patch antennas with optimized radiation and micromachined structures operating at desired high frequencies, LTCC substrates with separate areas of tailored permittivity are highly preferential. As low permittivity areas below the microstrip grid array antennas enhance both the bandwidth and efficiency of radiating elements such as in micro patch array antennas, high permittivity areas, on the other hand, allow for a compact feeding circuit design [1, 2, 6–9].

Besides, LTCC technology has advanced beyond the microelectronic circuit industry and is currently used for a variety of applications. A very important and promising application of LTCC technology which stems from the ability to create three-dimensional structures using multiple layers of tapes

is the fabrication of LTCC-based microreactors (μRs) [10, 11]. Porosified LTCC due to its much higher surface area compared to dense LTCC can be an interesting candidate for such applications.

1.2. Theory and basics in LTCC technology

The LTCC technology has experienced a significant market growth in the last two decades, particularly in microwave applications and automotive electronics. However, to expand the application fields of LTCC and to meet the high-quality standards, innovations in raw material development and ceramic processing as well as detailed knowledge about the sintering and densification behaviour, phase development, and the microstructure of LTCC tapes are necessary [8, 12]. In this section, both theoretical background and important basics in LTCC technology are given.

1.2.1. Inorganic, non-metallic materials

Solids depending on their crystalline structures are divided into two main categories: crystalline and amorphous. In crystalline solids, a long-range order can be found in which the structure repeats itself in form of a specific lattice. In contrast, ”amorphous” or “non-crystalline” solids lack this long-range order due to their random nature. According to the network theory of Zachariasen [13], cations can have different functions in glass structures; network formers build the glass-body, network modifiers change the glass network and intermediates can act either as former or modifier [14]. The difference in the crystalline and amorphous network in silicate networks has been illustrated in Figure 1.1. As shown in this Figure, for the crystalline network a long-range order of the atomic arrangements can be observed, but for the amorphous network the order found to be short-range.

Ceramic materials comprise ionic or covalent bonds or a mixture of both. While due to the electron pair sharing, the covalent bonding is categorized by the formation and overlapping of orbitals, in an ionic bonding due to electrostatic attractions an electron transition takes place between two atoms so that both atoms are oppositely ionized [15]. An important feature of ceramics is their extremely high melting point. Glass materials, on the other hand, are amorphous inorganic which are most often formed by thermal quenching (rapid cooling) from the molten state. Ceramics as substrate have a widespread in microelectronics where alumina (Al_2O_3) is a standard substrate material. Alumina plays an important role in hybrid circuit technology where thick-film, thin-film and various joining technologies such as glueing, are used to assemble microelectronic circuits and microsystems. Chemical inertness, mechanical stability and surface quality are of major importance. Adjusting the thermal expansion to silicon is also relevant, otherwise, the thermo-mechanical stress can damage the circuitry or even lead to a complete failure [16, 17].

LTCC material is typically composed of non-crystalline glass and one or more crystalline ceramic

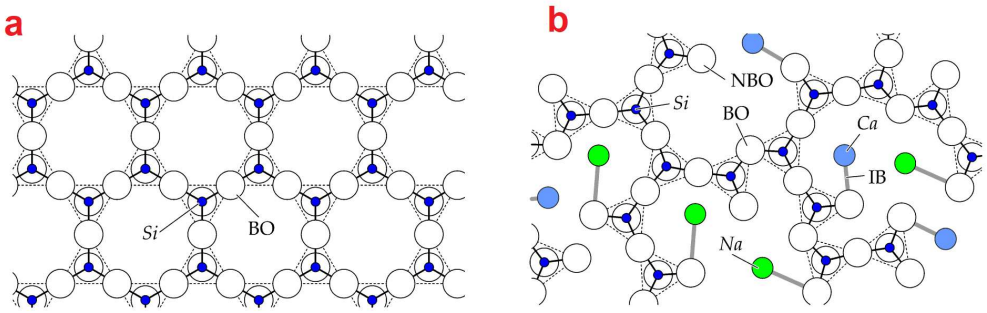

Figure 1.1: Comparison of **a)** amorphous and **b)** crystalline silicate networks. Si: silicon, Al: aluminum, Ca: calcium, Na: sodium, BO: bridging oxygen, NBO: non-bridging oxygen, IB: ionic bond[17].

filler and when exposed to adequately high temperatures, depending on the LTCC type which will be discussed later, additional crystalline phases are formed. The corresponding size of the resulting crystals depends on the heat treatment profile. This type of material has enhanced mechanical stress resistance, stiffness, and thermal shock resistance and requires lower sintering temperature in comparison to pure ceramics. As a consequence, LTCC is an advanced composite of glass and ceramics which combines the characteristic properties of both components and therefore, due to its unique dielectric, thermal and mechanical properties, has attracted massive interest in the last two decades. The microstructure of most LTCC materials consists of both glassy and crystalline phases, but the fraction of both crystallographic phases can strongly vary.

1.2.2. LTCC multilayer technology

Several technologies have been developed to fabricate multi-chip modules (MCMs). An MCM module is a hybrid circuit, which can contain different types of components and technologies. Thus, MCM technology allows for better integration of components when compared to a discrete and planar integration. The MCMs are divided into three main groups with respect to their manufacturing process type: MCM-D, MCM-L, and MCM-C. In MCM-D (deposited MCM) the modules are deposited on the base substrate using thin-film technology. This technique is especially suitable for the realization of fine structures. MCM-L (laminated MCM) is a multi-layer using laminated printed circuit board (PCB) technology. This technology allows for high-density integration and can be characterized by a simple manufacturing process and low-cost materials. However, this technology is based on organic materials such as FR4 and typically do not show thermal performance and are frequency limited [18–21].

MCM-C or ceramic substrate MCM is divided into two main variants of thick film and co-fired ceramics. While thick-film modules are fabricated by starting with a fired ceramic base material (typically Al_2O_3 and AlN), co-fired ceramics are fabricated with unfired green tape sheets which are fired after processing. In thick-film technology, the ceramic substrate is laser drilled to produce via

holes. Next, by using screen-printing technique metal conductors are created. Resistors, dielectrics, or additional metal layers can also be printed and fired. As thick-film technology enables only one level of layer, the integration density in this technology is relatively low when compared to the multilayer board. Co-fired ceramic substrates are fabricated through two separate processing phases including material preparation and green tape processing which will be discussed further.

LTCC can be most beneficially used for the realization of highly integrated and multifunctional microelectronic devices and robust substrates. This technology provides a way to achieve a multi-chip substrate using single sheets by applying conductive, dielectric and/or resistive pastes. The single sheets are then laminated together and co-fired in one step [22]. Basically, LTCC evolved in the 1980s from a very similar system which is called high temperature co-fired ceramic (HTCC). HTCC technology is based on alumina sintered at higher temperatures of around 1600 °C, and thus only high loss conductors with very high melting points such as Tungsten (W) and Molybdenum (Mo) can be employed. However, at high frequencies, for reliable and high-performance devices the conductors should exhibit high electrical conductivity, wire bond compatibility, high compatibility with other system-related materials, such as silicon, good electrical and mechanical integrity and good adhesion to the substrate which cannot satisfactorily fulfil by HTCC technology. The addition of glass to the ceramic powder in LTCC results in a significant reduction of sintering temperature to below 1000 °C (typically in the range of 850-900 °C), while the ceramic filler is primarily responsible for the adjustment of dielectric, mechanical, and thermal properties. The low sintering temperature allows for the co-firing of LTCC green tapes with low-resistivity conductors, such as Au, Ag, Cu, and their alloys which all have low melting points close to 1000 °C. The high conductivity of these metals enables rapid signal transmission between modules while minimizing energy loss [22]. Some of the commonly used conductors which are compatible with HTCC and LTCC are presented in Table 1.1.

Table 1.1: The commonly used conductors with LTCC and HTCC materials [4].

	Firing temperature *°C*	**Conductor**	**Melting point** *°C*	**Conductivity** *S/m*
LTCC	<1000	Cu	1083	5.9×10^7
		Au	1063	4.1×10^7
		Ag	960	6.2×10^7
		Ag-Pd	960-1555	-
		Ag-Pt	960-1186	-
HTCC	>1600	Mo	2610	1.9×10^7
		W	3410	1.8×10^7
		Mo-Mn	1246-1500	-

LTCC is best suited for applications which can take advantage of one or more of the following: good electrical performance; dimensional and electrical stability under harsh environment (temperature, pressure, moisture, and mechanical stress); 3D capabilities (for the realization of channels and cavities); hermeticity; high density (embedded passives and bare semiconductor die); matched CTE

with semiconductors; effective thermal managements (through thermal vias); multiple assemblies and packaging solutions. Therefore, based on characteristic features of each technique, LTCC technology offers several advantages over other popular substrates technology. Some of these advantages are summarised in Table 1.2.

Table 1.2: Some advantages of LTCC over other commonly used substrate technologies [23].

LTCC advantages over PCB	LTCC advantages over HTCC	LTCC advantages over thick-film
- Lower CTE	- Lower resistance metallization	- Cavities* and high layer number
- Superior high-frequency performance	- Higher number of layers	- Higher breakdown voltages between layers
- Higher integration density (embedded passives and higher layer count)	- Lower tooling costs	- Mixed metals easier to control – hermetic encapsulation of low cost silver interconnect
- Higher reliability (interconnections elimination by integrating passives)	- Shorter prototype cycles	- Surface topology smoother
- Smaller package size due to integration	- More embedded passive option, *i.e.* alternate dielectrics	- Surface topology smoother
- Cost effective for dense package due to parallel processing of layers	- Higher flexibility of post print metal and dielectric options	
- Hermetic packages possible	- Lower dielectric constant ceramic tapes available	
	- Higher level of part complexity and flexibility	

* Cavities allow for: localised hermetic sealing; reduced thickness under die (reduced thermal paths); short, profiled wire-bonds.

The microstructure of most LTCC materials consists of both glassy and crystalline phases. While alumina powder is the most often-used ceramic filler, other types of fillers (such as mullite [24], cordierite [25], AlN [26], barium titanate, and ferrite[27]) can also be used to achieve specific properties [28]. The glass phase consists mainly of borosilicate glass [29–32], which has a low softening point. Besides, other constituents (such as PbO, BaO, Na_2O, K_2O, CaO, or ZnO) are added to adjust the material properties of LTCC. Depending on the amount of glass in the tape composition, the LTCC shows a characteristic sintering mechanism. Therefore, it can be categorized into four main categories which are illustrated in Figure 1.2 [8, 33].

Most of the current commercial LTCC materials hold a glass fraction larger than 40 vol% and therefore, can be classified in either “glass-ceramic composites (GCC)” or “glass-ceramics (GC)” category [33]. In the GC type LTCC, the glass crystallizes by about 50% to 80% of the residual glass content after sintering [8, 34]. A typical example of this LTCC class is Ferro A6, which crystallized to wollastonite ($Ca_3[Si_3O_9]$) in a Ca-B-Si-O glass. In the GCC type, *e.g.* Heraeus CT 700, Du Pont 951, the crystallized fraction is only 20% to 50% of the residual glass content. Despite the occurrence of crystallization processes, the sintering of GCC is referred to as “non-reactive” because it is assumed that the emergence of new phases is not decisive for the densification. The densification of GCC during the sintering process takes place in three steps: liquid phase sintering through softening

and particle arrangement, solution precipitation and the assembly of the particles [35]. In LTCC technology, the minerals anorthite ($Ca[Al_2Si_2O_8]$), celsian ($Ba[Al_2Si_2O_8]$), albite ($Na[AlSi_3O_8]$), and cordierite ($Mg_2Al_3[AlSi_5O_{18}]$), are considered as materials with low dielectric losses, which makes them interesting for applications at high frequencies [36–39]. The degree of crystallization also affects the dielectric properties of the glass ceramic [40, 41]. Feldspars like anorthite and celsian, are also used as promotors of eutectic melting too [42].

Anorthite is a feldspar from the class of plagioclase that can form in Al-rich glass at around 1000 °C [39, 43]. In alkali-free calcium-aluminoborosilicate glasses, however, it can form between 900 °C and 950 °C from a wollastonite phase [31]. By adding other components such as corundum particles, the formation temperature can be even further reduced [44].

Typically, the Al_2O_3 dispersed in the glass matrix has a significant influence on the sintering process and the formation of new phases [4, 45]. In the crystallization of anorthite, a solution of the Al_2O_3 is being formed. In alkali-free calcium-alumo-borosilicate glasses, this dissolution at a temperature of 1050 °C can lead to a decrease of Al_2O_3 from about 33% to 10% [31, 44]. By the diffusion of Al from the corundum particles its concentration in the vicinity of the particles increases. This provides a favourable condition for the crystallization of anorthite, for which a higher Al content is required than can be provided by the base glass [46, 47]. At the same time, through devitrification, a matrix with amorphous residual glass is generated [34]. The addition of corundum is generally regarded as “reducing the tendency to devitrify” [4]. The size of the particles again has a major influence, which should be in the range of 0.5 μm to 3 μm [48]. Similar to anorthite, the formation of celsian also requires a high Si to Al ratio.

In addition, LTCC can also be produced with a low glass amount (about 10 vol%), which is typically referred to as “glass bonded ceramics (GBC).” In this configuration, to allow for a solution re-precipitation process below 950 °C, very low viscosity glasses with high reactivity against the crystalline phase are required. For a glass content of $>$ 60 to 70 vol% and at higher sintering temperatures, the nature of the dispersed component no longer influences the densification [28, 49]. From a glass content of less than 40 vol%, the densification is no longer ensured solely by the flux of the viscous mass, but also by the precipitation of new phases from the melt. This glass content limit of 40 vol% is also given by some authors as a transition from GCC to the GBC class [44], while others assume other limits between 20 vol% and 40 vol%. GBC contains only about 5% to 20% glass to maintain the sinter flow [8, 50]. Also, more recently “glass-free” LTCC was introduced, *e.g.* crystalline phases in the system Bi–Ti–Si–O.

Preparing high-quality green tapes is crucial for any category of LTCC technology since the quality of the final modules depends on the performance of the “green tape”. Tape casting is the main manufacturing process for fabricating LTCC green tapes, and after this process, important properties of the tapes are fixed. Typically, LTCC is cast from slurries of glass powder, ceramic, solvent, dispersant, and binders/plasticizers [22, 51]. The organic binders and plasticizers are used in order to control the viscosity of the slurry and binding of the powder to form the green tape. As

illustrated in Figure 1.3, the desired slurry is cast using a doctor blade, where the slurry is spread onto a moving tape carrier with a smooth surface. The doctor blade controls the tape thickness, which is typically 50 to 500 μm. After evaporation of the solvent, flexible and single layers of LTCC green tapes are obtained [51]. A profound control over the doctor blade is needed to avoid errors such as warpage and excess tape thickness [22, 52, 53]. Degasification helps to get rid of bubbles in the cast tape and it is followed by filtering through a sieve to discard common faults formed during this process. The coil movement system conveys the plastic carrier in a straight line at a constant speed.

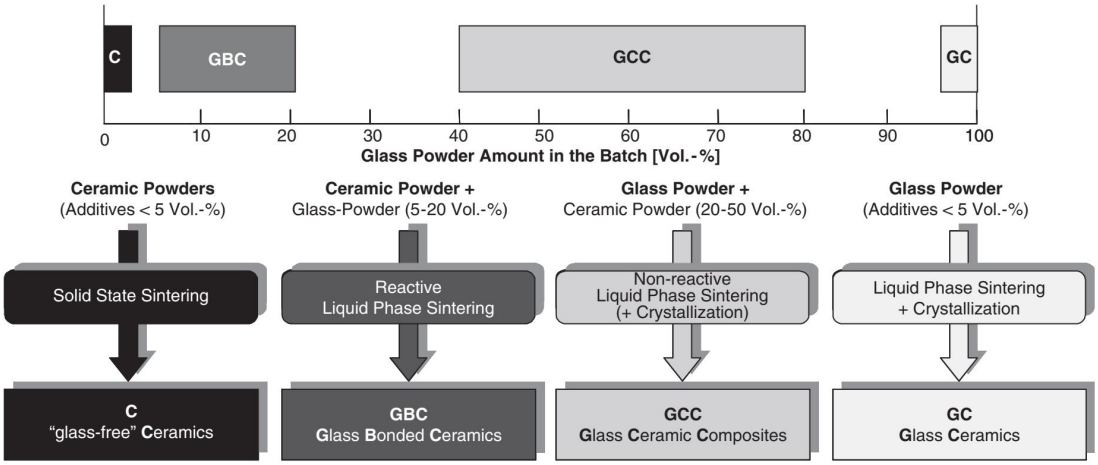

Figure 1.2: Different types of LTCC—composition, raw materials, and sintering mechanisms [8, 33].

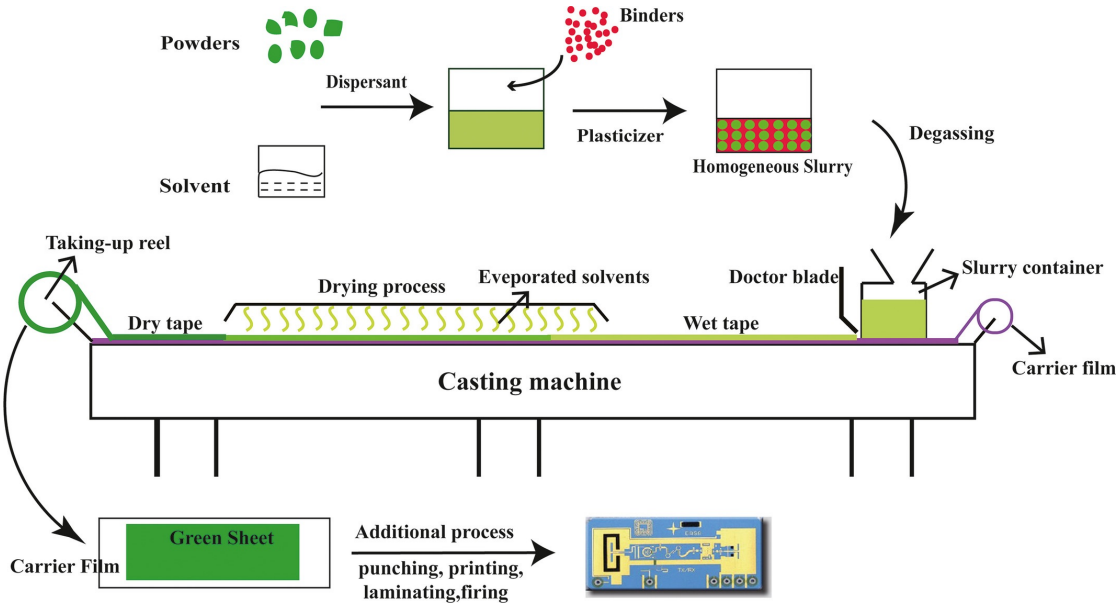

Figure 1.3: Tape casting process for the ceramic slurry [22, 53].

After the fabrication of LTCC green tapes, they are cut to specific dimensions and alignment holes are introduced. Using mechanical punching, drilling, laser formation or photo-patterning, the vias for interconnection between different layers are patterned into each sheet and filled with a special conductor ink. Conductors and passive components such as resistors and capacitors are placed by using the screen-printing technique. With the help of alignment holes on every distinct sheet, alignment is achieved. Several layers of these printed green tapes are stacked and laminated under heat and pressure, while the organic resin in the green sheets acts as glue for bonding the layers during lamination. During lamination, a single substrate is made from the stacked LTCC sheets and thick film structures. The whole LTCC substrate process is schematically represented in Figure 1.4a. After lamination, the co-firing is made to burn out the organic components and densify the ceramic composition. Since different constituents, tapes and pastes are sintered together simultaneously, the process is called co-firing. Throughout the co-firing, ceramic and conductor components are sintered together into a rigid multilayer structure. A typical cross-section of the LTCC module with buried passive components, thermal interconnections and cavities is shown in Figure 1.4b.

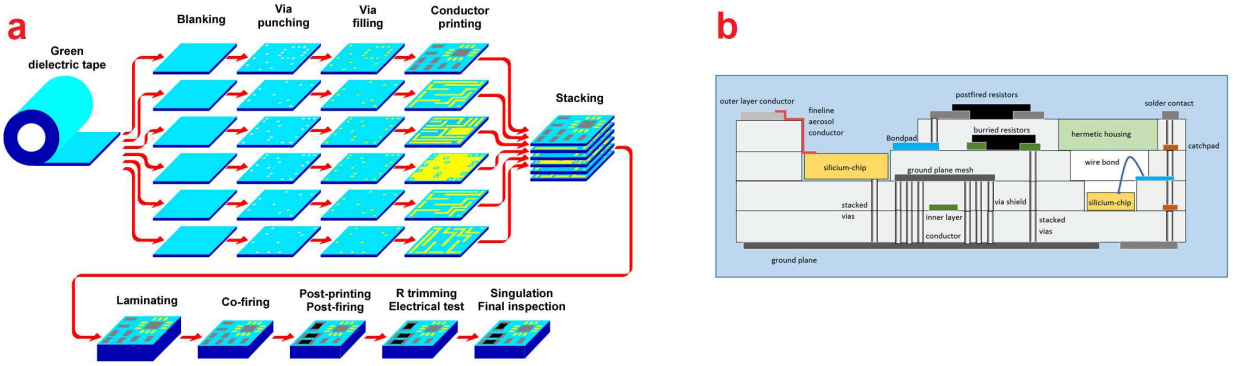

Figure 1.4: a) A typical LTCC packaging process [54] **b)** Cross-section of an LTCC module [55].

A typical firing profile consists of five regions as shown in Figure 1.5 preheating, burning, heating, sintering, and cooling phase [56, 57]. All these steps are typical for commercial LTCCs with only small variations in heating and cooling rates, peak temperatures (maximum temperature in the firing profile), and dwell times which are caused by their different compositions and additives. In the preheating phase, the absorbed moisture is evaporated. Next, organic components are burned out. Further heating of the samples in the peak temperature results in the sintering process. Afterwards, samples are facing preferably a slow cooling phase in order to prevent extreme thermal stressing and cracking. Supplementary active or passive components can be deposited on top or bottom surfaces of the finished LTCC structure after co-firing. LTCC structures can also be separated afterwards using a dicing saw, ultrasonic cutting or laser cutting [12, 58, 59].

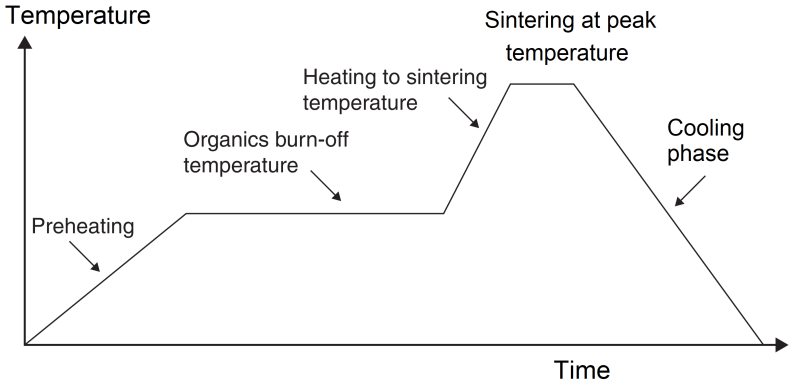

Figure 1.5: A typical LTCC firing profile.

1.2.3. Physical and chemical properties of LTCC materials

LTCC is most favourably used as substrate for micromachined devices operated at high frequencies typically ranging up to the microwave region. Although other types of high-density, multilayer substrates based on organic laminates are available, further outstanding features of LTCC for such application scenarios are the excellent thermal conductivity compared to organic materials and a coefficient of thermal expansion (CTE) close to Si and GaAs. LTCC materials show attractive thermal, mechanical, and dielectric properties, as well as high resistance to humidity, salt spray, and radiation. In addition to these benefits, the easy machining of LTCC tapes and the applicability of the multilayer approach based on LTCC green tapes also plays an important role in its multi-purpose application in microtechnology. These special features allow for the realization of robust and compact 3D structures with highly scalable manufacturing methods (*e.g.* microfluidic channels) as well as the embedment of passive electrical components such as capacitors, resistors, inductors, and conductor lines into the LTCC body [60–63]. For example, the radiation sensor shown in Figure 1.6 represents a multi-layered microelectronic device with a high integration and interconnection level.

CTE is a key parameter as it strongly affects the reliability of attached semiconductor chips. To avoid cracks in the die attach or interconnection rupture of the bond wire, the substrate must exhibit a CTE value close to that of Si and GaAs. LTCC substrates meet this demand. Compared to HTCC substrates, LTCCs have a CTE more similar to the CTE of printed components and soldered chips, what promises long-term stability of the interconnects. Furthermore, the thermal conductivity of LTCC materials is much higher than organic PCBs. This is an important feature as the thermal conductivity measures the ability of the material to conduct heat. Although the thermal conductivity of LTCC materials is lower than the HTCC materials (alumina), it can be significantly improved by using thermal vias. For comparison, the technical characteristics of HTCC, LTCC, and PCB

technologies are given in Table 1.3.

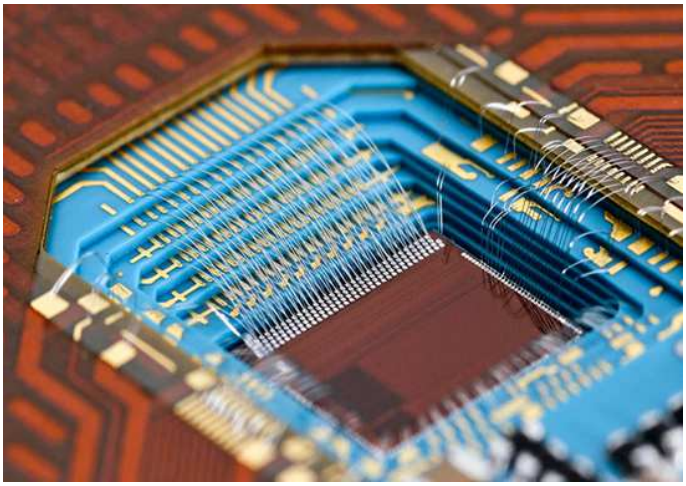

Figure 1.6: An LTCC-based radiation sensor of a satellite [64].

Table 1.3: Technical characteristics of LTCC, HTCC, and PCB substrates [65]. Typical values are listed.

	PCB	**LTCC**	**HTCC**
Volume resistivity (RT*) *ohm m*	>1011	>1012	>1012
Break down voltage $V\ \mu m^{-1}$	40	>40	15
***x,y* CTE** $ppm\ K^{-1}$	16	6	7
***z* CTE** $ppm\ K^{-1}$	60	6	7
Flexural strength *Mpa*	-	210	350
Thermal Conductivity, (RT to 400 °C) $W\ m^{-1}\ K^{-1}$	0.1	3	20
Water absorption *%*	<0.3	0	0
Hermeticity *Torr*	$>10^{-3}$	$>10^{-8}$	$<10^{-8}$

* Room temperature

Moreover, the mechanical properties of LTCC are very important during the manufacturing process, as well as for the later use of the LTCC modules, *e.g.* for manufacturing complex three-dimensional structures with buried cavities and channels or so-called micro-electro-mechanical systems (MEMS) [47]. The ceramic filler material in LTCC contributes the most to its mechanical strength. Therefore, the mechanical strength mainly depends on the type, the ceramic particles density, and the size of the ceramic particles. Basically, increasing the amount of ceramic filler leads to an increase in flexural strength, what in turn means that the flexural strength of LTCC materials is lower than the flexural strength of the pure ceramic component. Therefore, moderate flexural strength is one of the weaknesses of LTCC when compared to HTCC technology (see Table 1.3). Applying ceramic components with fine particle diameter results in higher flexural strength values. Another parameter that affects the flexural strength of LTCC substrates is the porosity of the substrate. The porosity can be initially formed during the firing process or be induced by an etching process. Regardless of the type and source of the flexural strength of the substrate decreases with the

increase of porosity. Varying the parameters mentioned above leads to LTCC composites with significantly different flexural strength properties. It should be also considered that increasing the flexural strength of the material might have a negative impact on firing temperature and dielectric properties as they are also related to the type and amount of ceramic filler.

To increase the mechanical strength of LTCC materials it is also possible to strengthen the glass phase. This can be achieved either with the crystallized glass or the ion exchange method. In the first approach, crystals with low thermal expansion which are formed due to compressive stress are precipitated into the amorphous glass matrix. Either the enveloping glass material crystallizes directly, or the precipitated crystals are formed based on reactions with the ceramic material during sintering. The second method induces compressive stress into the material by exchanging sodium ions with larger ions such as potassium. For this purpose, the glass is immersed for several hours in molten salts containing potassium ions [4, 34, 66, 67].

Also, as already mentioned the dielectric properties of substrate materials are very important especially when targeted for high-frequency operation. The LTCC substrate offers excellent dielectric properties, such as relative permittivity and dissipation factor, and low conductor loss, including high stability up to millimetre-wave frequencies. The relative permittivity also called dielectric constant is the real part of complex permittivity (ε') of the dielectric substrate (see Equation 1.1), and is affected by the LTCC composition. The relative permittivity is indeed a dimensionless ratio between the permittivity of the material under consideration and that for vacuum ((ε_0 = 8.854 $\times 10^{-12}$ F m^{-1}). The imaginary part of complex permittivity (ε'') is called dielectric loss and is generally expressed in terms of the dissipation factor or loss tangent (see Equation 1.2). Typically, the dissipation factor of LTCC materials is much lower than those of organic materials.

$$\varepsilon = \varepsilon' - j\varepsilon'' \tag{1.1}$$

$$\tan\delta = -\varepsilon'/\varepsilon'' \tag{1.2}$$

Besides the dielectric loss, high-frequency transmission loss occurs as a result of losses in the conductor lines. The latter loss mechanism depends predominantly on the skin depth δ_s and the surface roughness of the substrate. The skin depth (see Equation 1.3) represents the characteristic quantity of how deep the RF power penetrates the conductor whereas the reference is the conductor surface. At low frequencies, the current is uniformly distributed across the conductor cross-section. As the frequency increases, however, the RF current starts to concentrate surface-near. This results in a conversion of RF energy into waste heat, and thus increases the insertion loss [5].

$$\delta s = \frac{1}{\sqrt{\sigma\pi\mu f}} \tag{1.3}$$

where σ and μ are the conductivity and permeability of the metal, respectively, and f is the frequency. As already discussed, the low firing temperature of LTCC materials allows for the use of low-resistivity conductors such as Cu, Ag, and Au. However, the roughness of the conductor and the LTCC substrate has to be taken into account additionally, as they can substantially increase the conductor loss at millimetre-wave frequencies.

Depending on the desired physical, chemical, and electrical properties of the LTCC (*e.g.* dielectric constant, dielectric loss, thermal conductivity, and shrinkage ratio), different types and amounts of components can be used in LTCC manufacturing process. Some of the important commercial LTCC tapes, their composition, and material properties are listed in Table 1.4.

Table 1.4: Properties and compositions of some commercially available LTCC systems before and after sintering [50].

Trade name	A6	L8	CeramTape GC	DP943	DP951	CT700	CT2000
Manufacturere	Ferro	Ferro	Ceramtec	DuPont	DuPont	Heraeus	Heraeus
LTCC type	GC	GCC	GCC	GCC	GCC	GCC	GCC
Glass Components	Calcium borosilicate	Barium calcium silicate	Alkaline earth aluminosilicate	Calcium aluminoborate, Lanthanum calcium borate	Calcium lead silicate	Alkaline earth aluminosilicate	Calcium alumino titanate silicate
Dispersed phase		Corundum	Corundum	Corundum	Corundum Willemite Quartz	Corundum Rutile	
Permittivity	5.7±0.2	7.4±0.2	7.9±0.6	7.4	7.8	7.5-7.9	9.1±0.1
Composition after sintering	Calcium Silicate		Corundum/ Anorthite	Corundum/ Calcium	Corundum/ Anorthite	Corundum/ Celsian	Corundum/ Anorthite

1.3. Different approaches for the permittivity reduction

As already discussed, the possibility of integrating passive components combined with the compatibility to surface-mounted active semiconductor devices makes LTCC a highly interesting substrate for high-frequency applications. Therefore, a locally modified permittivity of the substrate would be highly preferential in order to decrease the losses of radiating elements such as patch antennas [68].

A controlled reduction in permittivity can be achieved by the introduction of low permittivity material components into commercially available high-k LTCC substrates. To do so, the combination of a commercially available LTCC with organic low-k substrates, such as Rogers/RT Duroid 5880, is a possible approach. This approach has been reported in a simulated design by Sethi *et al.* [69] for a compact antenna (30 x 30 x 6.9 mm^3) based on a hybrid structure. The feed portion was on a Ferro A6M LTCC substrate, while the square patches were deposited onto Rogers RT-5880 substrate layers.

Low permittivity polymer materials can also be utilized in combination with high-k LTCC substrates. Bittner *et al.* [70] investigated the permittivity of a tailored compound material consisting of a polyimide matrix in which hollow glass micro-spheres with a mean diameter of 30 μm are implemented as filler material. By adding this filler material to the liquid polyimide precursor with filler to polymer ratios of 1:7.5 and 1:10, the thickness of one single layer could be increased from a maximum of about 10 μm for pure polyimide films to above 80 μm so that cavities in LTCC substrates could be filled more reliable. Basically, the film thickness depends on the spin-coating speed as well as the micro-sphere content. The dielectric constant of the complete substrate comprising the LTCC and the compound material was measured with a ring resonator in micro-strip configuration. From the resonances occurring in the transmission S-parameter |S21| spectrum between 1 and 10 GHz, the relative effective permittivity was determined. Based on this approach the measured permittivity is a combination of both LTCC and polymer materials, and for 820 μm thick LTCC substrates the permittivity could be reduced from originally 7.8 of pure DuPont 951 tape down to 6.6.

These approaches, however, entail inherent disadvantages associated with bond wires such as parasitic inductances, expensive and complicated manufacturing processes, as well as different CTE values for the inorganic LTCC and the organic polyimide which result in thermo-mechanical stress generation and thereby may lead to a reduced lifetime of the device.

Also, air with the lowest permittivity value (ε_r=1), can be introduced into the LTCC substrates to reduce permittivity. The air can be implemented into the LTCC through different approaches, for example, by lowering the overall firing temperature to decrease the bulk density of the LTCC. However, this method which is also referred to as “partial sintering” has fundamental problems in controlling the essential features of porosity such as shape, size, distribution, and connectivity of the pores. The fabricated substrate is poor in mechanical strength since the ceramic particles are allowed only to form the neck and create a skeleton [71]. Thus, in fabricating desirable LTCC substrates, complete densification is necessary for achieving good mechanical properties.

Air can also be implemented by the addition of “pore former” materials such as poly (methyl methacrylate), polystyrene, spheroidal graphite, carbon black, and sucrose in the slurry preparation process and before tape casting [71, 72]. Pore formers can be burned out and leave more stable pores in the LTCC micro-structures after the firing process which resemble the features of the pore former particles even after sintering at elevated temperatures. Since the size, shape, and thermal properties of the pore formers can be controlled, this technique has more control over the characteristics of the porosity as well as mechanical properties of the LTCC. However, this is not a practical solution either, since, in addition to the aforementioned issue, different shrinkage behaviour compared to a dense LTCC layer is another limitation of this approach. Besides, these approaches are pre-firing processes and can be applied only to the slurries, not to commercially available tapes.

1.3.1. The state-of-the-art approach for the porosification in one layer

The problems mentioned in the previous section could be overcome by the development of a porosification technique which allows for a local permittivity reduction of LTCC substrates. This unconventional approach which was first reported by Bittner and Schmid is essentially based on the local air embedment in the LTCC through a wet-chemical etching process and thereby replacing high permittivity components by air which results in a decrease in the overall permittivity of the LTCC tape [73]. In the latter work, phosphoric acid was used for selective etching of the anorthite phase in commercially available Dupont 951 LTCC. Anorthite with the chemical formula of $Ca[Al_2Si_2O_8]$ is an end member plagioclase feldspar along with albite $Na[AlSi_3O_8]$. Anorthite forms a continuous three-dimensional silica tetrahedral framework like orthoclase feldspars, but half of the silicon ions are replaced by aluminium ions when calcium ions come in to restore the electrical neutrality [74]. The anorthite phase which is crystallized during sintering in the areas surrounding the Al_2O_3 grains shows high decomposition with phosphoric acid and a maximum porosification depth of about 40 μm was reported in previous research works. After longer exposure times, the Al_2O_3 dissolution is more pronounced. The penetration depth depends on important parameters such as the bath temperature and the exposure time [75]. In this approach by employing an accurately masked LTCC substrate a local permittivity reduction in a single LTCC layer is possible. Since this process is directly applied to the *as-fired* LTCC before final metallization, no alteration of the tape composition or the fabrication process is required which is considered as a major advantage of this technique. By employing this post-firing process, areas with different relative permittivity values can be realized, enabling the direct integration of, *e.g.* patch antennas together with feeding circuits on the same substrate [76].

By increasing the degree of porosification, more air is introduced into the LTCC substrate, and thereby a further decrease in the overall permittivity is achieved. The degree of porosification can mainly be increased either through lateral or axial growth of the nanoscale pores. The lateral pore growth may lead to wider pore openings and increased surface roughness, *i.e.* degraded surface quality. However, since for realization of, *e.g.* patch antenna elements, the long-term objective is to apply metallization on the porous LTCC, a high-quality surface is of great importance because it would offer a sufficient bearing plane in combination with regularly allocated openings for air embedment [77–80]. Also, with increasing frequency in the GHz range the skin depth, derived for ideally smooth conductor surfaces, decreases to the order of the surface roughness, thus causing a nearly linear increase in conductor loss. Therefore, the axial growth of the pores through deep etchant penetration while preserving the surface quality would be more suitable when targeting subsequent metallization. However, the mechanical properties of the LTCC will also be affected by the etching process. Deep porosification can lead to a significant reduction of mechanical stability and consequently results in a reduced lifetime of the substrate which is disadvantageous for any application. Therefore, an etching process which results in a controllable porosification depth and a high surface quality together with the preserved mechanical strength is the goal of this study.

Since its development in 2009, this approach has been investigated in various acidic etchant-LTCC systems at different conditions, and important information on the porosification mechanism has been obtained [68, 73, 79, 81–83]. Concentrated phosphoric acid at elevated temperatures of 100 °C and above was reported to be the most effective etching solution for the porosification of LTCC substrates. Further investigations on the concentration and temperature-dependent etch selectivity, on the metallization of porosified LTCC substrates, as well as on the impact of porosification on thermal conductivity have been carried out. Also, useful models were presented for the characterization of effective permittivity reduction due to the porosification process. However, no significant improvement in the degree and depth of porosification had been achieved and the best results were obtained by applying the orthophosphoric acid etchant to the commercial 951 LTCC tape from DuPont (DP951), where a maximum porosification depth (d_p) of about 40 μm was achieved. Nonetheless, even this limited porosification depth imposes large pore openings, sharp pore edges, significant surface roughness, resulting in a rather corroded LTCC surface compared to the *as-fired* state [ref 34-37].

In order to overcome this drawback, alternative etching solutions, as well as etching conditions, need to be investigated. Therefore, this thesis is chaptered based on the different types of etching solutions and essential etching parameters. Since in literature, only acidic solutions (specifically orthophosphoric acid) have been examined as etchants for the wet chemical etching of LTCCs, the impact of pH seems to be a major missing parameter in previous research works. Therefore, a mechanistic study on the effect of this parameter was carried out which will be presented later in this thesis.

1.3.2. Porosity and surface metrology

Porosity – Due to the penetration of the etchant from the LTCC surface, an open porosity is created on its surface which is essential to be investigated. The porosity goes directly into the description of the roughness and also porous materials with the same apparent porosity, but with pores of different size and geometry react differently under the same conditions and. Therefore, investigation of the porosity is decisive for the assessment of surface quality, which strongly affects the metallization quality. Porosity and surface quality depend directly on each other and determine the effective permittivity reduction of the overall process.

Classification of pores is one of the basic requisites of the comprehensive characterization of porous materials. Pores can be classified based on their common characteristics such as size, shape, and accessibility of external fluids [84]. The “pore size” is a property of major importance in practical applications of porous materials. Different categories of pore sizes have been described in the literature however, the most commonly accepted classification is presented by the International Union of Pure and Applied Chemistry (IUPAC), in which pores are classified into macro-, meso-, and micropores. This classification is mostly based on the different mechanisms occurring in

the pores during N_2 isothermal adsorption at 77 K and 1 atm. Multilayer adsorption, capillary condensation [85], and micropore filling are the processes that relate to macropores, mesopores, and micro-pores, respectively. Pores with diameters less than 2 nm are considered as micropores, those with diameters bigger than 50 nm are macropores, and those with diameters between 2 and 50 nm are known as mesopores [86, 86].

In addition to their size, pores can be classified according to their accessibility from the environment (see Figure 1.7). The pores which are communicating with the external surface and thus are accessible for molecules from the surroundings are named open pores, like (b), (c), (d), (e) and (f). On the other hand, the pores which do not communicate with the external surface through an adsorbed molecule are called closed pores (a). This type of pores occurs for example because of the collapse of the outer shell due to the heating of a porous substrate. That is to say, the pores with a very small opening (smaller than the probe's molecular size) that cannot be penetrated by He at 303 K, are called "closed pore" [87]. Some pores which are open only at one end (c and d) are described as blind or dead-end pores and the ones which are open at two ends are named through pores, (b). The latter pores may not associate with adsorption and permeability of molecules, but they influence the mechanical and dielectric properties of solid materials [86, 88–90].

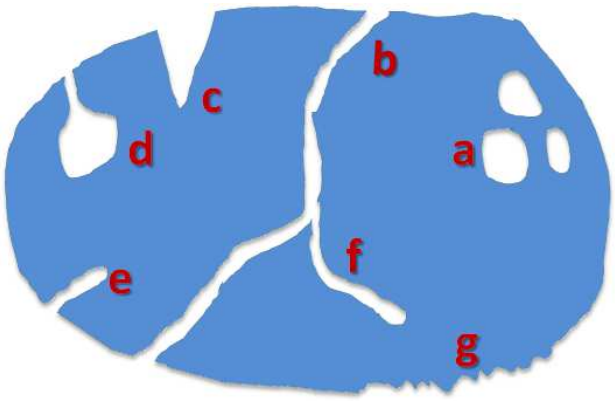

Figure 1.7: Schematic cross-section of different pore geometries.

Another possible classification of pores which is also used by IUPAC [89] is based on the pore geometry where the pores are divided upon the following geometrical shapes: cylindrical (b, e, and f), ink-bottle shaped (d), funnel-shaped (d), or slit-shaped. Close to, but different from the porosity is the roughness of the external surface, represented around (g). A rough surface is not considered to be porous unless it has irregularities that are deeper than they are wide.

Surface metrology – The surface roughness is part of the so-called "Shape deviations" of the real surface from its ideal shape. Generally, the measured primary profile entails deviations in the form of waviness and roughness. In material processing, roughness is often inherent, but waviness

reflects the deviations. As shown in Figure 1.8, with decreasing wavelengths (lateral structure distances), the waviness transforms into roughness. The cut-off wavelength λ_c describes exactly this transition wavelength between waviness and roughness [91, 92].

The roughness parameters are basically applicable to Primary, Roughness and Waviness profiles. They are denoted, depending on the profile, as; *P*, *R*, and *W* respectively, and the corresponding index which belongs to the parameter. The reference line can be selected in different ways such as the best-fit line, a compensating spline or polynomial curve, and by the use of appropriate wavelength filters. The latter is usually done by a digital Gaussian filter (DIN EN ISO 11562:1998) with an appropriate cut-off wavelength, λ_c, which separates the unfiltered primary profile to roughness and waviness (see Figure 1.9). At the cut-off wavelength, the filter reduces the amplitude of a sine wave to 50%. The reference line here results from the weighted arithmetic mean of the ordinate heights at each profile point. However, this is no longer applicable to surfaces with more pronounced valleys than peaks, since the reference line then shifts in the direction of the valleys.

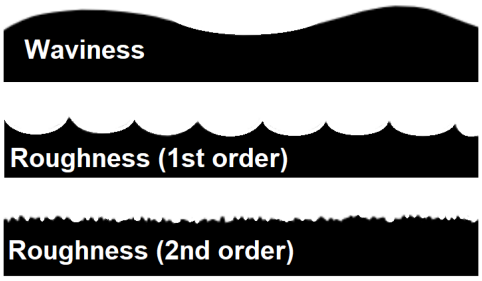

Figure 1.8: The transition from waviness to roughness with decreasing wavelength [93].

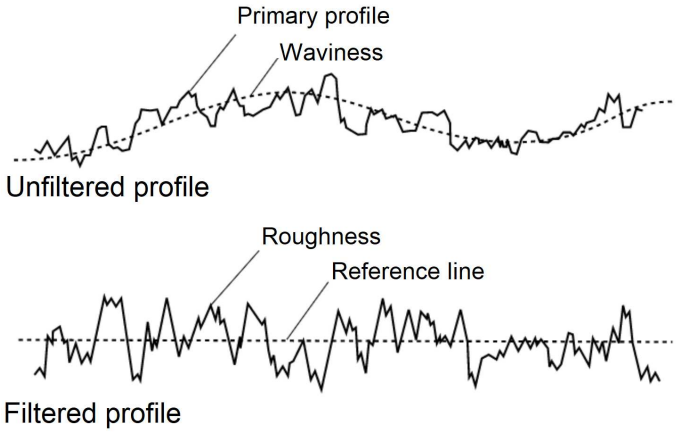

Figure 1.9: Unfiltered and filtered profiles [93].

The comparability of the roughness parameters depends on: 1) the lateral and vertical resolution of the measuring system, 2) the choice of the centreline or surface, 3) the length or size of the mea-

suring section or area, and 4) the filters used and, for example, cut-off wavelengths for separating the different form deviations.

Surface roughness can be defined by different parameters. Some of the most frequently used roughness parameters in engineering will be described here. For example, arithmetic mean value for line profiles R_{ar} is defined by:

$$R_{ar} = \frac{1}{l_r} \int_0^{l_r} |z(x)| \, dx \tag{1.4}$$

where *z(x)* describes the distance of the roughness profile from the centreline within the metering distance and l_r is the measured profile length [94]. In principle, R_{ar} which describes the average deviation of the profile from the centreline can be determined with all kinds of stylus instruments. The results of single metering points only scatter to a rather low degree, since the determination of R_{ar} is based on a strong averaging. However, it cannot give information about peaks and grooves, and it is unable to identify different profile forms.

The quadratic mean R_q, is the standard deviation or root-mean-square (RMS) roughness, is defined as:

$$R_q = \sqrt{\frac{1}{l_r} \int_0^{l_r} z^2(x) \, dx} \tag{1.5}$$

R_q is defined very similar to R_{ar} but it is more sensitive to large height deviations such as individual peaks and grooves [94]. Other often-used roughness parameters are listed in Table 1.5.

Table 1.5: Some commonly used roughness parameters and their definitions [94].

Parameter	Description
$\boldsymbol{R_t}$	Maximum peak to valley height of roughness profile within the evaluation length
$\boldsymbol{R_z}$	Mean peak to valley height of roughness profile within the evaluation length
$\boldsymbol{R_{max}}$	Maximum peak to valley height of roughness profile within the evaluation length
$\boldsymbol{R_p}$	Maximum peak height of roughness profile within the evaluation length
$\boldsymbol{R_v}$	Maximum valley depth of the roughness profile within the evaluation length
$\boldsymbol{R_c}$	Mean height of profile irregularities within the evaluation length
$\boldsymbol{R_{sm}}$	Mean spacing of profile irregularities of the roughness profile
$\boldsymbol{R_{sk}}$	Skewness of roughness profile (a measure of the asymmetry of the profile about the mean line)

1.3.3. Dissolution of minerals

The dissolution of minerals, the rate of dissolution, in particular, is of importance to several fields of endeavour including geochemistry, materials science and hydro-metallurgy. Knowledge of dissolution mechanisms can help to predict the behaviour of minerals in solutions, thus the rate can be accelerated or retarded, depending on the field of endeavour [95, 96]. The reaction kinetics of a mechanism is essentially described based on the slowest step in the reaction pathway which is called the rate-determining step (RDS). Also, the rate of dissolution is affected by the concentration of the reagents in solution and the bath temperature. This dependence is mathematically represented by the well-known Arrhenius equation [95]:

$$Rate = k[C]^n exp(\frac{-E_a}{RT}) \tag{1.6}$$

where [C] represents the concentration of a reactant, k is the rate constant, E_a the activation energy, R the gas constant, T the temperature, and n the order of the reaction. The order of reaction indicates how the rate of reaction depends on the concentration of the reactant.

Crystalline ceramics and non-crystalline glasses of similar composition often have a quite different dissolution behaviour showing that the atomic structure of the material plays an important role. A good example of the comparative behaviour of glasses and crystals of the same composition is provided by $NaAlSi_3O_8$, which occurs naturally as high-quality crystals of the mineral albite and which can be made into an aluminosilicate glass. As can be seen in Figure 1.10, the dissolution kinetics of the contributing elements are different for crystals and glassy structures[97, 98].

Crystalline ceramics and non-crystalline glasses of similar composition often have a quite different dissolution behaviour showing that the atomic structure of the material plays an important role. A good example of the comparative behaviour of glasses and crystals of the same composition is provided by $NaAlSi_3O_8$, which occurs naturally as high-quality crystals of the mineral albite and which can be made into an aluminosilicate glass. As can be seen in Figure 1.10, the dissolution kinetics of the contributing elements are different for crystals and glassy structures [97, 98].

Regardless of whether the source is crystal or glass, the uptake of Si into solution is almost. The parabolic shape to the curve results from the continued rise of pH rather than from diffusion-controlled kinetics. Sodium uptake from crystalline albite is almost one third Si removal as required from the formula, thus confirming a congruent dissolution of the crystal. The removal of sodium from the glass, however, is much larger than that of silicon suggesting that sodium is being leached from a depth in the glass in addition to its dissolution at the surface. The removal of aluminium from the glass occurs to a point where the Al/S ratio is a little less than 1:3, the expected value from the chemical formula. This Al concentration far exceeds the solubility of both aluminium hydroxides and the aluminosilicate layer silicates, so the retention of Al in solution

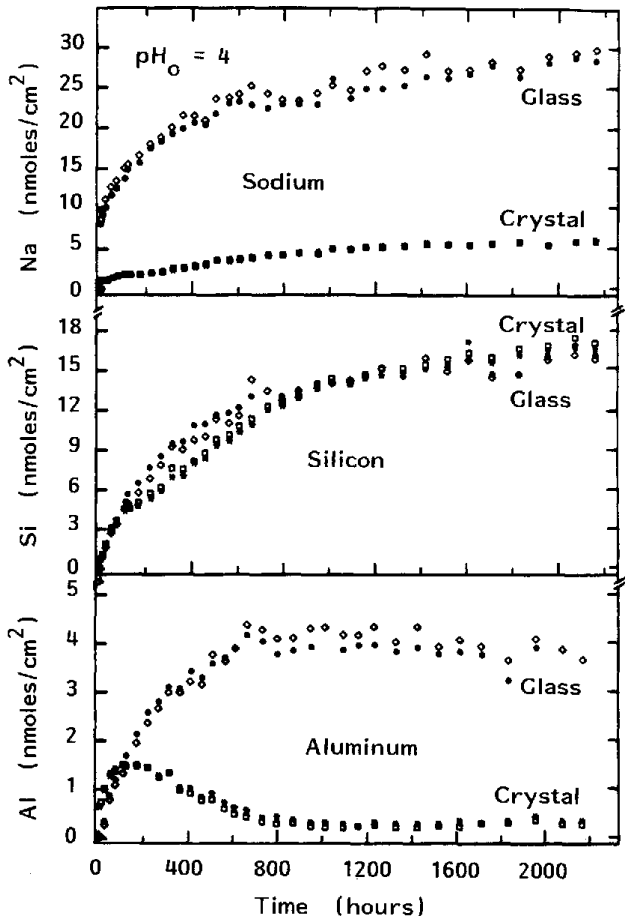

Figure 1.10: Comparison of the uptake of ions by the dissolution of crystalline albite, and albite composition glass [98].

must be metastable. However, at a relatively short time after the commencement of the experiment Al uptake from the crystalline albite rises to a maximum and then falls back to a low level [98].

The albite example demonstrates the challenge of how to deal with the reaction layers that form during glass dissolution. Preferential removal of leachable ions forms a leached layer that acts as a diffusion barrier to further extraction. Precipitation of network-forming ions such as silicon, aluminium, and boron not only forms an additional gel layer which may or may not act as a diffusion barrier, it also acts as a substrate for the adsorption and perhaps chromatographic separation of precipitating metal ions. The gel layer is metastable and eventually recrystallizes. Thus, the near-surface environment of a dissolving or corroding glass is quite complicated as illustrated in Figure 1.11. Rate and mechanisms of dissolution for crystalline ceramics and glasses depend quite critically on the initial surface and the evolution of leached layers, gels layers, and reaction product layers as the dissolution process proceeds. Therefore, characterization of these surfaces has brought into play surface characterization tools known to materials science [98, 99].

Extracted ions form a gel layer on glass, which acts as a diffusion barrier and adsorbs the precipitat-

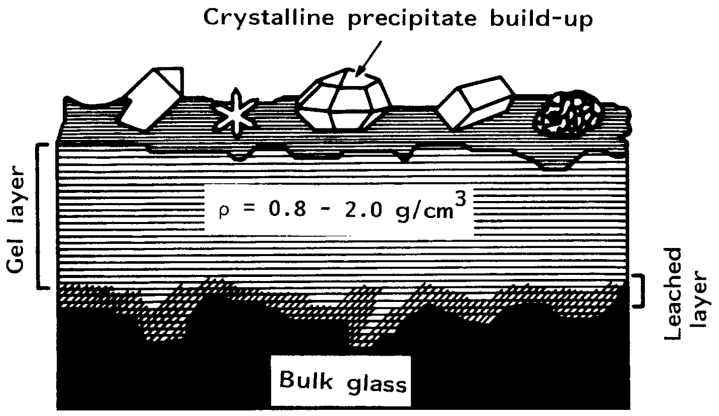

Figure 1.11: A corroded glass surface with ion-depleted leached layer, overlying precipitate or gel layer which ultimately recrystallizes on the surface [98].

ing metal ions. The dissolution of glass is controlled by a surface reaction. Studies of alkali-calcium phosphate glasses show that a uniform dissolution occurs by surface reaction, instead of a leached layer [97]. Similar to the albite phase, the silicate network also dissolves slower in crystalline configuration compared to the amorphous quartz glass [100].

The ion-transfer model proposes that the dissolution of ionic solids are reliant on the transfer of ions which are moving from the surface to the solution. The potential difference between the solid and the solution is responsible for the rate of the ion-transfer mechanism and shows an exponential dependency. From the equality of the cation transfer rate and anion removal rate, the charge neutrality in both bulk phases can be maintained. After solid dissolution, the participating atoms become less bonded to the others and form bonds within the compounds of the aqueous phase. The atoms in the solid depart from the surface. The interface between the bulk of the solid and the bulk of solution is charged due to the termination of the solid structure leaving unsaturated bonds and the adsorption of charged species present in the solution onto the surface.

Mineral solids are composed of atoms which are bonded by covalent and ionic bonds. As the solid dissolves, these atoms become less bonded to one another, the bonds break and form new bonds with components in the aqueous phase which are energetically more favourable. As they depart from the solid surface, the interface between the bulk of the solid and the bulk of solution is charged due to the termination of the solid structure leaving unsaturated bonds and the adsorption of charged species present in the solution onto the surface. These features result in the formation of three regions of changes in potential, as shown in Figure 1.12 [96].

The first region is the potential difference that occurs between the bulk of the solid and the solid surface and is referred to as the space-charge layer. The second region is called “Helmholtz layer” and occurs between the surface and the “outer Helmholtz plane”, which is the distance of closest approach of non-adsorbed ions. The third region occurs between the outer Helmholtz plane and

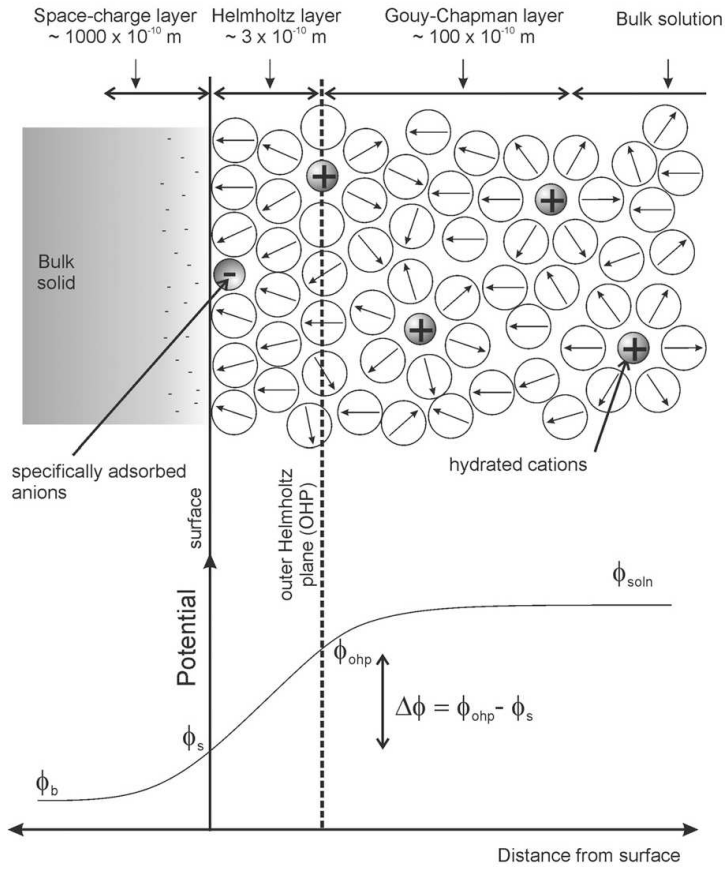

Figure 1.12: The structure of the charge interface, showing the changes in potential due to the space-charge layer, the so-called Helmholtz layer and the Gouy–Chapman layer [96].

the bulk of the solution and is referred to as called the Gouy–Chapman layer. As can be seen in Figure 1.12 the electric field, which is the change in potential as a function of distance, is at its maximum value along the Helmholtz layer This field influence ions, which are formed during dissolution, to aid their movement across the solid surface and into the solution. In the following sections, the dissolution of some commonly used glass and ceramics is discussed.

Dissolution of Silicates – Silicon forms a tetrahedral unit with four oxygen atoms, $SiO_4{}^{4-}$, in silicate minerals. There are various classes of silicates by sharing the oxygen atoms on the corners of the tetrahedral structure. The dissolution mechanism of silicates can be classified as congruent or incongruent dissolution where congruent implies that no new phase formed after the reactions and in-congruent indicates that new solid phases forms. It implies the formation of a partially leached zone or an alteration layer following [96, 101].

As a result of leaching or the re-precipitation of material after dissolution, an alteration layer is present on the surface, especially at lower pH values [102]. A pathway model in Figure 1.13 describes how the dissolution occurs in four steps as the bonds between the Si are broken by

reaction with protons. Tetrahedral silicon with four oxygen atoms departs from the surface by breaking bonds with other Si atoms [103].

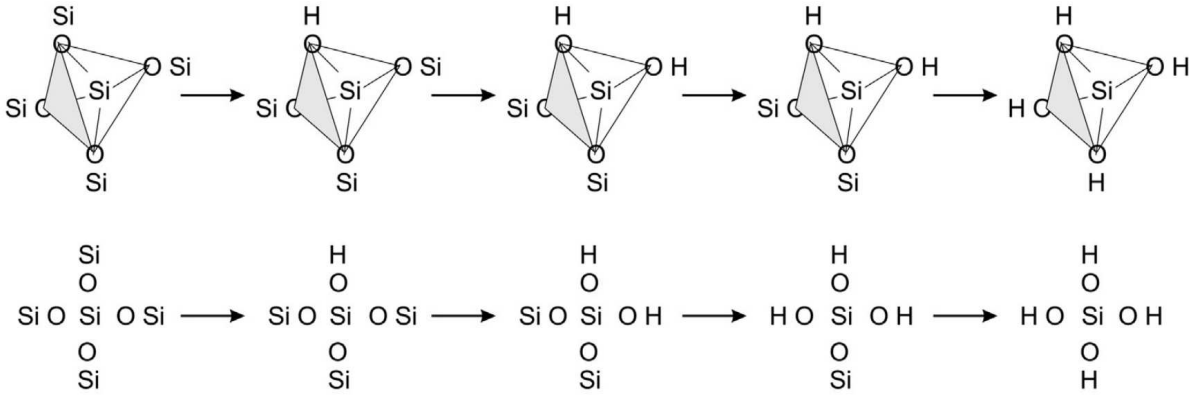

Figure 1.13: A model fo dissolution of silicate [103].

Dissolution of quartz – In quartz, oxygen atoms are shared by all silicate tetrahedra, without any metal ions separating the silicate tetrahedra. The dissolution mechanism is challenging due to the low rates of dissolution. As it has been shown in Figure 1.14, quartz dissolves both in acidic and in alkaline regions. Dissolution mechanism proposes that silicon-oxygen bonds are broken at the surface to produce products such as SiO_4^{4-} (aq) and $SiOH^{3+}$ (aq). These reactions occur in the inner Helmholtz layer. Although these steps are rate-determining, this is not the final product of the reaction. Further reactions continue at the outer Helmholtz plane between the rate-determining products and the solution [96].

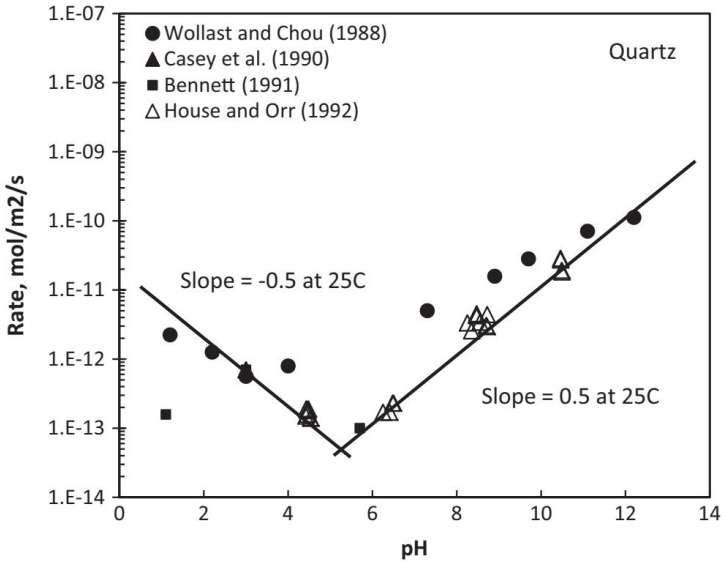

Figure 1.14: The pH-dependency of reaction rate for quartz dissolution [96].

Dissolution of feldspars – Feldspars are a group of rock-forming tectosilicate minerals containing potassium, sodium and/or calcium. The compositions in common feldspars can be defined between three endmembers; potassium feldspar (K-spar) $K[AlSi_3O_8]$, albite $Na[AlSi_3O_8]$ and anorthite $Ca[Al_2Si_2O_8]$. Solid solutions between K-feldspar and albite are called alkali feldspar and between albite and anorthite are called plagioclase. A basic classification of feldspars can be seen in Figure 1.15. Feldspars are important particularly in the glass-making and ceramics industries [96, 104].

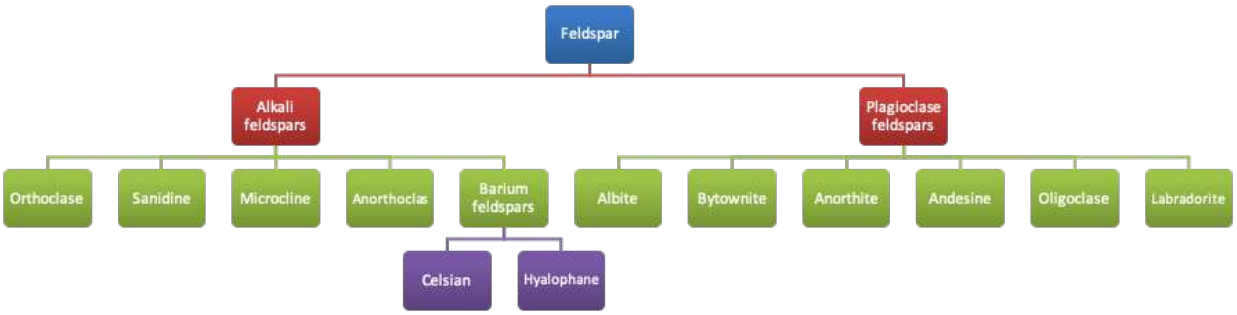

Figure 1.15: Classification of feldspars [104].

As it can be seen in the formula for feldspars, the molecular structure consists of double chains of $SiO_4{}^{4-}$ and $AlO_4{}^{5-}$ tetrahedra with aluminium, potassium, sodium, and calcium for the charge-balancing among neighbouring tetrahedral structures [96]. It has been reported that the feldspars dissolve both in acidic and alkaline solutions (see Figure 1.16). Open symbols represent rates obtained from experiments run in series for approx. 75 h, whereas filled symbols correspond to rates determined from individual experiments that ran for more than 250 h. Since the chemical compositions in the feldspar minerals are more complex than silicates, it is challenging to establish a dissolution mechanism and bond-breaking as the rate-determining step [96, 104, 105].

Previous studies also show that the rate of dissolution of the plagioclase feldspars is dependent on the aluminium content of the mineral. As the fraction of aluminium increases, the rate of dissolution increases exponentially [106]. The ion-transfer mechanism proposes that the Al–O and Si–O bonds are broken during dissolution. Departed $SiO_4{}^{4-}$ and Al^{3+} sites form complexes with water molecules and OH^- ions respectively. These interactions occur in the Helmholtz layer as discussed in the previous sections [96]. Besides, in the dissolution of an alkali feldspar, the first step is the relatively fast removal of alkali and alkaline earth metals from the mineral structure. This removal leads to a depleted surface layer and the bridging Al–O–Si bonds are subsequently hydrolyzed to release Al to the solution. This leaves the surface of the alkali feldspar enriched in silica in both acidic and basic conditions. In the final step, the Si–O–Si bonds from the silica enriched phase become hydrolyzed [107].

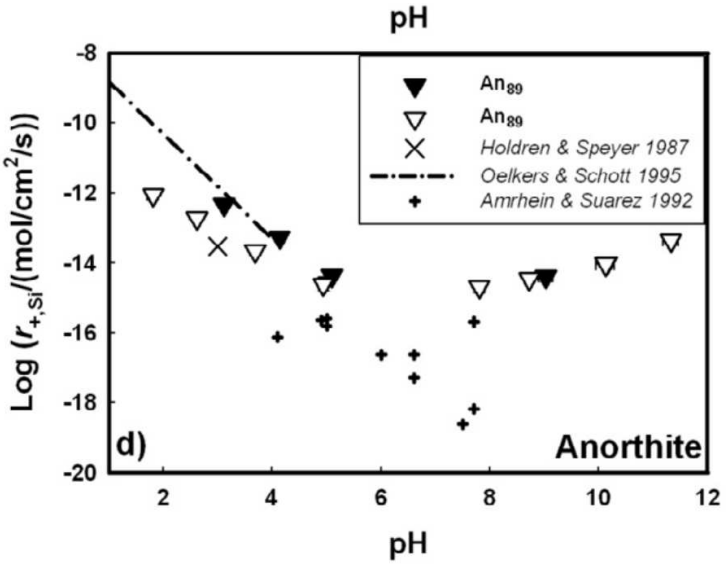

Figure 1.16: The effect of pH of the solution on the dissolution rate of anorthite [105].

1.4. State-of-the-art in LTCC devices and systems

In microelectronics, the packaging is defined as a discipline whose objective is to integrate one or several Integrated Circuits (ICs) in one system. As already discussed the LTCC multilayer packaging technology is becoming more and more popular for the production of complex multilayer radio frequency (RF) modules. This is due to the compactness, lightweight, high integration level, and the good compatibility of the LTCC technology with radio frequency microelectromechanical systems (RF-MEMS). Also, the integration of different technologies in one system saves space and reduces cost. LTCC offers the greatest ever flexibility to layout conducting circuitry in a three-dimensional fashion [108]. Many new compact passive circuit implementations, which were considered impossible to realize with traditional processes, have been proposed for various wireless application [109]. These applications include mobile telecommunication devices (0.8–2 GHz), Global Positioning Systems (GPS) (1.6 GHz), wireless local networks such as Bluetooth (2.4 GHz) and vehicle anti-collision radar (77 GHz).

However, the application of LTCC is not limited to these areas. Some of the LTCC application are briefly presented in the following, not requesting overall completeness, rather than providing a compact overview.

Xiong *et al.* [110] have reported on the development of a wireless high-temperature capacitive pressure sensor based on DP951 for the operation in harsh environments. They have used a unique process of screen-printing a sacrificial layer to avoid during lamination or sintering deformation of the capacitor embedded as cavity, which leads to a better performance of the sensor. An inductor-

capacitor (LC) resonant circuit was employed to detect the change in resonant frequency caused by the applied pressure, thus allowing for remote read-out.

Tan *et al.* [111] have reported on the development of an LC wireless sensor by applying the screen-printing technique, LTCC process, and imidization process on the DP951. The developed sensor was successfully tested for simultaneous monitoring of temperature, pressure, and humidity (TPH) and showed stable performance under harsh environmental conditions. The developed sensor could be stably operated at an ambient environment of 25–200 °C, 70–220 kPa, and 24–90 %RH.

Schmid *et al.* [112] have reported on the fabrication of a high-pressure resistive volumetric flow sensor for on-board monitoring of the injected fuel quantity within an automotive injection system. The hot-film anemometer with a Ti/Pt metallization on an LTCC ceramic substrate was integrated into the finished injection nozzle of a rail injection system. Its performance was evaluated at a high-pressure hydraulic test bench for pulse drives ranging between 0.3 and 1.5 ms and injection pressures up to 135 MPa.

Manjakkal *et al.* [113] have fabricated a miniaturized pH sensor on DP951 LTCC substrate, destined for wireless monitoring. Thick films of RuO_2-Ta_2O_5 and Ag/AgCl were screen printed and served as the sensing electrode and reference electrode, respectively. To reduce salt loss from the reference electrode, a polyurethane resin was applied on top of the reference electrode. The fabricated sensor exhibits very fast response (< 8s in acidic solutions) and good repeatability.

Brandenburg *et al.* [114] have developed an LTCC-based tube-type high-temperature gas sensor. Application of LTCC tapes together with screen printing allowed for the facile integration of heaters inside the structure as buried elements and the interdigital electrodes at the inner part of the tube. The LTCC tube itself was realized by wrapping the CT702 tape (Heraeus) around a rod and then laminating the wrapped tape to achieve a cylindrical shape. After lamination, the rod was removed and the structure was fired. Homogenous temperature distribution of the sensitive layer was achieved by optimizing the heaters structures and the suitability of the developed structure for sensor applications was demonstrated as a transducer for a resistive accumulating-type NO_x gas sensor. The rotational symmetric gas flow profile and the homogeneous temperature profile of the sensitive layer, with its large-area contact to the gas flow, was advantageous for NO_x sampling, especially at varying gas flow rates. The self-heated structure attained by buried heaters allowed for a sensitivity variation by adjusting the temperature and a periodic thermal regeneration of the storage sites. The sensor could be effectively thermally regenerated utilizing the buried heater.

Štekovič and Šandera [115] have reported on the fabrication of an electrochemical sensor based on HeraLock^{TM} HL2000 LTCC for potentiometric determination of analytes. The sensor was composed of a base which contained heater and a three-electrode system for electrochemical analysis. The integrated heater allowed for the increase in the current response and sensitivity of the LTCC sensor. The three-electrode system which was composed of gold as the working electrode, silver as the counter electrode, and Ag/AgCl as the reference electrode, was located in an opened cavity in

order to measure the small quantity of the analyte (30 μL).

Malecha *et al.* [116] have immobilized urease enzyme directly on tree different LTCC substrates (DP951, GC LTCC, and HL2000). Based on the obtained results GC LTCC was chosen for the fabrication of enzymatic μR. The reason for choosing GC LTCC was its high silicon dioxide content on the surface (which is the case for DP951 and GC LTCC) as well as its biological inertness (only GC LTCC). Besides this choice is following RoHS (restriction of hazardous substances) directive as GC LTCC does not contain lead. The μR consisted of two rounded chambers connected with 16 parallel microchannels and embedded heater. The enzyme of urease was immobilized on the microchannels' walls. Properties of the μR were examined using hydrolysis of urea catalysed by urease as a model enzymatic reaction.

1.5. LTCC technology for green energy production

1.5.1. Green energy production

Nowadays, most of the energy we use comes from fossil fuels, a nonrenewable and unclean energy source which is regarded as a major carbon dioxide (CO_2) emission source and driving factor for the climate change. Nuclear plants, as the second main source of energy, produce radioactive fission products. Hydroelectric plants require dams and large lakes. On the other hand, solar energy and wind energy, which are renewable and clean alternative energy sources, require large areas and are limited geographically. Therefore, it is economically and ecologically for all societies worldwide of utmost importance to explore sustainable and clean energy [117, 118]. Electricity, which is another main energy carrier beside hydrocarbons, cannot be stored efficiently, and electrical energy storage devices such as batteries fail to reach the levels needed for the creation of energy reservoirs for whole economies. The lack of a suitable storage and transportation form of energy after the era of hydrocarbons may even pose the most difficult challenge in the transformation of our energy systems. Therefore, besides green energy generation, alternative, but sustainable approaches for storing and transporting energy need to be considered [119]. Inexhaustible, non-polluting, and being one of the most plentiful elements in the cosmos, hydrogen (H_2) is considered as the fuel of choice for our future energy needs. However, H_2 is extremely difficult to store and to transport, and therefore scientists believed that if we had better ways of storing it, then hydrogen-based fuel cells (FCs) would make a big step towards a real breakthrough [120].

Reforming of hydrogen-rich sources such as alcohols and hydrocarbons allows for on-site and on-demand hydrogen production for FCs, which solves problems related to storage and transport of large quantities of hydrogen. Even if considering an overall FC system efficiency of 15% only, the attainable output energy densities (*e.g.* $\sim$7.4 MJ kg^{-1} for propane, $\sim$3.0 MJ kg^{-1} for methanol) are significantly larger than those of Li-ion batteries ($\sim$0.9 MJ kg^{-1}). However, the efficiency, process

temperature, and selectivity are some highlighted specifications of H_2 production by reforming reactions which can be controlled by the catalytic reaction and thereby significant investigations aimed at further improvements of reforming to H_2 are underway, and due to its fundamental and practical importance there is a rising interest in this field of research [121, 122].

Although the purpose of reforming reaction is the production of H_2, a wide range of other important, and often unwanted reactions may also occur in the reformer (*e.g.* decomposition, coke formation, and water–gas shift) that produce other products and must be taken into consideration. Some of the major reactions for hydrogen production are steam reforming (SR) (see Equation 1.7), decomposition (see Equation 1.8), and water gas shift reaction (see Equation 1.9). Catalysts are essential for these reactions, and significant improvements have been realized in the overall conversion of raw materials, the hydrogen production selectivity, and increasing the stability of the catalysts.

$$CH_3OH + H_2O \rightleftharpoons CO_2 + 3H_2 \qquad \Delta H = 49.7\ kJmol^{-1} \tag{1.7}$$

$$CH_3OH \rightleftharpoons CO + 2H_2 \qquad \Delta H = 90.7\ kJmol^{-1} \tag{1.8}$$

$$CO + H_2O \rightleftharpoons CO_2 + H_2 \qquad \Delta H = -41.2\ kJmol^{-1} \tag{1.9}$$

Both MeOH steam reforming (MSR) and MeOH decomposition are endothermic reactions, thus heat must be applied to shift the equilibrium to the right side and produce hydrogen. They can make use of engine exhaust heat and increase the fuel value when it is applied in internal combustion engines [123]. Therefore, a better understanding of the reaction mechanisms is required when searching for tailored, high-performance catalysts. Because the relative extension of all these reactions and the corresponding concerns depend on both the nature of catalytic material and the operating conditions such as water and fuel feed ratio as well as temperature. It has also been shown in the literature that many factors including the particle size, structure, chemical composition, and metal-support interaction can have a significant influence on the catalytic properties of catalysts [124–126].

1.5.1.1. Significance of catalyst support

The development of efficient catalysts is crucial for the implementation of hydrogen production from MeOH. The type of support material is expected to have a decisive effect on the rate and selectivity of the reaction, thermal stability of the metal nanoparticles (NPs), and hence the performance of catalysts [127–129]. Catalytically active metals can be deposited on a range of supports,

which are generally highly porous. For example, silicate structured mesoporous materials MCM-41 and SBA-15 are widely used as mesoporous catalyst supports in different reactions, representing low mass transfer resistance and less coking potential [128, 130–133]. However, due to their relatively low hydrothermal stability, rendering them not suitable for functionalization in aqueous media, the use of such catalysts is limited. For example, it is well-known that hydrothermal ageing of SBA-15 at high temperatures (>100 °C) does only not lead to an increase in primary pore size, but also to the disappearance of microporosity [134].

Moreover, the performance and stability of catalysts are determined by the density, nature, and accessibility of the active sites, which are largely defined by the support porosity and pore architecture [135]. Integrating the catalytic material within porous support can inhibit agglomerated nanoparticle nucleation and thereby increases the surface area and subsequently active catalytic sites. However, dispersed metallic catalyst over porous oxides exhibit complex nanostructures and its catalytic properties depend not only on particle size but also on the metal-support inter-facial interactions. The influence of support on the catalyst activity and selectivity is widely studied with respect to the strong metal-support interaction [136].

1.5.1.2. Metallic catalysts

As the functions and properties of metal NPs are closely correlated with their composition, size, shape, and structure, their controlled synthesis for various applications has been extensively studied in the literature. So far, many fabrication procedures have been developed for the synthesis of metal NPs. These methods mostly belong to the bottom-up synthesis approach, such as surfactant-mediated synthesis [137], wet impregnation [138], polyol reduction [139], template-assisted synthesis [140], photochemical synthesis [141], seeded growth and precipitation [142, 143], hydrothermal and solvothermal methods [144], CO and halide ion confined growth [145, 146], biological synthesis, and self-assembly of NPs [147]. However, in this present thesis, only wet impregnation method is used for fabrication of NPs. This nano-fabrication method is quite straightforward and consists of contacting a solid support with a liquid containing the components to be deposited on the support surface. The desired species are selectively adsorbed from the liquid phase onto the surface of the support [138, 148, 149]. The use of transition metal NPs such as Co, Ni, Fe, Pd, and Pt as catalysts for many important reactions like syngas production, electro-oxidation, hydrogenation-dehydrogenation reactions, and hydro-deoxygenation reactions has been extensively reported in the literature [136, 150–152]. However, due to the availability of new active sites not presented in mono-metallic systems, and the possibility of inducing synergistic effects, bimetallic catalysts display superior properties than their mono-metallic counterparts in several applications, including reforming reactions [153].

1.5.2. LTCC-based microreactors

LTCC technology is very attractive for small scale manufacturing and tailor-made solutions such as in lab-on-a-chip (LOC) and μRs. Small scale manufacturing, as it offers the advantages of being more cost-effective when compared to standard silicon technology while enabling the realisation of complex structures when compared to polymer-based microsystems [11, 154–157].

Chemical μRs typically contain fluidic channels with characteristic dimensions in the sub-millimetre range. By combining process intensification concepts with micro-fabrication techniques, these μRs have been rapidly developed to perform liquid or gas phase chemical reactions, particularly the quasi-instantaneous endothermic or exothermic ones [11, 157]. Ceramic-based materials in general feature high chemical and thermal stability. Consequently, they are preferable to be used as reactor materials, especially for reactors involved with high temperature and/or pressure levels [158]. Nevertheless, compared to alumina and SiC, LTCC-based devices have a relatively low operating temperature of below 800 °C, which is, however, significantly higher than the process temperature for most of the important common catalytic reactions including reforming reaction. Also, the possibility to integrate heating elements and temperature sensors for the precise and local control of the process temperature and real-time automation, as well as post-firing porosification capability for increasing the surface area, makes LTCC advantageous compared to SiC and alumina, as the latter technologies cannot fulfil both requirements each [159, 160]. Moreover, in comparison to the silicate structured mesoporous catalysts, LTCC substrates offer the advantage of higher thermal and mechanical stability, which is very important for future applications, especially when targeting hydrothermal or other high-temperature processes in combination with integrated metallic particles. For example, Berenguel-Alonso *et al.* have recently developed a robust LTCC μR for the synthesis of carbon dots at high temperature and pressure by a hydrothermal method. The μR integrates fluidics, heating system, and an optical window for monitoring of the reaction progress by fluorescence imaging. The results described in this work help to establish LTCC as a go-to material in μRs requesting high mechanical and chemical robustness, due to the presence of high temperature and/or pressure levels [158].

Typically, μRs as a robust solution for on-site H_2 production by reforming process, have received much attention both by the academic community and by industry. Also, since heat transfer becomes more efficient as reaction volumes shrink, the amount of energy consumed per unit temperature rise can be made extremely small, leading to environmental benefits [161–163]. Given the above-mentioned advantages of μRs, and the great potential of LTCC for the realization of robust μRs, this technology platform is an exceptional choice for conducting fundamental research in the area of green energy production by use of heterogeneous catalysis reactions.

Chapter 2.

EXPERIMENTAL DETAILS

2.1. Materials and technology aspects

2.1.1. LTCC materials and etching solutions

Commercially available LTCC tapes, Ceramtape GC (Ceramtec, Marktredwitz, Germany), L8 tape (Ferro Corporation, Mayfield Heights, US), GreenTape 951, and GreenTape 9k7 (DuPont Ltd., Bristol, UK), were provided in the *as-fired* form by the Micro Systems Engineering (MSE) Gmbh, Berg, Germany. Some important technical aspects and properties of the tapes are collected from the corresponding data sheets and are shown in Table 2.1. All LTCC tapes used in the etching experiments contain Al_2O_3 particles as filler embedded in a glass matrix. The samples which were used for porosification were square, with an edge length of approximately 15 or 10 mm and thicknesses in the range of 190 to 450 μm. However, for characterization of, *e.g.* permittivity or mechanical properties in the 3-point flexural test setup, different geometrical dimensions were required. This information is stated in the corresponding sections.

For each set of etching experiments, the etching solutions were freshly prepared by dissolving or diluting the calculated amount of the appropriate materials in deionized (DI) water. For example, alkaline etchants were prepared by dissolving the desired amount of potassium hydroxide (KOH) or sodium hydroxide (NaOH) pellets (from Sigma Aldrich and VWR, respectively), in DI water. Also, orthophosphoric acid solution (H_3PO_4 85 wt %) from Sigma-Aldrich after dilution with DI water was used as the acidic etchant.

For the investigation of the impact of orthophosphoric acid concentration on the etching treatment of LTCC substrates, commercially available 85 wt % solution was used to prepare 300 mL of each orthophosphoric solution through dilution with water (see Table 2.2).

Table 2.1: Technical information and properties of the tapes used in this work.

	Ferro L8	**GC LTCC**	**DP951**	**DP9k7**
Coefficient of thermal expansion *ppm/°C*	6	4.9	5.8	4.4
Flexural strength *MP*	>275	>170	320	230
Poisson's ratio	-	-	0.24	0.25
Loss tangent	<0.0131	≤0.0020	0.0140	0.0010
Permittivity	7.3±0.2	7.3–8.5	7.8±0.2	7.1±0.2
Typical tape shrinkage %	X,Y 13 Z 17	X,Y 20.5-21.9 Z 17.5-18.5	X,Y 12.7±0.3 Z 15	X,Y 9.1±0.3 Z 11.8±0.5
Density $g\ cm^{-3}$	3.1	2.87-2.97	3.1	3.1
Thermal conductivity *W/m K*	>3	1.2 – 3.20	3.30	4.6
Firing	Peak of 850°C for 30 min, heating heating temperature 6-8° C/min	Peak of 880-920°C for 10-40 min, heating temperature 1-4°C/min	Peak of 850°C for 17-23 min, heating temperature 4.5-13.5°C/min	Peak of 850°C for 17-23 min, heating temperature 0.7-2.5°C/min*

* 26.5 h of firing in a box furnace is recommended.

Table 2.2: Orthophosphoric acid etching solutions with different concentrations.

wt % **in H_2O**	**Abbreviated name**	**Amount of P85** *mL*	**Concentration** $mol\ L^{-1}$
85	P85	300.0	14.8
50	P50	176.5	8.7
25	P25	88.2	4.4
10	P10	35.2	1.7
1	P1	3.5	0.2
0.5	P0.5	1.8	0.9

To study the impact of etchant pH on the porosification of LTCC, phosphate buffer solutions (PBS) with a concentration of 0.2 mol L^{-1} and pH values in three representative regimes were prepared by dissolving the required amounts of the PBS components which are shown in Table 2.3. For this purpose, H_3PO_4 and its conjugate base, NaH_2PO_4 were used for the highly acidic range, Na_2HPO_4 and its conjugate base, $Na_3PO_4.12H_2O$ for the highly alkaline range, and finally NaH_2PO_4 and Na_2HPO_4 for the medium or neutral range, respectively.

For each regime, the amount of the buffer components were calculated through the well-known Henderson–Hasselbalch equation (Equation 2.1), and the mass balance equation (Equation 2.2).

$$pH = pk_a + Log\frac{[A^-]}{[HA]} \tag{2.1}$$

$$[PBS] = [A^-] + [HA] \tag{2.2}$$

Table 2.3: PBS buffer ranges, and the required amount of each component for preparing 500 mL of 0.2 mol L^{-1} solution.

Buffer components		pK_a	pH
H_3PO_4 (10.87 g)	NaH_2PO_4 (12.68 g)	2.15	1.2
			2.2
			3.2
NaH_2PO_4 (13.37 g)	Na_2HPO_4 (12.57 g)	7.2	6.2
			7.2
			8.2
Na_2HPO_4 (14.57 g)	Na_3PO_4 .$12H_2O$ (33.65 g)	12.32	11.2
			12.2
			13.2

where [HA], [A^-], [PBS] represent the concentrations of the acid, its conjugate base, and the buffer, respectively. Also, pK_a is the negative log of the acid dissociation constant. The prepared PBSs were labelled as "PBS_y", where y is the pH value of the buffer solution, *e.g.* "PBS7.2" refers to PBS with a pH of 7.2.

Additionally, solutions with the same concentration, *i.e.* 0.2 mol L^{-1} from individual PBS components as well as the deionized water in the presence and absence of HCl, NaOH, and NaCl were prepared without adjusting the pH and used as etchants. The experiments with pure water and NaCl were conducted to determine the impact of water and Na^+, as well as Cl^-, separately (see Table 2.4).

Table 2.4: Solutions prepared from individual PBS components without pH adjustment.

Solution	pH	Amount g
NaH_2PO_4	5.3	12.0
Na_2HPO_4	9.2	14.2
$Na_3PO_4.12H_2O$	12.4	38.0
NaOH	12.8	4.0
HCl	0.7	11.5
Water	7.0	507
Water + 3M NaCl	7.0	87.5 g NaCl
KOH + 3M NaCl	14	87.5 g NaCl + 84.1 g KOH

2.1.2. Etching process

The wet-chemical etching experiments were carried out at constant temperatures ranging from room temperature to 120 °C. All the etching experiments were done in a capped beaker made from borosilicate laboratory glass which is stable under acidic and alkali conditions [164]. The LTCC samples were flushed in propan-2-ol prior to treatment and were held in position by a fixture made of polytetrafluoroethylene (PTFE) which provides the advantage of high chemical and thermal stability up to 260 °C. The setup concept is based on the vertical reactor in which the samples are standing in an upright position, enabling a high sample throughput. The container setup is sealed to prevent the extreme evaporation of water proportion from the etchant. The evaporation leads

to an increase in the etchant concentration and affects the experimental process. However, some evaporation occurred at higher bath temperatures which were compensated during the etching experiments.

The etching temperature was controlled using a Heidolph hotplate (MR-Hei-Tec), and the obtained temperature was precisely checked with an external temperature sensor (see Figure 2.1). By the end of the etching process, the LTCC samples were immediately and thoroughly rinsed with DI water and propan-2-ol (isopropanol) and then dried in atmospheric air.

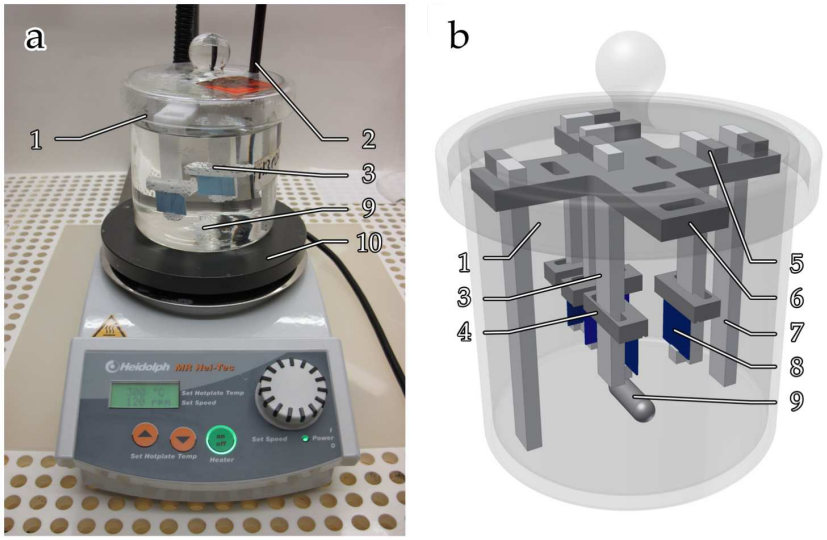

Figure 2.1: a) Photograph and **b)** schematic view of the etching setup with atmospheric pressure and 570 mL load capacity. (1: capped beaker, 2: temperature sensor, 3: sample holder, 4: sample clamp, 5: safety corner, 6: holder cross, 7: holder foot, 8: LTCC sample, 9: magnetic stirring bar, 10: hotplate) [164].

Additionally, for the flexural strength measurements by ball-on-three-balls (B3B) test the etching test setup had to be modified. This is due to the different geometry of the samples needed for these measurements, *i.e.* circular samples with a diameter of approximately 5 mm. The original fixture was specifically designed for square-sized samples and when applying the holding for the circular samples it was not firm enough and most of the samples were moving in the slits and touching others during the etching process. The adaptation was applied to the sample clamp part of the PTFE fixture enabling to securely hold several circular samples in position while ensuring good contact to the solution. For this purpose, in addition to the slits on the sample holding legs which were made for an easier sample loading and to prevent them from falling out, oblong holes were milled in the middle holder to avoid both any movement in the slit and contact with each other. These holes also minimize the contact area between fixture and samples. The whole etching setup and the sample holder are shown in detail in Figure 2.2. The capacity of the fixture amounts to 32 samples while for the original fixture the maximum capacity was about 8 samples.

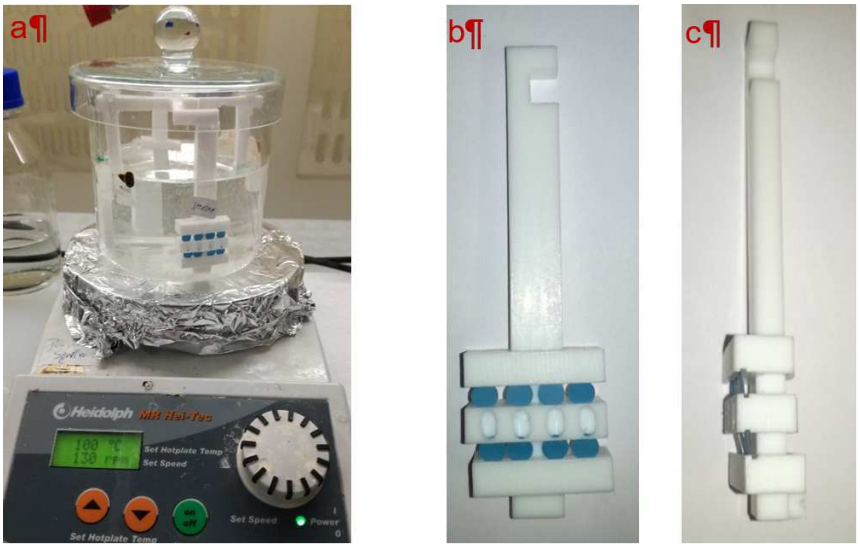

Figure 2.2: a) The setup with the fixture inside the beaker, **b)** and **c)** front- and side-view of the sample holder and clamps loaded with samples, respectively.

2.1.3. Preparation of LTCC samples

As already mentioned, the LTCC tapes used for studying the etching behaviour were provided by MSE GmbH in the *as-fired* state to ensure from the starting material high repeatability of the etching experiments. However, additional green tapes of LTCC samples were also provided by the same company which were used for the optimization of firing profiles, preparation of circular samples which were required for a specific measurement setup, and studying the impact of firing temperature on the morphology and microstructure of LTCC substrates. Those samples went through additional processes such as laser cutting (machining) and firing as described in this section.

GC LTCC green tapes were subjected to different firing profiles with varied peak temperature for 70 min total sintering cycle. The firing process was conducted in a six-zone belt furnace, at nominal peak temperatures between 800 and 950 °C and the impact of peak firing temperature on the morphology and composition of the LTCC substrates were studied. Next, selected samples were subjected to a wet chemical porosification process with an aqueous KOH solution. It should be mentioned that the real temperatures were measured later to be almost 10 °C less than the nominal temperatures. Therefore, to avoid misinterpretation the real values are given in this study. The fired GC LTCC samples were labelled as GCz, where z is the actual peak temperature used in the firing process. For example, GC890 refers to the GC LTCC fired at the peak temperature of 890 °C (*i.e.* nominal peak temperature of 900 °C).

To convert the LTCC green tape into a solid, dense material, a sintering process is needed. Three types of sintering processes are common: (a) *viscous flow*, (b) *liquid phase*, where a liquid is formed

during the sintering process and solid grains are soluble in the liquid; and (c) *solid-state*, where the sintering occurs between touching particles through diffusion [165]. In the case of LTCC tapes, the process is of viscous flow type due to the glass component. The glass components are in the liquid phase at the sintering temperature, while alumina grains remain in the solid-state. Due to compatible surface free energies and capillary forces, the alumina grains get wetted. With a decrease in temperature, the crystallization of the glass starts, and solid material is formed. In Figure 2.3, the process during sintering is schematically shown [166].

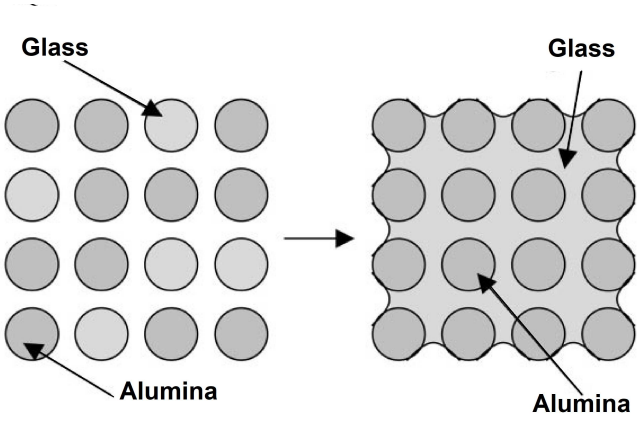

Figure 2.3: Model of viscous flow sintering; glass phase melts and wets the alumina grains [166].

Sintering of LTCC tapes can be realized in both box- or belt-furnaces. The belt-furnace transports the substrates on a belt and has the advantage that it can be operated continuously at very short cycle times. The disadvantage of belt-furnace is the inherent temperature gradient inside along the transport direction. Thus, it is merely suitable for rather thin and small substrates. Larger samples and laminates, especially when sacrificial material is used, require a long burn out cycle and slow sintering process. A box furnace offers this advantage at the cost that it has a long cool down time.

Since the glass component of the LTCC becomes fluid during the sintering process, part of the alumina can dissolve into the glass phase. The result of that is the formation of anorthite, $CaAl_2Si_2O_8$, phases or similar framework silicates (*e.g.* labradorite, $(Ca,Na)Al(Si,Al)_3O_8$, or celsian, $Ba[Al_2Si_2O_8]$). Those phases are primarily formed in the contact area between the alumina grains and the glass phase resulting in a mechanically stronger material.

The first step of sample preparation requires the unfired tapes to be cut into desired shapes. Typically, this can be done by punching tools or by laser cutting. The latter one is a more universal process for handling and machining LTCC green sheets as samples with precise geometrical properties and clean edges can be obtained. The cutting of all tape samples was performed using a diode-pumped Nd:YAG-Laser (ROFIN Sinar, Germany) equipped with an acoustic optical switch and an objective lens with a focal length of 160 mm, as well as a computer-controlled galvanometric beam deflection system (operating power: 12 W at TEM00-mode). The cutting behaviour of

this specific laser was investigated by Smetana *et al.* on various LTCC tapes [167]. Parameters used for the cutting were set based on these pre-investigated parameters.

A six-zone belt furnace from BTU systems depicted in Figure 2.4a was used for firing LTCC specimens. The length of the furnace was measured and amounts to approximately 250 cm. Each temperature zone is programmable via an industrial controller (PMA, KS 40-1). The belt speed is adjustable via three switches and is displayed in on a three-digit display. Both temperature and speed controls are given in Figure 2.4b. The airflow was adjusted in five different zones as depicted in Figure 2.4c. The airflow was set to the parameters specified in Table 2.5 and was not altered during firing processes.

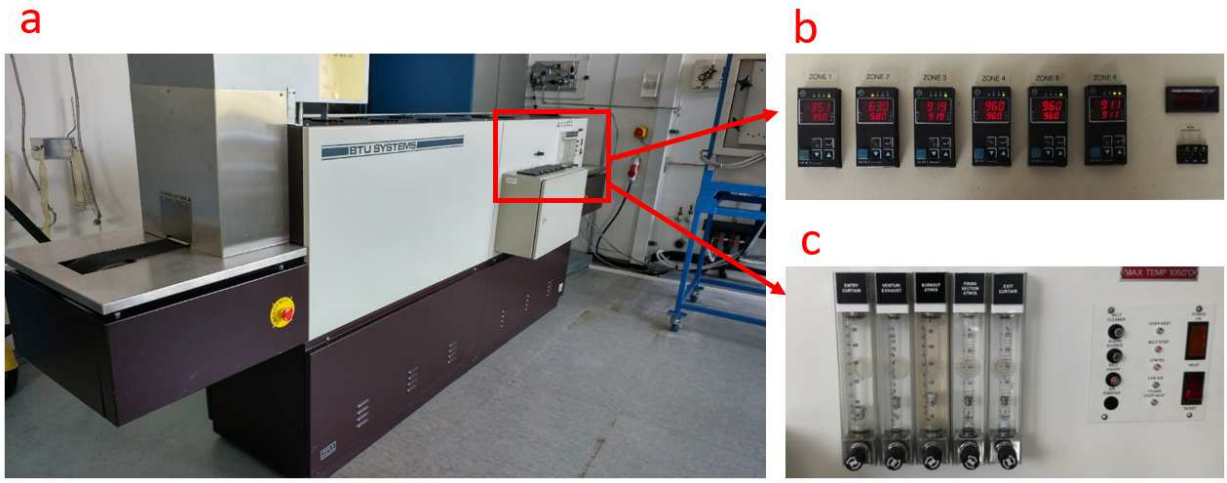

Figure 2.4: a) Belt furnace used for firing the LTCC specimens, **b)** temperature and belt speed control unit, and **c)** air flow control and general control units.

Table 2.5: Airflow parameters during firing

Entry curtain	Venturi exhaust	Burnout atmosphere	Firing section atmosphere	Exit curtain
5 L min^{-1}	3 L min^{-1}	16 L min^{-1}	6 L min^{-1}	6 L min^{-1}

It is already known that mechanical stress induced in the green state of tapes by handling and machining procedures leads to warping and inhomogeneous material thickness in the fired state. For the samples fired at ISAS, the already cut samples were only enclosed between two CeramTec A Tapes on a base alumina substrate, and no pressure and lamination was applied. However, as it will be shown in Chapter 3. that due to the small sample sizes of about 5 mm, the samples mostly did not wrap, and the wrapped samples were taken out before further investigation. The A tape is a pure alumina tape which is used to reduce the lateral shrinkage of LTCC tape during the firing process but results in increased thickness shrinkage. Furthermore, it reduces the bending of the specimen caused by the sintering process and also prevents specimen contamination within the

furnace environment. This tape serves as a sacrificial material and after firing coverts to a very brittle sheet which is removed from the fired LTCC substrates [168].

The temperature profile is very important for appropriate sintering of LTCC materials as it directly impacts its characteristics after firing. Therefore, precise control of the temperature and its changes by the time is critical for all sintering processes. For this reason, the furnace actual temperatures for all firing profiles were measured by using a flexible thermocouple type K (Ni-CrNi). The coated thermocouple was rolled around a barrel for easier handling. It was fixed onto the belt using copper wiring. The thermocouple was also put between two alumina substrates and covered with A tape to ensure measurement under the same conditions as the specimens are fired. The setup for recording temperature profiles is displayed in Figure 2.5. Recording of temperature was realized with a universal temperature measuring instrument (Voltcraft, PL 125 T2USB).

A typical sintering profile for LTCC is shown in Chapter 1. Two important temperature plateaus can be observed in the profile. The first plateau is for burning out the organic filler materials (*i.e.* binder and plasticizer), while the second plateau represents the peak temperature at which viscous flow sintering occurs. The most important parameters are the heating rate and the dwell time at peak temperature. As a variety of LTCC tapes is available, specific firing profiles are usually recommended by the manufacturer. To obtain a particular firing profile on the belt furnace the temperature of each zone, belt speed, and flow rates have to be delicately adjusted by the control units (see Figure 2.4). The investigations were conducted for various commercially available green tapes such as GC, DP951, DP9k7, and Ferro L8 (results are not shown here). The desired temperature profiles were realised by varying the settings on the furnace to generate temperature profiles close to manufacturer specifications. The most important parameters were the heating rate and the dwell time at peak temperature.

Furthermore, in order to evaluate the precision of temperature measurements, the firing process was repeated for three times and the mean values for the heating ramp with corresponding error bars are given in Figure 2.6. For GC LTCC which is studied in this section, the optimized temperature profile with the same furnace was reported previously [169]. Thus, this setting was taken as a starting point and the peak temperature was altered to investigate its impact on the surface properties of fired samples. For example, the temperature profiles for two peak temperatures of 890 and 940 °C are given in Figure 2.6.

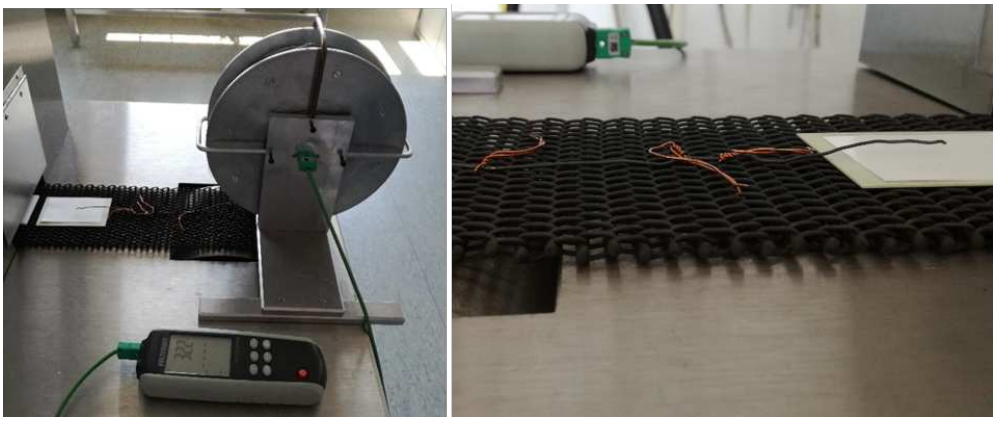

Figure 2.5: View on the setup to measure the temperature profile at large (on the left) and in detail on fixation of the thermocouple to the belt (on the right). A sheet of A-tape and an alumina substrate were placed on top after the image was taken.

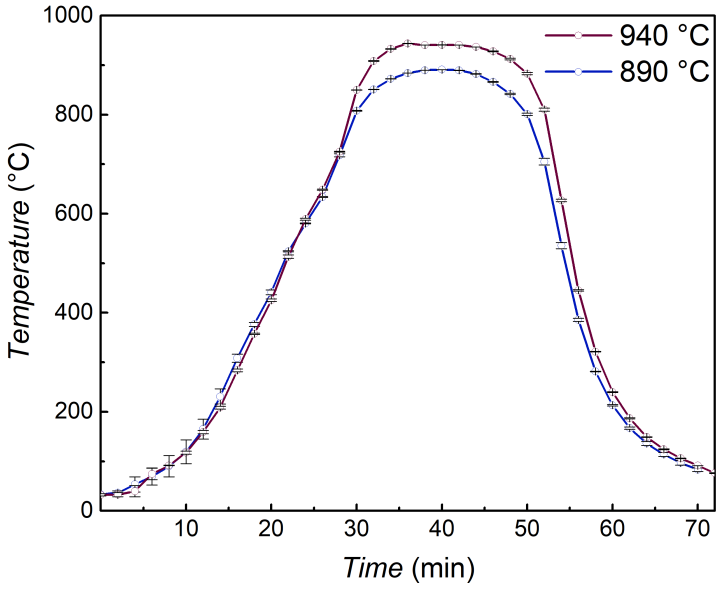

Figure 2.6: The firing profiles for GC LTCC with two different peak temperatures of 890 °C and 940 °C. To estimate the temperature repeatability, a mean value of three measurement cycles is given, whereas error bars indicate the deviations between the measurement cycles.

2.1.4. Experimental setup and measuring method for the catalytic hydrogen production

2.1.4.1. Experimental setup

The experimental setup essentially consisted of three parts, namely the gas supply including valve switching, the actual reactor and a gas chromatograph for product analysis. The reactor was a

quartz glass capillary that was installed in the pipe system with the help of two screw connections between the gas supply and gas chromatograph (GC). The capillary was surrounded by a thermostat which was operated and controlled using a computer by means of iToolsOPC Software. The temperature was measured every three seconds using a thermal sensor and recorded using the OPCscope software. The maximum temperature fluctuations were about 5 °C.

The thermocouple was inserted into the capillary and sealed. The capillary was loaded with the sample before installation in the apparatus. A little glass wool was added to the top third of the tube to hold the catalyst in the vertically installed capillary. Care was taken to ensure that the glass wool did not slip. At the same time, the glass wool should not be compressed too tightly to allow easy gas flow through the reactor. A sample amount of up to 60 mg could now be placed on the stably positioned glass wool. Care was taken to ensure that the tip of the thermal probe was in direct contact with the sample. The arrangement is shown schematically in Figure 2.7a. The gas supply supplied different gases and was computer-controlled via the FlowView Software. The pipe system is shown schematically in Figure 2.7b.

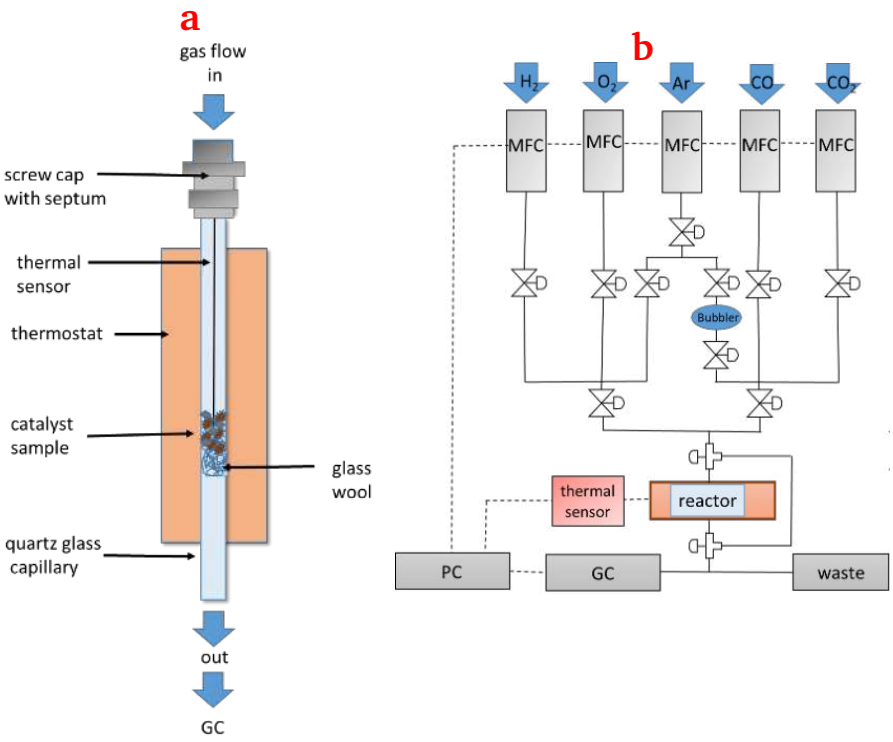

Figure 2.7: a) Schematic representation of the reactor setup. **b)** Flow diagram of the entire apparatus. The gas supply was controlled via the Mass Flow Controller (MFC). Solid lines show the pipeline while dashed lines represent the data transfer.

Argon (Ar) was introduced into the reactor after passing through a bubbler. The bubbler was filled with a MeOH/H_2O mixture with a 1:10 ratio. This mixing ratio was chosen based on the different vapour pressures of the components to achieve a 1:1 ratio of the components in the vapour phase. The Ar stream was moistened with the vapour phase when it was passed through the MeOH/H_2O

mixture using the bubbler. This made it possible to achieve a reproducible feed of the starting materials into the reactor. The bubbler was not heated or cooled because the vapour pressure of the components was sufficient to adequately humidify the Ar flow under atmospheric conditions. The setup also offered the possibility of introducing CO and CO_2 into the reactor as educts. However, since there was no need to use these educts, the valves provided were never operated.

Via the gas outlet of the reactor, the gas stream passed through the reactor and reached the GC. With the help of this analytical setup, the composition of the gas mixture in the reactor could be determined and recorded by automated sampling every four minutes. The entire setup is shown in Figure 2.8.

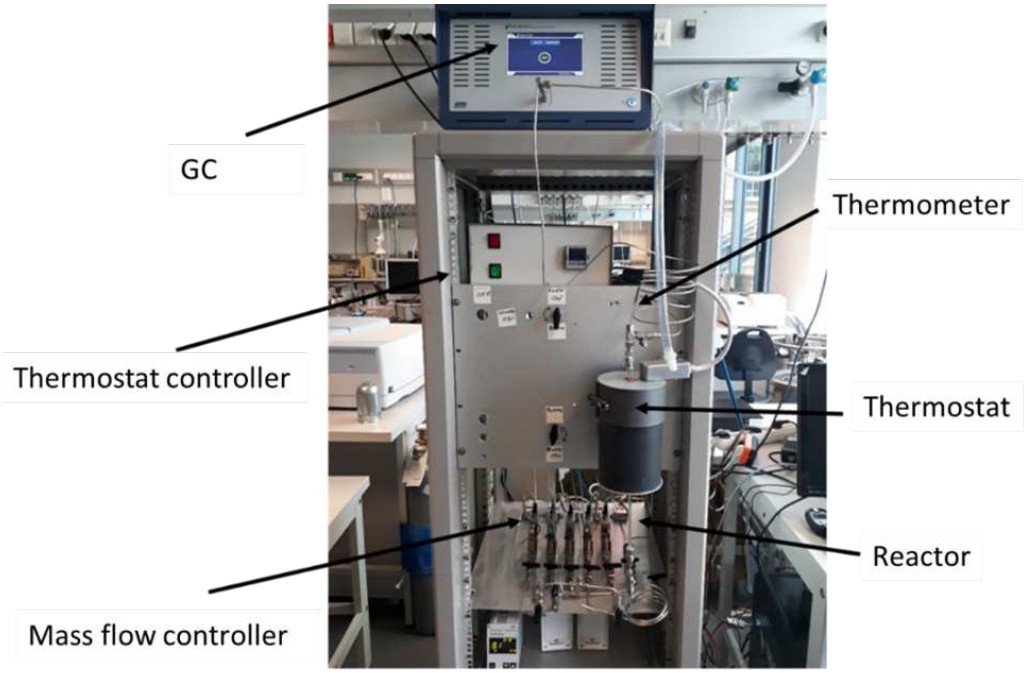

Figure 2.8: An overview of the measurement setup.

2.1.4.2. Measuring method

A temperature program was carried out for each sample as part of the measurement procedure (see Figure 2.9). Before each measurement series, the sample was crushed, weighed on the analytical balance, and placed on the glass wool in the capillary. The capillary was then mounted in the reactor. A thermal sensor was inserted into the sample to measure the actual temperature directly on the sample. Since the tip of the thermal sensor was also made of a metal alloy, any catalytic activity had to be determined in a blank test, where a sequence of the entire measuring procedure was carried out in the absence of the catalyst.

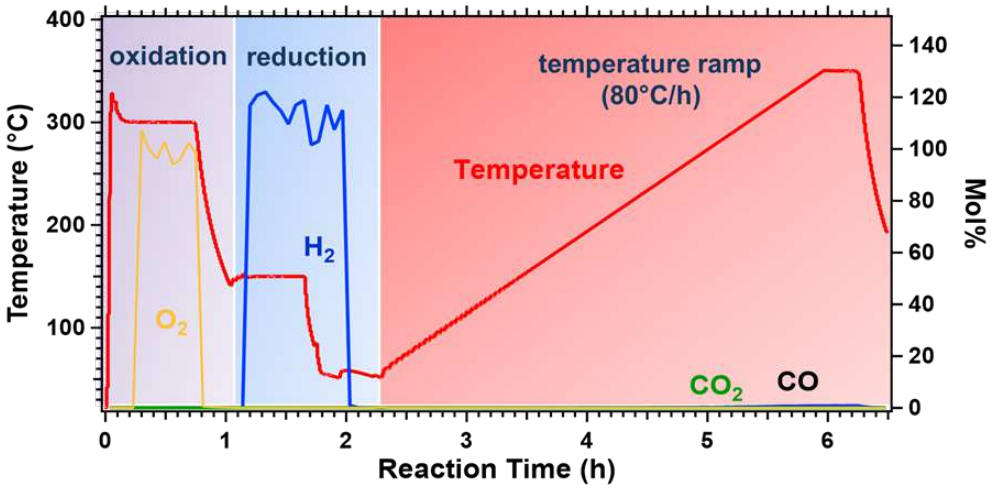

Figure 2.9: Representation of the measurement procedure. The curves for temperature (red) and the gases O_2 (yellow), H_2 (blue), CO_2 (green), CO (black) are shown. Also, the areas of oxidation step (highlighted in purple), reduction step (highlighted in blue) and temperature ramp (highlighted in red) are shown. The reaction time is plotted on the ordinate, the temperature (left), and the mole fraction of the reaction mixture (right) on the abscissa.

2.2. Characterization

2.2.1. Electron microscopy techniques

2.2.1.1. Scanning Electron Microscopy

The scanning electron microscope (SEM) is one of the most versatile tools existing for the analysis of microstructure morphology (physical features) and chemical composition. Instead of light, SEM uses a focused beam of electrons with the energy of a few hundred eV to 40 keV which is typically thermionically emitted from an electron gun. Due to the short wavelengths of electrons, SEM has remarkable advantages over light microscope such as high-resolution imaging and large depth of field. In the SEM technique, the electron beam is scanned across the sample surface and due to its interaction with the sample, a variety of signals, such as secondary electrons, backscattered electrons, and characteristic X-rays are produced (see Figure 2.10). The signals emitted from the specimen are collected by the detectors as a function of the position of the incident focused electron beam and form images which are then displayed on the PC screen.

When the electron beam hits the surface of the sample, it penetrates up to a depth of a few microns into the surface, depending on the accelerating voltage, density, and nature of the sample. Therefore, SEM can give information on the morphologies of sizes between few nanometers up to several micrometres [170, 171].

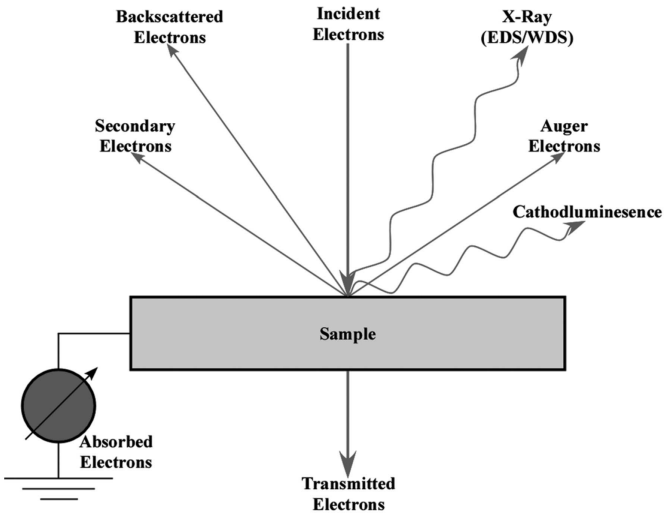

Figure 2.10: Existing signals in SEM analysis, upon those the backscattered electrons, secondary electrons, and characteristic X-rays are commonly used. Modified from [107, 172].

For surface topography measurements, the secondary electrons are used, which are a group of low-energy electrons typically below 50 eV. They are knocked out of the outer shells of the atom due to the inelastic scattering of the incident electron beam. Complementary to the secondary electrons, the backscattered electrons are used for additional information about element composition. They are formed by detecting the elastically scattered high-energy primary electrons. By using an energy dispersive spectrometer (EDS) more chemical information can be achieved by evaluating the emission of X-rays [170].

In this thesis, surfaces, and fracture planes of the LTCC samples were evaluated using a Hitachi SU8030 field emission scanning electron microscope applying the secondary electron (SE) detection mode. No metal coating was applied on the surface of specimens prior to characterization and an operating voltage of 2 kV in the charge suppression scanning mode was used. The thickness and also the porosification depth (d_p) for the samples etched at different conditions were measured by applying the open software ImageJ, which is widely used in scientific research [107, 173], for cross-sectional SEM images of the fracture planes. Since the two sides of the LTCC cannot be distinguished after firing followed by the etching treatment, the d_p values were measured at three different positions of each sample, and the average value was reported. Typically, the difference between the d_p values of the two sides did not exceed 5%.

2.2.1.2. Three-dimensional SEM imaging

There have been many attempts in converting grey scales from an individual SEM image into useful height information. This is not generally easy to accomplish since the grey level is not a function

of local height but contains information of the local material non-homogeneities and electric properties, and detector position [174]. For three-dimensional reconstruction, some methods have been proposed. One of them is based on the "shape from shadows" method which is appropriate for smooth surfaces. For this procedure, an SEM equipped with a quadruple detector is required. Vertical inaccuracies below 10% have been reported by utilizing this procedure [175].

For nanoscale applications, more specific solutions are implemented by exploiting the Monte Carlo electron transport modelling and iterative arrangement of parameters to create the best least-squares fit to the measured image. The accuracy of this procedure is proved with SEM images that are in good agreement with cross-section measurements [176].

However, the mainly used and investigated method for three-dimensional reconstruction of surface features is photogrammetry. There are some software packages available in the market for this purpose such as MeX, Scandium Solution Height, or 3D_TOPx. They deliver good qualitative and quantitative 3D reconstruction of surfaces, although, a certain scepticism is still expressed about these techniques when targeting quantitative analyses [178–180].

MeX software enables us to reconstruct stereo pairs, which is referred to as a digital elevation model (DEM) in the software. The digital elevation model needs two SEM images and it is gained from a 3D point cloud (a set of data points in a coordinate system). The "Creator" tool is used to obtain 3D reconstructions. There are two main creators in MeX software: Stereo Creator and Auto Calibration which are using stereo-pair and stereo-triplet, respectively. By the user manual, it is recommended to use the Stereo Creator tool if the tilt angles are truly known, for example by calibrating the SEM image. Also, the Stereo Creator tool is faster than the Auto Calibration tool, which needs to auto-calibrate the tilt information of the triplet images to one another. Enough height changes and structure information are needed to perform an Auto Calibration task. On the other hand, it is not necessary to perform a stage calibration, since the software performs a refinement of the nominal input values. The stereo-triplet procedure is based on the cross-check of the two stereo-pair reconstructions obtained from the left and centre tilt angle and the centre and the right one. At first, two images composing the stereo-pair, are imported on the Stereo Creator tool for a starting step. They must be aligned with the eucentric tilt direction if not there is an image rotation function in the software for this purpose [181].

There are three main input parameters needed for Stereo Creator reconstruction tasks:

Reference tilt angle: It is the nominal value or the reference value if a calibration procedure is carried out before. Typically, angles between 5 and 20 degrees are used. Tilt angles smaller or

larger than these lead to unreasonable results. It is recommended to use smaller tilt angles with thick specimens and higher tilt angles for thin specimens for better vertical resolution.

Projection distance P_d: This parameter is the summation of the SEM dependent ε-value and the working distance W_d. In general, an ε-value between 5 and 10 provides good measurement results (see Figure 2.11a) [181].

Horizontal measurement point size (pixel size): The pixel size represents the distance between two following pixels onward the horizontal direction. In MeX software, there is a tool provided for calculating this value. The operator is asked to draw a line on the image's scale bar and then to enter its nominal length so that an estimated result can be obtained. The measurement algorithm of MeX is based on associating the content of the left and right stereo images. This is called "Global Offset" and it helps to find corresponding points in the two images. Global offset describes an average value for various points, which are shifted according to their heights. Two processes are required for a 3D reconstruction: image matching and geometric assessment [174, 181].

The image matching step includes automatic identification of the stereo pair of homologous points, representative of corresponding features. The algorithm used in MeX applies a modified area-based approach. Individual pixels are used as matching elements. Pixel-to-pixel correspondence is evaluated on image rank values, after a relative ordering of the grey-level values and successive classification in rising order [182]. After carrying out two measurements under different perspectives, surface features of different elevations vary in their lateral dislocation. For each image pixel, the depth is calculated using the parallax movement of features from their location in the first image, to the new location in the second one (see Figure 2.12). A map of elevations at specific points is produced by interpolating between points [174].

It is recommended to use eucentric tilting which results in a horizontal offset between the left and the right image. However, an ideal eucentric tilting is often not practicable due to different reasons such as specimen positioning or misalignments. Consequently, an offset also along the vertical direction is present, which can be used as a hint of how close the tilt to an ideal eucentric one was. In ideal eucentric tilting, the principal axis and the tilt axis meet at the point K_{ez} on top of the surface (see Figure 2.11b). Hence, a tilting will result in a static centre point in the image. In the non-ideal case, the axes do not meet on top of the surface, but below or above (point K_{ne}).

A non-ideal tilting results in a movement of the centre point. There are some procedures recommended by MeX user manual to diminish possible errors [178]. According to the stereo-pair method described in Figure 2.12, the elevation measurement of each point on the surface can be linked to the parallax distance (x_{left}-x_{right}), the microscope magnification (M) and the tilting angle ($\Delta\Theta$) as shown by Equation 2.3.

$$z = \frac{(x_{left} - x_{right})}{(2 * M * \sin(\Delta\Theta/2))} \tag{2.3}$$

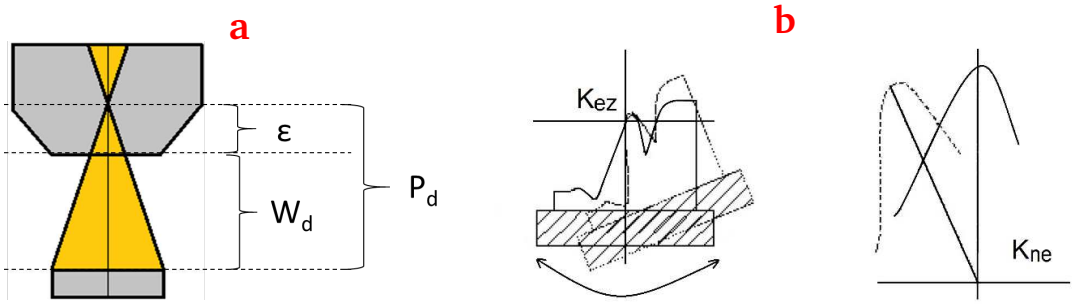

Figure 2.11: a) Illustration of projection distance parameter for Stereo Creator reconstruction. **b)** An ideal (left) and a non-ideal (right) eucentric tilting [178].

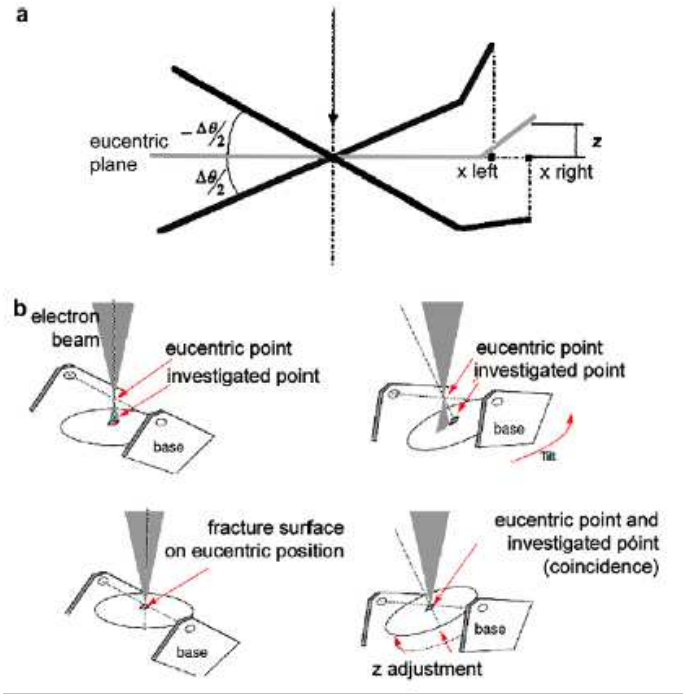

Figure 2.12: a) Configurations for stereo pair imaging in SEM. **b)** Adjustment in the SEM to obtain stereo images in the eucentric point. Top images show the error introduced by tilting the sample on the wrong plane, while bottom images show tilting on the eucentric plane [183].

As can be understood from this equation, higher tilt angles reduce the inaccuracy of elevation measurement calculation (z). The magnification (M) is defined as the ratio between the image distance to the object distance. Irregular surfaces lead to different magnification due to their geometrical distortions. To minimize the errors in elevation measurement calculation (z), values under 500x should be avoided [183]. Beside qualitative assessment, the MeX software can perform quantitative assessments regarding surface features such as roughness, waviness, area, and volume analysis [178].

In this thesis, three-dimensional information of the surface topography was calculated using auto-

matic image correlation with the evaluation software MeX (Alicona Imaging, Graz, Austria). Due to the facility of analyzing the structural function of the surface, areal (3D), surface roughness parameters have a clear advantage over common profilometry (2D) parameters for describing the real situation. Moreover, applying the 3D parameters results in a reduction in the influence of erroneous features, and the results are statistically more meaningful. Therefore, the area analysis mode available in the MeX software was used to calculate areal roughness parameters.

Using the above-mentioned conventional SEM, the same surface area of the sample was imaged twice with eucentrical tilting. The stereo-pair images were imported together with information regarding the total tilting angle, the pixel size of the images, and the working distance (W_d) in the microscope. The area Analysis Mode in the MeX software calculates the primary outline, roughness, and waviness parameters of the surface structure from its digital elevation model (DEM). The resulting images were evaluated using the window-roughness method, whereby values above a certain cut-off wavelength, λ_c, are identified as waviness and are not included in the surface roughness calculation. Detailed characterization of the surface roughness can be given through a set of parameters that are defined in the international standard ISO 25178.

2.2.1.3. Transmission electron microscopy

To achieve very thin foils of the *as-fired* and porosified LTCC with a thickness in the range of few nanometers, the 'lift-out' technique in a dual-beam focused ion beam (DBFIB) FEI Quanta 200 3D system was used. Next, these thin foils were analyzed using an FEI Tecnai F20 (scanning) transmission electron microscope ((S)TEM) employing the high angle annular dark-field (HAADF) detector. This technique is known to be sensitive to the chemical composition as the HAADF detector collects Rutherford scattered electrons. The amount of Rutherford scattering depends on the square of the mean atomic number and thus on the chemical composition. Crystalline and amorphous phases were also identified using selected area electron diffraction (SAED) patterns. Local chemical analyses were performed on the foils using energy-dispersive X-ray spectroscopy (EDX). Electron energy loss spectroscopy (EELS) was carried out using a Gatan GIF Tridiem ER energy filter which is brought into the irradiation beam. The peaks in the EDX and EELS spectra were used for the compositional ratio of the elements presented in LTCC composition. The collective application of these methods allowed the determination of most of the containing materials, their distribution as well as their state of crystallinity.

2.2.2. Porosimetry

In most applications of porous solids, the size of pores is a key parameter. The pore size has a precise meaning when the geometrical shape of pores is known and well defined, (*e.g.* cylindrical, slit-shaped, *etc.*). Nevertheless, typically the smallest dimension of the pore, in the absence of

any further precision, is referred to as the size of the pore *i.e.* the width of a slit-shaped pore, the diameter of a cylindrical pore, *etc.*

Several methodologies have been developed for the characterisation of the pore size distribution and the total porosity of porous media. The methodologies include but not limited to gas adsorption [184, 185], mercury intrusion porosimetry [184], synchrotron small-angle X-ray scattering (SAXS) [186], and TEM [26, 187]. Among these methods, mercury intrusion porosimetry is widely accepted as a standard tool for measuring total pore volume and pore size distribution of porous materials. In this technique employing a mercury porosimeter, which can generate appropriately high pressures, and measuring the volume of mercury taken up by the pores a wide range of information about the porous sample are obtained that no other porosity characterisation method can achieve. For instance, by employing this method valuable information about pore size distribution, total pore volume or porosity, and specific surface area are attained [188, 189].

By this technique, pores between approximately 3.6 nm and 400 μm can be investigated. However, mercury porosimetry gives no information about the actual inner size of the pores, but it rather determines the largest connection (throat or pore channel) from the sample surface towards that pore and the pore geometry is assumed to be cylindrical. Therefore, pore sizes obtained by mercury porosimetry technique are smaller compared with the ones obtained from SEM or optical micrographs analyses.

In principle, in this technique by applying a progressively increased hydrostatic pressure p, mercury (a non-wetting liquid with contact angle >90°) enters the pores of an evacuated porous medium. There is an inverse relationship between the applied pressure and the pore diameter, which in the simplest case of cylindrical pores is given by the Young-Laplace, also known as Washburn, equation (see Equation 2.4).

$$\Delta p = -\frac{4\gamma \cos\theta}{d} \tag{2.4}$$

where γ is the surface tension of mercury and θ the contact angle between the solid sample and mercury. Although, θ depends on the nature of the solid surface, for a standard calculation procedure the customary value of 140° can be used, and γ is generally assumed to be 484 mN m^{-1}, which is the surface tension of pure mercury at room temperature.

Pores with smaller radius diameter d, require higher pressures to be penetrated by the liquid. If all pores are equally accessible, only those will be filled for which d>$\frac{4\gamma|\cos\theta|}{p}$, so that each increment of applied pressure causes the next smaller group of pores to be filled, with a concomitant increase in the total volume of mercury penetrated the pores [190].

The process is then reversed by decreasing the external pressure allowing the gradual retraction of mercury from the pores. This process of mercury intrusion into the pores and extrusion from them

yields cumulative volume against pressure curve, which can be used for the determination of the pore geometries. In mercury porosimetry curves often hysteresis occurs when at a given pressure, the volume indicated on the extrusion curve is larger than that on the intrusion curve, and at a given volume, the pressure indicated on the intrusion curve is greater than that on the extrusion curve [191]. Figure 2.13 represents the hysteresis loop and trapping of mercury within the sample during the first intrusion process.

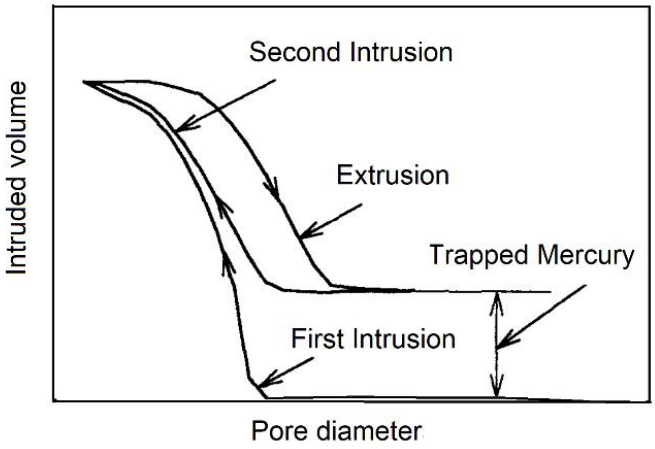

Figure 2.13: Hysteresis loop in pore-size distribution obtained from mercury porosimetry [192].

The hysteresis loop observed in porosimetry is mainly attributed to the presence of ink-bottle pores. As already explained, in this type of porosity "neck" or entrance opening to a pore is smaller than the actual pore body. Therefore, during the intrusion mercury enters the pore body at a pressure determined by the neck and not the actual body size. On the other hand, during the extrusion, the mercury thread breaks in all the necks between pores leaving many isolated packages of entrapped mercury inside the sample (see Figure 2.14). Likewise, the interconnected pores and narrow inlets lead to wide voids. Thus, during the extrusion process, mercury is trapped in the wide voids causing hysteresis.

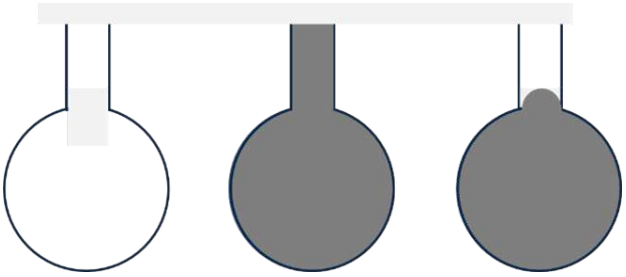

Figure 2.14: Schematic representation of an ink-bottle pore at different states; **a)** empty pore, **b)** pore fully intruded with mercury and **c)** mercury partially trapped after the experiment (adapted from [90]).

The hysteresis can also be attributed to the effect of contact angle. The surface tension and contact

angle from Equation 2.4, which relates the applied pressure to pore size, are known to depend on the radius of the pore, and whether the mercury is advancing or receding from a sample [193]. This results in a difference between intrusion and extrusion curves.

The purity of the mercury, evacuation of the sample prior to intrusion in order to remove adsorbed water or chemicals, and proper choice of equilibration times are critical for a successful experiment and reliable analysis results. Another source of possible problems is the creation of artificial pores due to the packing of the sample inside the penetrometer cell. The inter-particle voids between powder granules are an obvious example. However, even the voids between sheets of a sample (*e.g.* paper pieces) or the void between the sample and the glass wall of the penetrometer are possible error sources.

To conduct a mercury intrusion porosimetry measurement, the weighed sample is enclosed in a cell. After the evacuation, mercury is admitted filling the cell, surrounding the sample and is subjected to progressively increasing hydrostatic pressures. It is assumed that as the pressure is increased, mercury enters pores in decreasing order of size. Thus, if ΔV is the volume intruded between P and $P+\Delta P$, it will equal the volume of pores with radii between r and r-Δr. In this way, a volumetric distribution of pore sizes is obtained. For this purpose, at each pressure, the volume of mercury entering the pore structure is measured, and its value at the applied pressure p_i gives the cumulative volume of all available pores of radius equal to, or greater than the corresponding pore diameter d. Nonetheless, this interpretation obviously depends on the validity of the assumptions involved. The diameter d is to be regarded not as a literal pore dimension, but rather as the size of an equivalent cylindrical pore which would fill at a given pressure. Moreover, the presumption that the pores are invaded in decreasing order of size may be invalidated by network effects, which imply that the sequential filling of pores is dictated primarily by their mode of interconnection. It should be noted that although mercury porosimetry is largely accepted as a standard measure of total pore volume and pore size distribution in the macro- and mesopore ranges, it is a destructive technique. Because by employing high pressures, the sample may be deformed elastically or even damaged irreversibly, and on reducing the pressure, a substantial volume of mercury may be retained in the pores.

In this thesis mercury intrusion curves were recorded on a Thermo Scientific PASCAL 140/440 setup up to a maximum pressure of 400 MPa, corresponding to a minimum pore opening diameter of 4 nm. Also, to gain information about the pore structures, the extrusion curves during pressure release were recorded. Additionally, the experimental data were used to determine the cumulative pore volume, pore opening diameter distribution, and relative pore volume of each sample series as well as the porosity within the etched layer. Depending on the degree of porosification a minimum number of 8 to 35 specimens were tested in each run. As the flat specimens are aligned such to form stacks in the sample holder, increased volumes are found due to the intrusion of the interstitial space between individual LTCC substrates in the stack at lower intrusion pressures. To correct for this phenomenon, a non-porosified stack of *as-fired* samples was tested in addition to the etched

samples. Furthermore, a double intrusion treatment was conducted in the low-pressure region (where the increased volumes were observed), only using the second intrusion run for evaluation. Before testing, all samples were dried at 110 °C overnight to remove any water adsorbed on the LTCC surface.

2.2.3. White light interferometry

Scanning White Light Interferometers is a well-established optical instrument for the non-contact (and thus non-destructive), fast, accurate, and repeatable measurement of topography, high-resolution contour, and surface roughness. In this thesis, investigations on the surface topography of LTCC substrates were conducted via 2-D surface roughness measurements using an optical profilometer (FRT MicroProf., Fries Research & Technology GmbH) with an x–y-resolution of 1 μm and a z-resolution of 3 nm. Using 2D scanning mode, the surface Roughness parameters were acquired according to EN ISO 25178 for each LTCC tape. Each sample was scanned in 3 different directions on a length of 2 mm.

2.2.4. X-ray diffractometry

X-ray diffraction (XRD) is a non-destructive and widely used analytical technique for characterizing crystalline materials and is even believed to be the first level of characterization in ceramic and inorganic materials [194]. It provides information on crystal structures, lattice spacing, phases, particle size, and chemical composition information.

Diffraction effects are observed when electromagnetic radiation incident on regularly spaced structures with geometrical variations on the length scale of the wavelength. The interatomic distances in crystals and molecules typically are in the range of 0.15–0.4 nm which correspond to the electromagnetic spectrum with the wavelength of X-rays having photon energies between 3 and 8 keV. Consequently, phenomena like constructive and destructive interference should become observable when crystalline and molecular structures are exposed to X-rays [195].

XRD peaks are produced by constructive interference of the X-rays scattered at specific angles from each set of lattice planes in a specimen. Thus, XRD pattern is a fingerprint of periodic atomic arrangements in each material. Phase identification for a large variety of crystalline samples is possible by searching in the standard database for XRD patterns. Bragg equation relates the diffraction patterns with the crystalline plane (see Equation 2.5) [194].

$$n\lambda = 2D\cos\theta \tag{2.5}$$

where λ is the X-ray wavelength, θ is the angle of diffracted ray, and D is the separation in the lattice points.

In this thesis, XRD experiments were performed at *as-fired* as well as porosified LTCC sheets using a PANalytical X'PertPro MPD diffractometer with a filtered X-ray beam from a Cu anode was used. A soller collimator in the primary and secondary beam path provided a 0.04 rad divergence of the beam. The scans were taken from 5° to 90° with a step size of 0.02° in a continuous mode utilizing an X'Celerator detector with an opening of 2.1°. To detect possible X-ray amorphous factions in the diffraction diagram, each point was measured with a scan speed of up to 4 sec/step. The phase analysis based on the X-ray diffraction diagrams was performed using the High Score Plus software.

2.2.5. Inductively coupled plasma mass/optical emission spectrometry (ICP-MS/OES)

The inductively coupled plasma (ICP) is one of the most important excitations and ionization sources for the inorganic elemental analysis. A typical ICP source, so-called plasma torch, is shown in the schematic representation in Figure 2.15. The torch comprises three concentric quartz tubes trough which streams of Ar gas flow. The sample aerosol carried by the inner Ar flow is introduced into the centre of the plasma jet. The outer gas flow sustains the plasma and cools the plasma confinement tube to prevent melting. The intermediate tube contains the auxiliary gas, which has the function to lift the plasma away from the inner tubes. [196]. The top of the largest tube is surrounded by a water-cooled induction coil. For igniting the plasma, a spark of a Tesla coil is applied to ionize the first Ar atoms. The generated ions and electrons interact with the fluctuating magnetic field produced by the induction coil. By collisions, more and more atoms get ionized and the plasma is formed, which reaches typically a temperature between 5500 and 8000 K depending on the HF energy and the applied gas flows [197].

In inductively coupled plasma optical emission spectrometry (ICP-OES) technique a high-temperature plasma, produced through electromagnetic induction, is used to generate optical emission. The sample is introduced as a gas, vapour, or aerosol of fine droplets or solid particles into the plasma and the molecules/atoms get excited and ionized. By rapid relaxation of the excited species back to the lower states, ultraviolet and visible line spectra arise. The emitted radiation is monitored and used for qualitative and quantitative elemental analysis.

In inductively coupled plasma mass spectrometry (ICP-MS), after the sample aerosol is atomized, excited, and ionized in the inductively coupled plasma, the generated ions are transferred into the high vacuum of the mass spectrometer via an interface. There, the ions are separated according to their mass-to-charge ratios by a mass analyser and detected by a transducer.

Both ICP-OES and ICP-MS are widely used analytical techniques for trace element analyses [198]. These techniques feature very low detection limits, give a wide linear dynamic range, and have multi-element characters. The schematic representations of ICP-OES and ICP-MS are shown in

Figure 2.15. Typically, ICP-MS allows one to perform more sensitive measurements compared to the ICP-OES, and also isotopes which are barely accessible for non-mass spectrometric techniques can be analysed by ICP-MS technique. However, compared to ICP-OES, lower sample introduction rates are desired in ICP-MS and the operation costs are usually higher.

In this thesis, the phase composition of *as-fired* LTCC substrate was explored by inductively coupled plasma optical emission spectroscopy (ICP-OES) measurements using a Spectro Genesis FES.

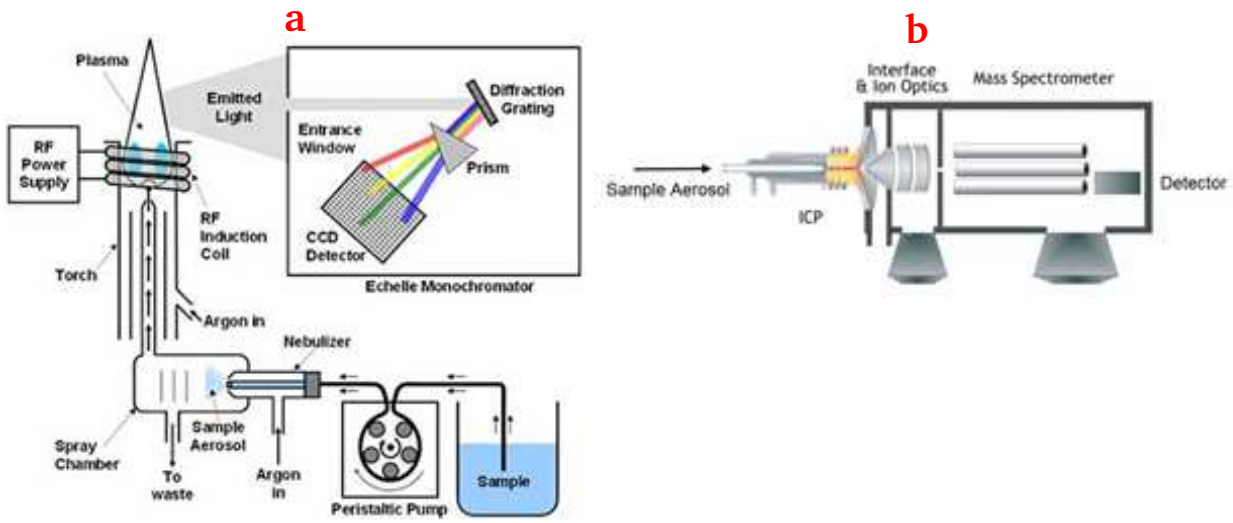

Figure 2.15: a) Schematic of an ICP-OES setup [199], **b)** Schematic set-up of an ICP-MS [200].

2.2.6. Laser ablation (LA) in chemical analysis (LA-ICP-MS)

Different techniques such as slurry nebulization, arc and spark ablation, laser ablation (LA) and electro-thermal vaporization can be used for the introduction of solid samples in ICP-OES or -MS. LA is a widely used technique for direct solid sampling and when combined with ICP-OES or -MS (LA-ICP-OES or -MS) introduces a powerful method for micro-local and direct elemental analysis of various sample types. LA-ICP-OES and -MS also enable spatially resolved analysis including microanalysis, depth profiling, and two-dimensional elemental mapping. Further advantages are the high sample throughput, minimal sample preparation, nearly non-destructiveness ($< \mu g$ of sample mass is required), the possibility of analyzing any type of solid material, and in the case of LA-ICP-MS even the access to isotopic information and very low detection limits in the range of $< \mu g\ L^{-1}$ [201–203]. Schematic of a LA-ICP-OES or MS is shown in Figure 2.16.

A short-pulsed, high-power laser beam is focused onto a sample surface. This results in ablation of a finite volume of the solid sample generating vapour, particles, and agglomerates. The formed aerosol is transported into the ICP-OES or -MS by a carrier gas flushed through the ablation chamber.

In this thesis, conclusive information about chemical compositions of etched and *as-fired* samples and thereby the etching mechanism was obtained by performing laser ablation inductively coupled plasma mass spectrometry (LA-ICP-MS). The measurements were conducted using an NWR213 laser ablation system (ESI, USA) with a frequency quintupled 213 nm Nd:YAG laser in combination with an iCAP Q quadrupole ICP-MS instrument (ThermoFisher Scientific, Germany). The coupling of the devices was accomplished using PTFE tubing. A fast-washout ablation cell always held above the actual ablation site was used for all experiments. Helium was the carrier gas, which was mixed with Argon make-up gas upon introduction into the plasma. For data acquisition, Qtegra software provided by the manufacturer of the instrument was applied. The tune settings of the MS instrumentation were optimized prior to each experiment using a NIST 612 trace metal in glass standard (National Institute of Standards and Technology, USA) for a maximum ^{115}In signal.

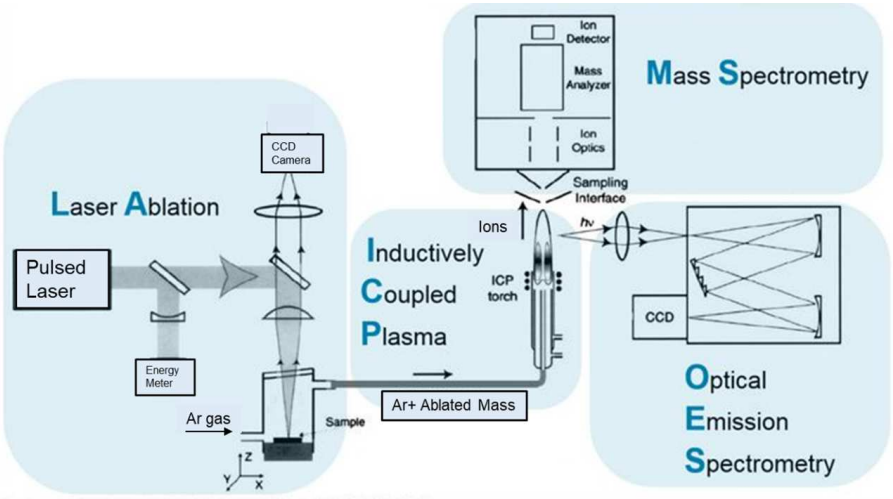

Figure 2.16: Schematic of a laser ablation system, using ICP-OES or ICP-MS for detection (adapted from [201]).

100 μm $\times$ 100 μm elemental distribution images were created using line scan ablation patterns with adjoining lines. For image processing, the software ImageLab (v.2.90, Epina GmbH, Austria) was used. Detailed information about the parameters used for the LA-ICP-MS experiments is given in Table 2.6.

2.2.7. Raman spectroscopy

Raman spectroscopy is a non-destructive technique which is based on inelastic scattering of photons from a sample exposed with a monochromatic laser light beam. This technique is commonly used to provide a structural fingerprint by which molecules can be identified. Typically, the spatial resolution that can be obtained by Raman spectroscopy is down to 1 micron. There are, however, several analytical arrangements where the resolution is far below 1 micron [204].

Table 2.6: Parameters of the LA-ICP-MS experiments.

Laser ablation system	**New Wave 213**
Average fluence	14.5 J cm^{-2}
Laser diameter	5 μm
Scan speed	10 $\mu m\ s^{-1}$
Repetition	20 Hz
Carrier gas flow (He)	0.6 L min^{-1}
Make-up gas flow (Ar)	0.8 L min^{-1}
ICP-MS instrumentation	**Thermo iCAP Q**
Auxiliary gas flow	0.8 L min^{-1}
Cool gas flow	14 L min^{-1}
Dwell time per isotope	10 ms
RF power	1550 W
Cones	Ni
Mass resolution	$m/\Delta m$ = 300
Measured isotopes	^{23}Na, ^{27}Al, ^{29}Si, ^{31}P, ^{44}Ca, ^{48}Ti, ^{90}Zr, ^{138}Ba, ^{142}Ce, ^{208}Pb

Upon the exposure of sample with a laser beam, most of the photons will scatter from the sample with no change of energy and the photons will thus have the same frequency as the incident light (ν_0), which is called Rayleigh scattering. However, a very small number of photons will exchange energy, causing molecules in the sample to vibrate with the vibrational frequency of ν_m. This type of scattering is referred to as Raman scattering and is characterised by frequencies $\nu_0 \pm \nu_m$. The ν_0-ν_m and ν_0+ν_m are called Stokes and anti-Stokes scattering, respectively. A Raman spectrometer measures the ν_m as a shift from the frequency of the incident light (ν_0) and the observed Raman shift of the Stokes and anti-Stokes scattering are direct measures of the vibrational energies of the molecules [204, 205]. These phenomena together with vibrational energy level diagrams are illustrated in Figure 2.17.

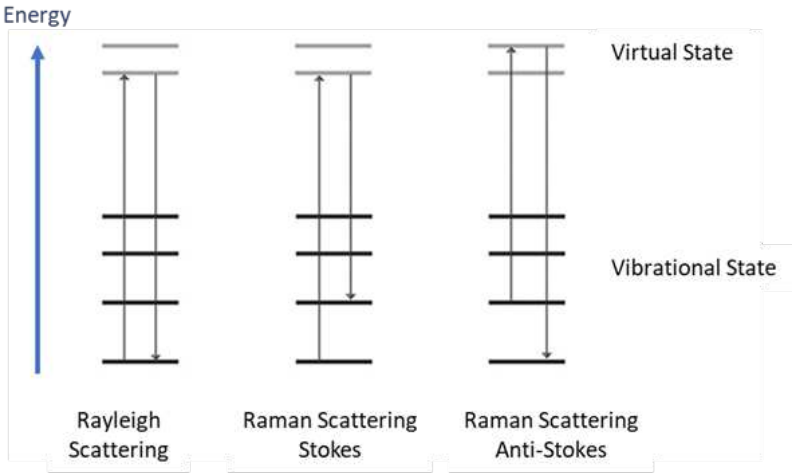

Figure 2.17: Energy-level diagram for the three different forms of scattering.

In this thesis, to acquire information about the dissolved phases and thereby of the etching mechanism, for the samples investigated in Section 3.1., Raman spectra were recorded with a Thermo Scientific Nicolet™ Almega spectrometer coupled with a high-quality Olympus microscope and high-resolution grating. Laser excitation was done at a wavelength of 532 nm.

For the samples investigated in Section 5.2., the Raman spectra of the films were measured at room temperature by a Renishaw In Via Reflex Raman spectrometer using a CCD camera and an excitation wavelength of 442 nm. Calibration of the spectrometer was performed with respect to the 520.7 cm^{-1} line of silicon single crystal. The impact of inhomogeneity of LTCC samples was minimized by taking measurements at different positions of samples.

2.2.8. X-ray photoelectron spectroscopy (XPS)

X-ray photoelectron spectroscopy (XPS) is a widely used surface analytical technique for measuring the chemical composition of surfaces based on the photoemission process. The basic components of an XPS instrument are a light source, an electron energy analyzer and an electron detector. When the sample irradiated by a beam of X-ray, the incident beam can penetrate up to several micrometres into the material, causing photoelectrons to be produced. However, only those photoelectrons originating from the outermost surface layers can escape the solid with the characteristic energy E_k. This is due to the very short mean free path of the low energy electrons in a solid (see Figure 2.18). Hence, the peaks observed in the XPS spectrum provide information on the surface composition of the specimen.

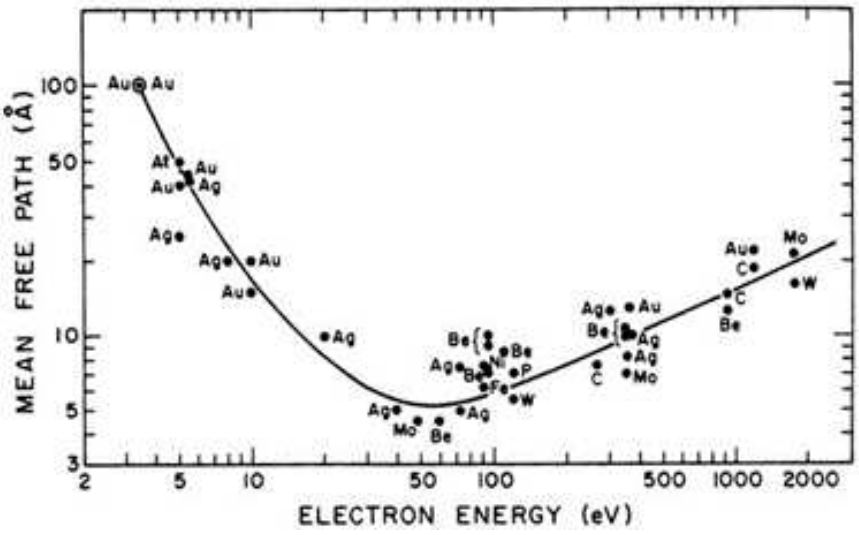

Figure 2.18: Mean free path of electrons in solids as a function of their energy [206].

The emitted electrons are energy-analyzed to provide a spectrum. Discrete peaks are observed,

corresponding to ionization from the core electron orbitals of surface atoms. Analyses of the spectral peaks are used to determine the composition and often the chemical state of the sample surface species [207]. When a solid sample is irradiated with X-ray of energy $h\nu$, electrons in orbitals with binding energies E_B, less than $h\nu$ can be ejected and emitted out of the surface, and subsequently detected in a spectrometer with a kinetic energy E_k, given by Equation 2.6. The corresponding energy level diagram is illustrated in Figure 2.19.

$$E_k = h\nu - E_B - \varphi_{sp} \tag{2.6}$$

where φ_{sp} is the work function of the spectrometer (typically 3–5eV) and E_k is measured by an analyser. Therefore, the binding energy E_B of the core level electron can be determined. Mg K_α and Al K_α are the two often used radiation sources because of their relatively high energy and narrow width. Much of the information obtained from XPS measurements is based on the observation of photoelectrons emitted from core levels of the atoms in the sample surface. All elements have at least one core level accessible to the ionizing radiation, with binding energies in the range of 10 to 1400 eV. These binding energies are well known, thus, the XPS spectrum provides an indication of all elements that are present (except hydrogen and helium).

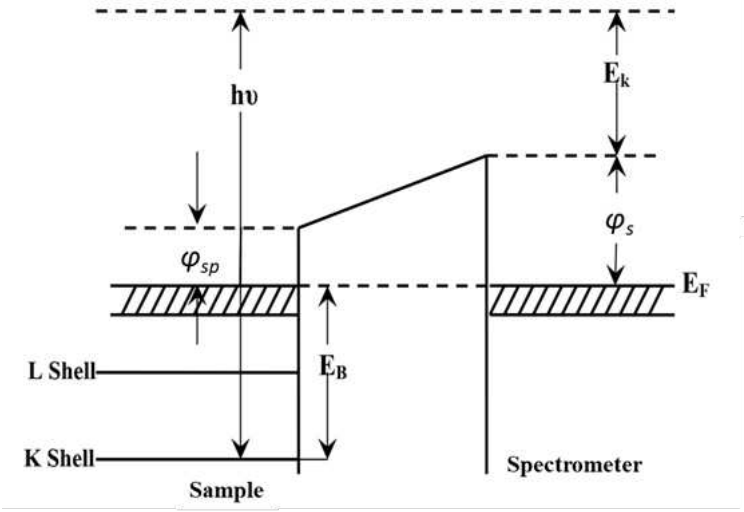

Figure 2.19: Energy level diagram [206].

In this thesis, the XPS spectra were measured in ultra-high vacuum AXIS-Supra photoelectron spectrometer (Kratos Analytical Ltd., UK) equipped with a hemispherical analyzer and monochromatic Al K_α source (1486.6 eV, analysed area –0.7×0.3 mm^2). The spectra were collected at the take-off angle 90°. The survey XPS spectra were recorded with the pass energy of 80 eV, whereas the high-resolution spectrum scans with a pass energy of 20 eV. The Kratos charge neutralizer system was used to compensate charging effects on the samples surfaces. However, we observed

the shift of the binding energies due to the surface charging effect even after neutralization by the low energy electron flood gun. Therefore, the obtained XPS spectra were calibrated on the C 1s peak maximum at 285 eV.

Atomic concentrations of chemical elements were calculated from high-resolution XPS peak after standard Shirley's inelastic background subtraction using the data system ESCApe provided by the producer and applying the relative sensitivity factor method. The CasaXPS software with Shirley baseline and Gaussian line shapes of variable widths for peak fitting was used for spectra processing. XPS peak positions were determined with an accuracy of ± 0.2 eV.

2.2.9. Mechanical Characterization

Flexural strength, σ, is a material property that defines the stress on material just before fracture in a flexure test (in N mm^{-2} or MPa). Other common notations for flexural strength are the modulus of rupture, bend strength or transverse rupture strength. The strength is calculated using the maximum bending moment, which depends on the applied force and geometry of the material. For flexure tests there is no involvement with end-tabs, or (normally) changes in the specimen shape; tests being conducted on simply supported beams of constant cross-sectional area.

Many test methods have been developed for the determination of flexural strength. The following section focuses on the two common methods which are used in this thesis.

2.2.9.1. Three-point bending test

A common test method for the determination of flexural strength is the three-point bending test. A rectangular specimen is mounted on two supporting pins near the ends of the specimen. A gradually increasing force is applied onto the specimen via a third pin which is placed in the equivalent distance to the support pins and has the same diameter. Due to the three pressure points at the pins, this test arrangement is called three-point bending test. A schematic representation of the setup is given in Figure 2.20a. Also shown in Figure 2.20b is the distribution of shear force and bending moment in the specimen.

A crucial requirement is that the force can be applied with a constant increase in load or constant transversal velocity. The maximum force or the failure load needs to be measured with the machine in an error range of approximately 1%. The distribution of shear stress is parabolic, with a maximum at the neutral axis and zero at the outer surfaces of the beam; the maximum value is given by Equation 2.7 [209].

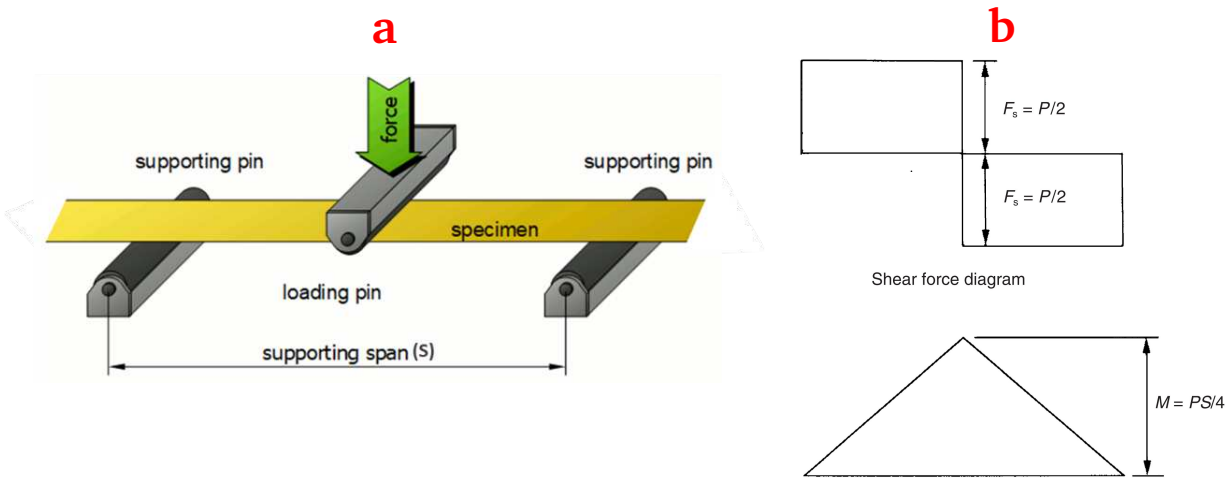

Figure 2.20: a) Schematic of three-point bending test setup [208], **b)** the corresponding shear force and bending moment diagrams [209].

$$\tau = \frac{(3F_s)}{2bh} \tag{2.7}$$

where F_s is the shear force on the specimen cross-section, with b and h being the specimen width and thickness, respectively.

The flexural response of the beam is obtained by recording the load applied and the resulting strain. In brittle materials such as ceramics, the failure of the material depends mainly on the density of defects or flaws located either on or in the specimen under test (see [210]). At these defects, a crack starts to form, so that structural defects affect the obtained results. Because the maximum of tensile and compressive stress is located on the surface of the specimen, preparation of the surface is a straightforward way to manipulate the mechanical robustness. Furthermore, the specimen needs to meet geometrical requirements as specified in [211].

A major disadvantage of the three-point bending test is that the maximum bending moment is one point of the longitudinal axis of the specimen. As previously described, defects or flaws on the surface of ceramics are the main reason for material failure. As the defects usually do not occur at the point of maximum bending moment, an over- or underestimation of flexural strength is possible [211, 212].

In this dissertation, to evaluate the stiffness behavior of the LTCC substrates (Ferro L8) due to the etching process, dynamic-mechanical analysis (DMA) was carried in bending mode in the temperature range from 25 to 550 °C using a TA Instruments DMA Q800. The span width was 10 mm, and the dynamic amplitude was 20 μm in the case of the specimens with a thickness of 180 μm and 7 μm for the 520 μm thick samples. A frequency of 1 Hz and a ratio of static to dynamic force of 1.25 were applied. The temperature was increased stepwise, starting at 25 C,

then ramped to 50 °C and from then the step size was 50 °C. After a dwell time of 10 min at each temperature step, the specimen was dynamically loaded for 30 s, and the storage modulus (E') was determined. E' is the stress-to-strain ratio in a system having sinusoidal loading and represents the energy storage capacity of a system and other relevant properties of the elastic portion. Basically, the quantity E' is a measure of the stiffness of the material [213].

2.2.9.2. Ball-on-three-balls (B3B) test

Uniaxial strength tests are commonly used to determine the flexural strength of ceramic materials because of their straightforward approach. However, these methods do not represent the multiaxial load situation on ceramic components in real service applications correctly. To determine the flexural strength, several biaxial test methods have been developed. Biaxial strength tests are usually performed on thin disks of ceramic specimens. A major benefit of biaxial strength test is that there is little to no stress on the edges of the tested specimen allowing a simpler sample preparation as the samples do not need to be polished and the sample geometry has less impact on the result, meaning that the specimens are not required to be perfectly shaped. It is possible to apply the methods to circular, square, or rectangular-shaped samples.

In this thesis, the biaxial strength of the LTCC specimens was determined using a miniaturized and specially built in-house B3B fixture to match the dimensions of the supplied components. In the B3B method, the specimen (or a disc) is supported by three balls that are equidistant to the centre on one side, and the other side is centrally loaded with a fourth ball, which produces a very well defined biaxial stress field [214]. Since the specimen is supported in four points it can be viewed as a four-point bending test. A simple scheme of a B3B-setup is displayed in Figure 2.21. The three-point support situation tolerates imperfections of disc flatness whereas other similar methods rely on perfectly flat discs and generally polishing of the specimen before the measurement is required. This makes the B3B setup suitable for quick testing of sintered disks without any further surface finishing. [215].

The four balls had a diameter of 5 mm. A pre-load of 5.2 N was applied to hold the specimen between the balls. The load was increased until a fracture occurs, and the fracture load was used to calculate the maximum tensile biaxial stress in the specimen at the moment of fracture.

Strength calculation – Analytical approaches based on linear-elastic thin plate theory have been investigated for different biaxial strength tests (see [211, 217]). The approximations lead to quite different maximum tensile stress values and stress distributions, depending on the sample and setup dimensions. Because a precise analytical calculation cannot be applied, a finite element (FE) analysis was performed by Andreas Börger *et al.* to obtain a numerical solution for this specific setup. Further detail on the procedure is given in [215]. A summary of the results and the formula

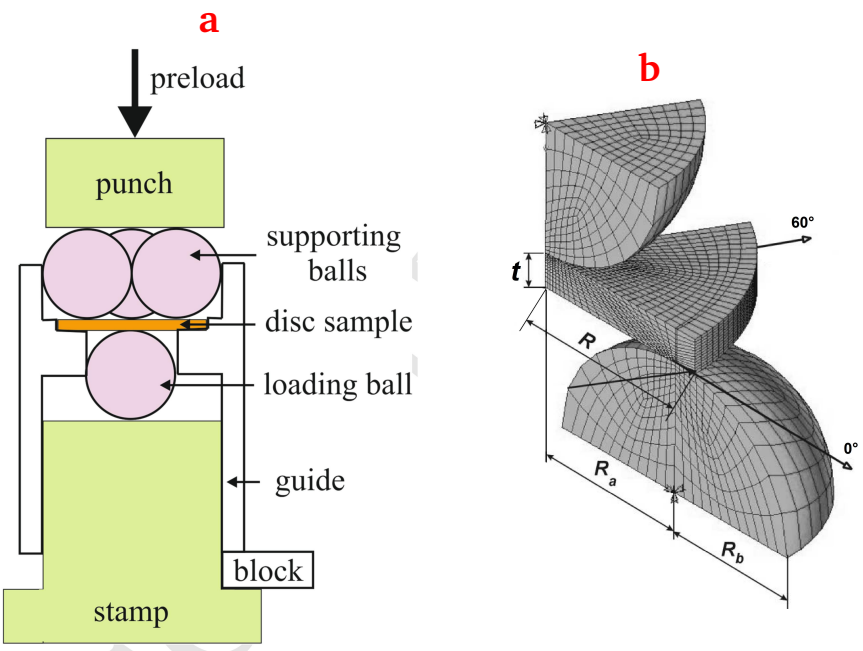

Figure 2.21: a) Schematic representation of a B3B setup and **b)** FE simulation of the ball on three balls test assembly [215, 216].

needed for the calculation are given in this section.

An example of the stress field in a disc during typical loading conditions in a B3B test is depicted in Figure 2.22. The support balls are fixed in their positions, the diameter of the support balls must be equal to that of the loading ball and they must be made from the same material. Also, the centre of the loading ball is allowed to move only perpendicular to the disc surface to apply the load on the disc. Under the condition that the support balls touch each other, forming an equally sided triangle of support points, the support radius can be calculated using Equation 2.8.

$$R_a = \frac{2\sqrt{3}}{3} R_b \tag{2.8}$$

where R_a is the support radius, and R_b the ball radius (see Figure 2.21b). The maximum tensile stress occurs in the centre of the specimen on the opposite side of the loading ball. In the contact area between the specimen and the loading ball high compressive stress values occur. The absolute value of compressive stress is significantly higher than the tensile stress amplitude in the centre of the tensile surface. This restricts the application of the test to materials with much higher compressive than tensile stress as it is the case with ceramics.

The maximum tensile stress σ_{max} in the disc depends on the applied force F, and the inverse square of the thickness of the disc T, as represented in Equation 2.9.

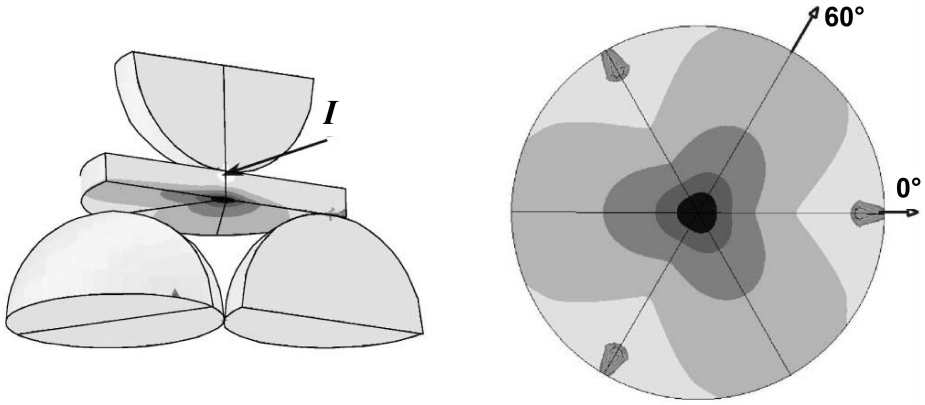

Figure 2.22: Stress distribution in a disc during typical loading conditions in a B3B test modelled with FE analysis. Dark areas indicate regions with high tensile stress, whereas the point marked with *I* represents the region of highest compressive stress [215].

$$\sigma_{max} = f\frac{F}{T^2} \tag{2.9}$$

where f is a dimensionless factor which depends on the geometry of the specimen, on the Poisson's ratio of the tested material, and the details of the load transfer from the jig into the specimen. Factor f is calculated using Equation 2.10 [215].

$$f(\frac{T}{R}, \frac{R_a}{R}, \upsilon) = c_0 + \frac{(c_1 + c_2(\frac{T}{R}) + c_3(\frac{T}{R})^2 + c_4(\frac{T}{R})^3)}{1 + c_5\frac{T}{R}}(1 + c_6\frac{R_a}{R}) \tag{2.10}$$

where R is the disc radius, ν is Poisson's ratio of the disc material, $c_0, \ldots, 6$ are constants, and R_a and R_b have been previously defined. The seven constants c_i (i=0,...,6) used in the calculation of the f are dependent on the Poisson´s ratio of the disc material, and their values for some specific Poisson´s ratios are given in Table 2.7 [215]. Basically, the equation fits the maximum tensile stress with an error of 0.5% compared to the FE analysis values.

Table 2.7: Constants evaluated for three different Poisson´s ratios [215].

	ν=0.2	ν=0.25	ν=0.3
c_0	-12.354	-14.671	-17.346
c_1	15.549	17.988	20.774
c_2	489.2	567.22	622.62
c_3	-78.707	-80.945	-76.879
c_4	52.216	53.486	50.383
c_5	36.554	36.01	33.736
c_6	0.082	0.0709	0.0613

The effect of specimen geometry on the factor f has also been investigated in a specific range as shown in Table 2.8. Therefore, the validity of the calculations is restricted to those parameters. Exceeding the limits of geometric specimen parameters can lead to significantly different stress situations and incorrect results. Compliance to these parameter ranges is crucial for the design of an actual test setup [215].

Table 2.8: Evaluated range of parameters for the factor f [215, 218].

Parameter	Evaluated range
R_a/R	0.55 - 0.90
T/R	0.05 - 0.60
ν	0.20 - 0.35

Börger *et al.* have analysed possible errors in the strength determination of brittle discs by B3B method[215]. Their study showed that the test is very tolerant for geometrical inaccuracies, misalignment, being out of the flatness of the disc. The most important property is the specimen thickness, which should be determined on the position of the loading ball. The influence of thickness enters with $\sigma_{max} \propto t\beta$ with $\beta \approx 2-3$ [218]. That means that an uncertainty of 2% in thickness causes an uncertainty in the strength of approximately 5%. In this regard, friction is much smaller than in the conventional three- or four-point bending tests. Based on this research results, for a maximum error in the σ_{max} of 1%, a relative difference in the thickness between the centre of the disc and its circumference of 5% can be tolerated. The thickness in the centre of the disc is of most relevance and it is suggested to use the thickness in the centre of the disc for data evaluation. The thickness at the circumference should only be checked to decide whether the above condition is fulfilled or not.

Furthermore, excentric positioning of the loading ball relative to the support balls and excentric positioning of one or more support balls to the disc lead to an uncertainty of maximum tensile stress smaller than 1% if the change in the support radius R_a is smaller than ± 0.1 mm. This is achieved by guiding the support balls and the loading ball as the impact of friction is negligible. An excentric positioning of the disc to the balls leads to a bigger overhang of the disc over the support radius on one side and a smaller one on the other side. This possible error is also negligible. If uncertainties of up to 5% regarding flexural strength can be tolerated, the B3B test is proven to be a simple and reliable method for the determination of strength in brittle materials such as ceramics [215].

Ball size and geometric parameter range of samples – As described before, the calculation of flexural strength is only valid in specific constraints, such as a R_a/R and T/R. According to Equation 2.8 the support radius for three touching balls depends on the ball radius. Thus, it is important to select balls with an appropriate radius to determine the flexural strength for the LTCC tapes. The important property of the samples is the thickness as the sample diameter can be varied. The

chosen ball diameter was 3 mm allowing the analysis of samples in a diameter range of 3.85 mm to 6.3 mm. It must be noted that the lowest and highest possible thickness is limited by the sample diameter. In this work, because of the small given thickness of the LTCC tapes (between 125 and 250 μm), the lower limit is more important. As a consequence, a LTCC sample diameter of approximately 5 mm was chosen. The samples with the lowest thickness (D9k7) can still be analysed properly and the sample geometry is not too small as that would make handling of the samples during the test more challenging.

Occurring forces and stresses – Prior to the design, some calculations were performed regarding the structural properties of the setup and induced stress during the test. The main concerns were that high Hertzian stresses might occur during the test because of the small ball diameter. Hertzian contact stress (tensile stress) is a specific type of mechanical stress that occurs when balls or cylinders are in contact with planes or themselves and is usually very high due to the small contact area between the two bodies. The value of Hertzian stress is an important factor for the design of the B3B setup as the material needs to withstand those pressures without deformation. Deformation of the setup would lead to a different test situation in general and may affect the validity of the FE analysis and hence, the calculated maximum tensile stress in the specimen. Consequently, the evaluated flexural strength value is not accurate.

The expected maximum force was calculated according to Equation 2.9 and the factor f with Equation 2.10 for a Poison's ratio of 0.25 with the parameters given in Table 2.1 The thickness values for GC, DP-951, and DP-9k7 in the *as-fired* state were 250, 150, and 125 μm, respectively. The support radius amounts to 1.73 mm with balls of 3 mm in diameter. Expected maximum force was calculated to be 5.11, 2.77, and 1.32 for the GC, DP-951, and DP-9k7, respectively.

Hertzian contact pressure – The Hertzian contact pressure between two spheres can be calculated using Equation 2.11. For the contact of two spheres, the effective radius is calculated using Equation 2.12. If the sphere is in contact with a plane the ball radius is used as the effective radius. The Young's modulus of the two materials is different and the mean value was calculated using Equation 2.13.

$$p_{max} = \frac{1}{\pi}\sqrt[3]{\frac{1,5FE^2}{R^2(1-\nu^2)^2}} \tag{2.11}$$

$$R = \frac{R_1 R_2}{R_1 + R_2} \tag{2.12}$$

$$E = \frac{2E_1E_2}{E_1 + E_2} \tag{2.13}$$

where E is the averaged Young Modulus, E_1 and E_2 are the Young moduli of material 1 and 2, R is the effective radius, in mm, and R_1 and R_2 are the radii of spheres 1 and 2.

The largest Hertzian contact pressure is supposed to occur between the loading ball and the stamp (see Figure 2.20a). To calculate the pressure correctly, the corresponding material data are required. The steel available for the stamp was Boehler K110 (DIN 1.2379) [219] with a modulus of elasticity of 200 GPa. The steel balls were purchased from Kugel Pompel [220] and were made from hardened steel, DIN 1.3505 [221], with a Young´s modulus of 210 GPa. For the Poisson's ratio, a typical value of 0.3 for steel was estimated. As for the applied force, the value of 5.2 N was estimated as an expected maximum according to previous calculations. The resulting Hertzian contact pressure was 1782 MPa which is high and therefore, the stamp, which is made from the less brittle material, might be irreversibly deformed during the test process.

Test on deformation of the material – Since there was no reliable information available regarding the tensile strength of the used steel, a test was carried out to determine whether the steel would be deformed under the given conditions. For that test, a plate made of the same steel was polished. After polishing, a grid was drawn onto the polished surface as described in Figure 2.23a. In each area of the grid, a force was applied with the purchased ball using a universal testing machine. The sample was analysed for imprints on a digital microscope

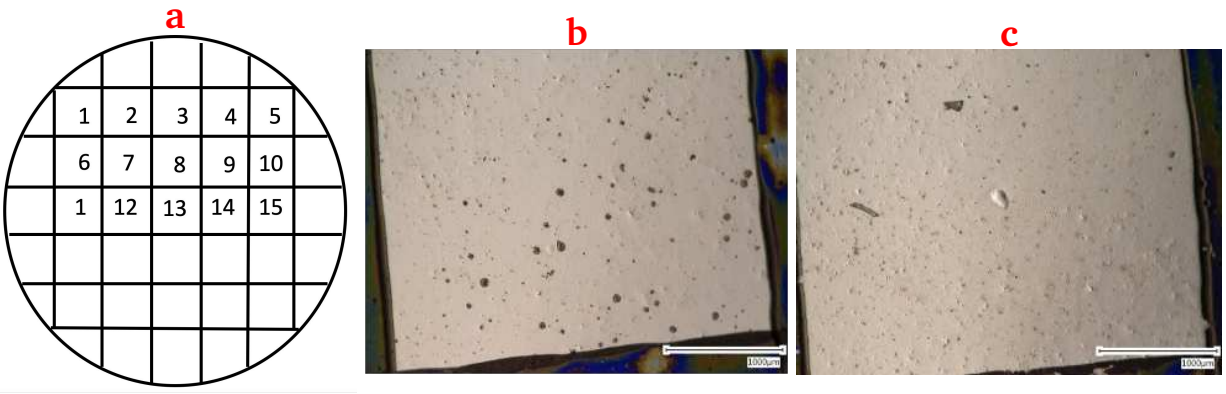

Figure 2.23: a) Schematic of the test plate with grid and test numbers, **b)** Optical image of area 4 (applied force of 3.9 N), a small imprint is visible in the area marked with the red circle, **c)** Optical image of area 15 (applied force of 10N), where a larger imprint is visible.

Forces of 0.75 N up to 10 N were applied. The first visible imprint was observed at a force of 3.9 N (see Figure 2.23b). As the maximum expected force exceeds that value, this steel could not be used for the manufacturing of the stamp without further treatment. That fact leads to a change of the setup as shown in Figure 2.21. Further details on the final setup design are given in the

following section.

3D design and construction sketches – The design of the B3B setup was carried out with the 3D CAD software Autodesk Inventor Professional 2019. Some changes were made in the initial setup that was designed in previous research (see Figure 2.21). A rendered 3D image of a quarter cut and an image of the actual setup are given in Figure 2.24.

The base had to be manufactured in two parts because the stamp or bottom punch needed hardening. During the hardening process, dimensions could change, and it is required that the punch fits the guide perfectly in terms of axis symmetry and diameter. The punch on top was hardened as well. It features a countersink with an angle of 90° that is supposed to support a fifth ball of 3 mm diameter. The ball is used to distribute the applied force equally onto the three supporting balls. It also allows a small out of the centre application of the force. Another change was the guide ring that should keep the sample centred in the setup. As no force is applied to this guide it was made of Polystyrene (PS) with a thickness of 0.3 mm. To enable measurement of samples with varying diameter, PS rings with inner diameters of 5.0, 5.1 and 5.2 mm were cut out using the laser cutter.

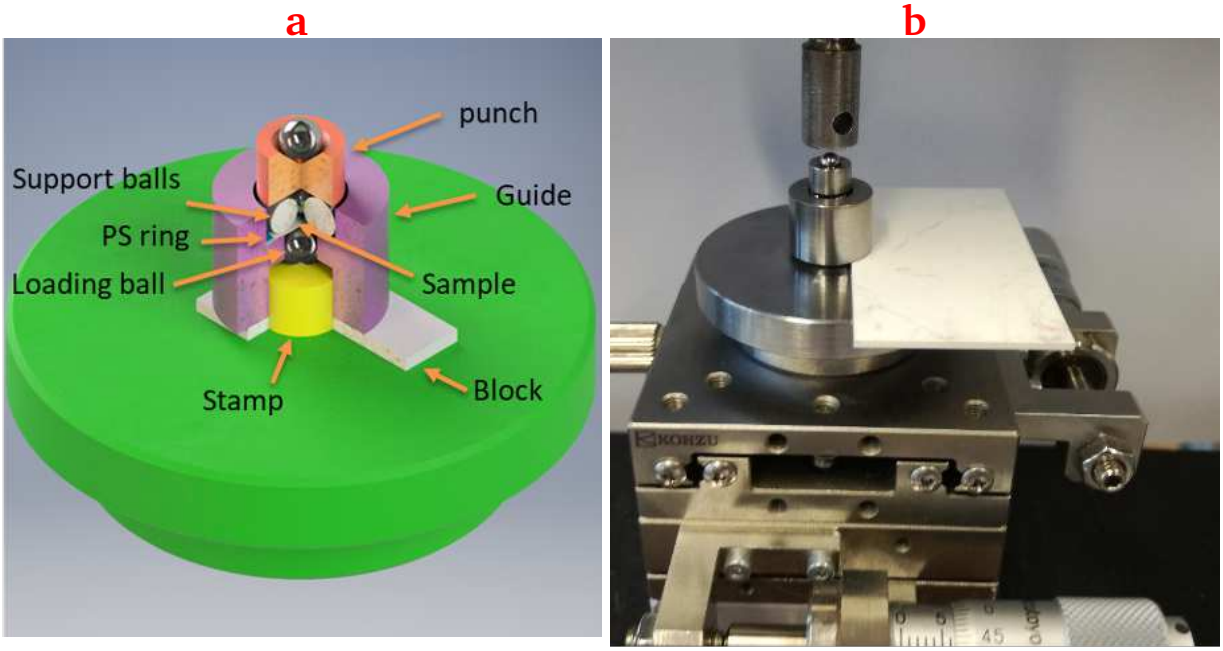

Figure 2.24: a) 3D rendering of a quarter cut of the B3B setup, **b)** actual setup. Note that the block has a different geometry as only the thickness is important to keep the guide in place, under the setup is a positioning stage used to centre the setup to the machine punch.

2.2.9.3. Determination of characteristic flexural strength

All tests were carried out using a universal testing machine. A pre-load of approximately 0.1 N was applied, and the force was continuously increased with a constant crosshead speed of 0.2 mm min^{-1}. Since the punch, the ball on top of the punch and the three supporting balls lay on the sample, their weight must be considered for force measurements. The weight of the components amounts to 1.19 g resulting in a force of 0.01 N. This force was added to the measured force for correct calculations. The block kept the guide in position, and the sample was not in contact with the loading ball. The setup was then transferred to the positioning stage (see Figure 2.24b) and loaded with the three support balls. After that, the punch was placed on top of the three balls, and the setup was centred to the machine punch using the positioning stage. Then the pre-load was applied manually using the control unit of the test machine, and the block was removed. The centring of the setup was checked, and then the test was started.

The flexural strength of each sample was calculated as described in Section 2.2.9.1.. Statistical analysis was performed according to DIN EN 843-5. For the evaluation, a two-parameter Weibull-distribution of flexural strength values for each sample is assumed. Using the Maximum-Likelihood-Method two parameters can be calculated: $\dot{m}$, the estimated value of the Weibull-modulus and σ_0, the characteristic flexural strength. The Weibull-modulus is a dimensionless parameter describing the width of the Weibull distribution. Regarding ceramic materials and flexural strength, a high Weibull-modulus indicates that the results show little variations and thus defects are distributed uniformly throughout the material volume. The characteristic flexural strength represents the strength value with a probability of failure of 0.632[211].

Maximum Likelihood-function L is described in Equation 2.14. To determine the maxima of the function its logarithm, $\ln(L)$, is differentiated and set equal to 0 resulting in Equation 2.15. This Equation is solved by iteration, varying the parameter $\dot{m}$ until the difference to 0 is smaller than 0.0001. After determination of $\dot{m}$, $\dot{\sigma_0}$ can be calculated using Equation 2.16 [211].

$$L = \prod_{j=1}^{N} \left(\frac{m}{\sigma_0}\right)\left(\frac{\sigma_{fj}}{\sigma_0}\right)^{m-1} e^{-\left(\frac{\sigma_{fj}}{\sigma_0}\right)^m} \tag{2.14}$$

$$\frac{\sum_{j=1}^{N} {\sigma_{fj}}^{\dot{m}} \ln \sigma_{fj}}{\sum_{j=1}^{N} {\sigma_{fj}}^{\dot{m}}} - \frac{1}{N}\sum_{j=1}^{N} \ln \sigma_{fj} - \frac{1}{\dot{m}} = 0 \tag{2.15}$$

$$\dot{\sigma_0} = \left[\left(\sum_{j=1}^{N} {\sigma_{fj}}^{\dot{m}}\right)\frac{1}{N}\right] \tag{2.16}$$

where L is the maximum-Likelihood-Function, N is the number of evaluated samples, m is the

Weibull-modulus, σ_0 is the characteristic flexural strength, σ_f is the strength of sample *j* out of the statistical population without ranking, $\dot{m}$ is the estimated value of the Weibull-modulus, and $\dot{\sigma_0}$ is the estimated value of characteristic flexural strength [211].

The calculated strength values are ranked in ascending order and given a rank number starting from 1. For each data point, a probability value is assessed using Equation 2.17. The data points are presented using Equation 2.18 as the y-axis and Equation 2.19 as the x-axis.

$$P_{fi} = \frac{i - 0.5}{N} \tag{2.17}$$

$$y_i = \ln\left[\ln\left(\frac{1}{1 - P_{fj}}\right)\right] \tag{2.18}$$

$$x_i = \ln\left(\sigma_{fi}\right) \tag{2.19}$$

where P_{fi} is the probability value, *i* is the rank number, *N* is the number of evaluated samples, and σ_{fi} is the Strength of sample *I* out of the statistical population with ranking.

2.2.10. Permittivity measurements

As already discussed, the relative permittivity of substrate material is a critical parameter that affects circuit performance. The performance of dielectric materials at RF is important for wireless communication circuits and components. In addition, the relative permittivity of the dielectric material affects the bandwidth (necessary for high-speed signal transmission) and circuit density. Thus, characterizing the permittivity at RF is becoming more important because of increased clock frequencies used in today's high-speed computers. Bandwidths of 10 to 20 times the clock frequency are required for good signal integrity. Therefore, in digital designs, analogue bandwidths to 1 GHz and higher are becoming common with clock frequencies of 50 to 100 MHz. However, measuring sheet dielectric material at RF has been difficult. No RF parallel plate measurement solution has existed until the introduction of the HP 4291B RF Impedance Analyser with the HP 16453A Dielectric Material Test Fixture.

In this thesis, the relative permittivity was measured by employing a newer generation of this device, Keysight E4991B RF Impedance Analyzer equipped with a Keysight 16453A dielectric material test fixture in the frequency range from 10 MHz to 1GHz with linearly increasing frequency at a voltage of 0.5 V. The number of points was 201 with a point averaging factor of 64. The sample thickness was measured using a micrometre screw. The complete set of samples was measured in a fixed sequential manner. The measurement sequence was repeated three times and the average values

are reported.

2.2.11. Design of experiments (DOE)

The effects of all wet chemical etching process parameters were studied using Design-Expert® Software. Central Composite Design (CCD), was used to create an experimental design plan. The ANOVA analysis uses the entered experimental data and fits them into a mathematical model. By doing so, the results from experimental conditions which are not studied can be estimated, and the overall experimental effort can be reduced significantly. The response parameters for modelling were chosen by assessing gravimetric results and corresponding SEM micrographs in terms of mass removal, d_p, and thickness reduction.

2.2.12. Optical microscopy

Several optical investigations were carried out on a digital microscope, Keyence VHX 5000. The microscope was used to determine the circularity of samples and for the dimensions required for the design of the B3B setup.

2.2.13. Gravimetric measurements

Gravimetric studies were conducted using a Sartorius R200D microbalance with a standard deviation in the range of $\leq$0.02 mg where the LTCC substrates were weighed prior and after the etching process. Gravimetric examinations are one of the most straightforward approaches for the investigation of etching rates. The mass removals were normed to the initial weight of the *as-fired* substrates and stated in %.

2.2.14. Geometrical measurements

Before the final sample preparations for B3B tests and also for shrinkage analysis of the samples due to the firing process, geometrical measurements were necessary. Several firing tests were carried out to determine the shrinkage of different LTCC tapes for different temperature profiles. Also, since for further experiments with B3B setup, the samples had to be inside a specific diameter range, the shrinkage measurements were essential for determining the diameter needed for cutting. For that reason, samples were measured before and after firing to determine the shrinkage in x-y dimension (x,y-shrinkage) and thickness (z-shrinkage). The x-y dimension of LTCC specimens was measured on a regular basis using a digital calliper with a precision of $\pm$10 μm. The precision was sufficient for most evaluations like shrinkage analysis. However, the thickness of the samples

had to be evaluated more precisely. Therefore, a digital dial gauge with a precision of ± 1 μm mounted to a precision measuring table was used (see Figure 2.25). For the B3B samples, the thickness of the samples was measured on both sides in the centre of the samples. The smaller value was taken as the accurate thickness to avoid measurement inaccuracies due to the bending of the specimens during the firing process. Moreover, when a systematic investigation of thickness change was targeted for higher precision cross-sectional SEM imaging was employed.

Figure 2.25: Dial gauge mounted to a precision measuring table.

Chapter 3.

POROSIFICATION OF GC LTCC AND FERRO L8 WITH H_3PO_4

Parts of this chapter have been published in [222, 223].

As it has been shown in previous works, by enhanced porosification of LTCC substrates through a wet chemical etching process more air is introduced into the LTCC, and thereby a further decrease in the overall permittivity can be achieved. Typically, the degree of porosification can be increased mainly through either lateral or axial growth of the nanoscale pores, whereas the former may lead to wider pore openings and increased surface roughness, *i.e.* a degraded surface quality. However, since for realization of, *e.g.* patch antenna elements, the long-term objective is to apply metallization on the porous LTCC, a high-quality surface is of great importance [77, 80]. Therefore, the axial pore growth through deep penetration of the etchant while preserving the surface quality would meet both requirements with respect to a significant air embedment and the applicability of a high-quality metallization. However, the wet chemical etching usually gives rise to channel-like, statistically distributed, and interconnected open meso- to macropores, which deteriorate the mechanical strength of the LTCC. Therefore, deep porosification of the LTCC could give rise to a reduction of the mechanical strength of the substrate and consequently in a reduced lifetime which is unfavorable for any application. Therefore, in this approach, a controlled porosification and a high surface quality together with the preserved mechanical strength are in the focus.

In this chapter, the porosification capability of two benchmark LTCC tapes, namely Ferro L8 as a celsian feldspar forming tape and Ceramtec GC (named GC LTCC in this thesis) as an anorthite feldspar forming tape is investigated. Wet chemical etching with orthophosphoric solution has already been comprehensively studied for the porosification of some LTCC tapes such as 951 LTCC (from DuPont), and CT 702 (from Heraeus). However, the effect of etchant pH and concentration

are two key parameters that are either not or inadequately studied, respectively. Thus, the impact of these two important parameters on the porosification process will be investigated in this chapter.

In the previous studies, a maximum porosification depth of about 40 μm had been achieved while applying concentrated orthophosphoric acid (85 wt%) to 951 LTCC (from DuPont) at 130 °C [73]. Further studies on the surface porosification of several LTCC substrates with various acidic etchants at different conditions have approved that concentrated phosphoric acid at 100 °C and above as the most effective etching solution for the porosification of LTCC substrates [68, 73, 75, 79]. However, the significant roughness and surface destruction caused by the etching process is still a challenge that retains the metallization problems.

Two types of LTCC systems as representative of anorthite forming tapes were used for the investigations, namely the Ceramtape GC (abbreviated as GC LTCC) which is one of the simplest systems due to the limited number of tape components and crystallographic phases involved.

3.1. Investigation of the porosification of Ferro L8 LTCC with H_3PO_4

This section deals with the porosification behaviour of Ferro L8 LTCC through the wet chemical etching process. Ferro L8 as a relatively new tape with promising features such as stable dielectric constant and low loss which make it ideal for producing components and modules with applications up to 40 GHz. The calculated mass removals as a function of etching time at different bath temperatures for both P50 and P85 etchants are illustrated in Figure 3.1.

Since a suitable etching process particularly requires the penetration of the etchant fluid into the pores and openings of the LTCC, the viscosity of the etchant is a crucial parameter for the etching process, and consequently, any etching bath parameters influencing this fluid parameter must be taken into account. Unlike gases, the viscosity of liquids decreases with temperature. Thus, when rising the bath temperature, the diffusion of the etchant into the depth of the LTCC is facilitated, and thereby the weight loss increases for a given time. This effect can be observed in the mass loss trends for both P50 and P85 at different bath temperatures. Similarly, a direct comparison of the weight loss values for P50 with those for P85 shows that due to the lower viscosity, for the less concentrated solution (*i.e.* P50), the weight losses are significantly higher, thus ruling out any major impact from the enhanced chemical activity at high concentrations.

3.1.1. Morphological and chemical characterization analyses for Ferro L8 LTCC

The impact of etching time and bath temperature on the depth of porosification is illustrated in the first two rows of Figure 3.2. Since the viscosity of a liquid solution decreases with temperature, the penetration of the etchant into the depth of LTCC is facilitated by the increase in the bath

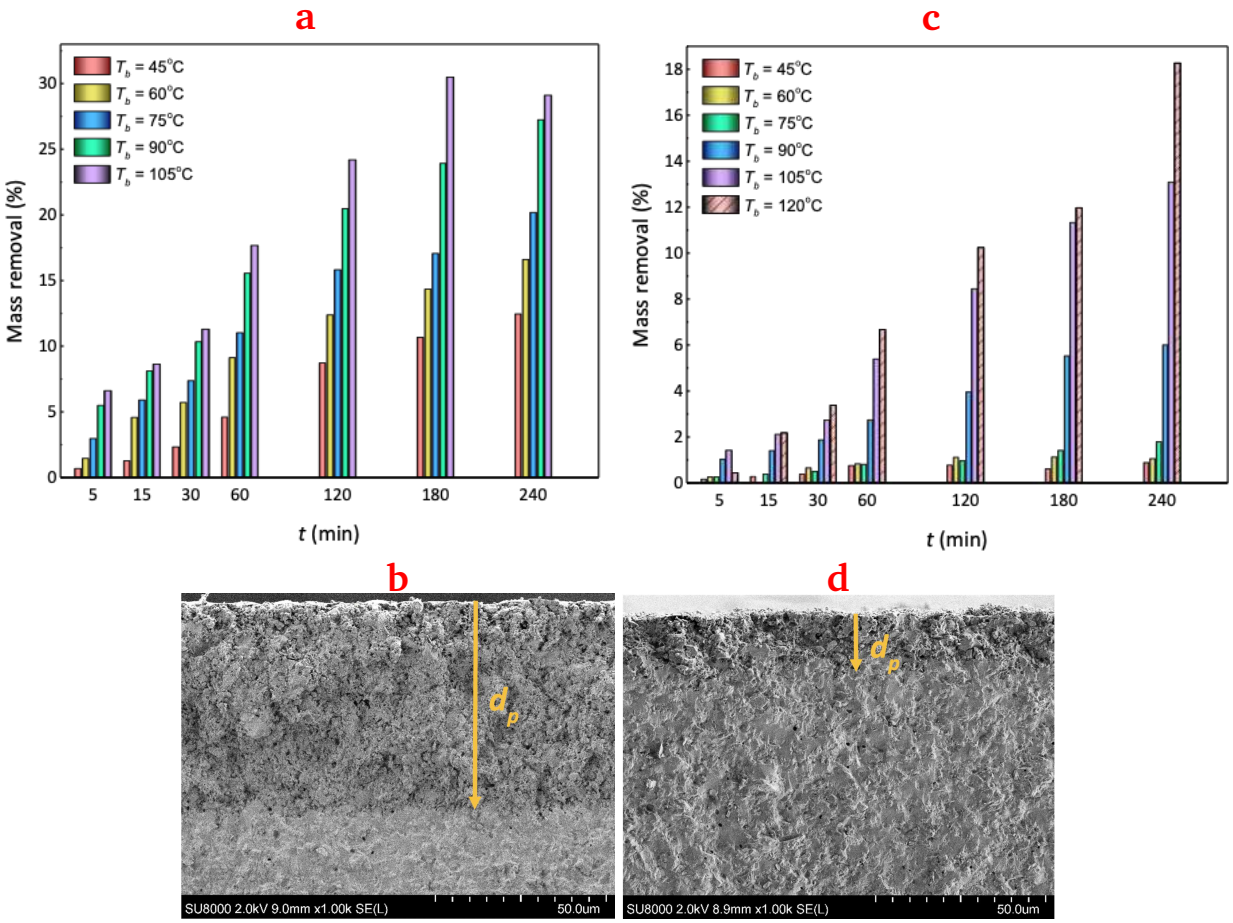

Figure 3.1: Mass removal of Ferro L8 as a function of time at varying bath temperatures, due to the etching with **a)** P50, and **c)** P85, and two representative cross-sectional SEM micrographs of Ferro L8 LTCC etched at 90 °C for 120 min with **b)** P50, and **d)** P85.

temperature. This agrees with the larger depth of porosification value for substrates etched at 90 °C compared to those etched at 75 °C.

Likewise, a direct comparison of cross-sectional SEM images for substrates etched at a constant bath temperature confirms the deeper diffusion of the etchant into the LTCC with time. After 240 min of etching at 90 °C, a significant porosification depth of 87 μm was realized which is a great achievement in comparison to the state-of-the-art.

Also, bath temperature has a significant impact on the porosification process in such a way that at higher bath temperatures (as known from Arrhenius equation) the etching rate is higher, thus higher depth values at a given time can be realized. By increasing etching time or bath temperature or both, the whole substrate (*ca.* 95 μm each side) gets porosified. While applying this approach to a thick multilayer LTCC, even a deeper porosification (*ca.* 200 μm each side) was reached. Therefore, by controlling the etching parameters, the porosification degree can be delicately tailored which is of great importance since tailoring the porosity secures the accurate decrease of permittivity to

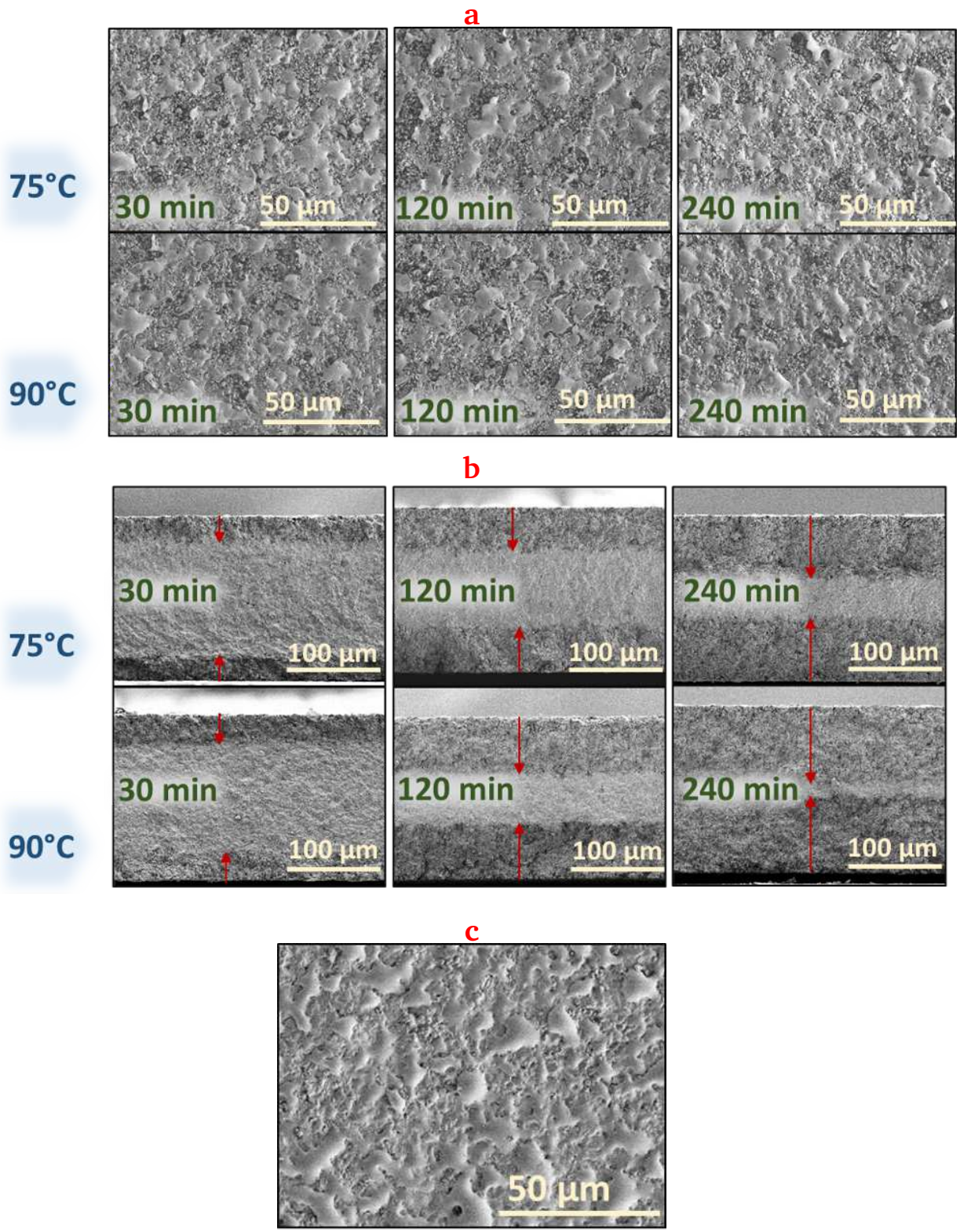

Figure 3.2: a) Top-view and **b)** corresponding cross-sectional SEM micrographs of Ferro L8 LTCC substrates etched with P50 at different etching times and bath temperatures. An SEM micrograph of an as-fired Ferro L8 LTCC is shown for comparison (**c**). Red arrows represent the depth of porosification.

the desired extent at a satisfactory mechanical strength. Despite the deep porosification, the initial thickness of the LTCC remains almost unchanged meaning that the etching treatment did not result in the overall dissolution of the substrate. Besides, as can be seen in the top-view SEM images of the substrates, the surface topography of the LTCC stays almost unaffected. This indicates that the etching of Ferro L8 in phosphoric acid solution results in a pure porosification, thus proving a good etch selectivity. This is an important result, especially when compared to the etching of Ferro L8 with NaOH solutions which will be discussed in the next chapter.

LA-ICP-MS measurements – In order to get qualitative information about the chemistry of the etching process, LA-ICP-MS measurements were conducted for the *as-fired* and porosified LTCC substrates. The ICP-MS analyses confirm the presence of Al, Si, P, Ca, Ti, Na, Zr, Ba, Ce, and Pb in the LTCC substrates, listing, however, only the most dominating LTCC elements. The local elemental distribution images of these elements for Ferro L8 substrates for both *as-fired* and etched states are shown in Figure 3.3. For securing direct comparability and clearly illustrating the trend in the depletion of certain elements due to etching, two different etching times of 60 and 240 min were investigated. In all these images, brighter areas indicate the presence of a higher amount of the corresponding isotopes, while darker areas show a lower concentration. Even though the exact quantification is not possible without suitable reference samples, information about relative elemental changes caused by the etching can be obtained by comparing the maps of the *as-fired* substrate with the corresponding images of the etched samples.

The maps illustrate a rapid and significant decrease in the amount of Ti and Ba after 60 min of etching while the Al count declines less significantly. The amounts are even reduced further after longer etching for 240 min. For Ca and Pb, the etching rate is so fast that even after 60 min of etching, a complete depletion is observed. The smallest change was observed for Si. All these observations indicate that the etching rate of the calcium aluminosilicate component of the tape is the highest while the corundum grains and glass phases are dissolved substantially more slowly. Due to the high permittivity attributed to the Ti-containing constituents such as TiO_2 and $BaTiO_3$ the significant removal of Ti is also very beneficial for permittivity tuning. For example, TiO_2 in the form of rutile, which exists in the Ferro L8 LTCC, has a relative permittivity of around 100 in the microwave frequency range [224, 225].

XRD measurements – X-ray diffractograms of *as-fired* and etched Ferro L8 were recorded and the results are shown in Figure 3.4a. In order to perceive the tape composition and the changes due to the firing process, the diffractogram of the Ferro L8 green tape is also shown. These results show that Ferro L8 is initially composed of Al_2O_3 and TiO_2 crystalline filler material dispersed in an amorphous glass matrix. By firing at a peak temperature of about 850 °C in a belt furnace, celsian as the new crystalline phase is formed in the vicinity of the alumina grains. This hypothesis

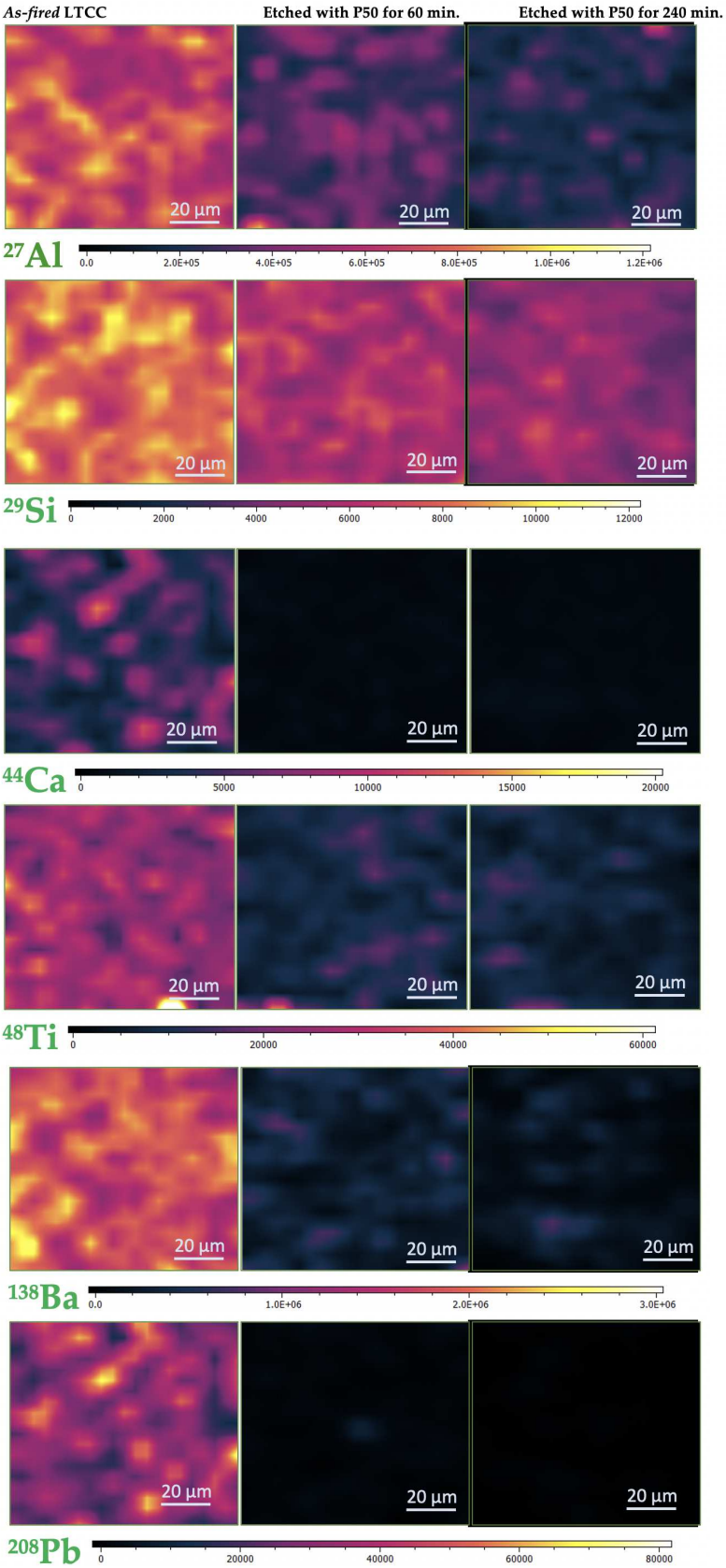

Figure 3.3: Elemental distribution in an area of 100 μm × 100 μm for the *as-fired* and P50 etched Ferro L8. The colour represents the measured signal intensities in counts per second (cps) according to the scale bars. For the reason of comparison, the same scaling was used for all three samples.

is proved in the TEM studies which are represented in this chapter. Emerged peaks in the *as-fired* diffractograms in comparison to the green tape are attributed to the celsian phase. However, in the diffractogram of the etched Ferro L8, no characteristic celsian-related peak is detected. This means that the celsian phase is very selectively etched via the phosphoric acid treatment of the substrate. This can also be observed in the top view micrograph (see Figure 3.4b) of Ferro L8 etched with P50.

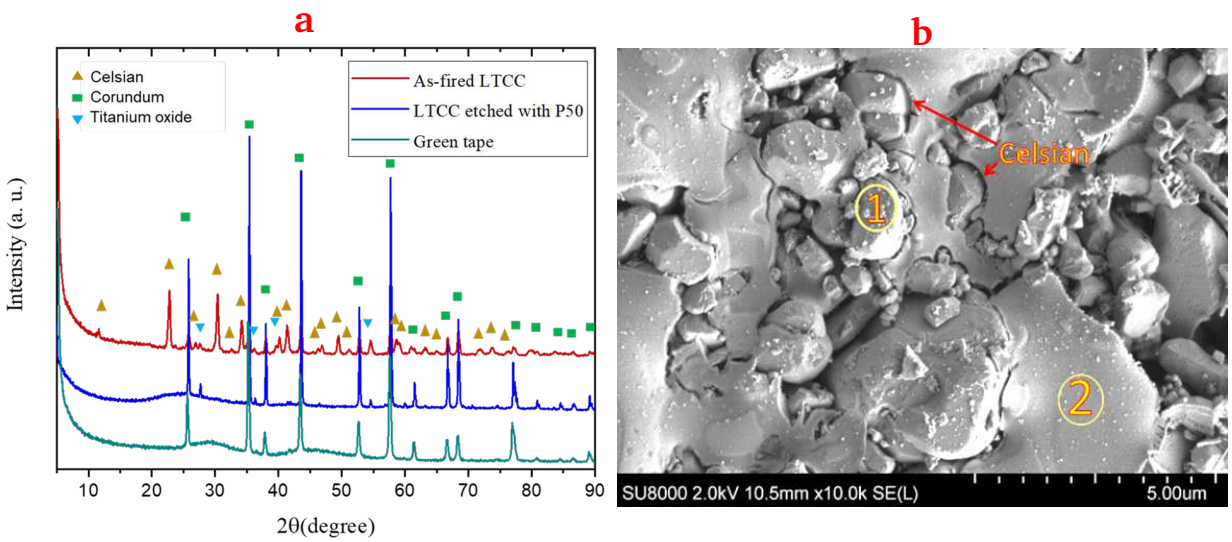

Figure 3.4: a) X-ray diffraction diagrams for Ferro L8 as green tape, *as-fired*, and etched with a P50 etching solution. The intensity levels are shifted for comparison reasons. **b)** SEM micrograph of Ferro L8 etched with P50. Positions 1 and 2 represent alumina grains and glass matrix, respectively.

In this figure, regions 1 and 2 represent the areas with high and no grain accumulation, respectively. Generated openings between alumina grains and glass matrix are attributed to the dissolved celsian phase. Since the corundum grains provide an Al source for the formation of rapidly dissolvable feldspars, their presence gives rise to areas with enhanced porosity. This image shows a very clear dependency between the grain distributions and porosification where the feldspar celsian phase close to the grains is predominantly dissolved and the surrounding glass phase remains almost unaltered.

Raman measurements – To acquire detailed information about the microstructure of the LTCC, Raman-based investigations were conducted to correlate the change in LTCC components due to the etching process. The investigated samples were LTCC substrates etched with P50 solution at 90 °C at different etching times of 5, 15, 30, 60, 120, and 180 min. Since the etching rate at low temperatures is very slow and at high temperatures difficult to control, T_b of 75 and 90 °C were chosen as representative etching temperatures for further analyses of the porosified LTCC substrates. For reasons of comparison, the *as-fired* LTCC was also subjected to the Raman measurements.

Either of the corresponding Raman spectra shown in Figure 3.5 is an average of 180 spectra which have been obtained from the cross-section of the LTCC substrates applying a step size of 1 μm. In the Raman spectra, major peaks corresponding to rutile (TiO_2), corundum (Al_2O_3), and celsian ($BaAl_2Si_2O_8$) phases are detected. For this purpose, besides the knowledge about the tape composition which was obtained via ICP-OES measurements where the composition of *as-fired* Ferro L8 was identified as 42.97% Al_2O_3, 30.45% SiO_2, 16.37 BaO, 6.52 B_2O_3, 2.67 CaO, and 1.02 TiO_2 (wt%), RRUFF Database was also employed. The corresponding individual spectra of these three phases are shown in Figure 3.5 [226].

For the *as-fired* sample, sharp peaks at Raman shifts below 200 cm^{-1} as well as small peaks at 509 cm^{-1} and 358 cm^{-1} are attributed to the crystalline celsian phase. By increasing the etching time, the intensity of these peaks decreases, and finally, they disappear, which represents the celsian removal due to the etching process. The peaks at 600, 450, and 220 cm^{-1} which are attributed to the rutile phase, and the peaks at 380, 420, and 640 cm^{-1} remain almost unaltered within the measurement accuracy. Similar to the well-known acidic dissolution reaction of anorthite ($CaAl_2SiO_8$) [107, 227], the following reaction was proposed for the celsian dissolution in LTCC:

$$BaAl_2SiO_8 + 8H^+ \rightarrow Ba + 2 + 2Al^{+3} + 2H_4SiO_4 \tag{3.1}$$

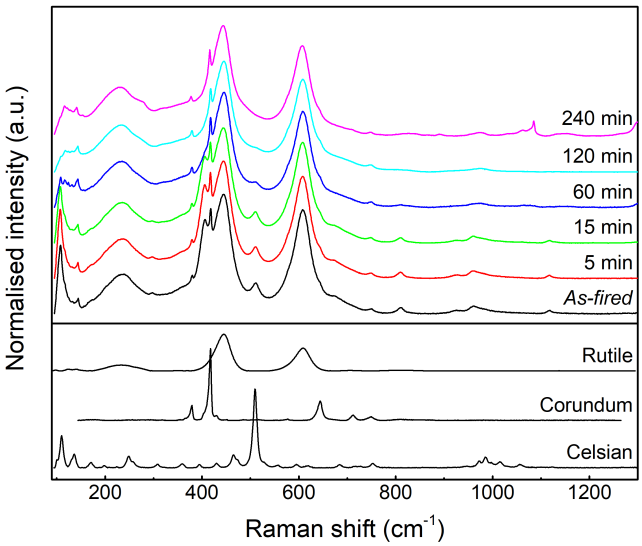

Figure 3.5: Raman spectra normalised to the maximum of the band in the Q-range, for *as-fired* LTCC and substrates etched with P50 at T_b=90 °C. Each spectrum is an average of 180 individual measurements. The reference spectra which were obtained from the RRUFF Database are shown at the bottom of the plot. The peak at 404 cm^{-1} which is marked with an arrow was used for estimation of etching depth.

In order to investigate the etching behaviour into the substrate depth, individual Raman spectra are shown in Figure 3.6 when starting at the surface (*i.e.* depth of 0 μm). Since displaying all 180 spectra will be inconvenient to distinguish especially the small peak changes due to the etching

process, only some selected spectra which are of interest to estimate the depth characteristics are shown. For the interpretation of the obtained results, however, minor differences in the spectra of a similar region even for the *as-fired* LTCC are reasonable, as LTCC is a composite of ceramic grains heterogeneously embedded in a glass matrix, what is the reason why the averaged spectra were shown in Figure 3.5. But, it is also intended to track the significant peak changes into the depth of the LTCC. Therefore, the etching depth was estimated from the disappearance of the peak at 404 cm^{-1} which was most sensitive to the dissolution, although the peak itself was not indexed. Three representative samples, *i.e. as-fired*, partially etched (120 min), and totally etched (240 min) are shown. For the *as-fired* substrate, except for the small peak found at large Raman shifts, the characteristic spectra remain unchanged. For the sample etched for 120 min no or merely weak celsian-related peaks were found at the surface. However, at a certain depth (approximately 70 μm), these peaks are getting perceivable. Nevertheless, for the sample etched for 240 min, which represents the maximum etching depth, no significant peak associated with the celsian phase was observed at any depth, thus indicating that through a highly selective celsian dissolution, the whole substrate has been porosified. These results are in a reasonable agreement with the d_p values obtained from cross-sectional SEM images as well as with those obtained from TEM investigations, which will be discussed next.

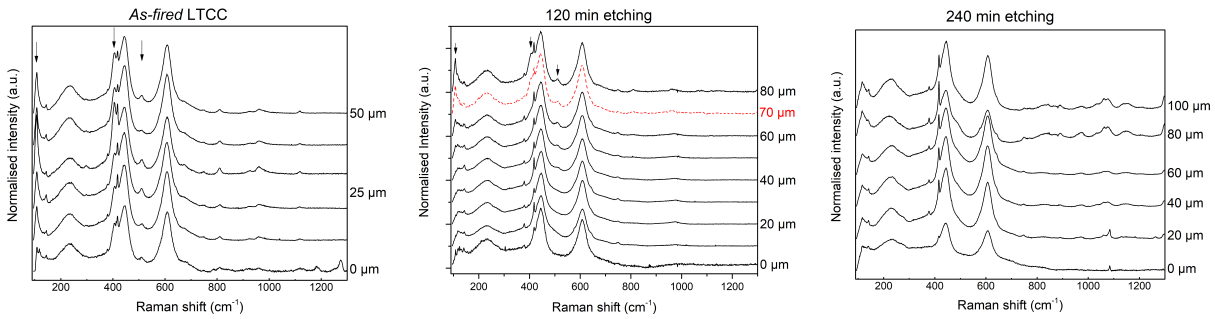

Figure 3.6: Raman spectra normalized to the maximum of the band in the Q-range, for the *as-fired* LTCC and substrates etched with P50 for different times at T_b=90 °C. All spectra were normalized to their overall area. The red spectrum is related to the estimated maximum depth of porosification, d_p. The values given next to the spectra represent the depth at which the spectrum is acquired.

TEM measurements – In addition to the chemical composition and morphology analyses, and in order to get a better understanding of the etching mechanism, it is necessary to study the crystallographic structure of the LTCC substrate in selected areas. For this purpose, the bright-field TEM overview of the Ferro L8 was obtained (the top left of Figure 3.7) and the selected area electron diffraction (SAED) measurements were conducted on the FIB cut lamella of the LTCC. The diffraction patterns were recorded for the three corresponding positions which are marked within the overview image and are shown in Figure 3.7. Positions 1 and 3 correspond to alumina grains and the Ba-rich aluminosilicate phase or celsian ($Ba[Al_2Si_2O_8]$) with a single-crystalline morphology, while position 2 represents the glassy matrix with an amorphous microstructure.

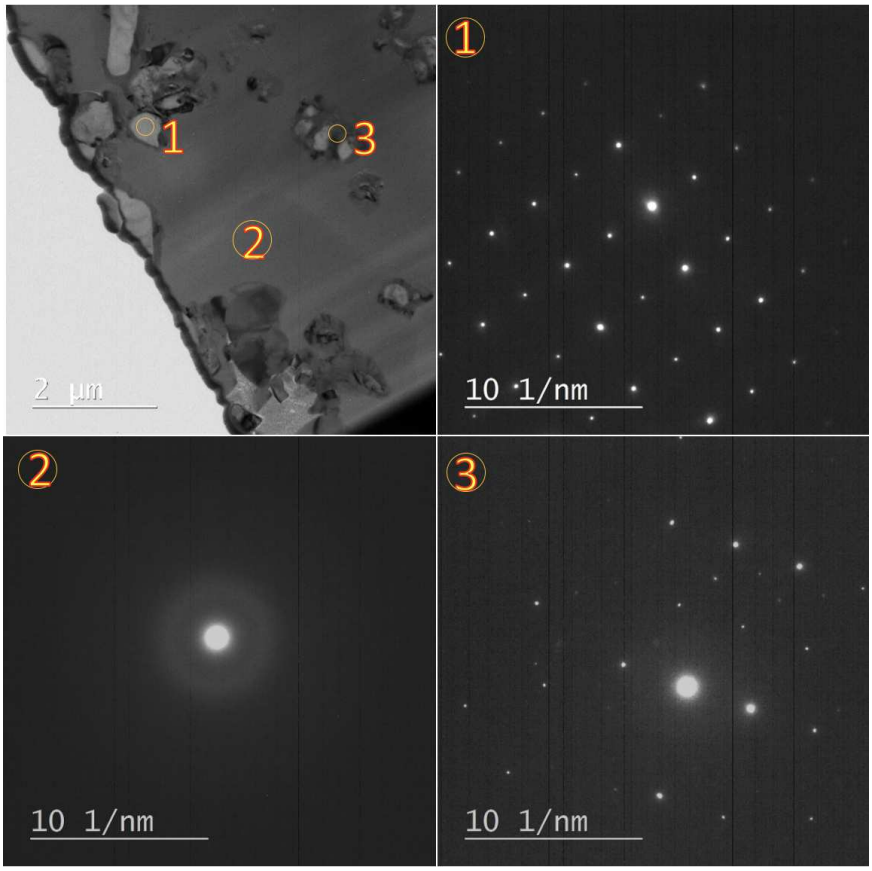

Figure 3.7: TEM lamella of a dense, *as-fired* Ferro L8 with three representative locations and the corresponding SAED patterns.

For microstructural analyses of Ferro L8 after the porosification process, the cross-sectional image of an LTCC substrate is shown in Figure 3.8a. On top, a platinum layer is deposited, which is applied to reduce charging effects and to avoid structural damaging of the sample surface during FIB preparation. As it can be seen, discrete alumina grains are distributed in the whole glass matrix, and the etchant penetrates via small grain-near gaps and openings into the LTCC body. Therefore, it can be concluded that this portion of the matrix is very important for enabling the penetration of the etchant into the LTCC body and for the realization of deeply etched samples. Nonetheless, due to the depth limitations of the FIB technique, the large penetration depths which were obtained in this work cannot be fully displayed. Hence, for studying the depth of porosification, cross-sectional SEM images of fracture planes of the LTCC were used.

In the next step, the fabricated FIB foil was subjected to TEM and STEM investigations. Figure 3.8b shows corundum grains and partially dissolved grain-near regions in a HAADF-STEM image.

The chemical composition of the LTCC was explored through an EDX line scan which is indicated by an arrow. The EDX line scans allow for a local identification of individual elements and thus a better understanding of the LTCC composition in the *as-fired* and etched states. The corresponding

EDX spectra and quantifications with respect to the elements Al, Si, Ba/Ti, and O are shown in Figure 3.8c and d. These spectra show that the major constitutions of the Ferro L8, are O, Si, and Al, where the counts of Si and Al change in opposite directions representing corundum grains and the glass matrix, respectively. The minor quantities of Ba and Ti in the intermediate area corresponds to the partially attacked or depleted celsian and rutile phases. These results are in good agreement with those from XRD and Raman analyses.

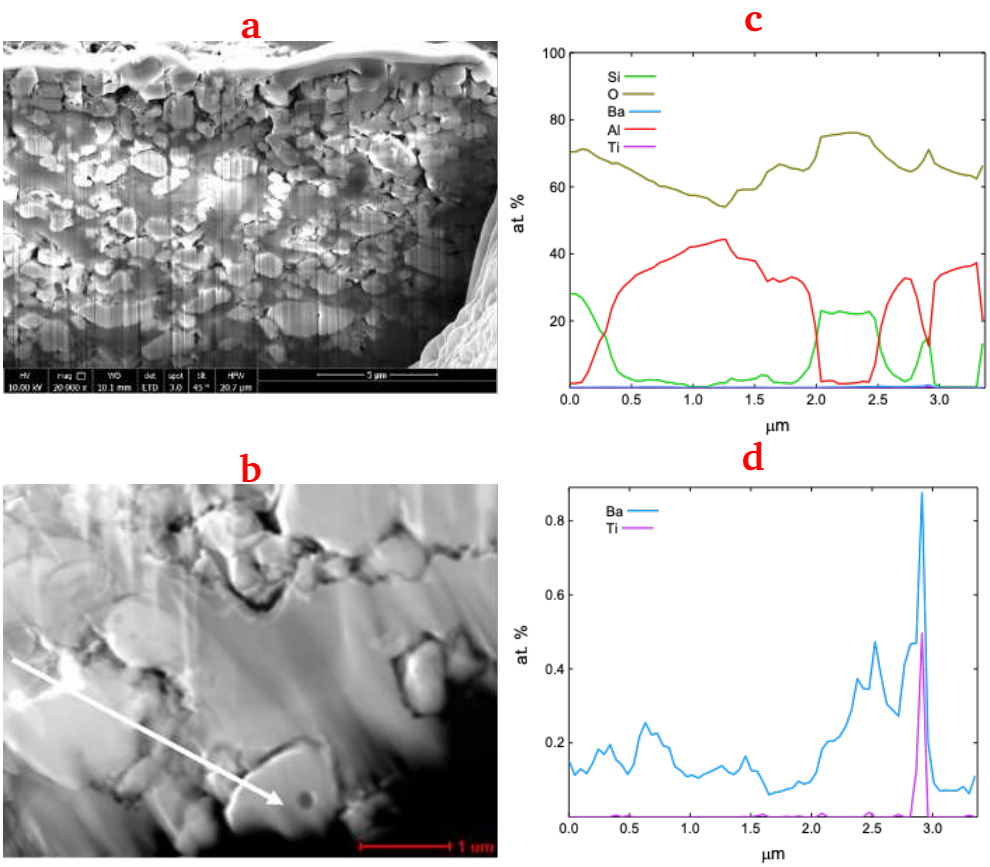

Figure 3.8: a) Cross-sectional view on the microstructure of surface-near porosified Ferro L8, and **b)** HAADF-STEM image **c)** and **d)** the corresponding EDX line profiles across a partially porosified section of the Ferro L8 LTCC etched with P50 for 30 min at T_b = 90 °C. For visualization purposes of the very low amount of Ba and Ti, these elements are plotted separately in **d**.

The celsian phase which has been crystallized from the glass matrix during liquid-phase sintering, and its dominant removal due to the etching process, are more clearly observable in the recorded bright-field TEM images (BFTEM) in Figure 3.9. In addition to the chemical composition and morphology of the LTCC, its crystallographic structure was explored in selected areas with Selected Area Electron Diffraction (SAED) measurements. The SAED patterns for three representative positions were recorded, and the results are shown in the lower row of Figure 3.9. Position 1 represents the amorphous glassy matrix, while positions 2 and 3 correspond to the crystalline corundum and celsian phase, respectively. Position 2 shows a typical single-crystalline diffraction

pattern, while in position 3 in addition to the diffraction pattern, which is far out from a low-indexed zone axis, concentric blunt circles are seen indicating the polycrystalline morphology.

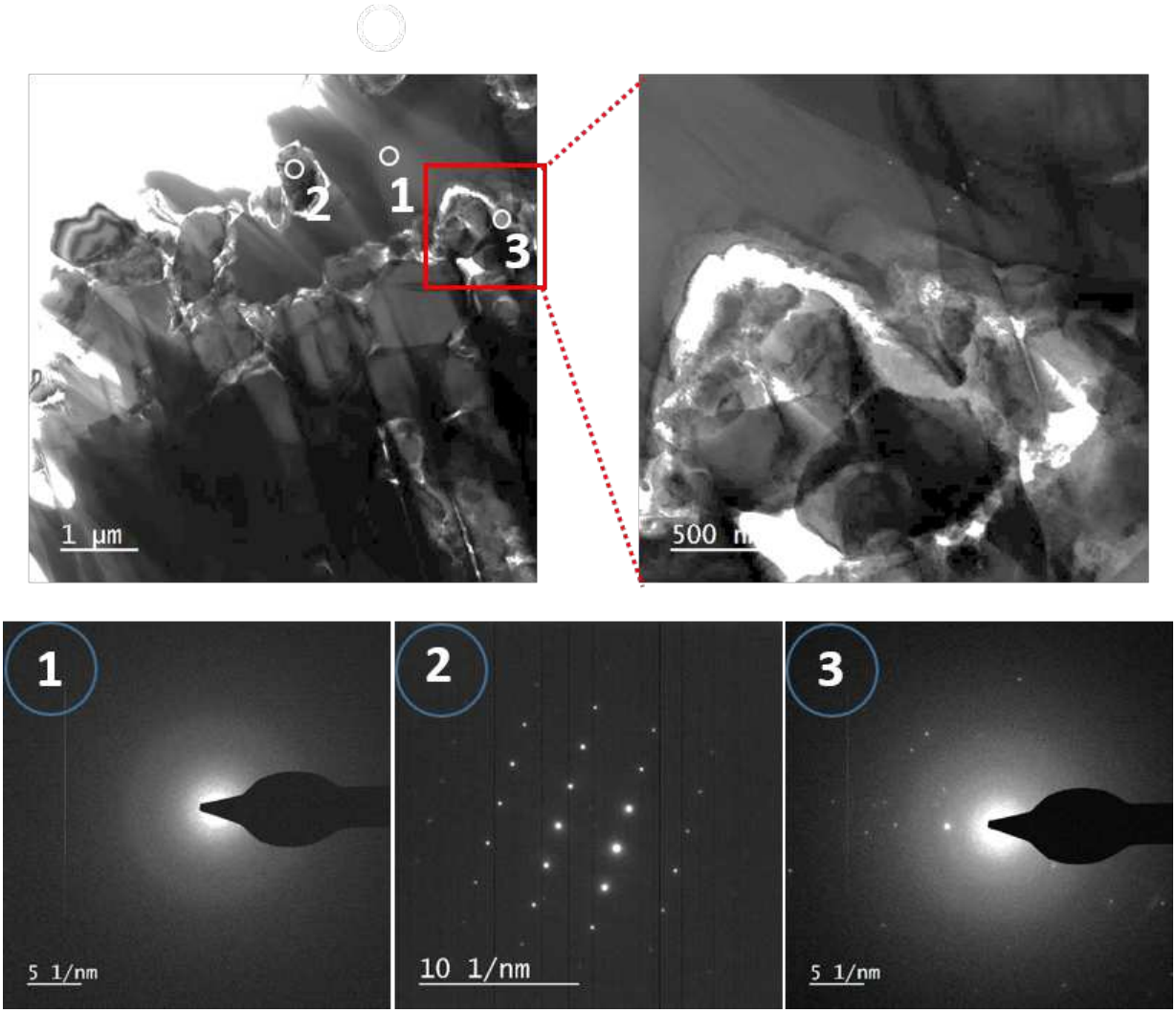

Figure 3.9: TEM images of a porosified LTCC substrate with three labelled locations for SAED analyses. At position 1, amorphous glass can be observed, whereas positions 2 and 3 represent crystalline corundum and celsian phase, respectively.

Porosimetry measurements – Porosimetry measurements were carried out for Ferro L8 substrates etched with P50 at 75 °C for 4 h. Figure 3.10 represents the results of mercury intrusion experiments. Based on these data, apparent porosity stemming from pores larger than 10 μm appears to be caused by the intrusion of interstitial space between individual, stacked samples, and can – in agreement with typical pore sizes observed on SEM cross-sections – thus be disregarded for further data evaluation. Furthermore, as the total volume of pores smaller than 10 μm is negligible in *as-fired* substrates, all porosity in this size region present in etched samples can be assigned to the etching procedure.

After Ferro L8 etching using P50, the material shows a broad pore size distribution. A maximum

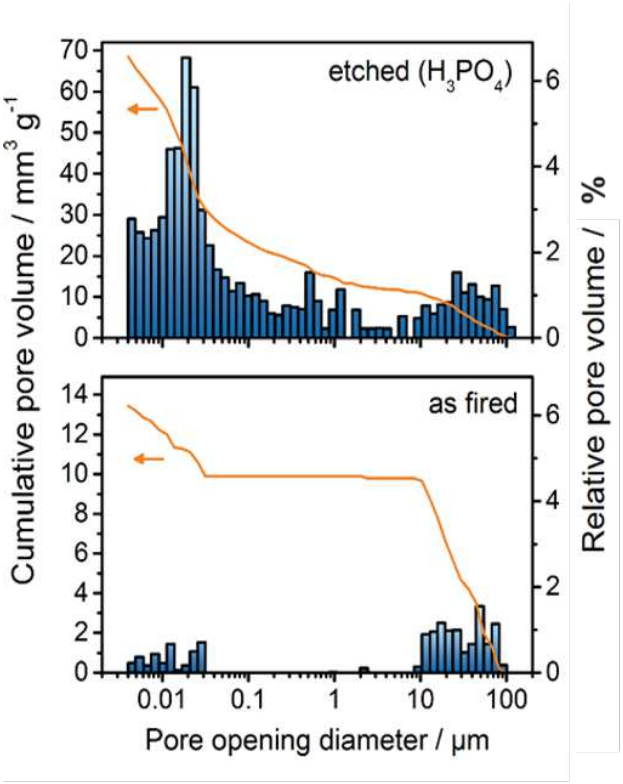

Figure 3.10: Pore opening diameter distribution and cumulative pore volume of samples in the etched (top) and the *as-fired* state (bottom). As seen from these results, apparent porosity larger than 10 μm can be primarily traced to the intrusion of interstitial space between aligned samples and hence, are disregarded during the interpretation of results.

relative pore volume is found at around 20-30 nm. However, it has to be noted that due to the nature of the measurement principle, pore necks are effectively limiting the intrusion of mercury into inner pore volumes, therefore, the results obtained by mercury intrusion only yield information on the pore neck size, not the actual pore size. Consequently, the results can also hint towards a network of larger pores connected by smaller pore channels. A potential scenario representing this behaviour is the selective etching of one of the constituents present in the fired Ferro L8 LTCC, *i.e.* celsian phase in combination with the selective etching of grain boundaries.

Excluding porosity with a pore opening diameters > 10 μm, and assuming a layer thickness of 70 μm of the etched, porous region (as extracted from cross-sectional SEM images of the porosified sample), a total layer porosity of around 18% can be estimated.

3.1.2. Investigation of the etching mechanism (kinetic analysis) for Ferro L8 LTCC

Based on the obtained gravimetric results, shown in Figure 3.1, the normalized rates of dissolution for the etching process with both P50 and P85 solutions were calculated, and the results are depicted as a function of bath temperatures in Figure 3.11. Both etchants show a very similar trend,

in which the dissolution rate is slightly increasing up to 75 °C, whereas at higher temperatures, an increase above average is observed. Nonetheless, due to the less difficult penetration into the openings and pores of the substrate, the dissolution rate for P50 is significantly higher in comparison with P85 for all bath temperatures.

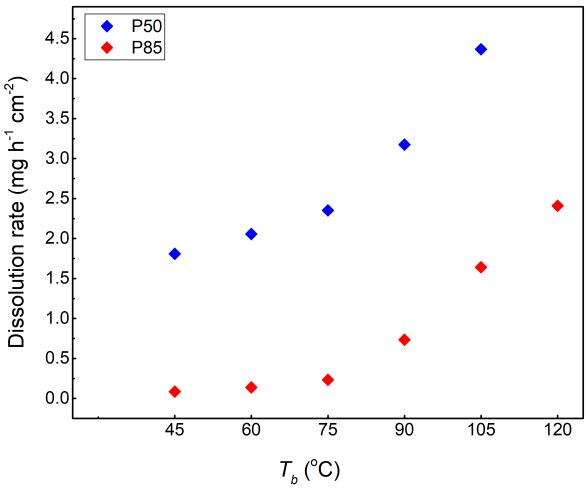

Figure 3.11: Comparison of dissolution rates when etching Ferro L8 with P50 and P85 etching solutions at different bath temperatures.

In addition, d_p values as a function of etching time for both P50 and P85 are plotted in Figure 3.12a and b. For both etching solutions, at a given temperature, d_p increases with etching time. For the P50 etchant, the slope is steeper at short etching times and then becomes flatter showing that, due to the facile diffusion of the etchant into the surface-near porosity, the porosification at the starting points of the etching process is fast. Because of the more difficult exchange of the etching solution through the generated micro- and nanopores at the etch front, the dissolution rate slows down, but does not reach any saturation level. On the other hand for P85, because of the less pronounced diffusion affinity, the slopes are milder than those for P50. Increasing the etching bath temperature for a fixed etching time results in increased d_p values what is due to the faster reaction kinetics and more facile penetration of the etching solution into the depth of the LTCC body. When further increasing the bath temperature to 105 °C, an almost linear relationship is observed between d_p and t until complete porosification of the substrate is reached after 180 min. It should be noted that the reported d_p values are only taken from one side of the substrates.

To verify the assumption on the presence of two dominating etching regimes, Arrhenius-type diagrams of d_p as a function of reciprocal bath temperature were plotted, so that the activation energy (E_a) was determined for fixed etching times through a linear regression procedure (Figure 3.12c and d). These figures indicate that the porosification of Ferro L8 with P50 follows the Arrhenius law over the whole temperature range up to 240 min. The calculated E_a values which are shown in Table 3.1 were used to acquire further information about the etching mechanism.

Typically, the activation energy (E_a) is a key indicator to elucidate the rate-controlling process. In

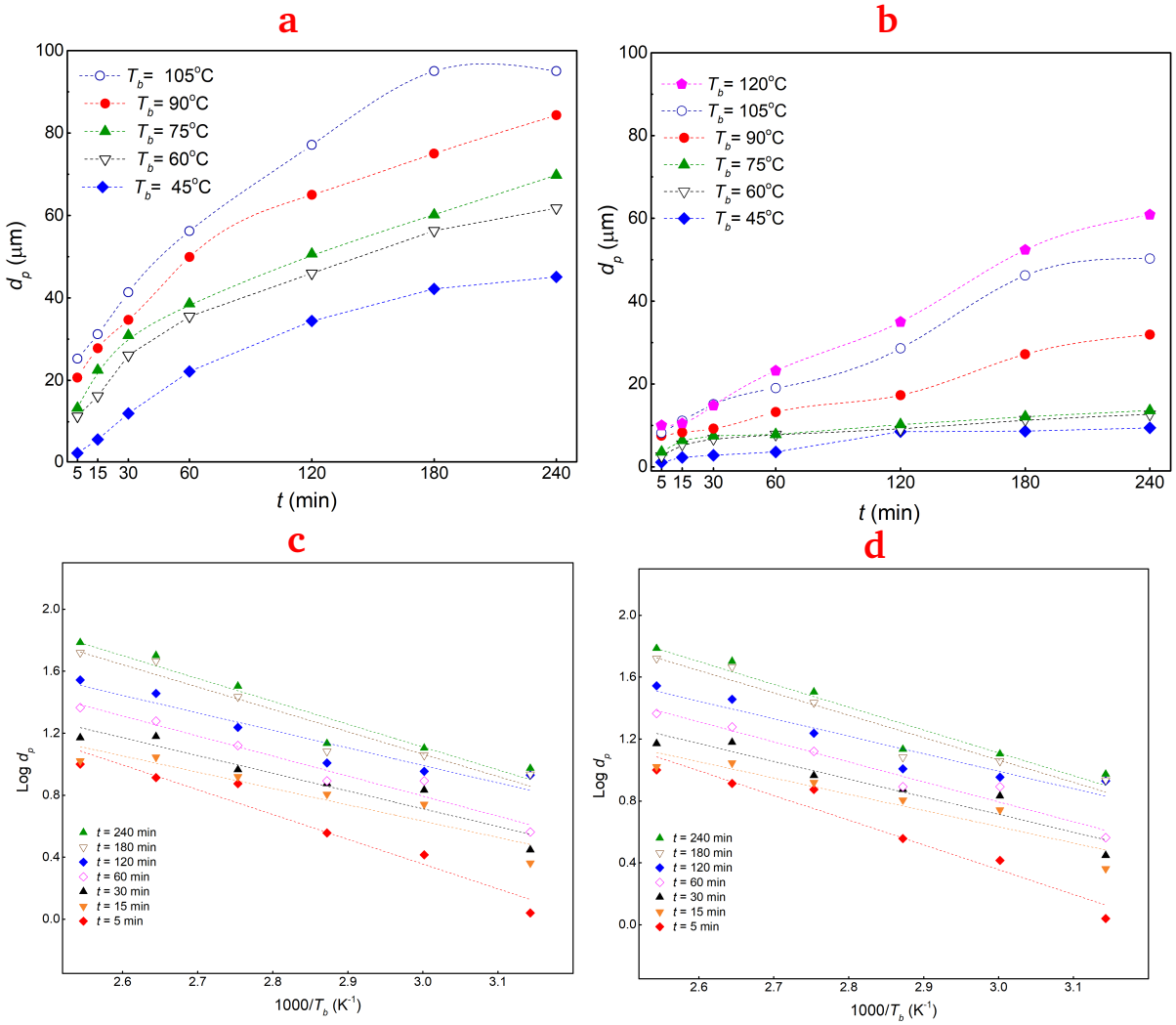

Figure 3.12: Porosification depth d_p and corresponding Arrhenius diagrams when etching Ferro L8 with P50 (**a** and **c**), and P85 (**b** and **d**) solutions at different etching times. The E_a values determined from the linearly fitted lines and the R-square values for the linear fitting are given in 3.1.

the case of diffusion-controlled dissolution, the activation energy for dissolution should be equal to the activation energy for diffusion [228, 229]. In an aqueous media, a value of approximately 0.2 eV (∼20 kJ mol^{-1}) should be expected. Appreciably higher activation energies indicate reaction-controlled dissolution rates. For example, reaction-controlled dissolution of silicates in aqueous solutions have activation energies that cluster around 60-80 kJ mol^{-1} [230], and the activation energies of alkaline earth fluorides, of which dissolution rates are proposed to be surface controlled, lie in the range of 72-86 kJ mol^{-1} [73, 231, 232].

Although the slopes of the linearly fitted lines and hence, the corresponding activation energies continuously decrease when increasing the etching time, the calculated activated energies with

Table 3.1: Activation energies from the Arrhenius diagrams in Figure 3.12.

Etching time *min*		**5**	**15**	**30**	**60**	**120**	**180**	**240**
P50	E_a *eV*	1.89	1.40	0.98	0.77	0.68	0.66	0.63
	Regression coefficient R^2	0.8026	0.8171	0.8109	0.9287	0.9796	0.9605	0.9723
P85	E_a *eV*	1.59	1.05	1.14	1.29	1.13	1.44	1.47
	Regression coefficient R^2	0.9362	0.8479	0.8831	0.9495	0.8813	0.9088	0.9184

values ranging from 0.63 eV for long etching times up to 1.89 eV for 5 min etching are well above the limit of the diffusion-controlled regime, *i.e.* 0.2 eV. Therefore, it can be concluded that for the etching reaction with the P50 solution, the process is reaction-controlled. Also, it should be mentioned that since at low bath temperatures the etching reaction is significantly slower, d_p values are reduced, and the impact of potential error sources is more pronounced, resulting in a larger deviation of the fitted straight lines from the data points.

By increasing the etching time, the depth of etchant penetration increases and the diffusion into the deep pores of the LTCC becomes more and more dominating but does not reach the pure diffusion-controlled regime. For the P85 solution, however, as can be seen in Figure 3.12d, that there is not a clear trend in the slopes of the fitted lines with etching time, which might be due to the enhanced temperature dependence of the P85 viscosity compared to that of P50, thus strongly affecting the diffusion ability. Nonetheless, the calculated activation energies for all etching times stay significantly above 0.2 eV (between 1.05 and 1.59 eV) suggesting a dominating reaction-controlled mechanism also for this etchant.

3.1.3. Mechanical characterization of the Ferro L8 LTCC substrates by 3-point bending test

As mentioned already in the introductory paragraph to this chapter, by employing the wet chemical etching process a defined porosity can be introduced to the LTCC although the high penetration of the etchant into the depth of LTCC may also raise concerns about the mechanical robustness of the LTCC. Therefore, a detailed study was carried out on the mechanical stiffness behaviour of the LTCC substrates. For this purpose, *as-fired* and porosified LTCC substrates were subjected to DMA analyses. Substrates treated for different etching times, corresponding to different depths of porosification, were chosen. First, the samples etched with P50 at 90 °C were investigated. However, for this etching condition, the reaction rate is so high that within an etching time of 20 min, the stiffness of substrates decreases by about 90%, and after that, the samples become too fragile to be handled and measured. Consequently, to have a lower reaction rate and better control on the depth of porosification, samples etched at an etching temperature of 75 °C were chosen.

Furthermore, along with the LTCC substrates with a thickness of approximately 180 μm, another set of substrates with a thickness of about 520 μm were used, as they represent two typical thickness values in LTCC substrate technology. Results of room temperature analyses for both sets of 180

and 520 μm thick samples are shown in Figure 3.13.

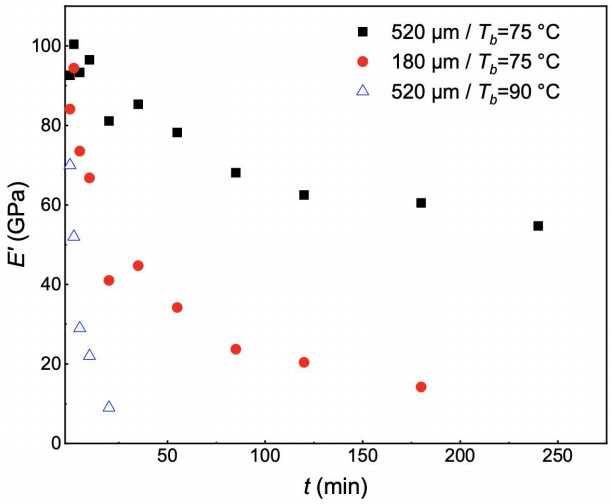

Figure 3.13: Room temperature storage modulus of Ferro L8 substrates with two different thickness values of 180 and 520 μm etched with P50 at 75 °C for different etching times. The results for 180 μm thick LTCC etched at 90 °C are shown for comparison.

Independent of substrate thickness, and due to the mass removal and the introduction of air up to a certain depth into the LTCC body, the stiffness of both sample sets decreases with the etching time. However, for the 520 μm, thick samples due to the lower percentage of mass removal in comparison to the 180 μm thick samples, the decrease with respect to their corresponding *as-fired* samples is with about 40% lower compared to 80%. This confirms that choosing thicker multilayered substrates for the etching experiments secures to a higher degree the original mechanical properties after porosification.

DMA scans of the *as-fired* and etched LTCC samples indicate almost constant values for all substrates up to measurement temperatures of 550 °C, which means that the proposed method does not limit the application of the LTCC even at such elevated temperatures (see Figure 3.14).

After the DMA test, the samples were taken for cross-sectional SEM imaging to measure the porosification depth values and correlate the measured storage moduli with the different sample thicknesses. Therefore, the measured porosification depth values were normalized to the thickness of the substrates, and the resulting plot is shown in Figure 3.15a. Both sets of substrates follow a very similar trend in the decrease of stiffness. However, for the thicker substrates due to the reduced percentage of the porosified area, the decrease in stiffness is also less. Basically, this plot is independent of the sample thickness, etching time, and etchant temperature.

In order to be able to predict the correlation between storage modulus E' and the relative porosification depth, a modification of well-established minimum solid area (MSA) models was employed. These models are typically used to describe the porosity-dependency of Young's modulus E in ceramic materials by the relationship $E = E_0 e^{-bP}$. Here, E_0 is the modulus of the non-porous base

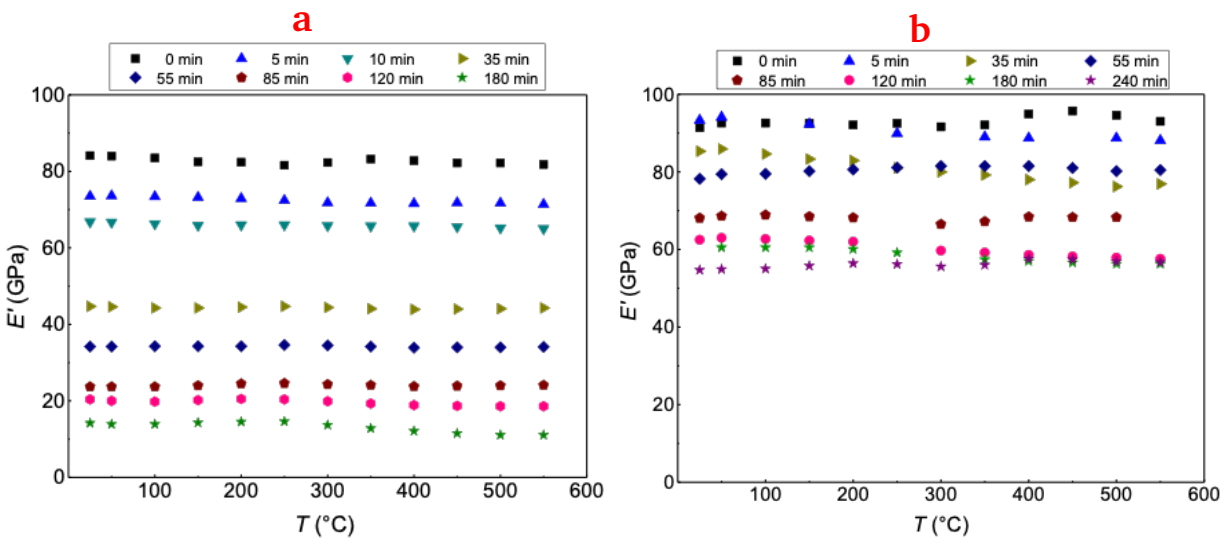

Figure 3.14: The temperature-dependent storage modulus of Ferro L8 substrates with two different thicknesses of **a)** 180, and **b)** 520 μm, etched with P50 at 75 °C for different etching times.

material, P is the total porosity, and b is a fitting factor which is, in part, affected by the type of pore structure [233]. Here, the model was modified by introducing a modified porosity $P' = (d_p/L)P_l$, which takes into account the relative porosification depth (d_p/L), whereas L is the thickness of the substrate and P_l the porosity within the etched layer.

For a total porosity within the etched layer of $P_l = 0.2$, which was estimated by mercury intrusion porosimetry measurements of comparable specimens [222], a fit convergence as shown in Figure 3.15b is achieved with $E_0 = 100.5 \pm 4.0$ GPa and $b = 11.5 \pm 1.0$. The former value is in good agreement with the values of the *as-fired* Ferro L8 as reported in the material data-sheet [234]. A b value of 11.5 hints towards a pore structure derived by the stacking of solid spheres [233]. This type of pore structure can be confirmed by cross-sectional SEM images (see, *e.g.* Figure 3.8a showing the continuous removal of the celsian phase during etching while solid particles primarily correspond to the remained alumina grains.

Consequently, these findings can be applied for a direct estimation of elastic sample properties of Ferro L8 LTCC with P50 for any etching time and bath temperature, solely by knowing the depth of porosification which can be measured straightforwardly by cross-sectional SEM imaging, assuming a homogeneous porosity within the etched layer.

Hence, for obtaining a given storage modulus, the substrate thickness and etching conditions can be carefully chosen to acquire the appropriate relative depth of porosification. Therefore, these results confirm the applicability of the proposed etching method for obtaining porosified LTCC substrates with tailored mechanical properties by choosing the suitable depth of porosification for a substrate of the desired thickness.

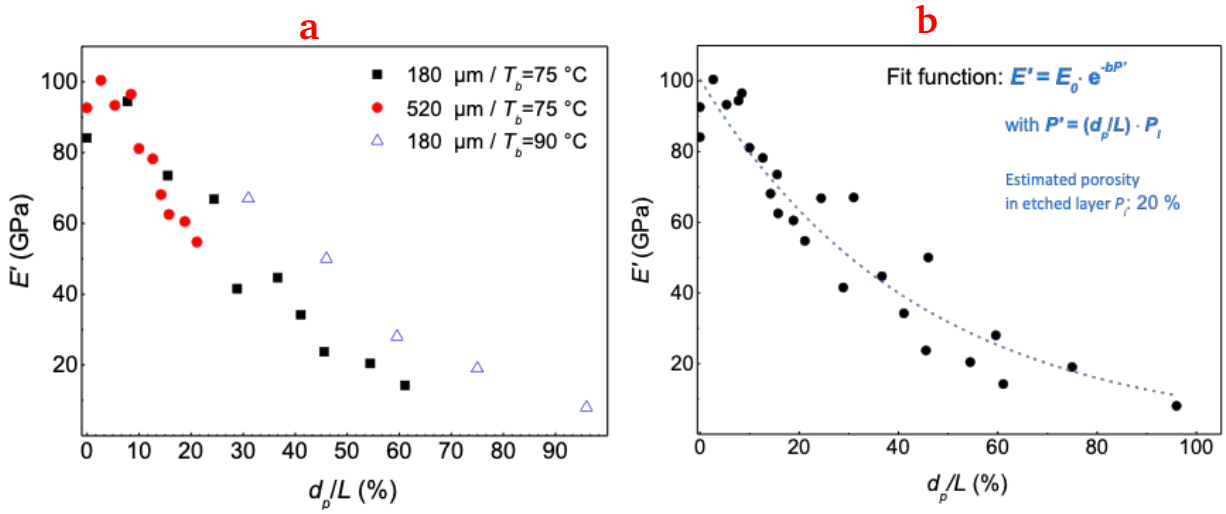

Figure 3.15: a) Storage modulus of Ferro L8 substrates with two different thicknesses of 180 and 520 μm etched with P50 at T_b=75 °C for different etching times indicating results that are independent of the etching conditions. The results for 180 μm thick LTCC etched at T_b=90 °C are shown for comparison. **b)** The relation between storage modulus and the relative depth of porosification can be adequately described by an exponential fit function, assuming a porosity of 20% within the etched layer based on mercury intrusion porosimetry results.

3.2. Investigation of the etchant pH and concentration on the porosification of GC LTCC

Effect of etchant pH and applicability of orthophosphoric acid with reduced concentrations (below 50 wt%) for the porosification of LTCC are new approaches with less understood etching kinetics. Therefore, this part aims towards providing a comparison of dissolution rates when etching LTCC tapes with those etchants. For this purpose, commercially available Ceramtape GC (GC LTCC) was selected which possesses one of the least complex chemical compositions among LTCC tapes and has been widely studied in the previous studies [169, 235–237]. Multiple experiments were conducted at fixed pH values and concentrations with varying temperatures and etching times, to determine the impact of temperature and etching time on the etching performance.

3.2.1. Impact of pH value

Phosphate buffer solutions (PBS) with a concentration of 0.2 mol L^{-1} and pH values in three representative regimes of highly acidic, highly alkaline, and neutral were as described in Chapter 2.. The microstructure and morphology of the samples were investigated by SEM and some of the representative results are shown in Figure 3.16. As it can be observed in the SEM micrographs, the PBS solutions showed different etching behaviour in all different pH regimes. In the neutral pH range, meaning solutions with pH values of 6.2, 7.2 and 8.2, nearly no etching, or only very small holes and gaps are detected after exposure. This is due to the very low rate of dissolution process

(below 0.05 mg h^{-1} cm^{-2}). Even after treatment of the substrates for four hours, either no etching or only very small holes and gaps were detected.

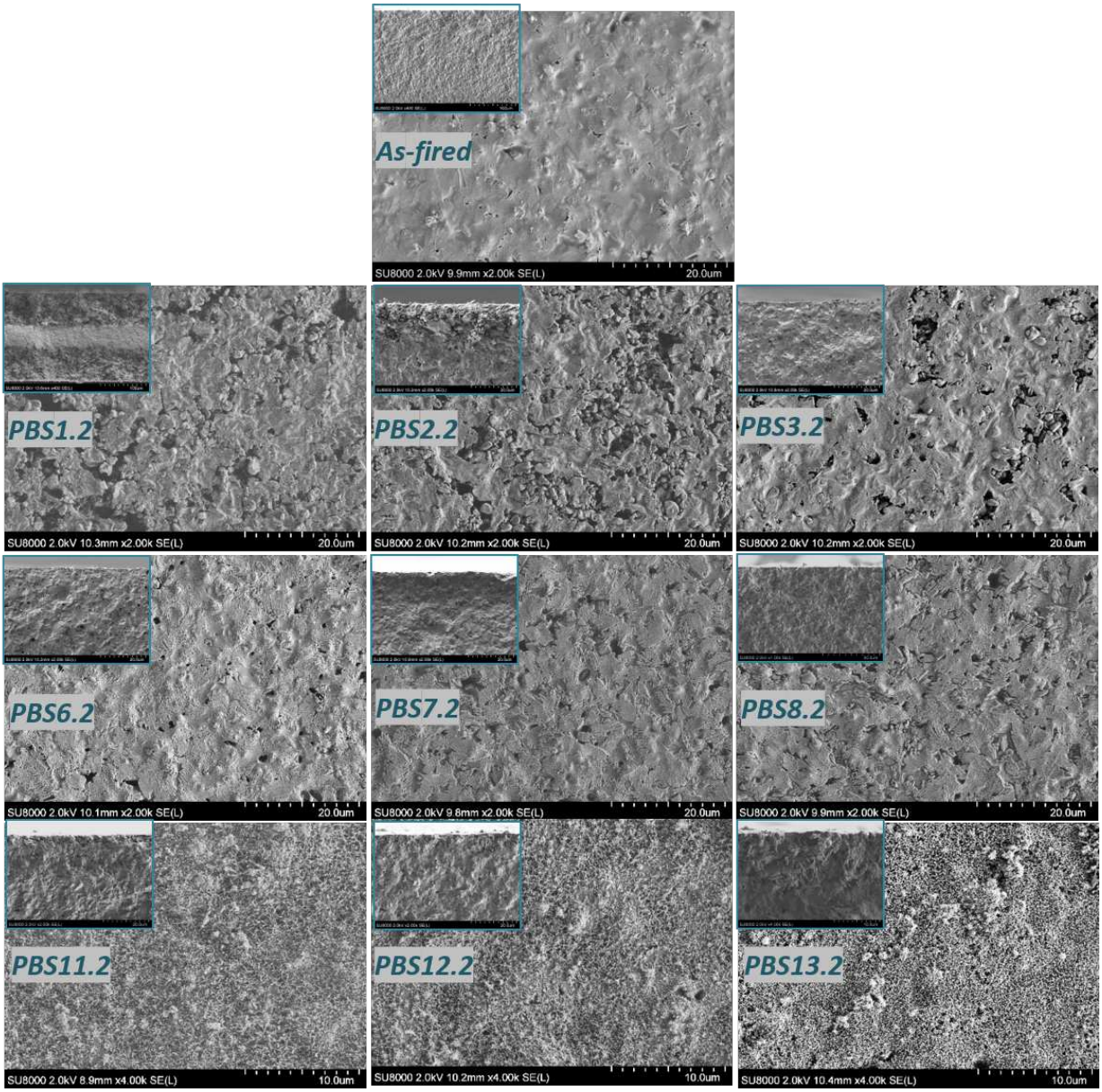

Figure 3.16: SEM micrographs in top view of GC LTCC in the *as-fired* state as well as etched with 0.2 mol L^{-1} PBS with different pH values for 60 min at 90 °C.

A look at the micrographs of the samples treated in the highly acidic range shows larger and deeper voids and pores, whilst keeping most of the surface regions quite intact. Also, it can be remarked that in this pH range the porosification degree decreases significantly by increasing the pH, as pH 3.2 shows almost negligible mass removal, especially when compared to the massive mass removal at the pH of 1.2 or 2.2. Also, increasing the etching times resulted in higher porosification depths

and higher mass removals. This is quite important for the solution at, *e.g.* pH 1.2 since it porosified nearly the whole substrate at higher etching times. Experiments with other etching temperatures and concentrations for the PBS 1.2 etchant also showed that the porosification degree (both mass removals and the porosification depths) increases with bath temperature. On the other hand, increasing the concentration counteracts this effect for 0.2 to 1.0 mol L^{-1} solutions.

The highly alkaline condition shows the most unfavourable surface quality among the others and also the d_p values in this regime are significantly lower compared to those of the acidic range. A closer analysis of the LTCC substrates etched at the highly alkaline condition (see Figure 3.17) shows the formation of needle-like structures with lengths of about 2 to 3 μm both on the surface and in the porosified top layer. Therefore, in this condition, the calculated mass removal is a result of different phenomena, *e.g.* materials dissolution, change in the chemical composition, introduction of new crystals to the surface and within the etched layers of the substrate; and thus cannot be directly correlated to the material dissolution.

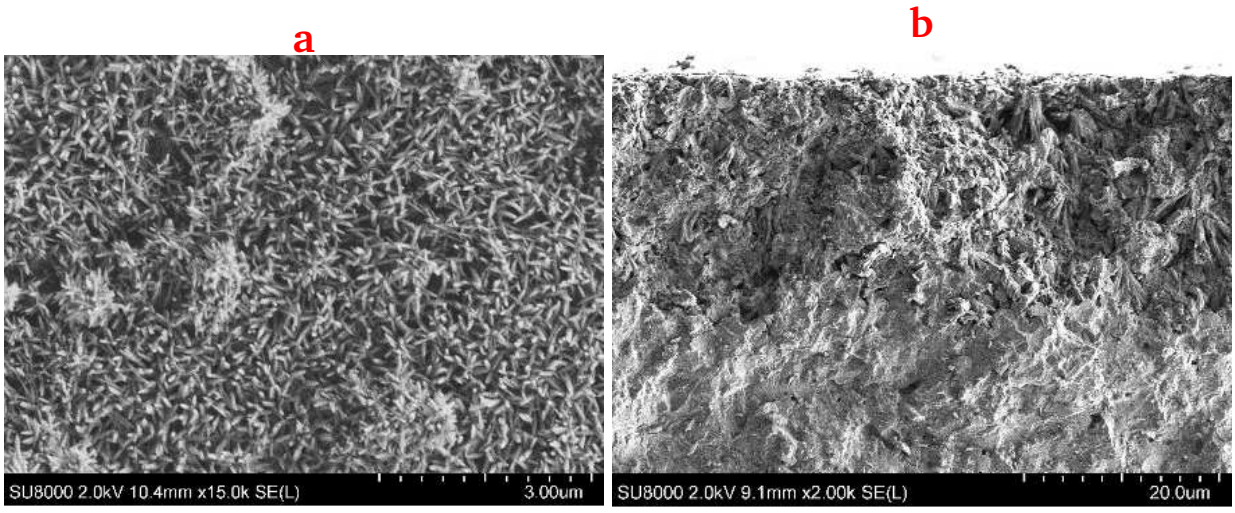

Figure 3.17: Surface (**a**) and cross-section (**b**) of the GC LTCC etched with 0.2 mol L^{-1} PBS13.2 for 240 min at 90 °C.

For each etching condition, the porosification depth values correlate with mass removal (see Figure 3.18). Except for the highly alkaline region where mass removal is lower than expected from the corresponding porosification depth which is indeed due to the formation of new crystalline phases during the etching process.

As described in the experimental section, after the etching process, samples were fractured to create fracture planes, which were evaluated using SEM technique. ImageJ software was utilized to determine the porosification depth values for each sample. The depth was measured at three different points enabling to calculate the mean value and the standard deviation.

Since in a buffer system both acid and the conjugated base components can be found, studying the effect of individual components is also interesting, possibly leading to a better understanding of the etching process. As illustrated in Figure 3.19, SEM images of the LTCC treated with individual PBS

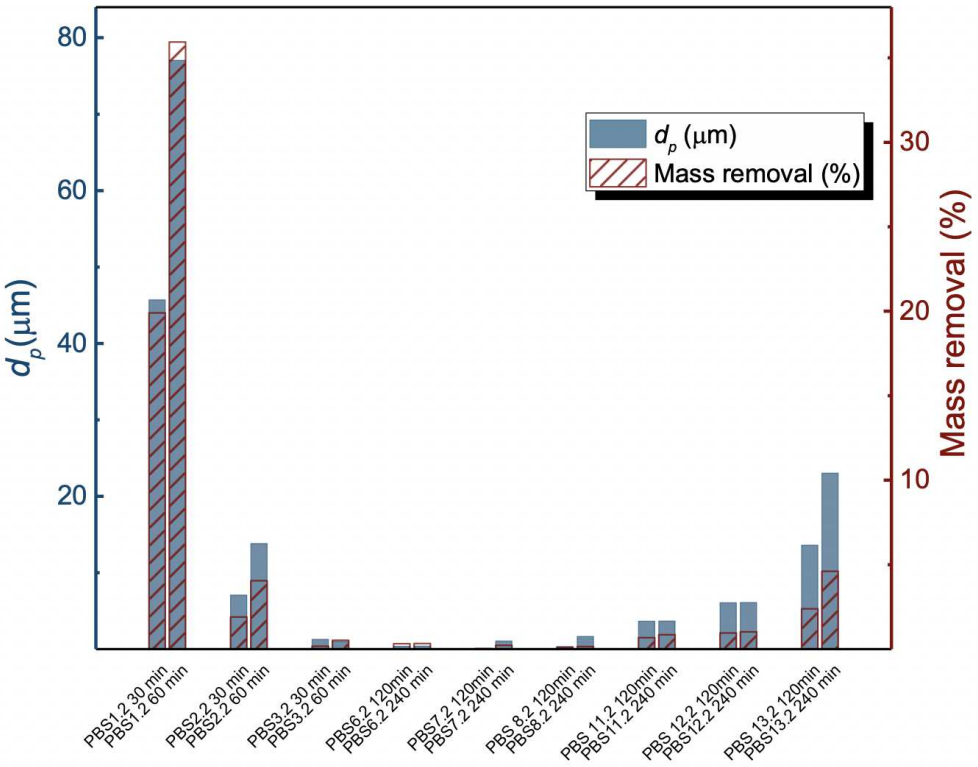

Figure 3.18: Mass removal and porosification depth of GC LTCC substrates etched with PBS of different pH values. Due to the exceptionally high etching rates in the highly acidic region, etching times longer than 60 min were avoided.

components are in excellent agreement with the previous findings. The solution containing only Na_3PO_4 (pH 12.4) shows the same crystal formation behaviour as the highly alkaline PBS solution, as illustrated in Figure 3.17. Pure Na_2HPO_4 solution (pH 9.2) also appears to etch the samples, so both components contribute to the etching process. The sample treated with pure NaH_2PO_4 solution (pH 5.3) shows a very small alteration of the surface topography, and only minor etching is observed close to the surface-near grains. However, almost no porosification is determined by the cross-sectional SEM analyses. This means that the excellent etching performance which was observed for the buffer solutions at highly acidic condition, *i.e.* PBS1.2 and PBS2.2 is primarily due to the H_3PO_4 component.

Moreover, as mentioned in Chapter 2., for pH adjustment of PBS, small amounts of NaOH or HCl were added to some of the solutions. Although the concentrations of these admixtures were low, thus ignoring their impact, 0.2 mol L^{-1} solutions of them were prepared individually and their etching behaviour was examined. As can be seen in Figure 3.20a, by applying HCl, the whole substrate is completely porosified while the surface is strongly attacked. The obtained porosified LTCC was extremely fragile and the reduction in the initial thickness was more than 12% demonstrating that HCl is a quite aggressive etchant for GC LTCC. Therefore, high amounts of HCl affect the etching process with PBS too. At neutral ranges, even lower amounts of HCl (less than 0.5 mmol L^{-1}) seem to alter the process, but gravimetric measurements showed that its effect

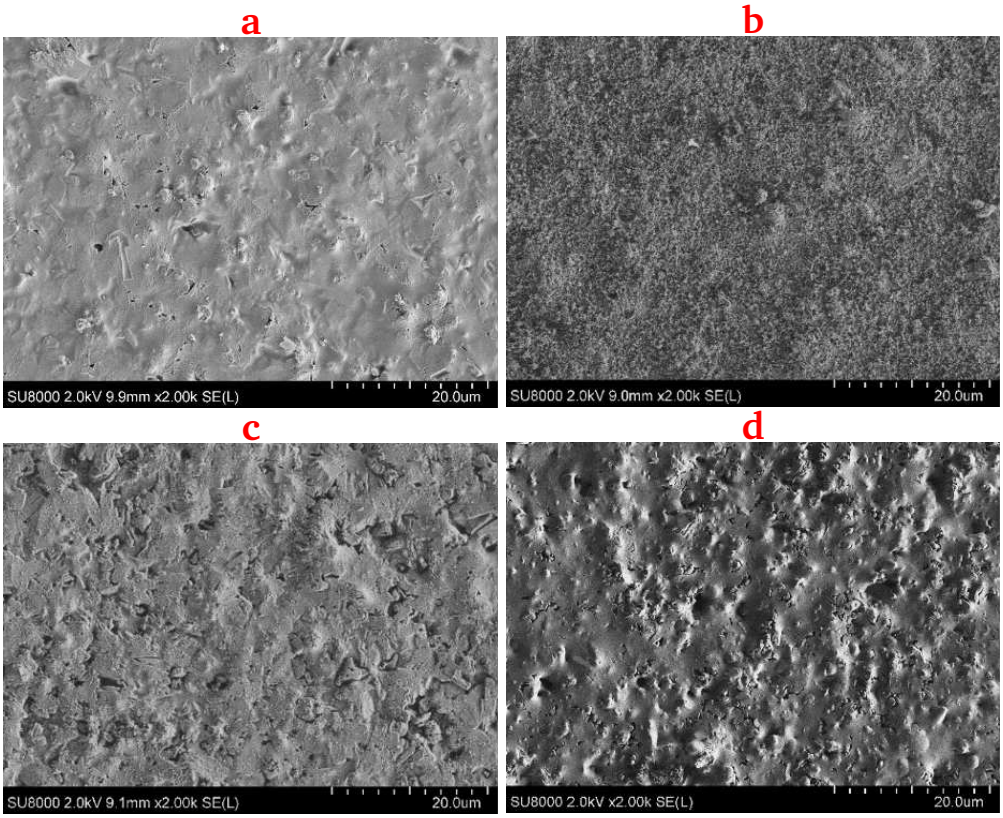

Figure 3.19: SEM micrographs in the top view of the GC LTCC **a)** in the *as-fired* state, and etched at 90 °C with 0.2 mol L^{-1} solutions of **b)** Na_3PO_4 for 240 min, **c)** Na_2HPO_4 for 240 min, and **d)** NaH_2PO_4 for 60 min.

is negligible for the highly acidic and alkaline ranges.

On the other hand, when using a 0.2 mol L^{-1} solution of NaOH it reacts with the LTCC material during the etching process similar to the treatment of GC LTCC with PBS13.2. The corresponding SEM micrograph (see Figure 3.20b) shows several needle-like crystals. The XRD results of the treated sample (see Figure 3.20c) show that two possible candidates for the formed crystals are sodium aluminium silicate ($Na(AlSi_3)O_8$) and sodium calcium aluminium silicate ($Na_{0.5}Ca_{0.5}Al_{1.5}Si_{2.5}O_8$). However, due to the same crystallographic space groups, they cannot be differentiated by XRD measurements.

The XRD measurements show selective etching of the anorthite phase in the acidic range (see Figure 3.21a). The PBS1.2 etchant removes the anorthite phase entirely from the LTCC, while for treatment with PBS 2.2 and 3.2, characteristic peaks of the anorthite phase, but with decreased intensity, can still be observed, which is attributed to the milder etching performance at these conditions. In the neutral range, no changes compared to the *as-fired* sample are observed. XRD patterns for the alkaline range, on the other hand, show additional peaks (see Figure 3.21b), as well as changes in the relative intensities of the peaks. This together with the crystals observed on the surface in SEM images, indicate a change in the crystalline structure of the sample. As

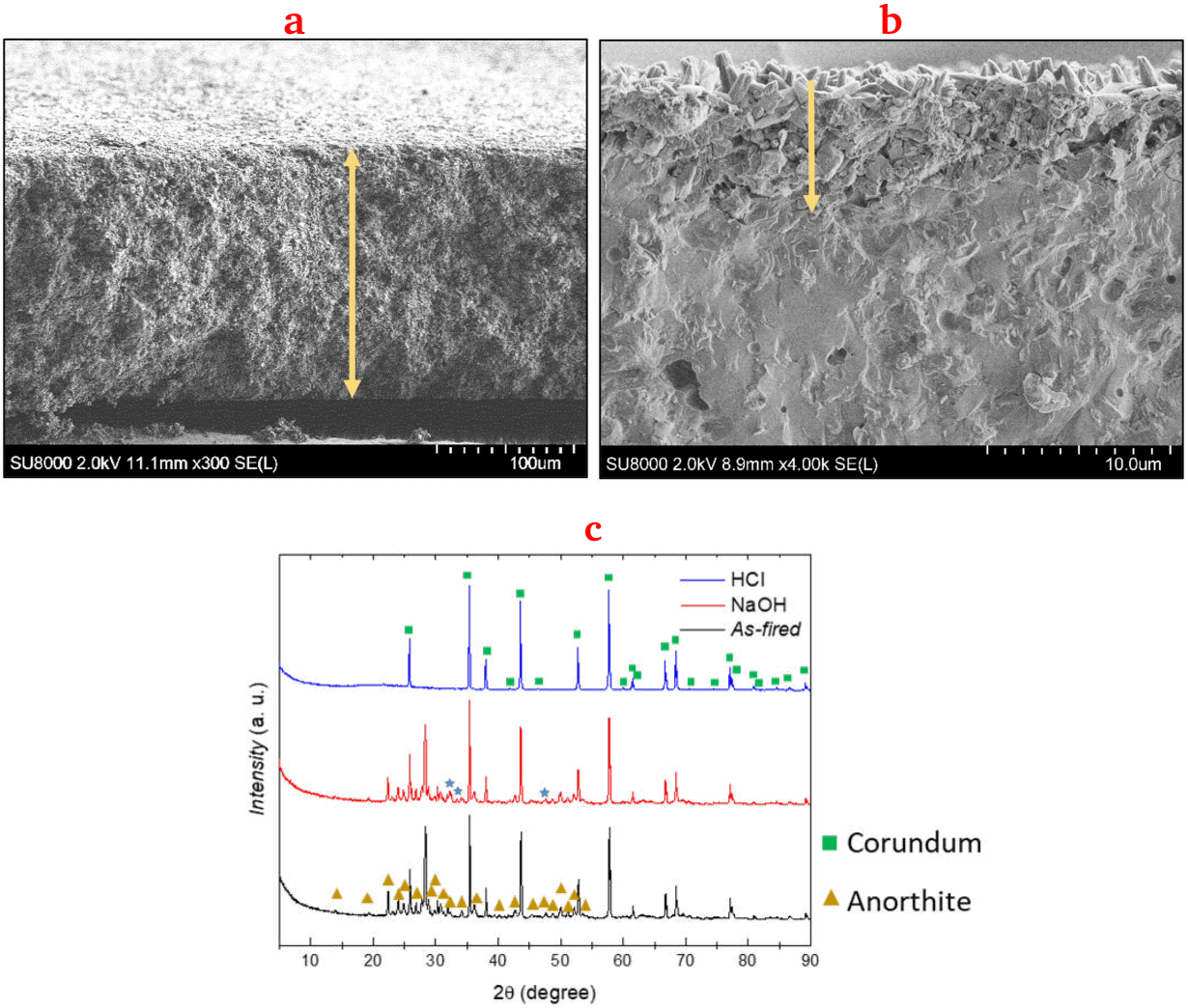

Figure 3.20: Cross-sectional SEM micrographs of the GC LTCC etched with 0.2 mol L^{-1} solutions of **a)** HCl for 1 h and **b)** NaOH for 4 h at 90 °C; **c)** the corresponding X-ray diffractograms. The peaks indexed by star sign are related to the new crystals formed on the surface of GC LTCC due to NaOH treatment.

already explained in Chapter 1., these crystals are due to the crystallization of the metastable gel layer which is typically formed during the glass dissolution process. From the knowledge which we have about PBS, the peaks can also be attributed to phosphate crystals. Typically, in PBS at very high pH values, phosphate anions (PO_4^{3-}) are the dominant species in the solution. The phosphate anions react with some counter ions from the LTCC surface, such as Ca, K, Al, or Si, or even ones dissolved in the solution, thereby forming crystals [238–240]. Considering the LTCC composition and stability of the corresponding phosphates at alkaline conditions, hydroxylapatite, $Ca_5(PO_4)_3(OH)$, is the most probable candidate among others. The XRD pattern for this compound is also in agreement with literature [241, 242].

It should be mentioned that the evaluation of new formed crystals with the High Score Software

showed some other candidates such as sodium calcium aluminium silicate ($Na_{0.5}Ca_0.5Al_{1.5}Si_{2.5}O_8$) and sodium aluminium silicate ($Na(AlSi_3)O_8$). However, due to the same crystallographic space groups and overlapping of the peaks, they cannot be differentiated by XRD measurements.

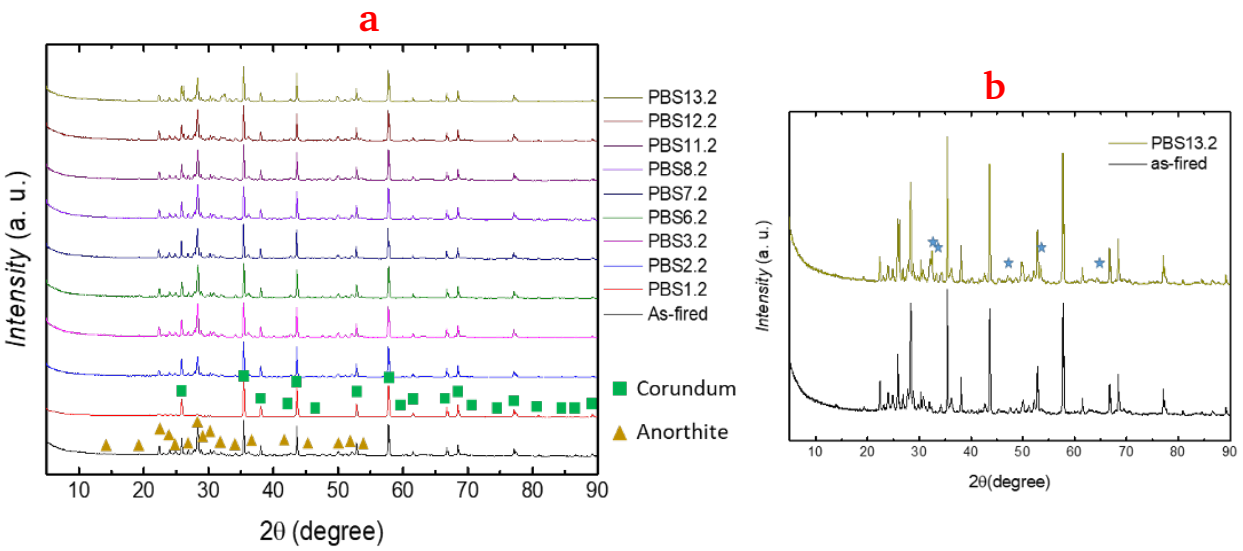

Figure 3.21: a) X-ray diffractograms of GC LTCC etched with PBS at different pH-values compared to the *as-fired* LTCC; **b)** For better illustration of the small peaks observed after etching with PBS13.2, which are marked, the corresponding diffractograms are compared separately to the *as-fired* state in b. Stars label the new peaks formed after the etching treatment.

Samples etched with PBS1.2, which showed the best etching performance in the examined pH range, were further investigated by TEM. FIB technique was applied for the preparation of the TEM lamella. Figure 3.22 yields SEM micrographs of a cross-cut made utilizing FIB for a GC LTCC etched with PBS1.2 at 90 °C for 2 h. This image indicates the distribution of alumina grains in the whole glass matrix. The etchant penetration via small grain-near gaps into the LTCC body results in a defined etchant penetration, thus promising a homogeneous permittivity of the porous substrate material.

However, due to the detachment of grains from this highly porous lamella, the obtained foils were mechanically too fragile to handle. Therefore, only 30 min etching treatment was applied to the sample for TEM analyses.

As can be observed in Figure 3.23, with EDX mapping the distribution of Si, Al, and Ca elements in a selected area of the TEM lamella along the arrow was measured, while ignoring the obvious presence of oxygen and other minor LTCC components such as B. The Si-rich phase corresponds to the glassy matrix, while Al- and Ca-rich phases represent the corundum grains and the surrounding anorthite phase, respectively.

The EDX mapping confirms the presence of anorthite phase at the boundary of filler grains and glass matrix as well as its partial dissolution due to the etching with PBS1.2. Etching with this etching solution for longer times results in further dissolution of the anorthite phase. Based on

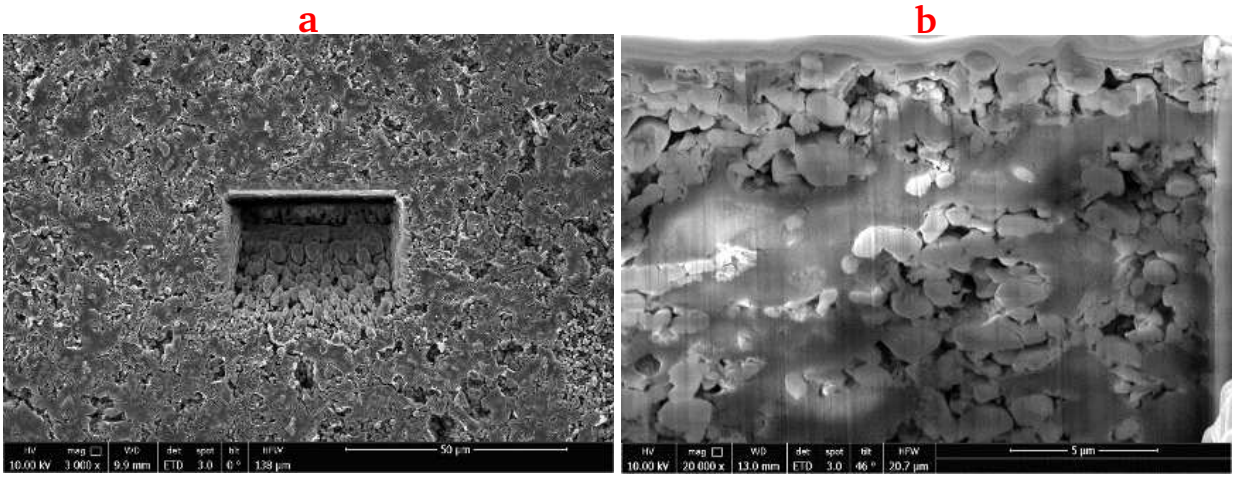

Figure 3.22: SEM micrographs in the top (**a**) and the cross-sectional (**b**) view of the GC LTCC etched with PBS1.2 at T_b = 90 °C for 120 min.

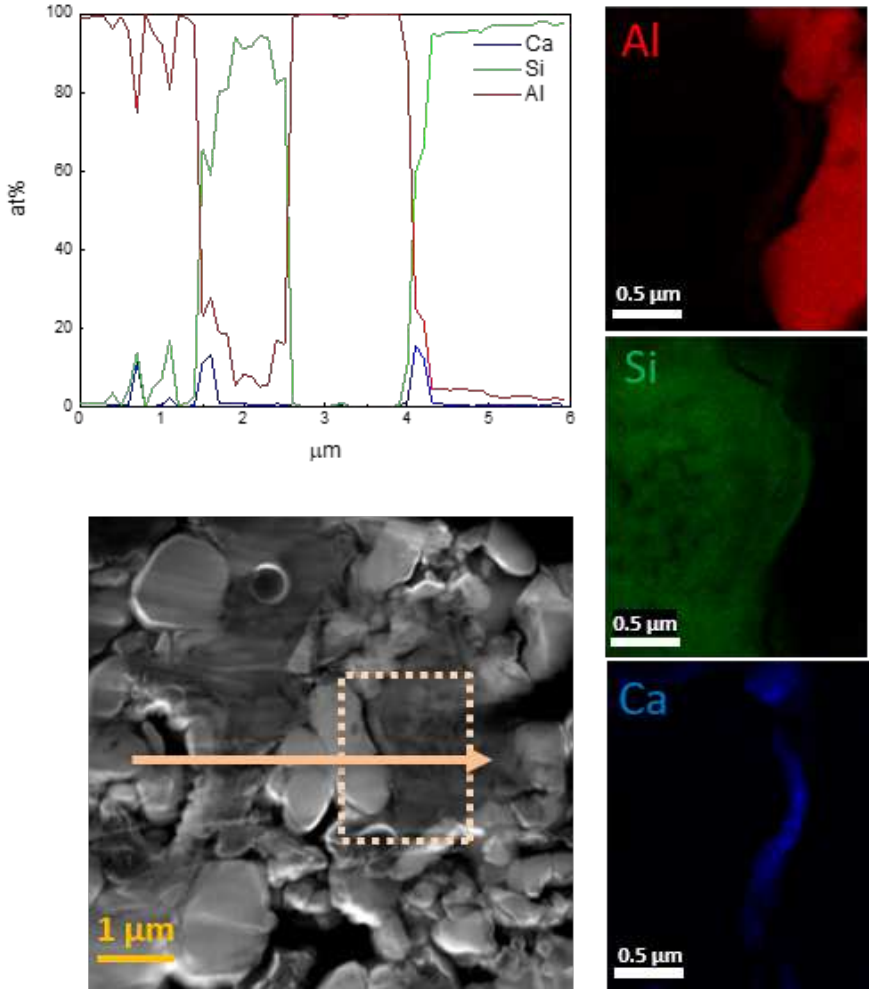

Figure 3.23: EDX line profile (along the indicated arrow), and elemental mapping (inside the indicated rectangle) for Al, Si, and Ca as key elements of the GC LTCC tape etched with PBS1.2.

these results, the etching behaviour for the etching treatment of GC LTCC with PBS1.2 is very similar to the one with P85 which is reported in our previous work[243].

Moreover, studying the crystallographic structure of the LTCC substrate in selected areas is of great interest. For this purpose, the bright-field TEM overview of the GC LTCC was obtained (the top left of Figure 3.24) and selected area electron diffraction (SAED) measurements were conducted on the FIB cut lamella of the porosified LTCC. The diffraction patterns were recorded for the three corresponding positions which are marked within the overview image. The circles show the size of the selected aperture for the area of interest for the diffraction pattern. Positions 2 and 3 correspond to the crystalline alumina grains and the residual anorthite phase, which remained after the etching treatment, while position 1 represents the glassy matrix with an amorphous microstructure.

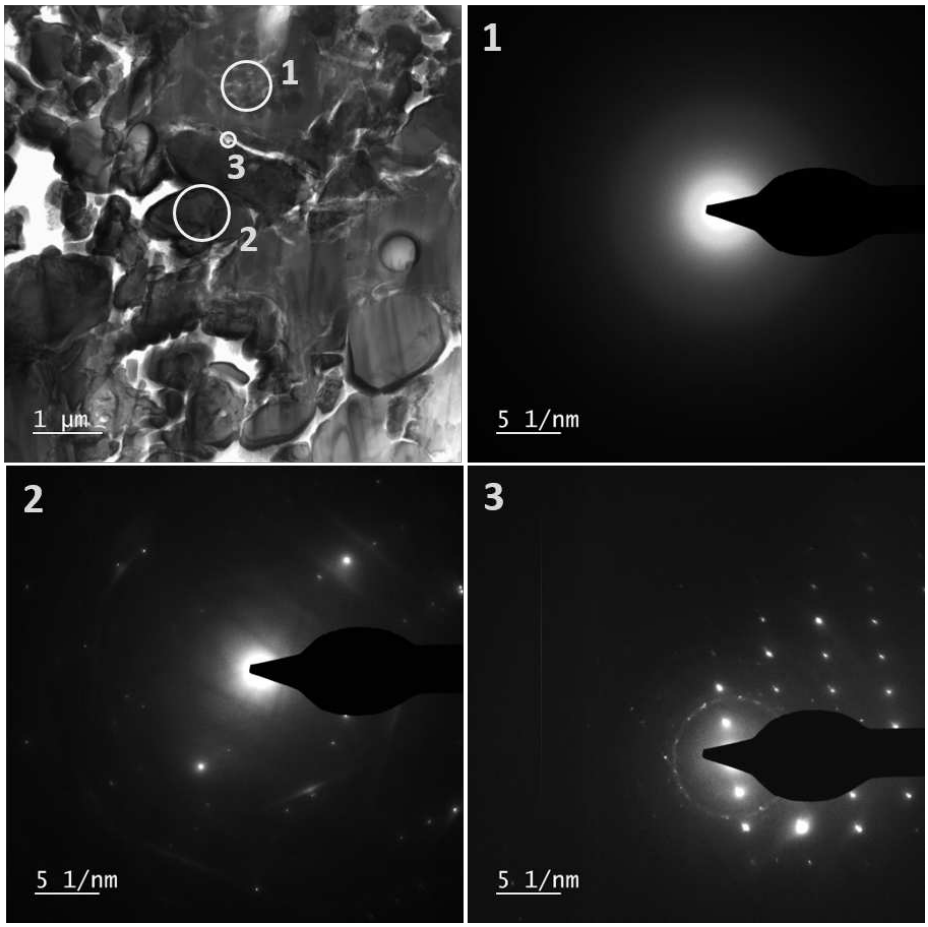

Figure 3.24: TEM images of a porosified GC LTCC with three labelled locations for SAED analyses.

Figure 3.25a displays the mass removal of LTCC substrates after etching with PBS1.2, at different bath temperatures and exposure times. From these plots and also in Figure 3.25b, by increasing the bath temperature from 45 to 90 °C the mass removal is substantially enhanced. For all temperature ranges an almost linear increase in mass removal is observed with etching time except for the 90

°C solution. Under this condition, the linear correlation is preserved only up to 1 h, whereas above, the mass removal and hence, the dissolution rate slows down, but does not reach any saturation level. This can be attributed to the higher diffusion rate of the etchant near the surface and the more difficult exchange of the etchant at the etching front deeper inside the substrate, due to the more difficult exchange of the etching solution through the generated micro- and nanopores. From the slope of LTCC mass removal plots (see Figure 3.25b), the dissolution rates for each temperature can be calculated. As can be seen in Figure 3.25c, by increasing the bath temperature, due to the Arrhenius theory and facilitated diffusion of the etchant into the LTCC pores, the dissolution rate also increases constantly.

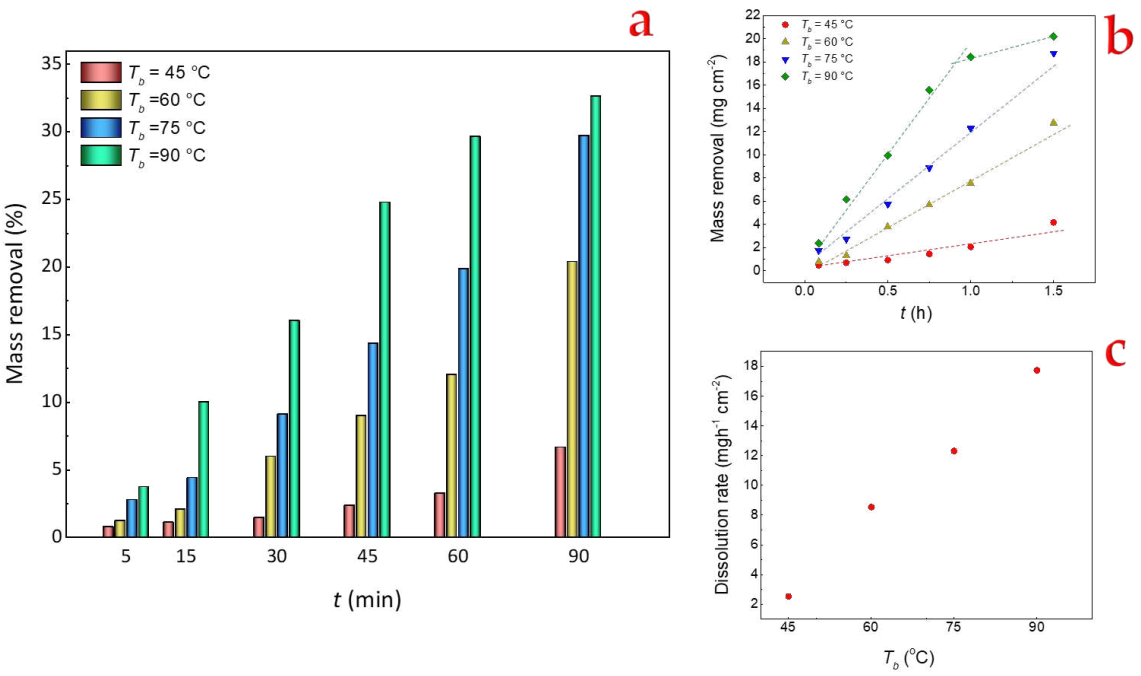

Figure 3.25: a) and **b)** Mass removal of GC tape as a function of time at varying bath temperatures, due to the etching with 0.2 mol L^{-1} PBS1.2, and **c)** dissolution rates as a function of bath temperatures, of the graphs given in b). For T_b= 90 °C only the first regime up to t=1 h is considered.

Figure 3.26a displays the porosification depth d_p as a function of etching time t for GC LTCC substrates treated with 0.2 mol L^{-1} PBS1.2 solution at different temperatures. At a given bath temperature, T_b increases with etching time almost linearly and with no significant change in the slope which hints toward a reaction-controlled mechanism. For a fixed etching time the increased porosification depth which is observed when enhancing the bath temperature is explained with the more facile diffusion of the etchant into the depth of the LTCC body at higher temperatures. Besides, due to the faster reaction kinetics at higher temperatures, by increasing the bath temperature an increase in the steepness of the plots can be observed.

To assess the assumption of the reaction-controlled mechanism, Arrhenius-type diagrams of d_p as a function of the reciprocal bath temperature were plotted in Figure 3.26b. The linear regression

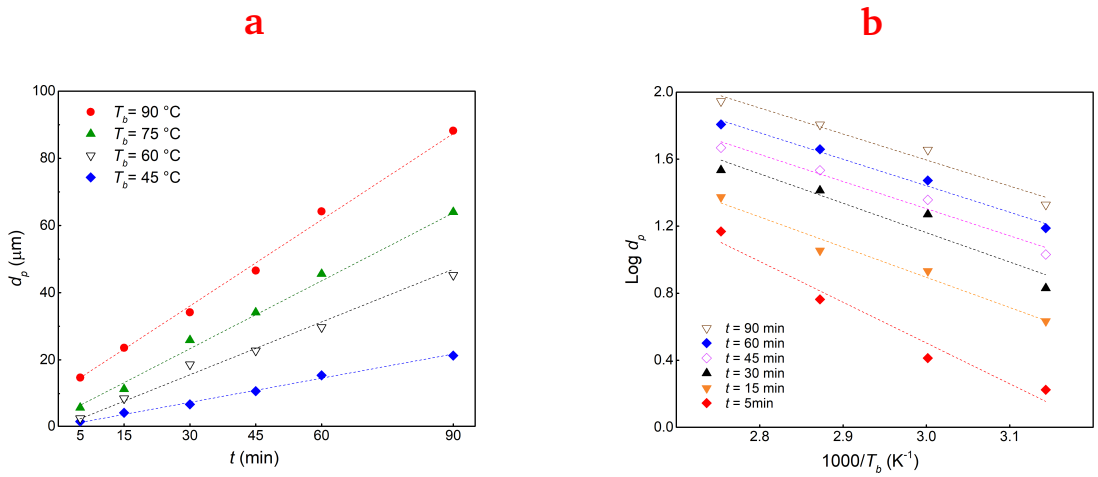

Figure 3.26: Porosification depth d_p (**a**) and corresponding Arrhenius diagrams (**b**) when etching GC with 0.2 mol L^{-1} PBS1.2 at different etching times and bath temperatures.

of the plots shows that the porosification with PBS1.2 follows the Arrhenius law over the whole temperature range up to 90 min, and the corresponding activation energy E_a values are determined from the slope of the fitting lines.

Table 3.2: Activation energies from the Arrhenius diagrams in Figure 3.26.

Etching time *min*	**5**	**15**	**30**	**45**	**60**	**90**
E_a *eV*	2.43	1.80	1.76	1.62	1.58	1.55
Regression coefficient R^2	0.9445	0.9724	0.9178	0.9715	0.9875	0.9661

The slopes of the linearly fitted lines and hence, the corresponding activation energies continuously decrease when increasing the etching time, from 2.65 eV for 5 min down to 1.55 eV for 90 min (see Table 3.3). However, the calculated activated energies remain well above the limit of the diffusion-controlled regime, *i.e.* 0.2 eV. Therefore, it can be concluded that for the etching treatment of the GC with PBS1.2, the process is reaction-controlled, while by increasing the etching time, the depth of etchant penetration increases and the diffusion into the deep pores of the LTCC more and more dominates the whole process, but does not reach the pure diffusion-controlled regime.

3.2.2. Impact of etchant concentration

After investigating the effect of the etchant pH on the etching process, further investigation was carried out on the etching process with orthophosphoric acid which is the standard etchant for the wet chemical etching of LTCC substrates and the impact of its temperature and etching time has been extensively investigated in previous reports [75, 222, 223]. However, there is no com-

prehensive study on the effect of concentration on the etching process, and only the commercially available 85%, as well as 50% concentrations, have been investigated previously. As illustrated in Figure 3.27, a series of etching experiments by using orthophosphoric acid solutions with different concentrations were conducted at a fixed bath temperature of 90 °C, which has been demonstrated as an optimized bath temperature in previous studies. Commercially available 85 wt % orthophosphoric acid was used to prepare 300 mL of each solution through dilution with water. The prepared solutions were labelled as described in the Experimental section in Chapter 2.

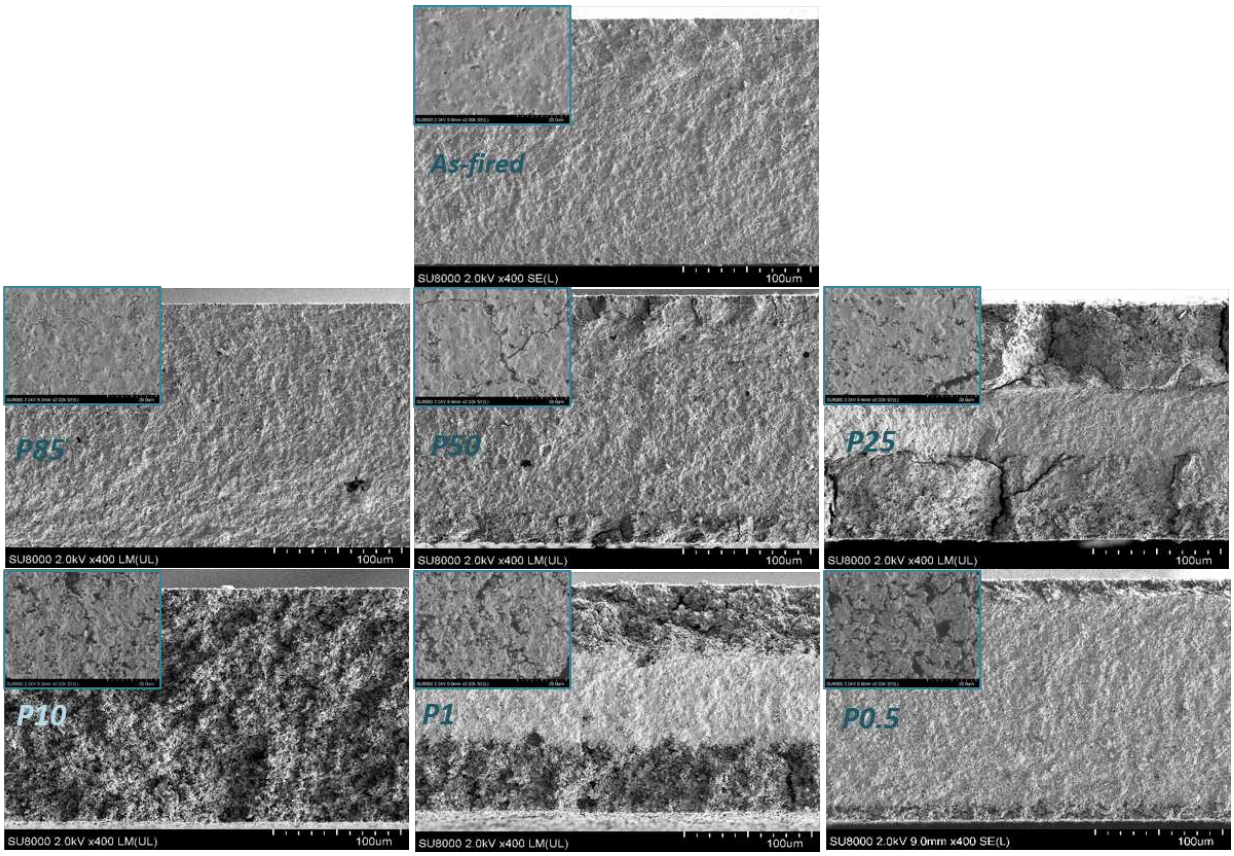

Figure 3.27: SEM micrographs in cross-sectional and top view (insets) of GC LTCC etched with H_3PO_4 at different concentrations for 60 min at T_b = 90 °C.

As it can be seen in this figure, the samples etched with orthophosphoric acid at concentrations of 85, 50, and 25% (labeled as P85, P50, and P25) represent smaller pore openings and a denser porosified layer than those etched with orthophosphoric acid at concentrations of 10, 1, and 0.5% (labeled as P10, P1, and P0.5). By decreasing the orthophosphoric concentration from 85% to 10% the d_p increases dramatically, and for the P10 etchant, the etching process is so fast that by only 60 min of etching treatment the LTCC substrates is completely porosified, with less than 6% reduction of the initial thickness.

Mass removals of the substrates due to the etching process by using different concentrations of orthophosphoric acid as etchants were determined for the above-mentioned etching parameters.

The mass removal percentages due to the etching process were normed to the initial weight of the corresponding *as-fired* substrates. The calculated mass removals and corresponding porosification depth values for all etchants are shown in Figure 3.28.

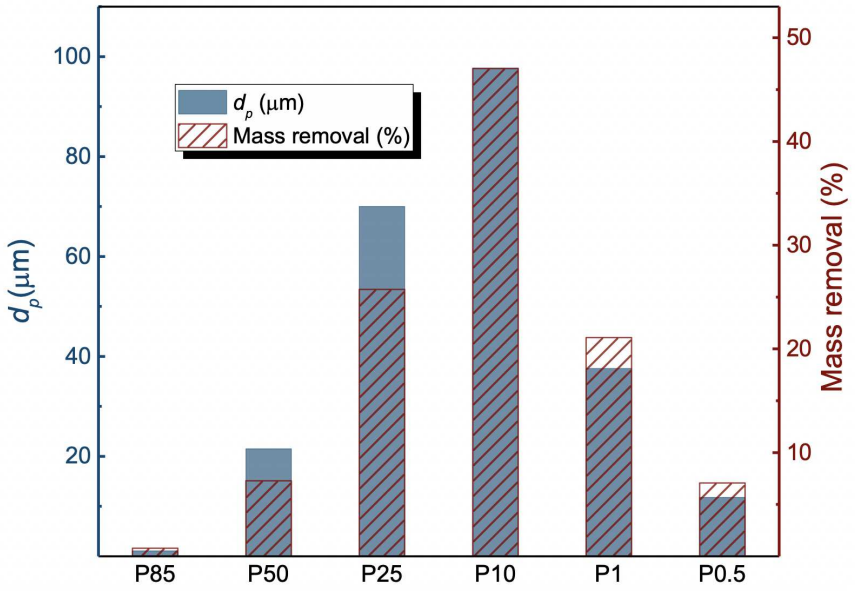

Figure 3.28: Mass removal and d_p values for GC LTCC etched by orthophosphoric acid-based etching solutions with different concentrations.

As observed in Figure 3.28, the mass removal and d_p values for GC LTCC substrates etched by orthophosphoric acid solutions with different pH values, follow a quite similar characteristic behaviour with concentration. The least values for both d_p and mass removal are obtained while applying the standard P85 etching solution. By reducing the etchant concentration these values are significantly increasing with an upper limit for P10 solution, while a further decrease in etchant concentration leads to a decrease. The obtained mass removal and d_p values can be analysed with respect to the conventional parameters influencing dissolution reaction rates as well as the etching bath parameters influencing etchant viscosity and thus its diffusion ability.

The viscosity of phosphoric acid has been reported to increase with its concentration (see Figure 3.29). Also, pure phosphoric acid consists of tetragonal groups which are linked by hydrogen bonds. This structure results in a high viscosity fluid, especially at enhanced concentrations. The dimeric anion ($H_5P_2O_8^-$) has been observed at high acid concentrations but has not been found in dilute solutions at room temperature. For solutions below 50%, there are more bonds between the phosphate ions and water than between the phosphate ions, what results in further reduction of viscosity of these solutions [244].

Moreover, as known from the concentration dependency of the orthophosphoric acid reported in literature [245], for solutions more concentrated than 10%, the viscosity strongly rises with increasing orthophosphoric acid concentration. On the other hand, below 10% the changes are

insignificant. Therefore, due to the superior penetration affinity of P10 and its relatively high concentration, this etchant shows the highest porosification, while for the etchants above or below this limit, due to the difficult diffusibility and lower amount of H^+ ions, the d_p and mass removal values are reduced.

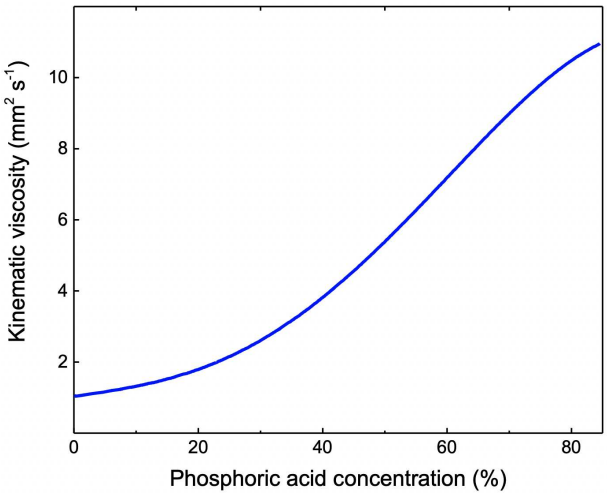

Figure 3.29: Concentration-dependent kinematic viscosity of orthophosphoric acid at room temperature [245].

An interesting observation in Figure 3.28 is that the 100-fold dilution of P50, whereas the latter is known as a reference etching solution and has been extensively studied for LTCC porosification, does not have a remarkable effect on the relative weight loss of GC LTCC and the obtained mass removal values for both etching solutions, *i.e.* P50 and P0.5 are nearly the same. However, the d_p value for P50 is noticeably higher. This hints toward the formation of remarkably larger pores while etching with P0.5 due to the more aggressive etching behaviour of this etchant compared to P50. This can be due to the significantly higher vapour pressure of P0.5 compared to the P50 which gives rise to the bubble formation close to the boiling temperature, leading to a harshly attacked LTCC surface. The more aggressive etchant dissolves more of the surface and results in large pores, openings, and surface roughness, while the milder etchant shows higher etch selectivity and hence larger porosification depths. Similarly, for the etchants below 10% the mass removal values are substantially higher than what expected from the corresponding d_p value which shows the more aggressive behaviour of the etchant. These findings are in good agreement with the obtained SEM micrographs which were shown in Figure 3.27. Also, the original thickness of GC LTCC due to the 60 min etching treatment at 90 °C with different concentrations of orthophosphoric acid was reduced from its initial value of approximately 210 μm to 209, 209, 202, 198, 195, and 206 μm for P85, P50, P25, P10, P1, and P0.5, respectively.

Finally, mercury porosimetry measurements were performed to get information about the impact of etching condition on the porosity and the pore size. PBS1.2 and P1 etching solutions at 90 °C were used as two representative etching conditions since they show great etching performance and also have almost the same concentration of 0.2 mol L^{-1}. Besides, to study the impact of bath

temperature the PBS1.2 solution was examined at 75 °C too and the results are shown in Figure 3.30. The porosification with either PBS1.2 or P1 etching solution creates pores with relatively broad pore size distributions ranging from few nanometers up to a few micrometres. However, the cumulative pore volumes show that the size distributions are dominated by pores of diameter > 1 μm. Also, PBS is found to be a milder etchant compared to the H_3PO_4 as PBS1 produces relatively smaller pore openings in comparison to the P1 and the total pore volume is approximately 30% lower. A very similar distribution is observed for the pores up to 0.4 μm when applying either PBS1.2 or P1 etching solutions. However, etching with P1 produces a higher number of pores with diameters above 0.4 μm compared to the PBS1.2.

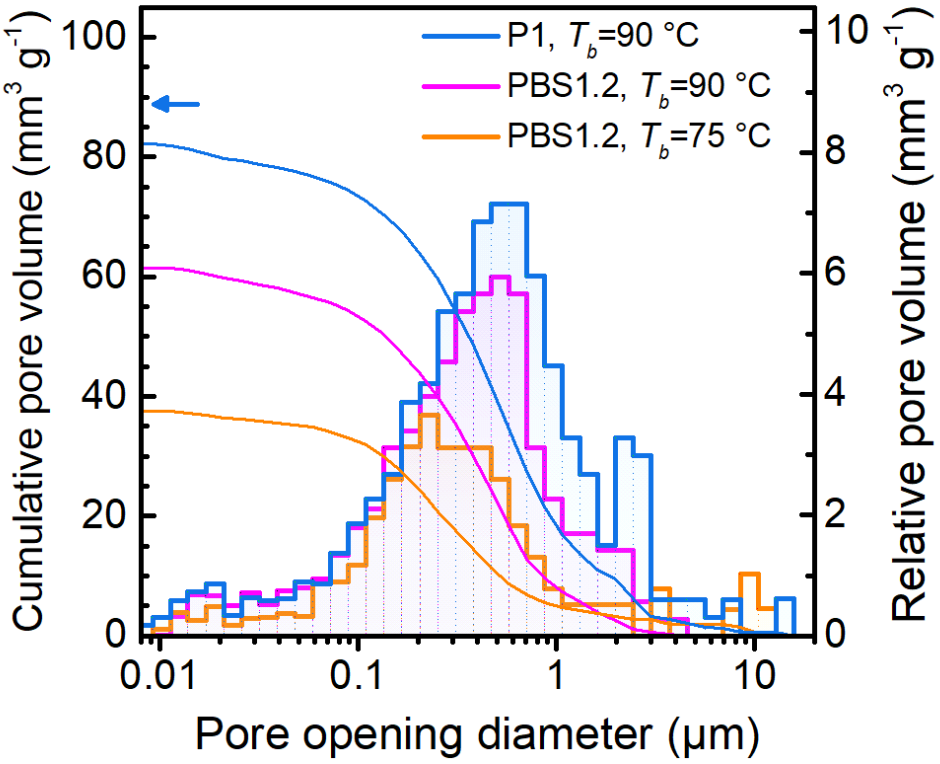

Figure 3.30: Cumulative pore volume, pore opening diameter and relative pore volume for GC LTCC etched under different etching conditions.

The total porosity in the etched layer was determined with respect to the porous layer thickness obtained by cross-sectional SEM imaging (left images in Figure 3.31), and also by excluding porosity with pore opening diameters > 5 μm, which is an artefact from the porosimetry experiment itself. The results are shown in Table 3.3.

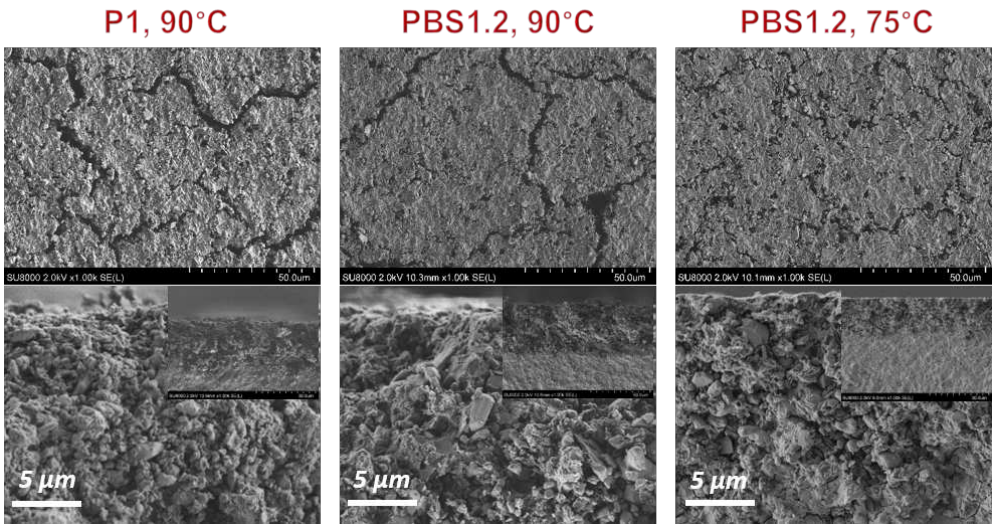

Figure 3.31: SEM micrographs in top and cross-sectional view of GC LTCC etched with P1 at 90 °C and PBS1.2 at 90 °C and 75 °C, respectively. Insets in the second row represent lower magnification SEM images of corresponding cross-sections.

Table 3.3: The d_p and porosities of the GC LTCC substrates treated for 30 min at different etching conditions. Pore openings larger than 5 μm are excluded.

Sample	d_p μm	Average weight losses %	Porosity %
PBS1.2, T_b=90 °C	42.0	21.09	37.0
PBS1.2, T_b=75 °C	27.5	9.06	36.0
P1, T_b=90 °C	39.6	17.84	50.0

3.2.3. Permittivity measurements

The effective relative permittivity (ε_r') at 1000 MHz was evaluated by averaging the results of three measurements of each sample. In the frequency range of 1-1000 MHz, the obtained ε_r' values were constant within the measurement accuracy. The results for the 1000 MHz are graphically illustrated in Figure 3.32. As shown in this figure, the relative permittivity values of GC LTCC samples etched either with PBS1.2 or P1 solutions decrease as the etching time increases. This is due to an increase in d_p at increased etching times, which results in the embedment of increased amounts of air in the LTCC. The maximum permittivity reduction achieved by using P1 is quite comparable to that when using a PBS1.2 etching solution, *i.e.*, approximately 10.8% *vs.* 10%, respectively. The permittivity reduction achieved in this work is comparable to or even than those reported in literature, where the permittivity has been measured at GHz-range frequencies by applying a ring resonator on the LTCC surface [75, 76].

For calculating the permittivity of the porous layer, the whole porosified LTCC can be considered as three series capacitors, *i.e.* the bulk LTCC confined between two porous LTCC layers. Therefore, by assuming the same depth of porosification for both sides of the LTCC, the overall capacitance of

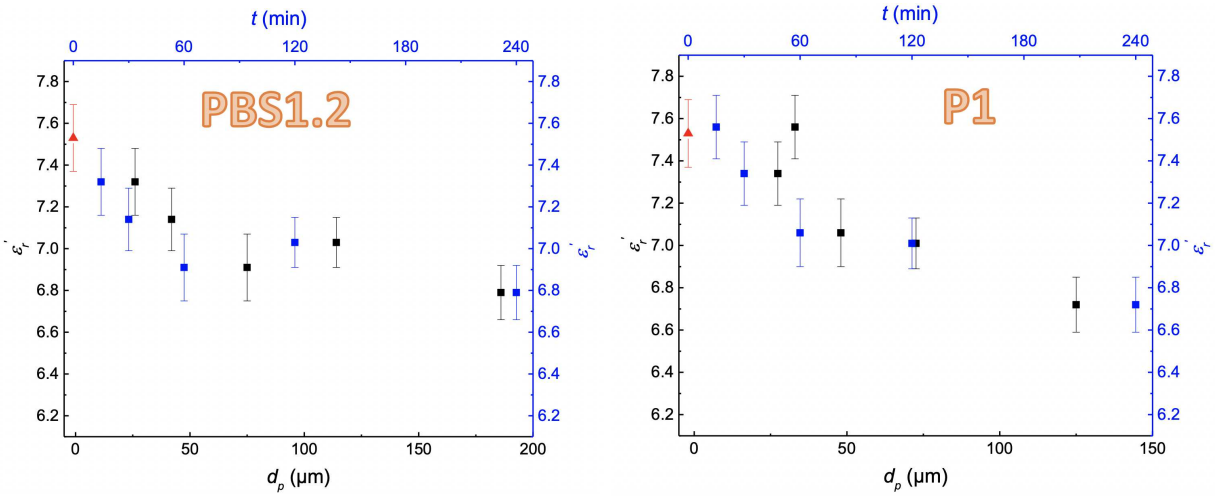

Figure 3.32: Effective relative permittivity of GC LTCC samples etched with PBS1.2 (left) and P1 (right) etchants at 90 °C, in dependence of etching times and corresponding d_p values. The red triangle represents the measured permittivity for the *as-fired* GC LTCC.

the porosified LTCC can be defined by Equation 3.2.

$$\frac{1}{C} = \frac{1}{C_b} + \frac{2}{C_p} \tag{3.2}$$

where C refers to the capacitance of the porosified LTCC and C_b and C_p represent the capacitance of the bulk (dense) and porosified layer, respectively. Therefore, by measuring the permittivity of a partially porosified and *as-fired* LTCC, *i.e.* $\varepsilon_r{}'$ and $\varepsilon_{r,b}$, respectively, and by using the standard equation for the parallel-plate capacitor (see Equation 3.3), the permittivity of the porous layer,$\varepsilon_{r,p}$, can be estimated as follow:

$$C = \varepsilon_0 \varepsilon_r{}' \frac{A}{d} \tag{3.3}$$

$$\varepsilon_{r,p} = \frac{2d_p \varepsilon_{r,b} \varepsilon_r{}'}{d\varepsilon_{r,b} - (d-2d_p)\varepsilon_r{}'} \tag{3.4}$$

where d refers to the whole LTCC thickness. By inserting d=600 μm, $\varepsilon_{r,b}$=7.53, the measured $\varepsilon_r{}'$ values, and their corresponding d_p values in Equation 3.4, the average $\varepsilon_{r,p}$ for etching with PBS1.2 and P1 was calculated to be 6.18 and 5.87, respectively.

Chapter 4.

ALKALINE SOLUTIONS AS ALTERNATIVE ETCHANTS FOR LTCC POROSIFICATION

Parts of this chapter have been published in [78, 243].

Since its introduction in 2009 the wet chemical etching of LTCC substrates to reduce their permittivity has been based on acidic etching solutions and no other solutions were reported to achieve successfully the porosification of LTCC. The commercially available solution of orthophosphoric acid 85 wt%, as well as the 50 wt% solution, were thoroughly examined for the porosification of glass-ceramic composite (GCC) systems and the most effective etching was achieved at temperatures above 100 °C. However, realizing high-quality and intact surfaces after the porosification process remained a major challenge. The significance of high-quality surface is emphasized taking into consideration the long-term objective of this approach which is to apply metallization on the porous areas for the realization of, *e.g.*, patch antenna elements where a high-quality surface and relatively low surface roughness could offer a bearing plane with regularly allocated openings for air embedment. Also, those investigations showed that in GCC type LTCC, the distribution of the pores directly depends on the distribution of the embedded alumina grains and as a direct consequence on the selectively solvable feldspar phases, which are formed during the sintering process in this part of the glass matrix partly enveloping the alumina grains.

Therefore, in this chapter, an alternative approach has been investigated for the porosification of LTCC surfaces targeting a better surface quality which features a suitable bearing plane for further metallization lines. According to standard literature and data sheets of commercial LTCCs, they are usually based on aluminium oxide and/or an aluminium oxide containing compounds as the ceramic filler material. Aluminium oxide is an amphoteric compound which can be dissolved by both acidic (Equation 4.1) and alkaline (Equation 4.2) solutions according to the following

reactions:

$$Al_2O_3 + 6H^+ \rightarrow 2Al^{3+} + 3H_2O \tag{4.1}$$

$$Al_2O_3 + 2OH^- + 3H_2O \rightarrow 2Al(OH)_4^- \tag{4.2}$$

Similarly, aluminium oxide-containing compounds can also be dissolved in both acidic and alkaline media. Their dissolution rate in acidic media, however, is usually higher compared to alkaline media. This fact could hint towards better control of the etching process and possibly higher surface quality of the etched LTCC. Therefore, relatively low concentrations of alkaline etchant were used at temperatures below 100 °C to porosify commercial LTCC tapes. Compared to the state-of-the-art approach which uses 50 wt% H_3PO_4 (*ca* 8.5 mol L^{-1}) at >100 °C, this condition is quite milder. Two types of LTCC systems as representative of anorthite forming tapes were used for the investigations, namely the CeramTape GC (abbreviated as GC LTCC) which is one of the simplest systems due to the limited number of tape components and crystallographic phases involved and the Ferro L8 as a relatively new tape with promising dielectric properties which make it ideal for producing components and modules with applications up to 40 GHz. Further information on the material properties of both tapes is given in Chapter 1..

Moreover, as discussed in Chapter 1. in the dissolution of alkali feldspar, it is believed that the first step is the relatively fast removal of alkali and alkaline earth metals from the mineral structure. This removal leads to a depleted surface layer and the bridging Al-O-Si bonds are subsequently hydrolysed to release Al to the solution. This leaves the surface of the alkali feldspar enriched in silica in both acidic and alkaline conditions. In the final step, the Si-O-Si bonds from the silica enriched phase become hydrolysed [107].

4.1. Porosification of GC LTCC with KOH

In the present study, commercially available GC LTCC tapes were used for investigating the porosification process. Local porosification of a substrate with a relatively high permittivity allows to locally lower the permittivity and to arrange areas of different permittivity in one single layer. More detailed information about the material properties of the GC LTCC and the individual fabrication processes can be found in literature and the corresponding data sheet [169]. The etching solution of 3 mol L^{-1} potassium hydroxide (KOH) was freshly prepared by dissolving the desired amount of KOH pellets (≥99.97% from Sigma-Aldrich) in deionized water. The GC LTCC substrates were provided in the *as-fired* state by Micro Systems Engineering GmbH (MSE, Berg, Germany). After firing of GC LTCC, a complex material is generated consisting of a glass matrix with different crystalline

and chemical phases in which Al_2O_3 particles with a typical size in the μm-range are embedded. The analysed LTCC substrates were square-shaped, with an edge length of approximately 15 mm and a thickness of about 450 μm. The wet-chemical etching experiments were carried out in 3 mol L^{-1} aqueous KOH solutions at constant temperatures ranging from 70 to 100 °C (see the etching setup in Chapter 2..

In general, several parameters are affecting the wet chemical etching of LTCC. Concerning the etching solution and for a given chemical composition, the most important parameters are etchant concentration, bath temperature, and etching time. However, our primary investigations showed that "bath temperature" is the major parameter as, at not sufficiently high bath temperatures, the etching process would be too slow for practical use, even by applying a suitable etchant concentration for long times. For example, as can be observed in 4.1a and b, the comparison of SEM micrographs for the *as-fired* GC and the sample treated with 3 mol L^{-1} KOH solution for 2 h at room temperature shows no perceptible difference.

Increasing the temperature to 55 °C caused some small etch-related features to be introduced into the surface (see 4.1c). This change in the surface morphology demonstrates the partial etching of the LTCC surface. However, contacting the LTCC sample with the same bath solution at a more elevated temperature of 70 °C resulted in a noticeable amount of etching as can be observed in 4.1d, where some parts have been removed from the LTCC surface and near-surface regions, and the surface characteristics is considerably altered in comparison to the *as-fired* state. Further increase in bath temperature to $\geq$80 °C, results in a more noticeable amount of porosification of the LTCC surface and an increase in penetration depth of the etchant (see 4.1e and f). These findings suggest that the etching experiments should be carried out at temperatures above 70 °C. However, due to the massive bubble formation at temperatures close to the boiling point which results in the significant surface damages, bath temperatures above 100 °C were avoided.

Next, the impact of etching time, as another important parameter for the porosification process was studied. Figure 4.2 presents SEM micrographs of the GC LTCC samples etched with the 3 mol L^{-1} KOH solution at a constant temperature of 80 °C for different treatment times. A noticeable etching of the LTCC surface starts after 1 hour of exposure to the KOH solution and specific surface features resulting from the porosification process are identifiable in Figure 4.2a. By increasing the treatment time, the etchant penetrates further and deeper holes are created which are observable by darker areas in the SEM image (see Figure 4.2b). By increasing the treatment time to 330 min, even though the basic surface features are still preserved a lateral growth in pore size occurs which results in wider pore openings (see Figure 4.2c). Long-time etching of the sample for 930 min resulted in the severe dissolution of large LTCC fractions which create laterally disconnected grains on the surface and thereby the surface of the LTCC transforms strongly (see Figure 4.2d).

The change in the topography of GC LTCC was further characterized by stereo-SEM images. For this purpose, SEM micrographs were recorded with similar contrast and brightness settings to prevent differences in parameter values for further analyses. MeX software was used for calculating 3D-

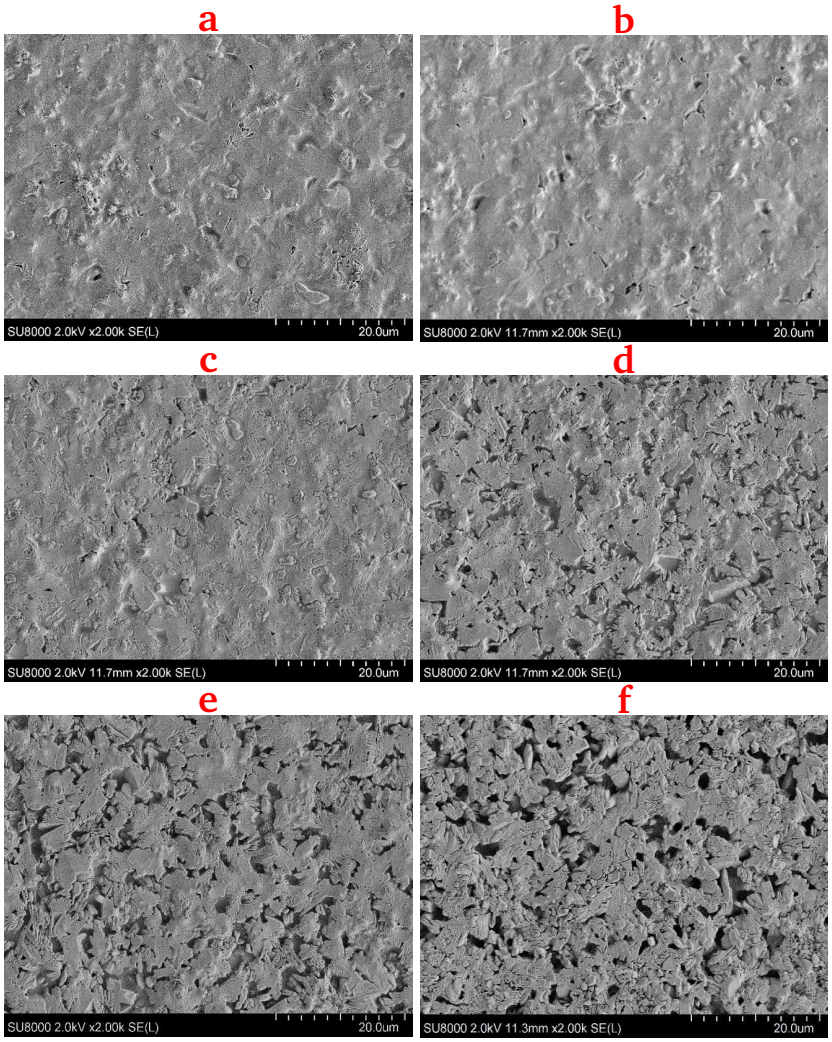

Figure 4.1: SEM micrographs in top view of GC LTCC for **a)** *as-fired* state, and etched for 2 h with 3 mol L^{-1} KOH at **b)** 25 °C, **c)** 55 °C, **d)** 70 °C, **e)** 80 °C, and **f)** 90 °C.

surface roughness parameters, and a cut-off wavelength value of 2.8 μm was applied for both *as-fired* and etched samples. The stereo-pairs SEM micrographs of the *as-fired* and etched LTCC, reconstructed with MeX show a clear alteration of the surface morphology, as illustrated in Figure 4.3a and b.

As a result of the material removal, relatively deep valleys are generated and also small pores are introduced into the surface. These changes in surface topography which can be clearly observed in the stereo-SEM images lead to an increased roughness of the LTCC compared to the *as-fired* state. To provide a direct comparison of the KOH-based porosification of the GC LTCC with the one developed by our group in the past, orthophosphoric acid solution 85 wt% (P85) was applied as a well-established and commercially available etchant. As shown previously, treatment with P85 forms the porous structure through selective etching of the anorthite phase, which is generated in the alumina grain near-portion of the glass matrix in the *as-fired* LTCC. Figure 4.3c represents

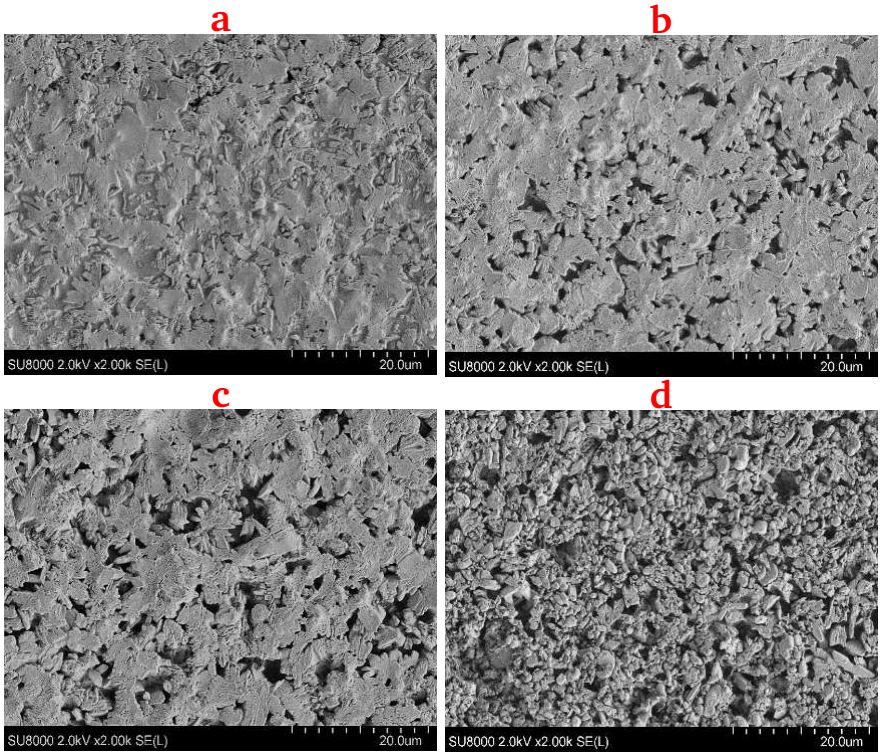

Figure 4.2: SEM micrographs in top view of GC LTCC etched with 3 mol L^{-1} KOH at 80 °C for **a)** 60 min, **b)** 220 min, **c)** 330 min, and **d)** 930 min.

the stereo-SEM image of the GC LTCC sample etched with P85 at 100 °C. As a result, applying P85 creates stronger surface devastation compared to the KOH-treated sample. It should be noted that T_b=100 °C is a relatively mild condition for P85 as an etchant to achieve an effective LTCC porosification. Etching at higher temperatures although significantly improving the porosification degree, results in even more attacked LTCC surface. A detailed study on the impact of different parameters on LTCC etching treatment with orthophosphoric acid is represented in the previous section.

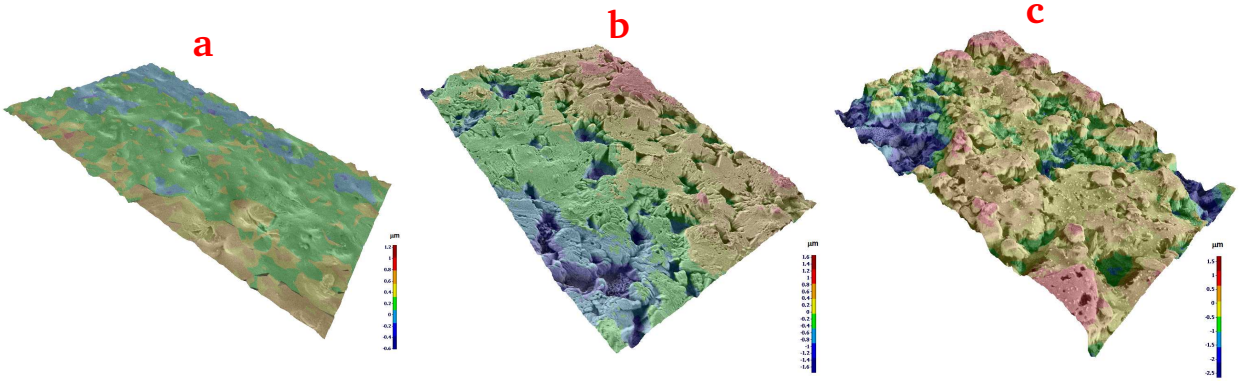

Figure 4.3: Stereo-SEM images of GC LTCC substrates **a)** *as-fired*, and **b)** etched with 3 mol L^{-1} KOH at 75 °C, and **c)** etched with P85 at 100 °C to illustrate LTCC surface modifications due to etching.

Important parameters for the areal roughness analysis, such as S_a, S_p, and S_v, are defined in Table 4.1. As the representative quantity of the surface changes due to the etching S_a was selected, whereas peaks and valleys of the surface were predominantly captured by S_p and Sv, respectively. The reported values are averaged for four different areas randomly selected from the surface.

Table 4.1: Roughness parameters for *as-fired* and etched GC LTCC.

Parameter	*as-fired*	KOH etched	P85-etched	Definition
$\mathbf{S}_a$	53.1 nm	91.7 nm	151.8 nm	Average roughness across the selected area
$\mathbf{S}_p$	447.7 nm	513.7 nm	745.7 nm	Maximum peak height within the selected area
$\mathbf{S}_v$	518.0 nm	765.7 nm	933.3 nm	Maximum valley-depth within the selected area

The average height of a selected area represented by the S_a parameter is defined as the arithmetic mean of the absolute height values within a sampling area. S_a shows an increase for the etched sample compared to the *as-fired* LTCC independent of the etchant. However, the increase in the maximum peak height within a selected area (S_p parameter) compared to its maximum valley-depth (S_v parameter) is less significant. This kind of surface roughness is the main advantage of the present porosification approach since a reliable metallization of surfaces with sharp edges and high peak roughness is most challenging. As was expected, the more the surface is distorted as observed by the P85 treatment the larger the areal surface roughness parameters compared to those obtained by KOH treatment.

The XRD diffractograms of GC LTCC before and after treatment with KOH etching solution are shown in Figure 4.4. Besides the reduced peak intensities of the porosified LTCC compared to the *as-fired* sample it is clear that some anorthite peaks have become significantly smaller or vanished entirely. These observations confirm that upon alkaline treatment of the Ceramtape GC LTCC, the predominantly etched phase in the LTCC is the anorthite phase.

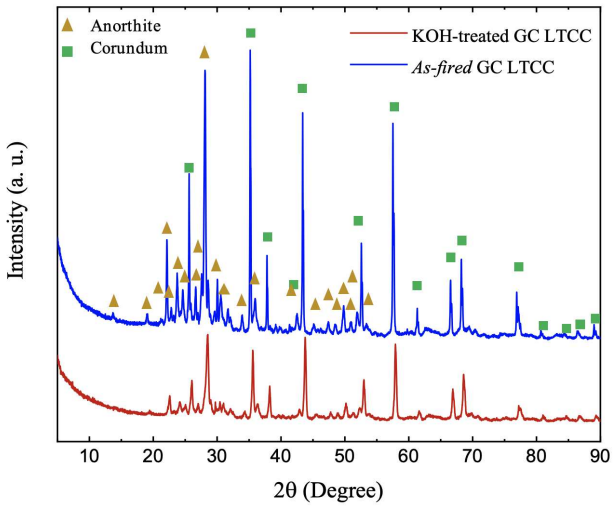

Figure 4.4: X-ray diffractograms of powdered GC LTCC before and after treatment with 3 mol L^{-1} KOH at 90 °C (an: anorthite, c: corundum). The intensity levels are shifted for comparison reasons.

Basically, GC LTCC consists mainly of aluminium (Al), silicon (Si), calcium (Ca), and oxygen (O) elements in which alumina grains (in the form of rhombohedral corundum) are dispersed in the amorphous glass matrix [79]. The corundum grains are discrete and clearly visible in the FIB foils. GC LTCC provides a high degree of crystallization and only a low glass fraction remains amorphous after firing due to the low amount of viscosity lowering glass modifier oxides and thereby the relatively high maximum firing temperature of 900 to 950 °C [31].

The TEM images of the GC LTCC etched in 3 mol L^{-1} KOH solution at 90 °C for 4 hours are shown in Figures 4.5–4.7. The overview images of the porosified LTCC indicate that the maximum etching depth is about 4.6 μm and below this depth, no further etching was detected. As indicated by the white arrow line scan, an EDX line scan at the depth of 5 μm and parallel to the sample surface, which is below the formed etched front, was recorded applying STEM. Every five nanometers an EDX spectrum was taken.

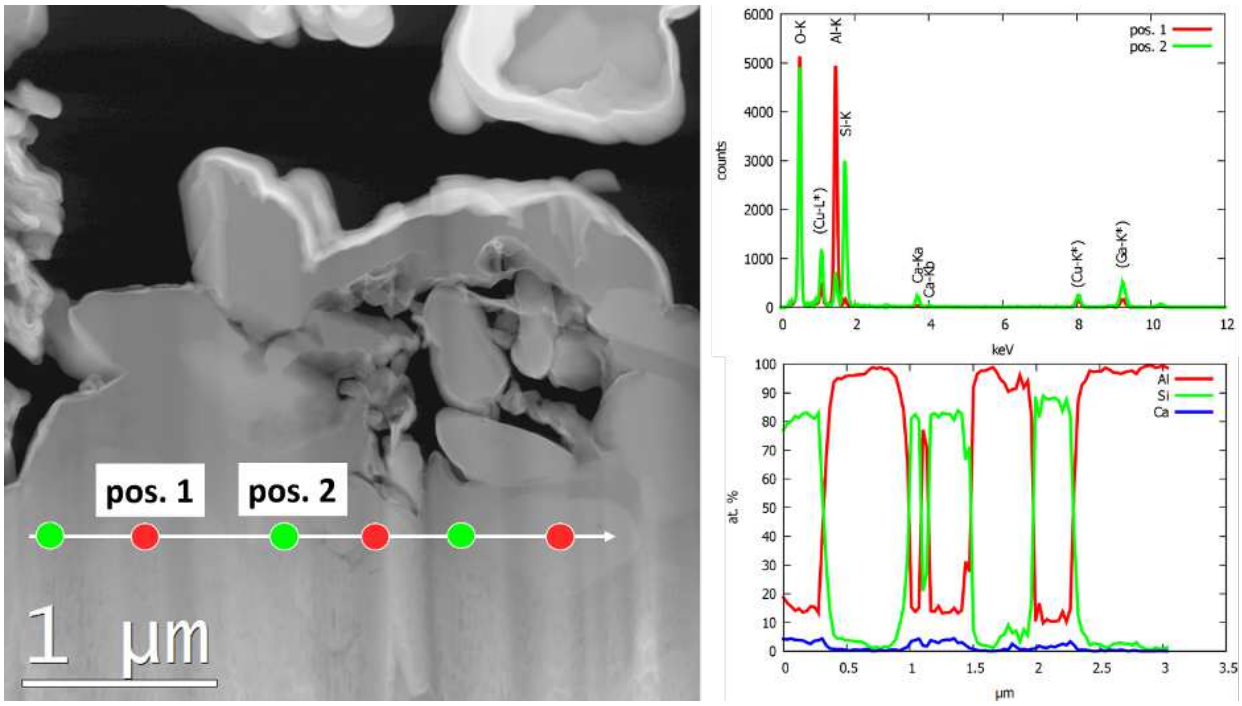

Figure 4.5: EDX line profile across an unmodified, *as-fired* area of the GC LTCC etched in 3 mol L^{-1} KOH solution at 90 °C for 4 hours.

Corundum and glass phases (Si-rich) can be observed in Figure 4.5. Also, in the vicinity of corundum grains the amount of Ca is increased which indicates the formation of Ca-rich aluminosilicate phases (anorthite) in these areas. The respective EDX spectra and the quantification of the whole EDX line scan for the elements Al, Si, and Ca are shown on the right-hand side of Figure 4.5. As can be seen in the scan lines, counts of Si and Ca change simultaneously and in opposite direction to Al. However, the highest Ca amounts are in these areas close to the corundum grains in which Al count is maximum. Furthermore, like the intermediate regions between corundum grains in the porosified layer which is shown in Figure 4.6, an increase in Si and Ca was observed parallel

to a reduction in Al. This confirms the presence of discrete corundum grains surrounded by an anorthite phase which is formed during the diffusion of Ca from the glass phase to the corundum grains during the sintering process. The presence of the Al, Si, Ca, and O as main constitutes of the GC LTCC was also confirmed with EELS. The intensities of the EELS-ionization edges, which are dependent on the chemical element, concentration, and sample thickness, are depicted for different positions along the arrow line.

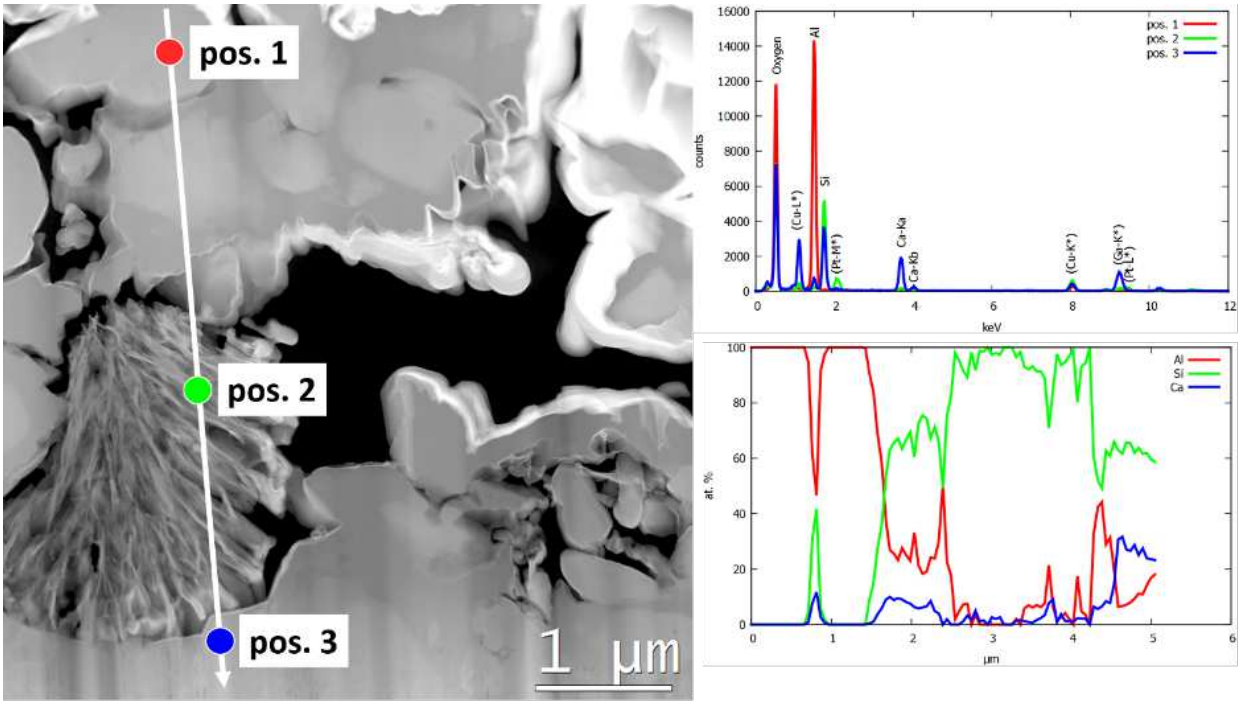

Figure 4.6: EDX line profile across an etched region indicating three different phases: pure Alumina at position 1, pure Silica at position 2 and Ca-rich aluminosilicate at position 3. The color used for each position is in correspondence with the chemical which is dominantly found in that position. Thus, position 1 is Al-enriched, while positions 2 and 3. are enriched in Si, and Ca, respectively.

In order to investigate the changes in elemental composition due to the etching process, an EDX line scan through the porosified part of the LTCC was recorded. Three different EDX spectra in the region where porosification occurred are shown as an example in Figure 4.6. Position one (pos. 1) corresponds to the corundum phase and position two (pos. 2) represents a very porous silica-rich phase formed during the etching process. In position three (pos. 3) in addition to Al and Si, the presence of Ca is also detected.

Unlike the former EDX line profile (see Figure 4.5), where no position could be found indicating the presence of pure silica, at the line scan recorded in the porosified segment of the LTCC, pure silica in a foam-like structure was detected. Furthermore, an increased amount of Ca was detected close to the pore walls of the etched LTCC, which are indeed residual parts of the dissolved anorthite phase, and the etchant has not penetrated further into the depth of the LTCC. The elemental analysis of Al, Si and Ca from the EDX line scan along the indicated arrow is depicted in the

right lower corner. From this image, it can be concluded that the intermediate regions between corundum grains feature a reduction in the amount of Al accompanied by an increase of Si and Ca, respectively. This part which envelops the corundum grains and consists of Al, Si, Ca, and also O which is not shown here, can be referred to the anorthite phase.

It can be seen in the TEM overview image of the porosified GC LTCC that the generated porosity mainly consists of pores with narrow necks (*i.e.*, small pore openings) and a relatively wide pore body. These so-called ink-bottle type pores result in a better surface quality with only a moderate increase in the surface roughness.

In addition to morphology and chemical composition, it is also of interest to study the crystallographic structure of the sample in selected areas after the etching process. For this purpose, Selected Area Electron Diffraction (SAED) measurements were carried out and the results are shown in Figure 4.7. The top left image gives an overview of the TEM lamella. A layer of platinum is applied on top of the specimen to prevent any charging effects and also to avoid any structural damage to the surface during FIB preparation. The three diffraction patterns were recorded from the corresponding positions marked within the overview image.

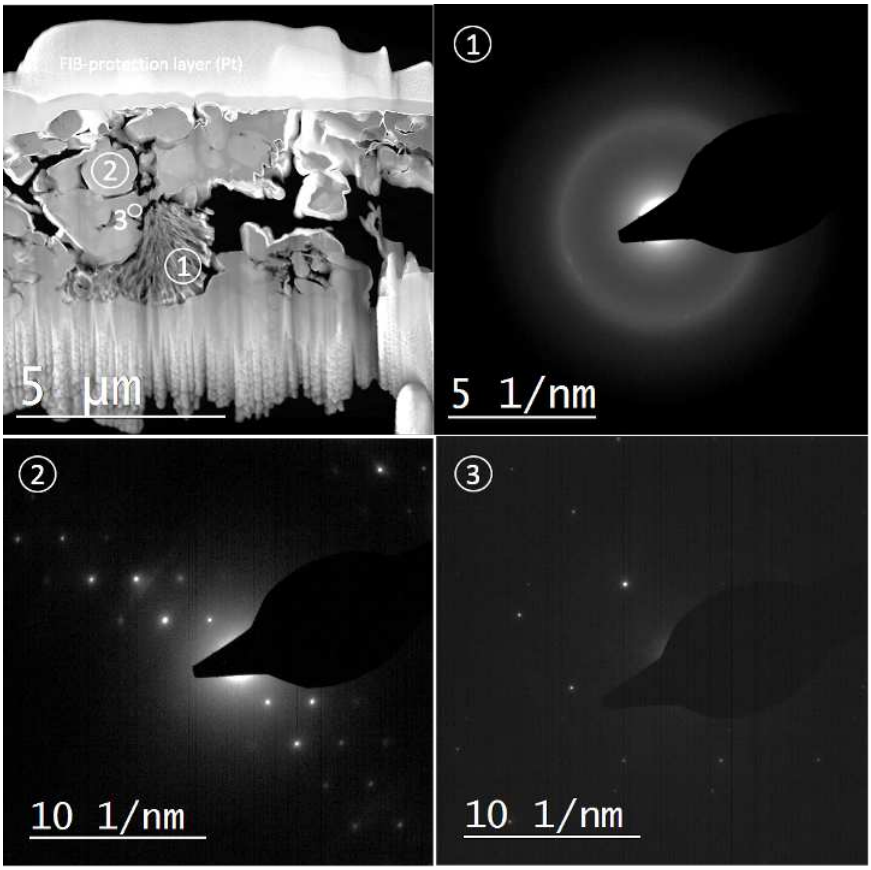

Figure 4.7: TEM lamella of a KOH-etched GC LTCC with three representative locations labelled and the corresponding SAED analyses. At position 1 pure silica shows a nano-crystalline microstructure, close to an amorphous phase, whereas positions 2 and 3 feature pure alumina and Ca-rich aluminosilicate with a single-crystalline morphology.

The formed foam-like silica which is formed due to the etching process consists of a nano-crystalline or quasi-amorphous microstructure. These foam-like silica structures can be better visualized by the SEM micrographs in Figure 4.8. The sharp ring in the SAED pattern at position one, however, indicates a well-defined near ordering which can be found only in single-crystalline microstructures. But since the whole ring is visible with constant intensity, the crystallites are of arbitrary orientation and of a very confined size. Positions two and three show a typical single-crystalline diffraction pattern far out from a low-indexed zone axis.

The EDX analyses of the LTCC in both porosified and non-porosified areas show that regardless of where the analysis is performed, the presence of Al changes in the opposite direction to Si. The areas with the maximum amount of Al were attributed to the corundum phase while the intermediate regions between the grains contain an increased amount of Si and Ca. Moreover, it was found that similar to the etching with orthophosphoric acid, also the anorthite phase is etched faster and more effectively compared to the corundum phase. But etching with orthophosphoric acid is faster and also more selective, as the glassy phase of the LTCC is also partially dissolved when applying KOH. On the other hand, this concurrent and competitive dissolution of the LTCC components in KOH etching assists in avoiding the sharp and emerged edges around the corundum grains which have been reported in literature after the etching with orthophosphoric acid. This etching behaviour additionally provides pores scaled down in size in the remaining top part of the LTCC surface. This is regarded as a significant achievement for the long-term objective of the porosified LTCC which is the air embedment through applying metallization on the porous areas.

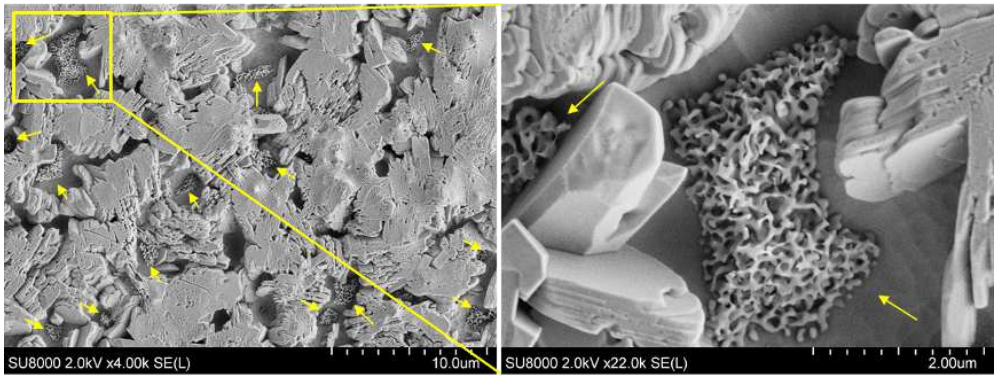

Figure 4.8: SEM micrograph in top view of the GC LTCC etched with 3M KOH (left) and the magnified SEM micrograph of the indicated rectangle (right). Arrows indicate the foam-like silica structures developed due to the etching process.

For reasons of comparison, the GC LTCC treated with P85 for 4 hours at 100 °C was FIB cut and analysed with TEM (see Figure 4.9).

As it has been shown in Figure 4.9 and also has been studied in the previous chapter the etching behaviour of GC LTCC with orthophosphoric is quite different from that observed with KOH. Although etching of the GC LTCC with KOH resulted in a localized porosity and locally modifies the surface and near-surface regions by the creation of mainly ink-bottle-type pores, a delocalized porosity is observed for the sample etched with P85. Furthermore, in contrast to the KOH-treated

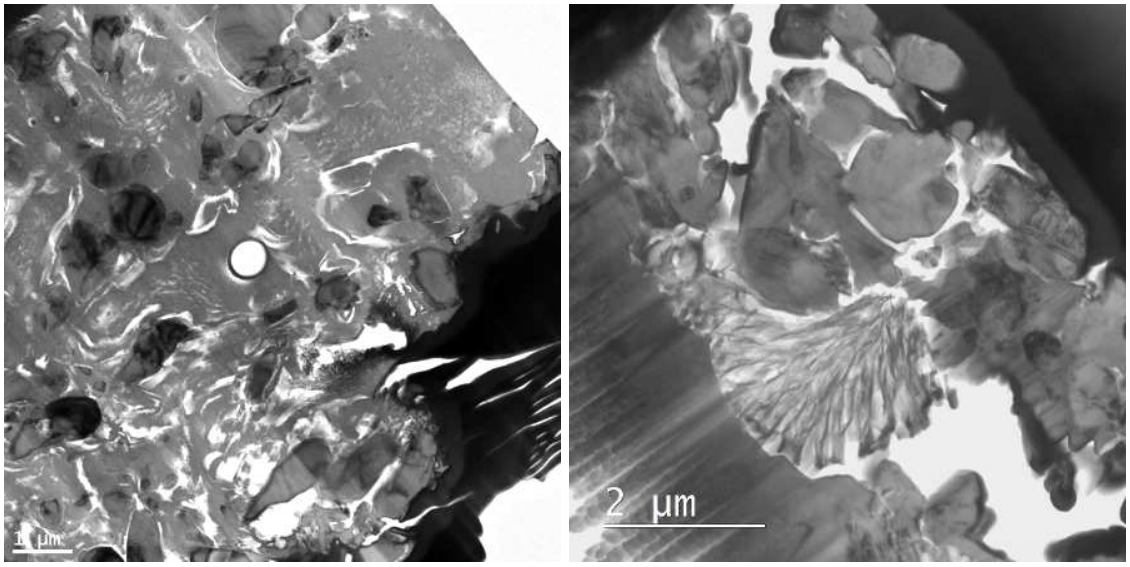

Figure 4.9: Bright-field TEM images of the GC LTCC etched with orthophosphoric acid (left) and KOH (right) etching solutions. White areas in the TEM image are indicating the pores.

LTCC which comprises mainly ink-bottle-type type porosity, the acid-treated sample contains a network of cylindrical pores that are formed due to the preferential dissolution of anorthite phase and are distributed within a much deeper region of the GC LTCC. Moreover, based on the detailed investigation on the elemental composition of the acid-treated samples in Section 3.2.1., it can be concluded that etching of the GC LTCC with phosphoric acid results in a more selective dissolution of the anorthite compared with the KOH solution.

4.2. Ferro L8 Porosification with NaOH

After introducing the potential of alkaline etching solutions for the porosification of LTCC substrates as an alternative to the widely studied acidic etching treatment, the porosification of another commercially available system (Ferro L8) by these types of etching solution was intended. However, preliminary investigations showed that for this tape the mass removal due to the etching treatment with NaOH is higher than the one with KOH. This could be attributed to the reduced viscosity of NaOH solution compared with KOH at high temperatures which are known to be more suitable for the porosification process. Therefore, the present study aims towards a detailed investigation of the introduced alkaline porosification process on a Ferro L8 tape and consequently, on the identification of the etching conditions needed to achieve the pre-defined porosification results. Due to its stable dielectric constant and low loss tangent, Ferro L8 is suitable for cost-sensitive low- to mid-frequency telecommunications, automotive, and medical modules, components, and sensors as well as higher frequency aerospace, satellite, and other applications requesting high reliability. Further information about the material properties of the Ferro L8 and the individual

fabrication process can be found in the corresponding data sheet [246, 247].

The investigated Ferro L8 substrates were square-shaped, with an edge length of approximately 10 mm and a thickness of approximately 190 μm. The wet-chemical etching experiments were carried out in aqueous NaOH solutions at constant temperatures below 100 °C with varying concentrations between 0.5 to 6 mol L^{-1}. Detailed information on the preparation of etching solutions, the test setup, the etching process, and gravimetric studies can be found in the experimental section.

4.2.1. Morphological and chemical characterization analyses

The surface morphology of LTCC substrates was investigated by SEM and some representative images are shown in Figures 4.10–4.12. Figure 4.10 displays the SEM micrograph of the Ferro LTCC surface in the original, *as-fired* state before etching, and as can be observed in this image, the surface of Ferro L8 LTCC even at this state is wavy and bumpy. Changes in the surface morphologies of the *as-fired* LTCC substrates due to the alkaline porosification can be observed in Figure 4.11 and Figure 4.12.

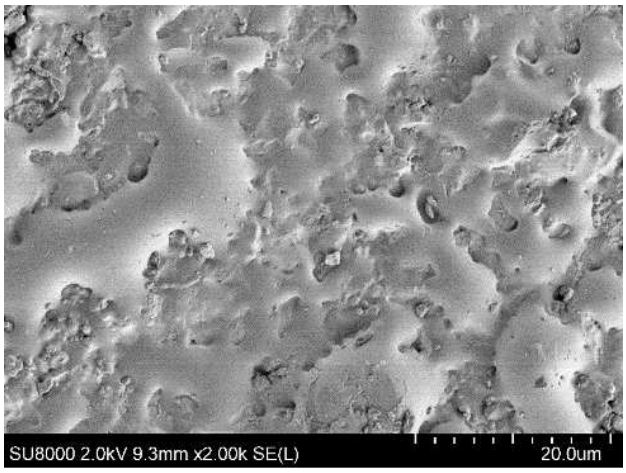

Figure 4.10: SEM micrograph in top view of the Ferro L8 LTCC surface in the *as-fired* state.

Figure 4.11 illustrates the impact of 1 mol L^{-1} NaOH treatment with time on the surface morphology of LTCC substrates where first etch-induced grooves appear on the surface followed by a widening of pore openings with increasing time. This also corresponds to the mass removal results which are shown in Figure 4.16.

SEM micrographs in Figure 4.12 demonstrate the LTCC substrate surface porosified with NaOH etching solutions at two different concentrations of 3 and 6 mol L^{-1} and at bath temperatures of 45, 60, 75, and 90 °C. From these SEM images as well as the gravimetric analysis (see Figure 4.16), it is concluded that an increase in bath temperature leads to the widening of pore openings. Therefore, the surface characteristics are altered resulting in an easier and expedited diffusion of

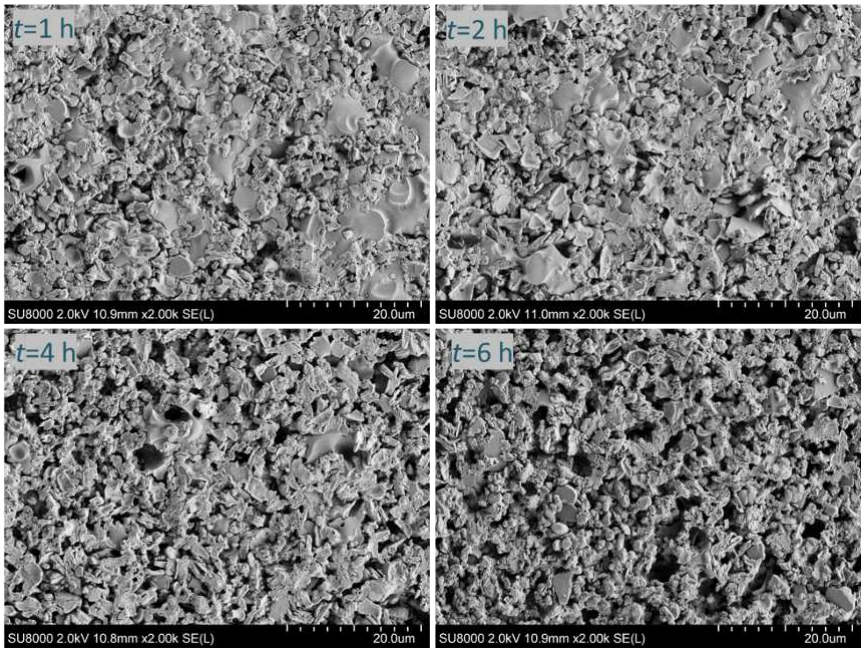

Figure 4.11: SEM micrographs in top view of the Ferro L8 LTCC substrate surface etched with 1 mol L−1 NaOH at 75 °C for different etching times.

etchant into the depth of the LTCC and thus an enhanced mass removal rate.

A comparison of SEM images for samples treated with etchants of different concentrations at a given bath temperature confirms the trend in mass removal observed by gravimetric analyses. However, for the substrate etched in a highly concentrated etchant (*i.e.* 6 mol L^{-1}) at high temperature (*i.e.* 90 °C), the surface appears to be less destroyed. This behaviour which disagrees with the gravimetric results is attributed to the premise that the complete substrate surface gets dissolved. This assumption is supported by an overall reduction in the total thickness of the sample as well as in the final depth of porosification.

In order to get information about the etchant attack on the LTCC surface, thickness measurements were conducted through cross-sectional imaging of the substrates using the SEM and the measured values are shown in Figure 4.13. The thickness decrease is a very important parameter as it gives essential information about the etchant attack to the surface.

The massive mass removal which is observed for 6 mol L^{-1} NaOH solution at high temperatures results in a substrate thickness decrease of approx. 110 μm. This corresponds to a 58% decrease for the initial sample thickness of 190 μm. These results show a very good match if compared to the same gravimetric analysis in Figure 4.16, with the calculated mass removal of approx. 60%. Assuming thickness decrease of 10 μm (*ca.* 5% of initial thickness) as a threshold at which the mechanical and geometrical characteristics of the LTCC are not altered severely, then for example etching at 75 or 90 °C using a 6 mol L^{-1} solution is not recommended. Therefore, a highly concentrated solution in combination with high bath temperatures would be very interesting when

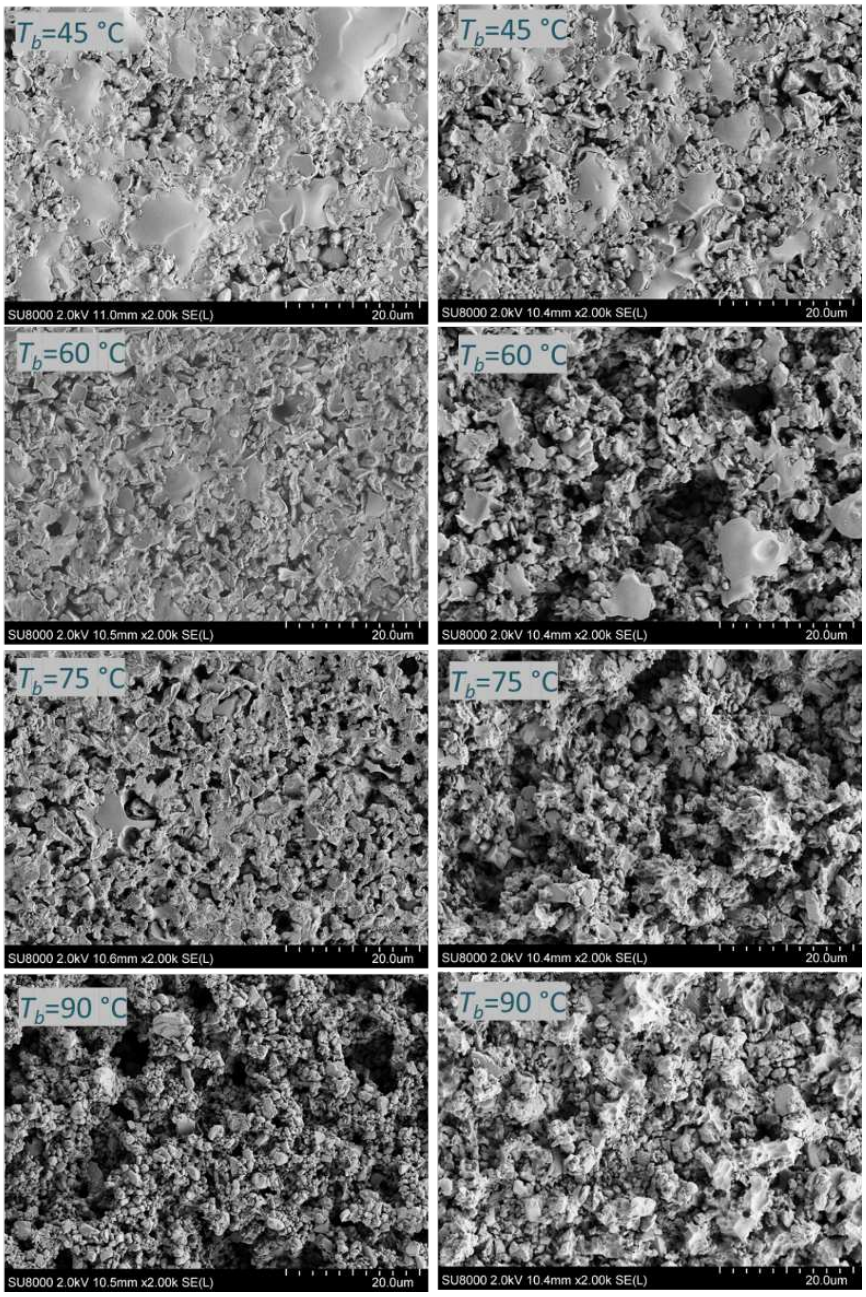

Figure 4.12: SEM micrographs in top view of the Ferro L8 surface etched for 4 h with 3 mol L^{-1} (left column) and 6 mol L^{-1} NaOH (right column) at different bath temperatures.

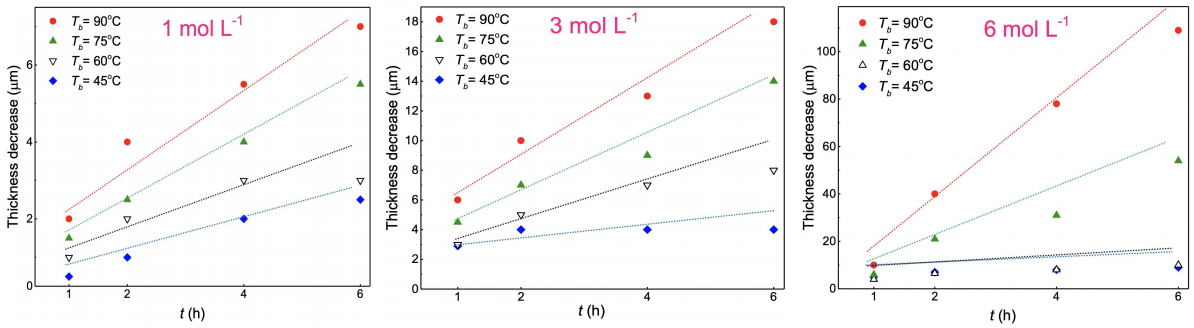

Figure 4.13: Decrease in thickness of Ferro L8 as a function of etching time t due to treatment with NaOH etching solution at various bath temperatures and different concentrations.

any defined thickness modification of the LTCC substrate is targeted in the fired state.

Basically, the surface roughness of the porosified samples is an indicator of its surface quality. Therefore, the root-mean-square roughness (R_q) parameter was measured with a chromatic white light (CWL) sensor of an FRT profilometer and was evaluated using the commercial software Mark III (FRT). The measurement length ln and respective cutoff wavelength λ_c were chosen according to EN ISO 3274 and EN ISO 13565-1 to $l_n = 4$ mm and $\lambda_c = 0.8$ mm, respectively. The measured (R_q) values for the substrates etched with NaOH solutions of different concentrations at different etching times and bath temperatures are shown in Figure 4.14. The reported values are averaged for three different areas randomly selected from the LTCC surface.

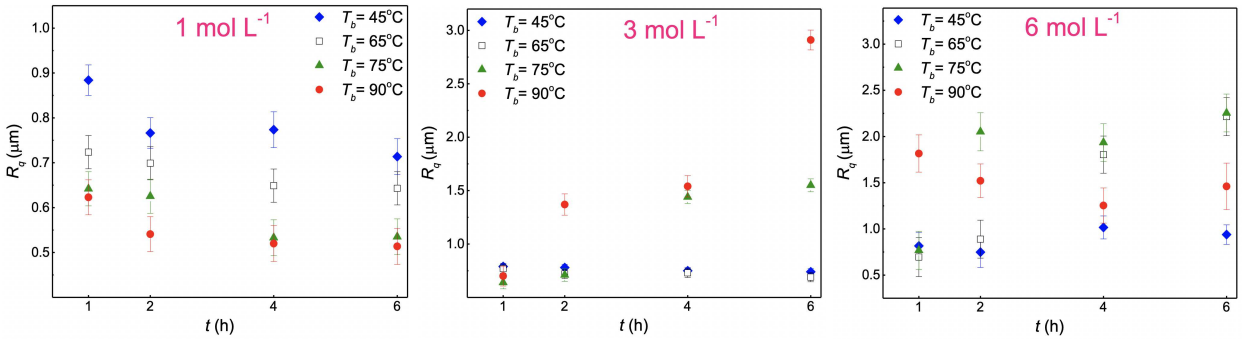

Figure 4.14: Roughness values for Ferro L8 LTCC substrates etched with NaOH at different times and etchant temperatures for varying NaOH concentrations.

As can be seen in Figure 4.14a, applying the 1 mol L^{-1} NaOH etching solution, at all examined bath temperatures and treatment times, generates a decreased surface roughness in comparison to the *as-fired* Ferro L8 substrate (R_q of approx. 0.9 μm). When increasing the bath temperature, a smoother surface results for every parameter set investigated. This can be attributed to the initial removal of bumps and peaks protruding out of the LTCC surface (see Figure 4.10) by low concentrated etching solutions due to increased etching rates of exposed surface features. By increasing the molarity to 3 mol L^{-1}, a different kind of roughness trend is observed (see Figure 4.14b), as the overall roughness is increased compared to the results obtained from the 1 mol L^{-1}

etching solution. For bath temperatures of 75 and 90 °C, the Rq values are clearly increasing with etching time when applying a higher bath temperature, while for 45 and 60 °C, the roughness values fall in the range of 0.6 to 0.9 μm. By increasing the etchant molarity to 6 mol L^{-1} (see Figure 4.14c), the etching mechanism changes from surface porosification to a partial substrate dissolution, which will be discussed in the kinetic analysis section, thus making the quantitative roughness interpretation very different from those gained at lower concentrations. For example, for the 6 mol L^{-1} solution at 90 °C, d_p values decrease at t>120 min (see Figure 4.18) Basically, these results are in good agreement with those of thickness change and porosification depth analyses (see Figure 4.13 and Figure 4.18).

To obtain additional information on the porosity and pore structure of the etched LTCC substrates, mercury intrusion porosimetry measurements were performed. Same as in the acid-treated substrates, to exclude misinterpretation of the space between stacked LTCC substrates in the sample holder as porosity, intrusion data of etched samples were compared to those obtained from dense, *as-fired* LTCC substrates (see Figure 4.15a). Porosimetry measurements were conducted for Ferro L8 substrates etched with 3 mol L^{-1} NaOH solution at 90 °C for 6 h. Based on the histogram shape and intrusion curve, these results show that interstitial space between individual substrates causes significant mercury intrusion at low intrusion pressures, equivalent to pore opening diameters above 10 μm, visible in both etched and *as-fired* samples. However, in *as-fired* substrates, no porosity appears to be present in the lower pore size regime. As a result, a valid interpretation of intrusion data is possible at pore opening sizes below 10 μm, appearing to coincide with the actual range of pore opening sizes as evidenced by cross-sectional SEM images.

For the etched samples, in addition to macroscopic pore throats in the size range between 1 and 5 μm, a smaller pore size fraction with a maximum in the range of around 20–30 nm is identified. The latter may be attributed to pore channels in deeper regions generated during the etching process. In terms of pore shape, a hysteresis observed in the intrusion in comparison to the extrusion curves recorded during the porosimetry measurement indicates the possible presence of ink bottle-type porosity, *i.e.* larger pores with small pore openings. In the cross-sectional SEM image as illustrated in Figure 4.15b, the top surface layer appears to consist of pore openings smaller than the mean pore diameters in sub-surface regions, thus being an additional indication for the presence of this particular pore structure.

Excluding porosity with pore opening diameters >5 μm, and assuming an average total d_p of around 30 μm on both sides of the etched samples (as extracted from SEM images of samples cross-sections), a total porosity of 20% within the etched layer can be estimated.

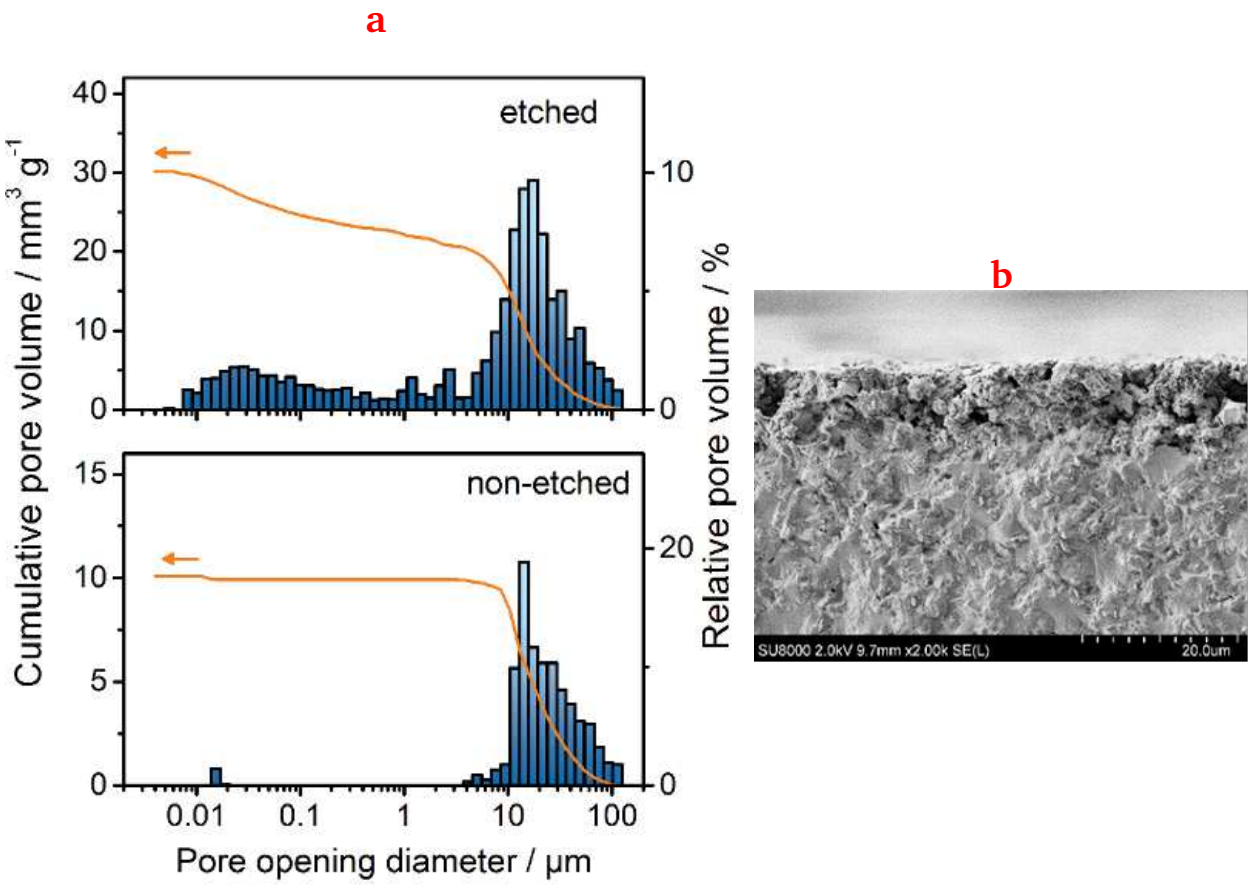

Figure 4.15: a) Pore opening diameter distribution and cumulative pore volume of etched (top) and *as-fired* (bottom) samples, showing the bias caused by interstitial intrusion between specimens at pore opening diameters above 10 μm. **b)** Cross-sectional SEM image of the Ferro L8 LTCC etched with 3 mol L^{-1} NaOH solution at 90 °C for 6 h.

4.2.2. Investigation of the etching mechanism (kinetic analysis)

For each concentration value, mass removal of the LTCC substrates was measured at different temperatures and etching times, and the results are depicted in Figure 4.16. Since the dissolution reaction rate at room temperature is so low even long-time exposure of the samples with the etchant solution does not result in a remarkable etching effect. Also, due to the massive bubble formation close to boiling, when etching at such high temperatures the surface of the LTCC gets strongly attacked resulting in a highly destroyed surface topography. Therefore, 45 °C and 90 °C were chosen as lower and upper-temperature limits for the bath, and by applying temperature steps of 15 °C etching was investigated at bath temperatures of 45, 60, 75, and 90 °C.

The gravimetric analyses indicate that mass removal increases when etching time increases. This is also in agreement with the SEM micrographs which are shown in Figure 4.11. At a given etching time, the mass removals are correlated to conventional parameters influencing dissolution reactions as well as parameters influencing the etchant diffusion into the depth of the LTCC. Thus, on one

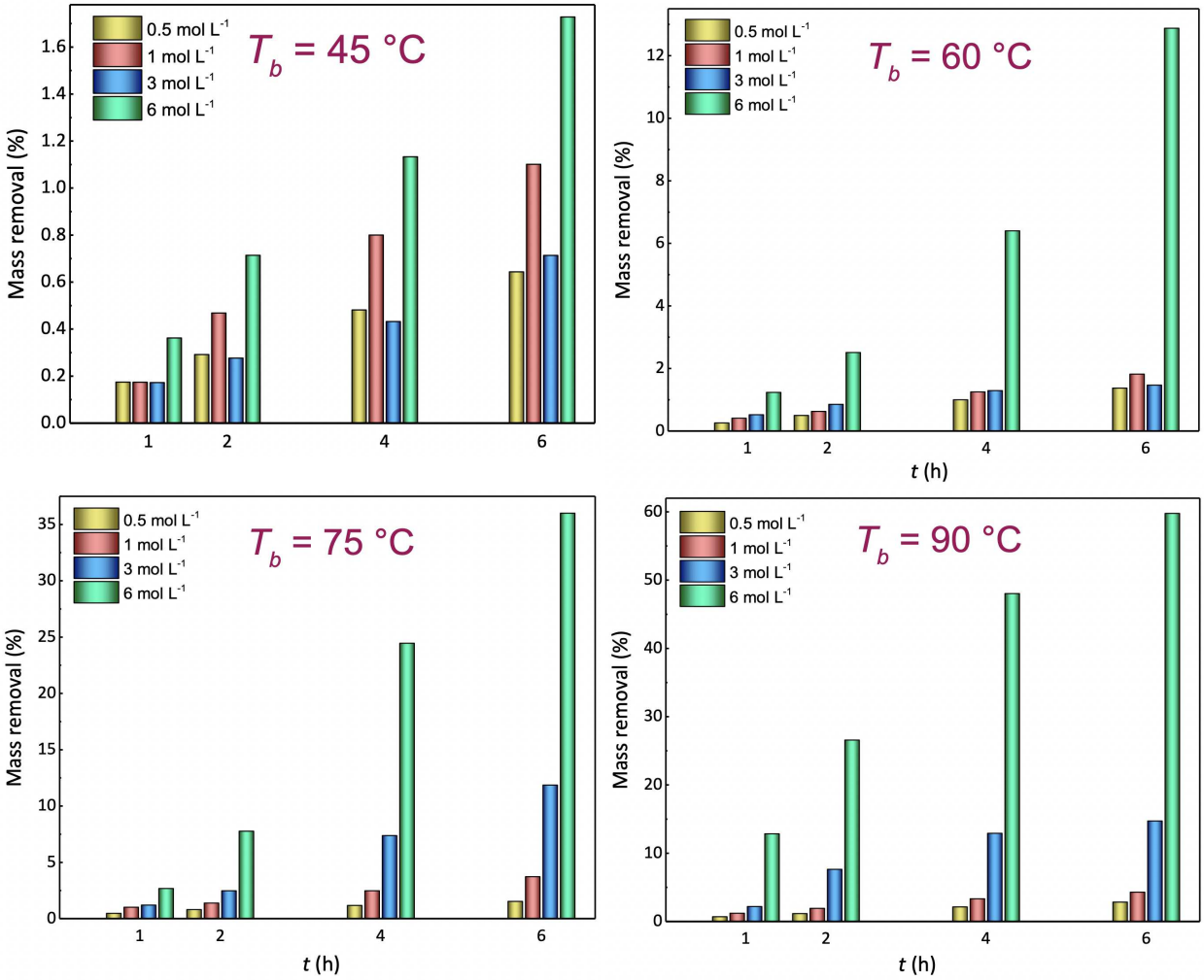

Figure 4.16: Mass removal of Ferro L8 LTCC due to etching with different NaOH concentrations as a function of etching times at varying bath temperatures

hand, like other dissolution reactions, an increase in etchant temperature and/or concentration results in an increased dissolution rate. On the other hand, the diffusion rates depend on the viscosity of the etchant, and the parameters affecting etchant viscosity must be considered. The dynamic viscosity of the NaOH solution depends strongly on temperature and concentration, and similar to phosphoric acid the warmer and less concentrated NaOH solution can penetrate more easily through the pores and openings of the LTCC surface, enabling a faster porosification.

Therefore, mass removal at low bath temperatures of 45 °C is significantly lower compared to those measured at higher temperatures. In all experiments, 6 mol L^{-1} etching solution results in the highest degree of mass removal due to the high concentration of the hydroxide ions in the etchant solution. Nevertheless, for 1 mol L^{-1} solution at 45 °C, the mass removal was found to be larger in comparison to both 0.5 and 3 mol L^{-1} solutions. This increased value of mass

removal for the 1 mol L^{-1} solution compared with the 3 mol L^{-1} solutions, can be attributed to both the lower viscosity of the etching solution. For the higher bath temperatures, however, the viscosity of more concentrated NaOH approaches those for more diluted solutions. Consequently, the impact of viscosity becomes less significant at higher etching temperatures and for temperatures above 60 °C, the content of hydroxide ions becomes the more influential parameter, suggesting a reaction-controlled mechanism for the etching reaction. Additionally, mass removal is significantly enhanced with increasing etchant concentrations [78].

Based on the obtained gravimetric results, shown in Figure 4.16, dissolution rates normalized to the surface area for the etching process with NaOH solutions with different concentrations were calculated, and the results are depicted as a function of bath temperatures in Figure 4.17. To provide a direct comparison with the Ferro L8 substrates etched with the orthophosphoric acid solution, the corresponding etching rates which were shown in the previous chapter, are also inserted.

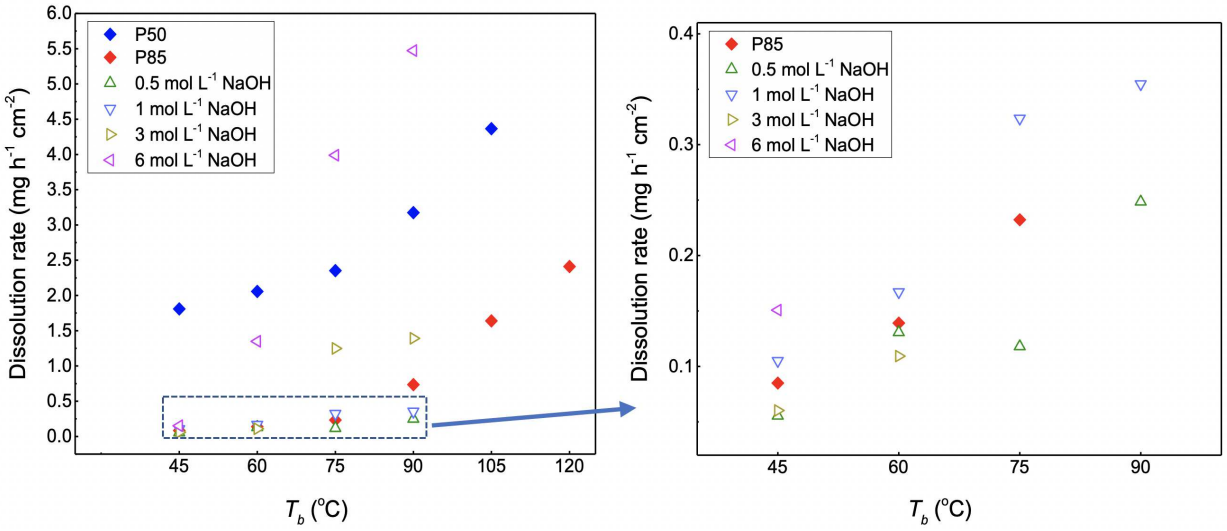

Figure 4.17: Comparison of dissolution rates when etching Ferro L8 with different etchants (left), and magnified plot of the data points in the area indicated by a rectangle (right).

As can be seen in Figure 4.17 the etching rate increases when enhancing bath temperatures. For 6 mol L^{-1} solution, an almost linear increase in dissolution rates is observed and rates are significantly higher than the other examined concentrations. Also, the temperature-dependency of etching rates for more concentrated solutions is more prominent. For instance, once using a 6 mol L^{-1} solution increasing the bath temperature from 45 to 90 °C results in a more significant rise in etching rate (from 0.15 to 5.47 mg h^{-1} cm^{-2}) in comparison to the experiments using 3 mol L^{-1} (from 0.06 to 1.39 mg h^{-1} cm^{-2}). Likewise, for 3 mol L^{-1}, the etching rate is more temperature-dependent compared to the 1 mol L^{-1} (from 0.10 to 0.35 mg h^{-1} cm^{-2} by increasing the bath temperature from 45 to 90 °C). The reaction rate when using 0.5 mol L^{-1} solution of NaOH is substantially lower compared to the higher concentrations of NaOH and does not exceed

0.25 mg h^{-1} cm^{-2} at its highest investigated temperature, *i.e.* 90 °C. Thus, for convenience, this concentration was excluded from further investigations.

A comparison of all etching results shows that the P50 solution results in the highest rate of dissolution (up to 4.37 mg h^{-1} cm^{-2} at 105 °C) except for the 6 mol L^{-1} NaOH at high temperatures. However, as already discussed for the 6 mol L^{-1} NaOH especially at high temperatures instead of pure porosification, a complete material dissolution occurs. This phenomenon will be further discussed in this chapter.

In addition to the gravimetric analyses, porosification depth measurements were conducted through cross-sectional SEM imaging of the substrates and the obtained results are shown in Figure 4.17.

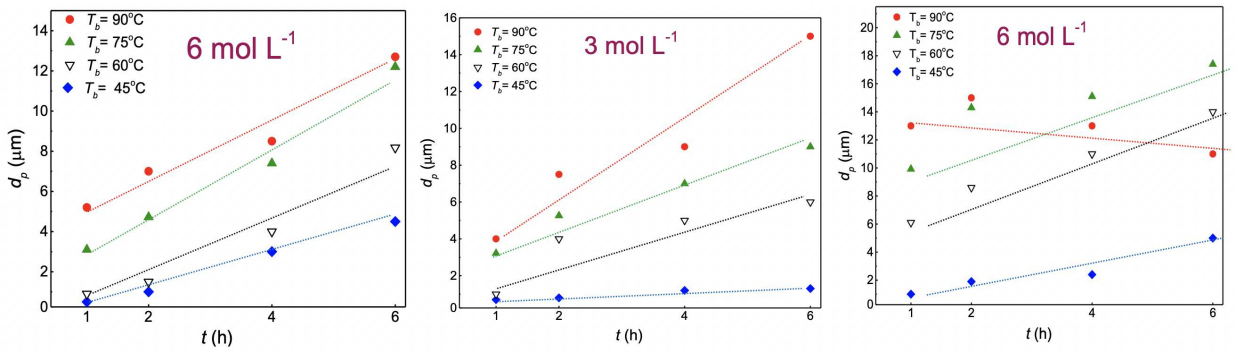

Figure 4.18: Porosification depths, d_p, values of Ferro L8 etched at various bath temperatures and different NaOH concentrations. The inserted straight lines serve as guide to the eyes

As can be observed in these plots, at a given bath temperature d_p values increases when increasing the etching treatment time, except for the 6 mol L^{-1} solution at a high temperature of 90 °C, while not reaching a saturation level. This linear behaviour hints towards a reaction-controlled mechanism for the etching process. Also, a similar behaviour was observed when increasing the bath temperature while keeping the etching time fixed. For the etching process with the 6 mol L^{-1} solution at 90 °C (see Figure 4.19), d_p and thickness decrease analyses reveal that in the initial stages of the etching process, surface porosification can be considered as the dominating mechanism. For 120 min and above this temperature, the dominating etching mechanism changes to a partial substrate dissolution, *i.e.* complete material dissolution instead of porosification.

This behaviour results in surface layers removal, which can be seen in the corresponding thickness diagrams too. Consequently, for this concentration, long-term etching at enhanced temperature levels above 75 °C results in an increased “substrate dissolution” tendency. Moreover, when plotting the sum of both etching regime, *i.e.* d_p and the decrease in LTCC substrate thickness (shown by d_p' parameter) versus the etching time (see Figure 4.20), a linear behaviour of this parameter is in good approximation observed for all etching solutions and all bath temperature ranges.

Coupled with thickness decrease measurements, d_p analyses confirm the assumption about the partial substrate dissolution for other extreme etching conditions at enhanced temperatures and

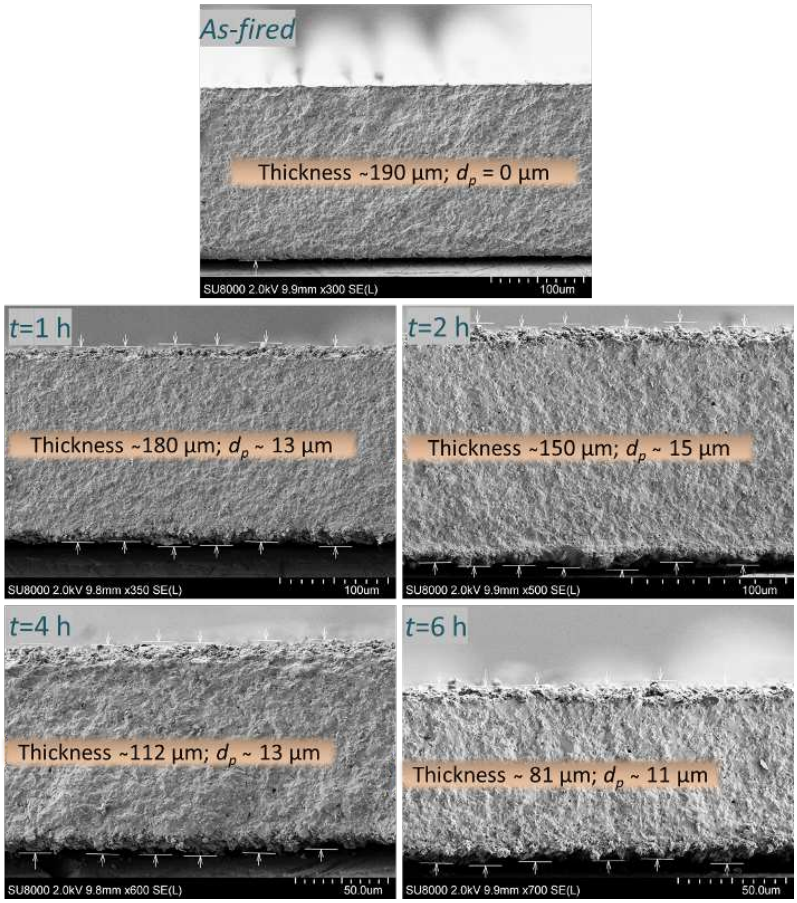

Figure 4.19: Cross-sectional SEM image of the Ferro L8 LTCC in the *as-fired* state, and etched with 6 mol L^{-1} NaOH solution at 90 °C for different etching times.

concentrations. For instance, in the case of 6 mol L^{-1} at 75 and 90 °C and etching times of more than 120 min, mass removal, and thickness decrease values are larger, but the d_p values are lower than at more moderate etching conditions. This behaviour is a good verification for the substrate dissolution during the etching process.

Plots of d_p versus the corresponding substrate thickness decrease values which are shown in Figure 4.21 illustrate an interesting correlation. At a lower concentration of 1 mol L^{-1}, an almost linear relation between d_p and thickness decrease values is observed independent of bath temperature. By increasing the concentration to 3 mol L^{-1}, the linear trend is still visible except for the samples treated at 75 and 90 °C. Finally, for 6 mol L^{-1} etchant solution, the linear trend is observed only at the very beginning up to approx. 14 μm thickness removal. Above, d_p is constrained by thickness decrease due to the substrate dissolution above average. For samples etched at 90 °C even a reduction in d_p is observed after 120 min of etching. These deviations from the linear trend indicate a change of the etching mechanism from predominantly porosification to the substrate dissolution which is not favourable for the intended purpose because the maximum d_p has been already exceeded and after that mainly complete dissolution takes place.

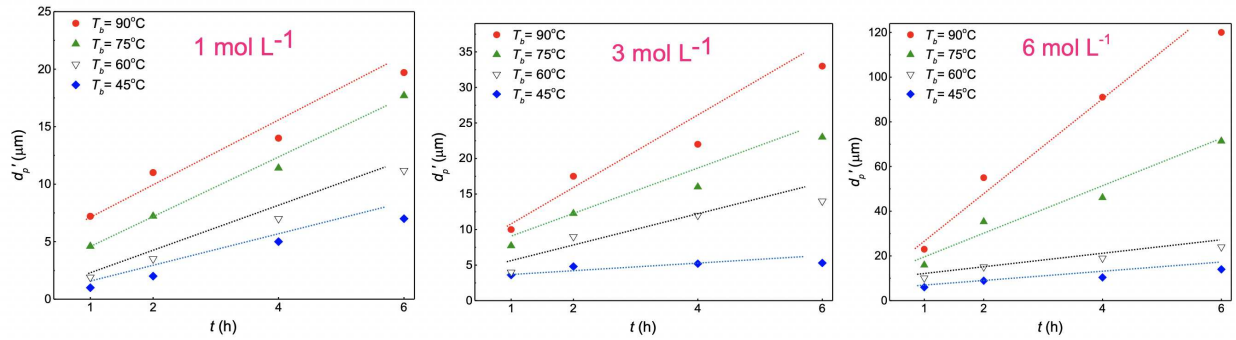

Figure 4.20: Porosification and partial substrate dissolution, represented by d_p' versus time for Ferro L8 etched with various bath temperatures and different NaOH concentrations. The inserted straight lines serve as guide to the eyes

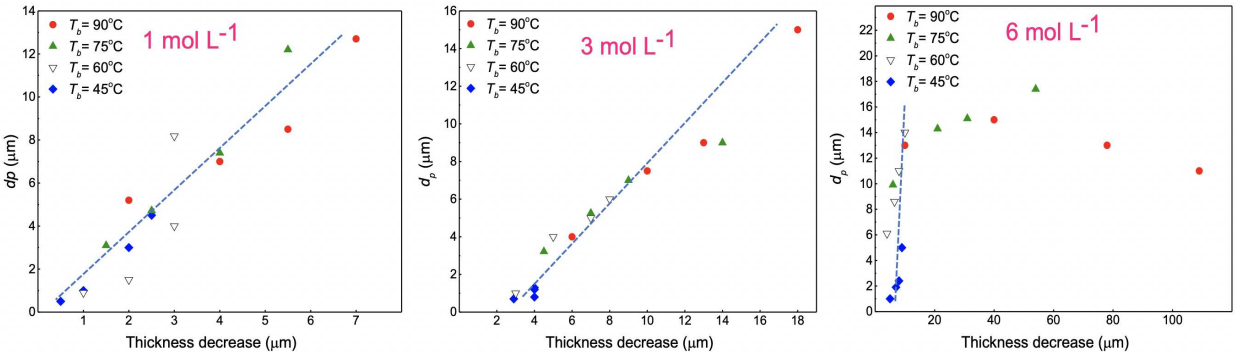

Figure 4.21: Porosification depths, d_p, of the etchant versus the decrease in thickness as a function of etching temperature for various NaOH concentrations. Inserted lines serve as guides to the eye.

Figure 4.22 illustrates the two mechanisms of surface porosification and partial substrate dissolution which are observed under defined etching conditions. These schematics illustrate the change in porosification depth and roughness parameters due to the etching at different conditions.

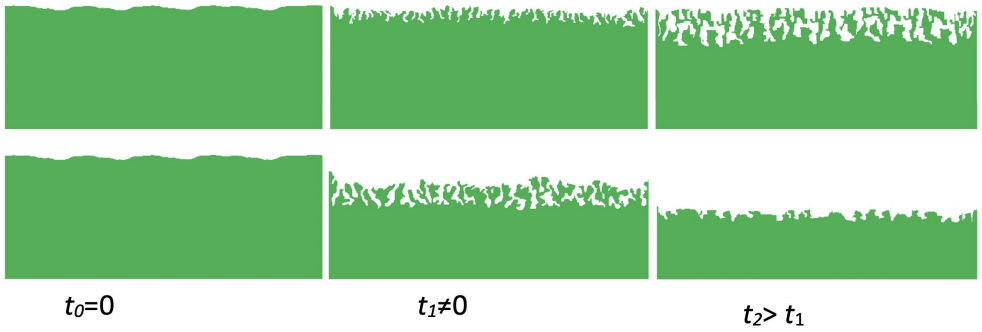

Figure 4.22: Schematic representation for pure surface porosification at different etching times (upper row) and porosification with partial substrate dissolution at different etching times (lower row).

Additionally, to verify the reaction-controlled mechanism of the etching process, overall activation energies were calculated at fixed etching times in Arrhenius-type diagrams from the corresponding slopes. As discussed in previous sections, in a wet chemical etching process when a

diffusion-controlled reaction regime dominates, activation energies are about 0.2 eV and higher activation energies specify reaction-controlled dissolution mechanisms. The d_p results for different etchant concentrations were used for plotting Arrhenius-type graphs at given etching times. Typical Arrhenius diagrams with the linear fitting results for the NaOH etching solution with different concentrations of 1, 3, and 6 mol L^{-1} etching solution are shown in Figure 4.23.

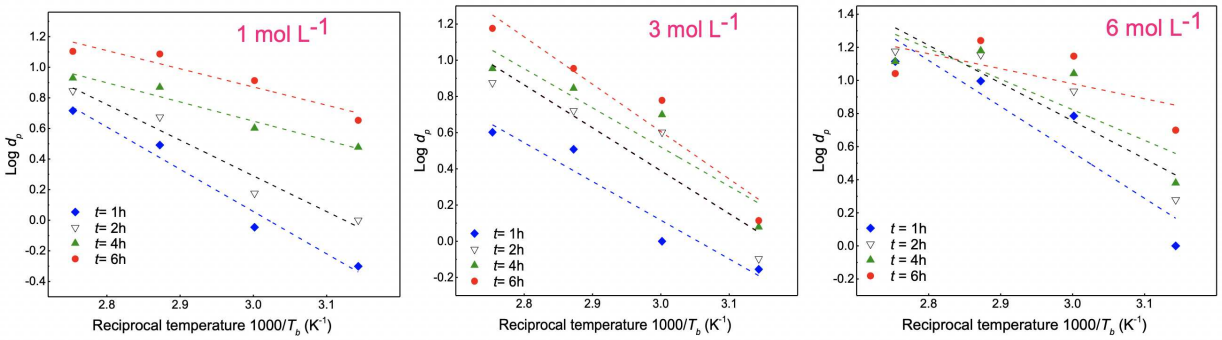

Figure 4.23: Logarithm of d_p versus reciprocal bath temperature when etching Ferro L8 with NaOH solutions of various concentrations for different treatment times.

As can be seen in this figure and also the corresponding linear regression results in Table 4.2, best linear fitting is obtained when using 1 mol L^{-1} NaOH as etching solution where the slopes of the linearly fitted lines, *i.e.*, the corresponding activation energies, decline with increasing etching time. The results of the linear regression for all three solutions are shown in Table 4.2. For the 3 and 6 mol L^{-1} solution, however, a deviation from linear fitting is observed. This is due to the combination of porosification and partial LTCC dissolution mechanism for these etching solutions which makes data evaluation more challenging. Nonetheless, the calculated activation energies for all investigated concentrations and etching times stay far above the 0.2 eV limit which confirms the reaction-controlled regime.

Table 4.2: Activation energies from the Arrhenius diagrams of Figure 4.23.

Etching time h	**1**	**2**	**4**	**6**	
1 mol L^{-1} NaOH	E_a *eV*	2.76±0.33	2.33±0.36	1.25±0.2	1.19±0.26
	Regression coefficient R^2	0.9725	0.9546	0.9533	0.9099
3 mol L^{-1} NaOH	E_a *eV*	2.14±0.42	2.37±0.68	2.17±0.61	2.62±0.55
	Regression coefficient R^2	0.9287	0.8574	0.8635	0.9194
6 mol L^{-1} NaOH	E_a *eV*	2.78±0.78	2.28±0.72	1.85±0.85	0.91±0.76
	Regression coefficient R^2	0.8637	0.8338	0.7024	0.4141

To have a better interpretation of Arrhenius type plots, in addition to the pure porosification which was considered in calculations above, here the partial dissolution of LTCC substrates was also taken into account. Therefore, the Arrhenius-type plots were plotted considering d_p' instead of d_p. The corresponding results are plotted in Figure 4.24 and the corresponding linear regression results are shown in Table 4.3.

Comparison of linear regression results for the Arrhenius-type plots when taking partial dissolution

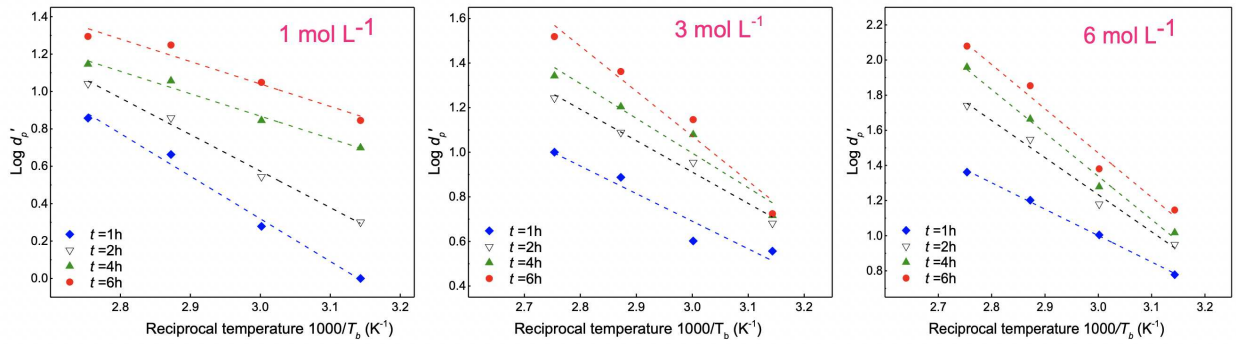

Figure 4.24: Logarithm of $d_p{}'$ (Porosification + partial dissolution of the substrate) versus reciprocal bath temperature when etching Ferro L8 with NaOH solutions of various concentrations for different treatment times.

of LTCC into account with the ones excluding this parameter, *i.e.*, $d_p{}'$ instead of d_p, indicates a significantly better fitting for the former case with respect to the regression coefficients in Table 4.2 and Table 4.3. For example, for the 6 mol L^{-1} NaOH solution when using d_p the regression coefficients are in the range of 0.8637 and 0.4141, while for the plots obtained using $d_p{}'$, the regression coefficients for the linear fitting are in the range of 0.9986 and 0.9769. Similar to the plots from d_p, the fitting lines and therefore the corresponding activation energies for the ones from $d_p{}'$ also fall far above 0.2 eV, although their time-dependent behaviour is essentially different. Also, similar to the porosification of Ferro L8 with an acidic solution (P50) which was shown in the previous chapter, and probably all successful wet chemical etching tests which are already reported in the literature, for 1 mol L^{-1} NaOH etching solution the activation energies decrease with the etching time up to 4 h. This is due to the more difficult penetration of the etchant into the porosified LTCC body as the pores become deeper.

Table 4.3: Activation energies from the Arrhenius diagrams of Figure 4.24.

Etching time h	**1**	**2**	**4**	**6**	
1 mol L^{-1} NaOH	E_a *eV*	2.28±0.17	1.95±0.11	1.20±0.11	1.20±0.17
	Regression coefficient R^2	0.9894	0.9933	0.9836	0.9580
3 mol L^{-1} NaOH	E_a *eV*	1.24±0.25	1.41±0.13	1.56±0.26	2.02±0.28
	Regression coefficient R^2	0.9226	0.9818	0.9443	0.9634
6 mol L^{-1} NaOH	E_a *eV*	1.50±0.04	2.11±0.17	2.8475±0.16	2.9521±0.27
	Regression coefficient R^2	0.9986	0.9866	0.9916	0.9769

On the other hand, for 3 mol L^{-1} NaOH the changes in the slopes up to 4 h are less significant (13.7% increase in the E_a values from 1 to 2 h and 10.6% increase from 2 to 4 h) and after that, they become more remarkable (29.5% increase in the E_a values from 4 to 6 h). Also, for 6 mol L^{-1} solution, the slopes of the fitting lines are constantly increasing with increasing the etching time (from 1.50±0.04 for 1 h up to 2.52±0.27 for 6 h). This behaviour can be interpreted with respect to the two mechanisms of porosification and partial substrate dissolution, which were proposed for the d_p and thickness decrease measurements. In Fact, both mechanisms occur simultaneously for etching treatment with all three examined solutions, but for 1 mol L^{-1}, the porosification

mechanism is dominant. When using more concentrated solutions, *i.e.*, 3 and 6 mol L^{-1}, especially at higher temperatures and longer etching times, the partial dissolution of the substrate becomes more dominant. Therefore, the d_p value does not increase significantly, or even decreases, *e.g.*, for 6 mol L^{-1} at 90 °C and after 2 h. Therefore, there is no increase resistance against etchant penetration into the pores, and thus no decrease in activation energy is observed.

4.2.3. Modelling of etching parameters by DOE

In order to determine suitable etching conditions, a full study on the porosification behaviour of Ferro L8 using aqueous NaOH was carried out by employing Design-Expert Software which has been described in detail in the experimental section and the obtained results will be discussed here. Based on the analysis of variance (ANOVA) approach experimental results can be fitted into a nonlinear polynomial model so that key parameters of the LTCC-related porosification process can be modelled by technology-related parameters such as bath temperature (T_b), treatment time (t) and etchant concentration (C) as shown in Equation 4.3 - Equation 4.5. Basically, predicted values were found to be in good agreement with experimental data.

$$\begin{aligned}\text{Mass removal} = {} & 3.52 + 7.61T_b + 3.8t + 4.02C + 5.43T_bt + 9.2T_bC + 5.54tC + 3.43T_b^2 \\ & -0.79t^2 + 3.83C^2 + 5.87T_btC + 0.22T_b^2t + 4.02T_b^2C - 1.33T_bt^2 + 3.78T_bC^2 \\ & -0.79t^2C + 2.64tC^2 - 0.82T_b^3 - 0.34t^3 + 1.96C^3\end{aligned} \tag{4.3}$$

$$\begin{aligned}\text{Porosification depth} = {} & 6.88 + 5.12T_b + 1.82t + 4.09C + 0.40T_bt + 0.92T_bC - 0.77tC \\ & -2.01T_b^2 - 0.25t^2 + 2.18C^2 - 1.31T_btC - 1.64T_b^2t - 2.53T_b^2C - 0.17T_bt^2 \\ & +0.18T_bC^2 - 0.73t^2C + 0.21tC^2 - 0.96T_b^3 + 1.71t^3\end{aligned} \tag{4.4}$$

$$\begin{aligned}\text{Thickness change} = {} & 7.64 + 12.13T_b + 0.89t + 7.71C + 10.47T_bt + 13.66T_bC + 8.64tC \\ & +7.24T_b^2 - 0.93t^2 + 3.95C^2 + 11.98T_btC + 4.65T_b^2t + 9.19T_b^2C - 0.85T_bt^2 \\ & +6.52T_bC^2 - 1.20t^2C + 4.10tC^2 - 3.3T_b^3 + 3t^3\end{aligned} \tag{4.5}$$

The predicted mass removal according to the fitted data by the Design Expert software is shown in Figure 4.25. The contour lines under the model show the slope changes across the model surface. The predicted planes for mass removal indicate its intensification by a simultaneous increase of the etching time and bath temperature. The predicted planes of porosification depth and the thickness decrease are also shown in Figure 4.25. A quadratic model for the porosification depth and a two-factor interaction (2FI) for the thickness is recommended by the software. The

porosification depth planes show a continuous increase by the increase of etching time and bath temperature for an etchant concentration of 1 mol L^{-1} while for the 3 and 6 mol L^{-1} a maximum is observed. These findings indicate that in order to reach a maximum porosification depth, 1 mol L^{-1} is not strong enough as etchant concentration within the considered data frame, while for the 3 and 6 mol L^{-1} concentrations a maximum is achievable. The obtained planes for mass removal and porosification depth as well as thickness decrease can certainly be applied for the optimization of etching parameters for intended requests, desiring defined values of thickness decrease or porosification depth.

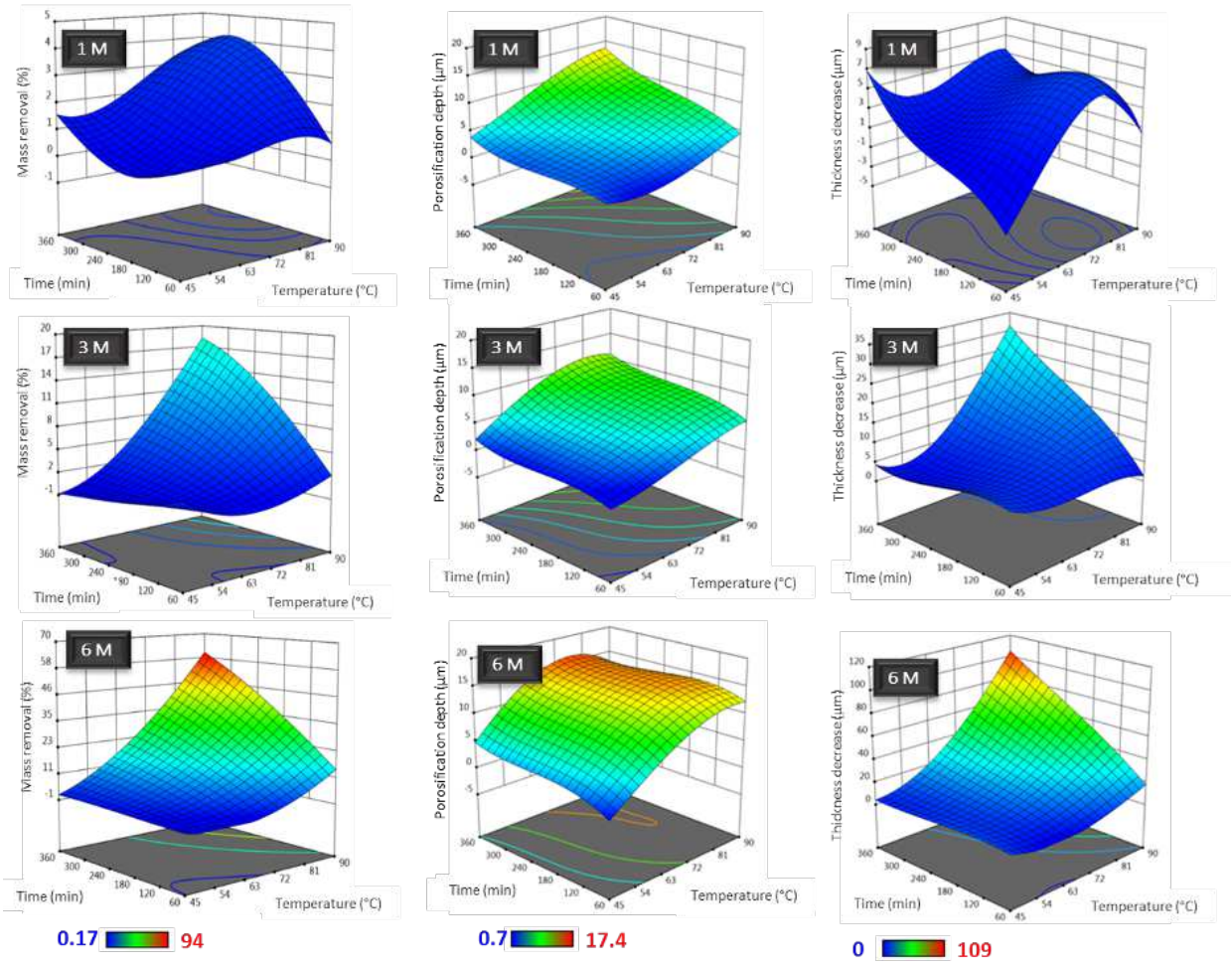

Figure 4.25: Predicted response for mass removal, porosification depth, and decrease in thickness of Ferro L8 LTCC substrates due to the etching with NaOH solutions according to the polynomial model.

Chapter 5.

IMPACT OF FIRING TEMPERATURE ON THE PHASE COMPOSITION AND POROSIFICATION OF LTCC

Although the tapes studied in this thesis were provided by a company, thus garuanteenig a high reproducibility in tape properties, investigations of the sintering behaviour of such material systems is of great importance as it strongly affects the final properties of the LTCC. These investigations can provide not only useful information regarding the dimensional control and mechanical properties of the sintered tape, but also regarding surface properties, porosification, and chemical composition. The latter is quite important for the wet chemical etching process. Therefore, in this part, the phase development and changes in the crystalline composition of GC LTCC during the sintering process are studied by employing *in-situ* XRD analysis. Afterwards, the microstructures of the tapes fired with some representative firing profiles were investigated.

5.1. *In-situ* high-temperature XRD measurements

For the *in-situ* XRD studies, the GC LTCC green tape was heated using a temperature program which is shown in Figure 5.1. This temperature profile provides information regarding the phase development at different peak temperatures up to 1000 °C. Therefore, it is useful for all investigated sintering profiles which are used for GC LTCC. After increasing the temperature at each step, it was kept constant for 24 minutes and meanwhile the corresponding diffractogram was recorded. All measurements were performed in air atmosphere.

The corresponding X-ray diffractograms are represented in Figure 5.2. At room temperature, the alumina filler is the only crystalline phase which is observed. From room temperature up to

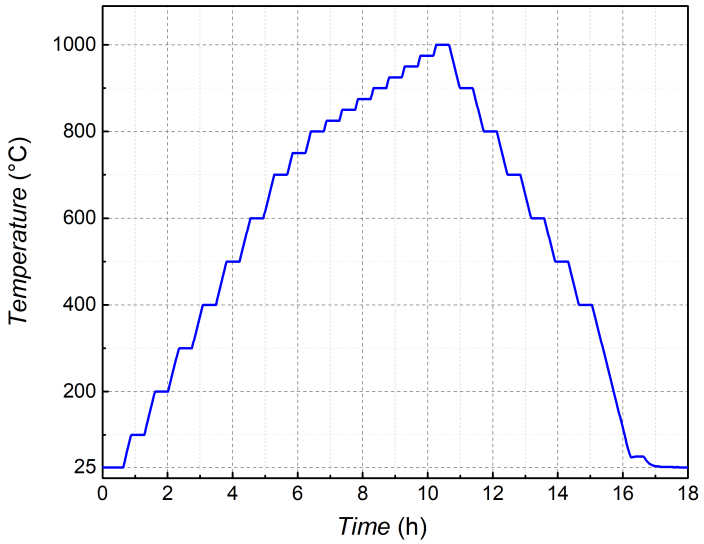

Figure 5.1: Temperature program for XRD measurements while in-situ sintering the GC LTCC substrate.

825 °C no changes in the crystalline composition was measured (see Figure 5.1a). By increasing temperature, no significant changes in the diffractograms appear up to 850 °C, where a new peak appears at around 31. This peak could be attributed to the formation of a calcium silicate phase (wollastonite) [12, 31]. In contrast to anorthite, wollastonite crystals do not preferentially grow in the neighbourhood of alumina grains, but in glass/pore interface [31]. By further increasing the temperature to above 875 °C other peaks start to appear which correspond to the crystallization of anorthite phase from the glass phase.

A further temperature increase up to 925 °C results in the formation of additional anorthite phase while simultaneously the wollastonite fraction declines. Beyond 925 °C, except for the slight increase in intensity of the newly formed anorthite peaks together with the decrease in the intensity of the corundum phase, no perceptible change in the diffractograms can be observed. Furthermore, above 950 °C, the wollastonite almost disappears. From these observations it can be concluded that the amount of formed anorthite phase increases by the dissolution of the dispersed alumina particles as well as of the formed wollastonite phase (see Figure 5.2b). The simultaneous formation of anorthite and dissolution of alumina was already confirmed in a similar LTCC system by Müller *et al.* [31]. Based on this study, anorthite crystallization occurs as a result of two solid phase-boundary reactions involving (*i*) alumina dissolution and a reduction of the amount of residual glass phase, and (*ii*) alumina and wollastonite dissolution, without a further substantial reduction of the residual glass mass fraction. These two steps can be demonstrated by the following reactions:

$$C + G_1 \rightarrow A + G_2 \tag{5.1}$$

where C is alumina, A anorthite, and G_1 and G_2 the residual glass after wollastonite and anorthite

crystallization, respectively. Then, by a further increase of temperature to above 950 °C, the second step of anorthite crystallization occurs, where it grows at the expense of alumina and wollastonite according to:

$$C + W + G_2 \rightarrow A + G_3 \tag{5.2}$$

where G_3 is the resulting residual glass.

Based on these results temperatures between 875 and 925 °C are recommended for the firing of GC LTCC. This is also in a good agreement with the values given in literature [169]. The relatively high maximum firing temperature for GC LTCC, which is for example about 40 °C higher than for 951 LTCC from Dupont, can be explained by the low amount of viscosity lowering glass modifier oxides in GC LTCC [79].

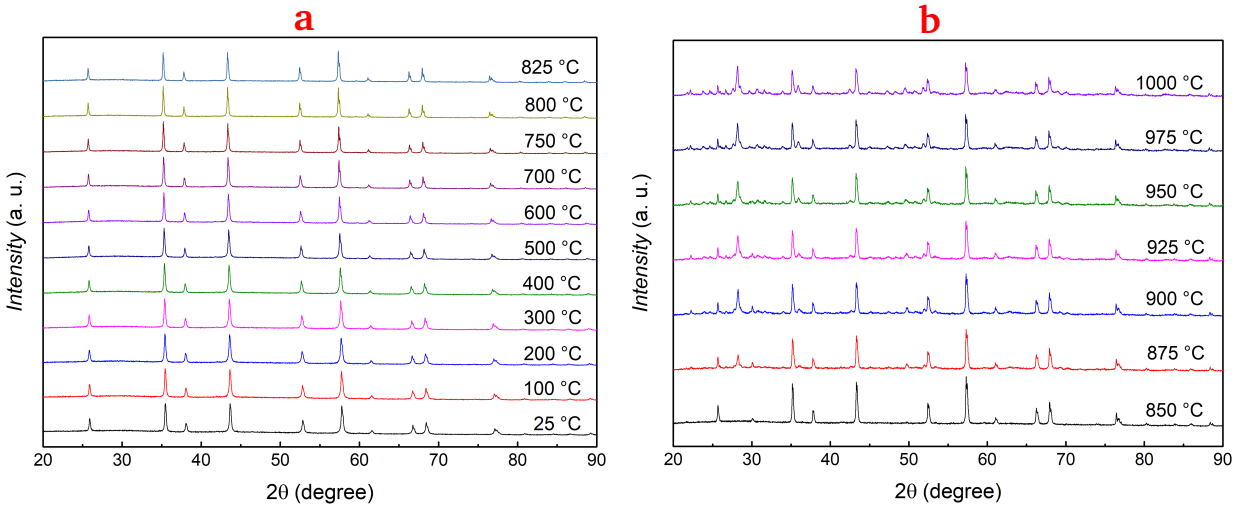

Figure 5.2: *In situ* X-ray diffractograms of a GC LTCC subjected to different temperatures between **a)** 25 and 825 °C, and **b)** 850 and 1000 °C. The intensity levels are shifted for comparison reasons.

5.2. Morphological and chemical characterization

SEM micrographs of the GC LTCC in the unfired state ("green tape") as well *as-fired* at different peak temperatures are shown in Figure 5.3. The results demonstrate that for GC790 no effective sintering is observable, and the surface morphology is very similar to that of the unfired tape. Therefore, GC LTCC with this low sintering temperature was excluded from further investigations. By increasing the firing peak temperature to 840 °C due to the softening and diffusion of the glassy phase, the LTCC gets densified and the discrete grains get connected. However, a lot of large open pores and gaps between individual grains are still observed on the surface. The onset of densification occurs with softening of the glass phase and continues with its viscous flow, what

means that the sintering kinetics are predominantly controlled by the viscosity of the glass phase. However, in general, densification mechanisms during the sintering process of LTCC are very complex and have been the subject of several studies[12].

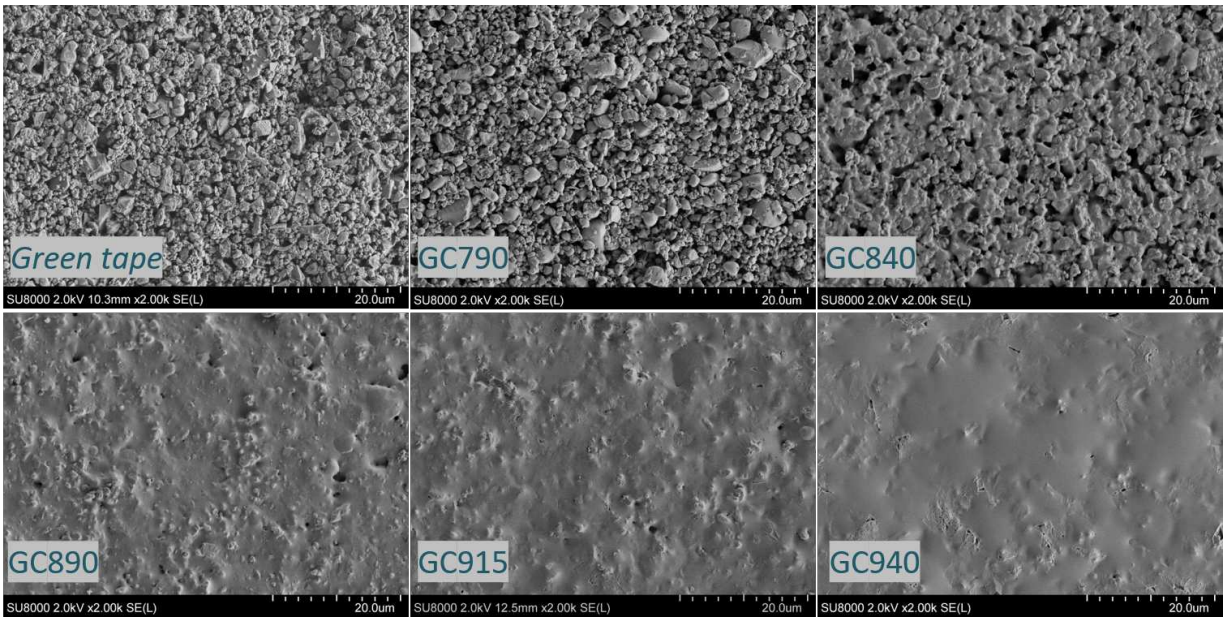

Figure 5.3: SEM micrographs of the GC LTCC green tapes, as well as substrates sintered at different peak temperatures.

By increasing the firing peak temperature to 890 °, sintering process occurs more efficiently, and a densified composite of glass matrix and ceramic filler is produced. However, due to the grains protruded out of the surface, a rough topography with sharp edges is realized. When further increasing the firing peak temperature to 915 ° and then 940 ° the LTCC sample becomes more densified and its surface becomes much smoother what is beneficial for subsequent metallization. The corresponding X-ray diffractograms are also represented in 5.4. From this diffractograms, it is concluded that a sintering temperature of 840 °C is not sufficiently high for the formation of anorthite phase and only a very small peak at around 31° which is attributed to wollastonite crystallization was observed. On the other hand, for the GC890 and above, the glass crystallizes partially to the anorthite phase. By further increasing the firing temperature to 915 ° the intensity of anorthite peaks is increasing which confirms the growth of anorthite crystals. However, the intensities of the peaks related to the alumina grains remain almost unaltered meaning that the dissolution of these grains at this firing temperature has not been started yet or is too minor to be detected. These results show a very good agreement with the high-temperature XRD results (*in-situ* firing of an LTCC substrate) as illustrated in Figure 5.2.

The samples were also subjected to TEM analyses and the results are shown in Figure 5.5. This figure represents the overview images of an unfired GC LTCC in the dark field and bright field modes. The sample is mainly composed of alumina grains and glass. The specimen looks as if covered by a transparent and adhesive material. This is due to the organic materials (binder,

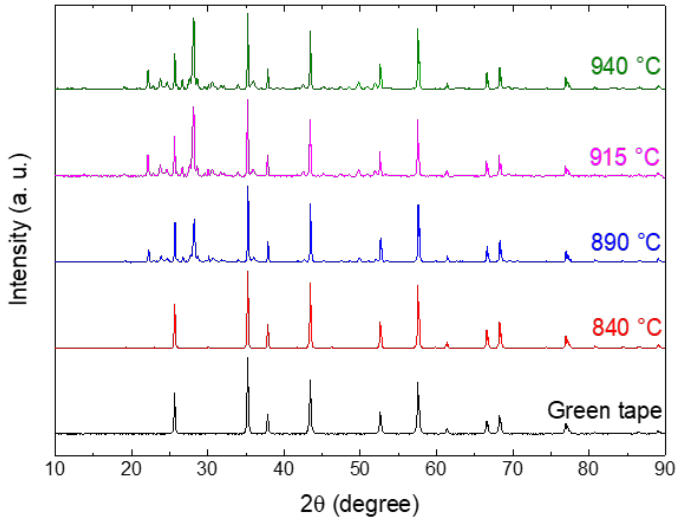

Figure 5.4: X-ray diffractograms of GC LTCC green tapes fired with profiles of different peak temperatures. The intensity levels are shifted for comparison reasons.

plasticizer, *etc.*) which are typically applied in green tapes.

EDX analysis reveals that the sample in the indicated area at the dark field image is mainly composed of Al, Si, O, Ca, and B with weight percentages of approximately 21, 13.5, 46.8, 8.3, and 9.2 wt%, respectively. Considering the EDX mapping results for the selected area, three representative images were taken for the SAED analysis, where amorphous glass phase and crystalline corundum grains were identified in areas 1 and 2, respectively. The area 3 which is rich in boron, also appears to be crystalline. No clear reason was found for this finding as boron trioxide usually is present in the amorphous phase and also in the XRD pattern for the green tape (see Figure 5.2) no crystalline phase besides corundum was found. After annealing, however, boron trioxide can appear in crystalline form. Thus, this very small area which is found here could be attributed to the boron trioxide dissolved in the glass during glass fabrication process.

As already mentioned, by increasing the peak temperature, LTCC substrates become more densified and a smoother surface can be realized. This is due to the diffusion of the glass to the surface of LTCC which results in filling up the surface porosities and also covering the protruded grains. This is very important for the realization of a very smooth surface and also the targeted porosification because of the penetration of the etching solution into a glass-covered surface expected to be different from that of a standard LTCC. Therefore, studying the chemistry of LTCC is of great importance. Thus, samples were analysed by Raman spectroscopy and XPS.

The Raman measurements revealed significant changes in the vibration mode for the fired samples (GC 790-940) in comparison with unfired sample (GC green tape), particularly, in the area of Raman shifts higher than 800 cm^{-1} (see Figure 5.6). The vibrational structure in the region up to 800 cm^{-1} can be attributed to the presence of corundum in the glass-ceramic mixture. Peak

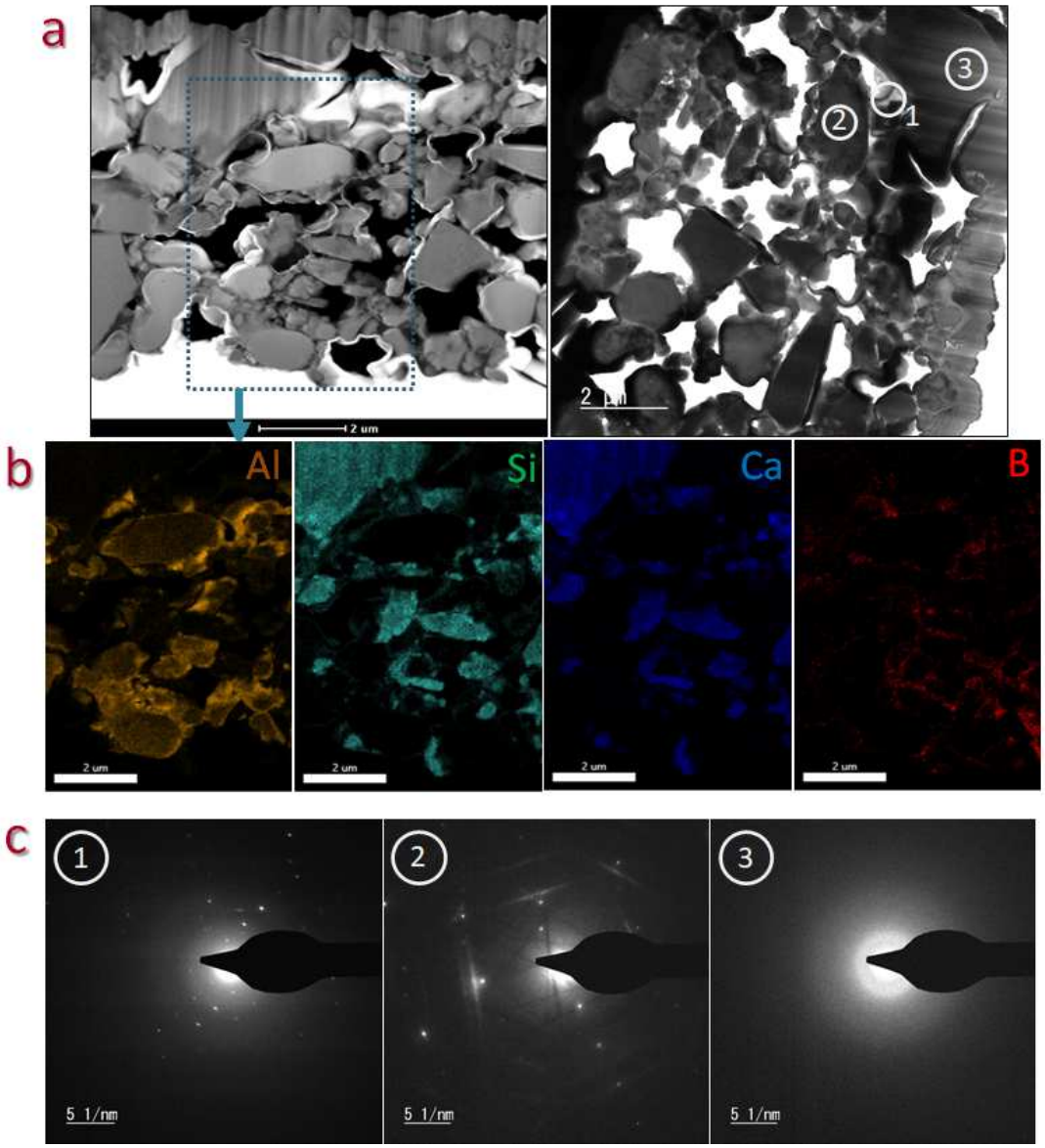

Figure 5.5: a) Overview of the GC LTCC green tape in the dark field (top left), and bright field (top right) modes. The bright-field image is clockwise rotated for 90°. **b)** EDX mapping results for the indicated area (O is excluded), **c)** SAED analyses of three locations labelled in the bright field image.

assignment was performed using the RRUFF database, however, the interpretation of some individual peaks (like $CaO.(B_2O_3)$) was complicated and several peaks could not be indexed (see Figure 5.7). Especially, for the green tape due to the presence of organic, *e.g.* binder and plasticizer the spectrum is more complicated. However, during the firing process, these materials are completely burned out and the remaining peaks can be attributed to the inorganic constituents of the GC LTCC, which are produced from the firing of calcium aluminosilicate and the alumina filler.

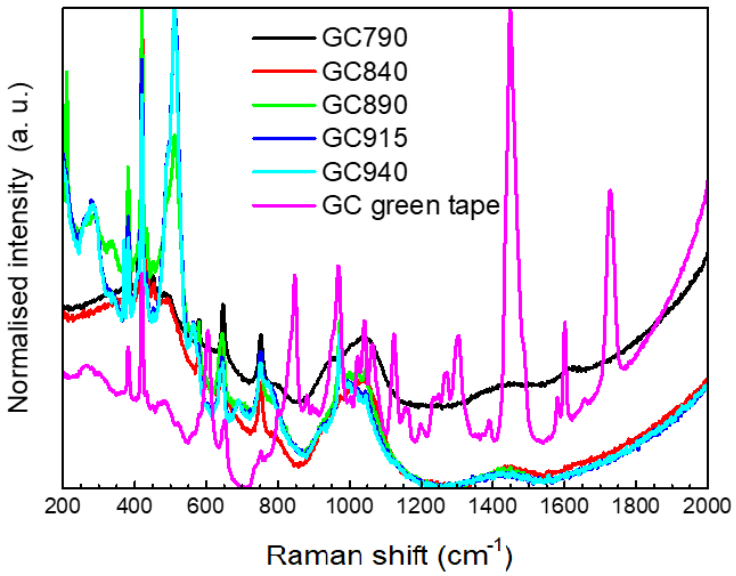

Figure 5.6: Normalised Raman scattering spectra for GC green tape, and GC790 to GC940 samples.

The comparison of Raman spectra for the fired samples showed that the beginning of the total vibration structure transformation started at about 890 °C, as can be seen in Figure 5.8. For the GC890 sample anorthite features are more pronounced in the spectrum, whereas for the GC790 and GC840 spectra, the corundum vibration peaks are predominantly present. By increasing the firing temperature especially for the GC940, the intensity of some corundum peaks reduces. This could be a result of the phase transition of the alumina phase or different concentration of corundum and anorthite in the investigated volume. Considering the temperature range, in which the specimens were prepared, the theta or gamma phase of alumina are expected, but they are not observable or are low intensive in the this spectral range [248, 249]. Nevertheless, these phases are metastable and their impact on Raman spectra should be measurable for temperatures lower than 890 °C. Anorthite has also several phases (polymorphism), as reported in [250], but Raman spectra of particular phases do not differ significantly. Thus, the influence of the phase transformation should be excluded.

Furthermore, the surface chemical composition of the samples was analysed by XPS. In Table 5.1, the relative atomic concentrations of the chemical elements are summarized. The significant reduction of the carbon concentration on the fired sample surface indicates the cleaning from hydrocarbon species due to the burning out of the organic components of the LTCC. Thus, for

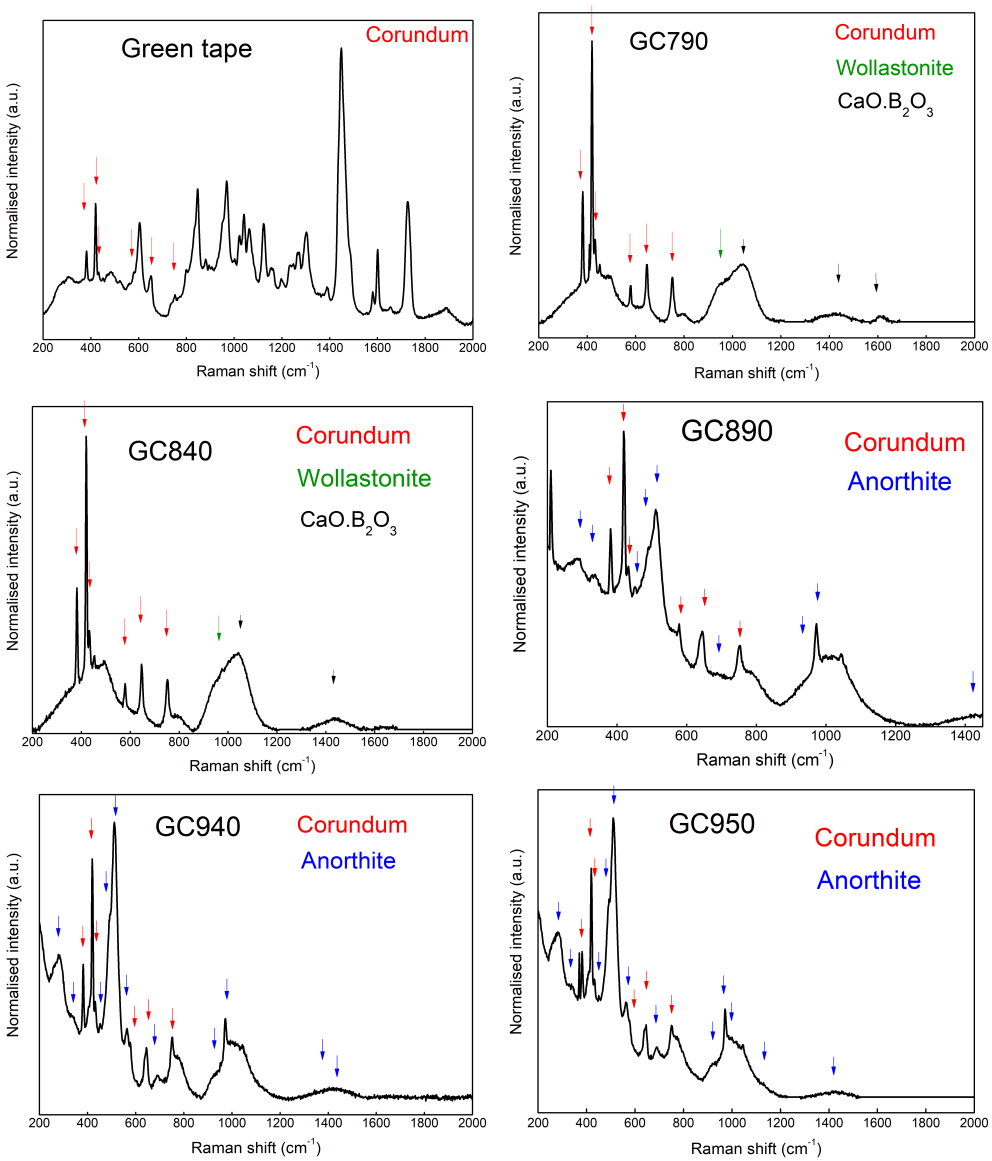

Figure 5.7: Normalised Raman spectra of the different GC samples. The maxima of the sample peaks were attributed to the reference peaks from RRUFF database. Blue arrows - anorthite, red arrows - corundum, black arrows - CaO (B_2O_3) matrix, green arrows - wollastonite.

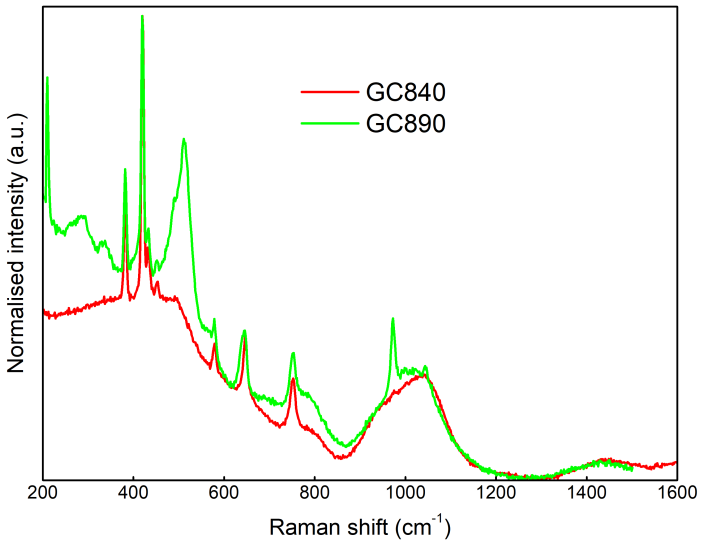

Figure 5.8: Normalised Raman spectra of GC840 and GC890 samples.

GC790 due to reduction of C content, the relative atomic concentration of all other elements increases significantly.

The obtained XPS data from the surface of the samples correlates with observations of CaO.(B_2O_3) peaks in bulk Raman spectra (Figure 5.7) and allows for speculation about the diffusion of CaO.(B_2O_3) glass to the top layer of the sample surface. Moreover, XPS analysis revealed a significant increase in the silicon content by the firing process (from 2.8 for the green tape to 13.1 for the GC790). By further increasing the firing temperature from 790 °C to 940 °C, the silicon content constantly increases up to 19.4 at%. In contrast to Si, the Al content decreases from 11.5 for the GC790 to 4.2 for both GC915 and GC940. These results hint towards the diffusion of glass phase to the surface of LTCC and covering the alumina grains during firing and the densification phase. This is also in agreement with the SEM micrographs of GC LTCC substrates fired at different peak temperature (see Figure 5.3). For the GC890 in which anorthite growth occurs, the Ca count is maximum (5.4 at%) and by increasing the firing temperature declines down to 4 at% for GC940. This behaviour can be attributed to the formation of anorthite phase in GC890 and then due to the glass diffusion to the surface this phase together with the enveloped alumina grains are covered. On the other hand, for these conditions the B counts changes in the opposite direction to the Ca counts.

The analysis of the high-resolution XPS spectra of the fired samples showed shifts of the peak maximums of the chemical elements for about 0.5 eV to the higher binding energy region compared to the green tape. The high-resolution Al 2p peaks were deconvoluted into 3 peaks: α-Al_2O_3 (74 eV), transition-Al_2O_3 (75 eV), Al-OH (76 eV) [251]. As the literature reports that the Al 2p

Table 5.1: The relative atomic concentration of chemical elements on the surface of the samples calculated from high-resolution XPS spectra.

	Relative atomic concentration *at%*					
	O	**C**	**Ca**	**Al**	**Si**	**B**
GC-green tape	24.5	67.6	1	3.2	2.8	0.9
GC790	52.5	14.7	4.7	11.5	13.1	3.5
GC840	53.5	14.6	4.6	8.6	15.8	2.9
GC890	54	15.7	5.4	6.4	16.7	1.8
GC915	56	14.2	4.6	4.2	18.6	2.4
GC940	56.4	13.4	4	4.2	19.4	2.6

spectra of successive transition aluminas (γ, δ and θ) cannot be distinguished by their chemical shift, it was proposed to introduce in the deconvolution process a transition alumina component with the fitting peak (transition-Al_2O_3) at a binding energy value of 75.0 eV [251]. Table 5.2 presents the concentrations of chemical bonds calculated from the deconvoluted Al 2p peaks. As the sintered LTCC samples have in their composition both the corundum (Al_2O_3) and the anorthite ($CaAl_2Si_2O_8$), the fluctuation of the aluminium bond concentrations could be explained either by reconfiguration of the surface caused by annealing (anorthite replaced the corundum) or by the phase transition of corundum (as mentioned in Raman studies).

Figure 5.9 shows the comparison of peaks shapes of fired LTCC samples with the reference deconvoluted Al 2p peak. At 840 and 940 °C, a slight shift of Al 2p to the higher binding energy region (about 0.2 eV) was observed.

Table 5.2: Chemical bond concentration determined from deconvoluted Al 2p peaks of the samples.

	α-Al_2O_3 %	**transition-Al_2O_3 %**	**Al-OH %**
GC-green tape	73	21	6
GC790	67	31	2
GC840	75	24	1
GC890	66	30	4
GC915	59	39	2
GC940	33	61	6

The high-resolution Si 2p peaks were fitted with 3 peaks: SiC (100.6 eV), SiO_2/Si present in Al_2O_3, B_2O_3 and CaO (102.4 eV), SiO_2 (103.5 eV) [252, 253]. The concentrations of chemical bonds are shown in Table 5.3. The decrease of SiC bonds (from 5 to 0.5%) for the sintered samples well corresponds with the decline carbon content (see Table 5.1). The significant increase of SiO_2 bond (from 25 to 64.5%) is well correlated with the increase of atomic concentration of silicon and oxygen component on the surface of the fired samples.

Figure 5.10 shows the comparison of peaks shapes of annealed samples with the reference deconvoluted Si 2p peak. As can be seen, the maximum of Si 2p peaks of the annealed samples was

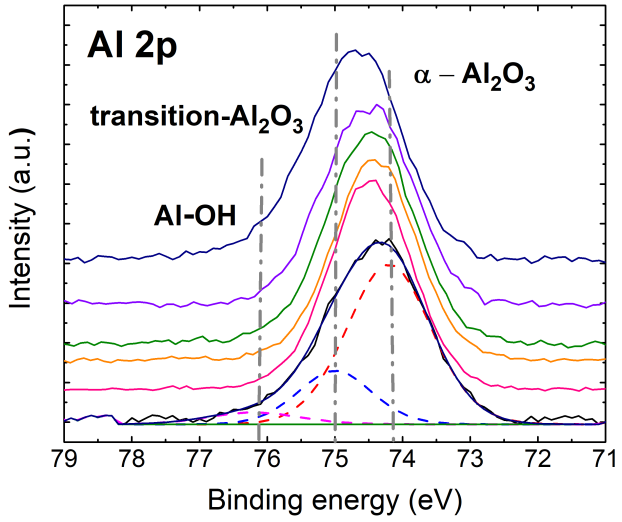

Figure 5.9: Comparison of calibrated high-resolution Al 2p peaks of the samples.

Table 5.3: Chemical bond concentration determined from deconvoluted Si 2p peaks of the samples.

	SiC %	SiO_2/Si %	SiO_2 %
GC-green tape	5	70	25
GC790	1	64	35
GC840	1	57	42
GC890	1	64	35
GC915	1	53	46
GC940	0.5	35	64.5

shifted to the higher binding energy region (from 102.6 to 103.1 eV).

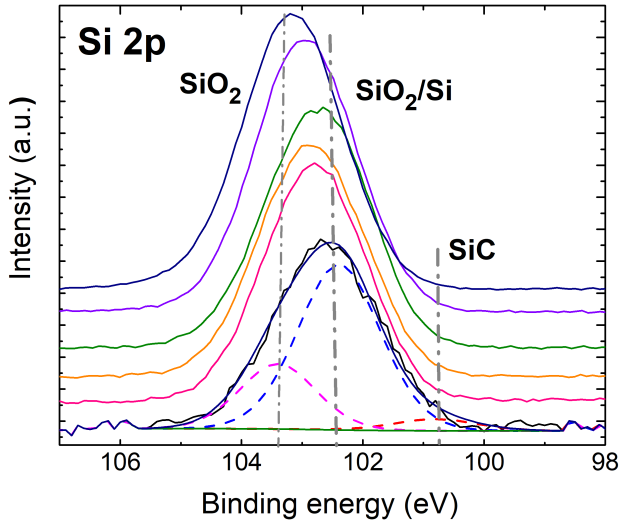

Figure 5.10: Comparison of calibrated high-resolution Si 2p peaks of the samples.

Deconvolution of the high-resolution O 1s peak was made in accordance with [251, 254–257] into 3 peaks: O bulk (530.7 eV) [254], Al-OH/CaCO (532.1 eV) [254, 255], $B_2O_3/SiO_2/H_2O$ (533 eV) [254, 256, 257]. Table 5.4 presents the chemical bond concentration determined from the deconvoluted O 1s peaks. The significant decrease of the peak $B_2O_3/SiO_2/H_2O$ concentration (from 41 to 14 %) revealed the desorption of the H_2O molecules from the fired samples. However, increasing of the temperature up to 940 °C, probably, led to the increase in B_2O_3/SiO_2 bonds which correspond to the presence of CaO (B_2O_3) and anorthite ($CaAl_2Si_2O_8$) on the sample surface. The changes in the O bulk concertation can be explained by possible diffusion of the glass to the top surface of the fired samples.

Table 5.4: Chemical bond concentration determined from deconvoluted O 1s peaks of the samples.

	O bulk %	Al-OH/CaCO %	$B_2O_3/SiO_2/H_2O$ %
GC-green tape	16	43	41
GC790	35	51	14
GC840	31	49	20
GC890	22	55	23
GC915	17	52	31
GC940	12	66	22

Figure 5.11 shows the comparison of peaks shapes of fired samples with the reference deconvoluted O 1s peak. As can be seen, the firing caused significant changes of the O 1s peak shape ($B_2O_3/SiO_2/H_2O$ bond at 533 eV decreased) and shifted the maximum of O 1s peaks of the fired samples to the higher binding energy region.

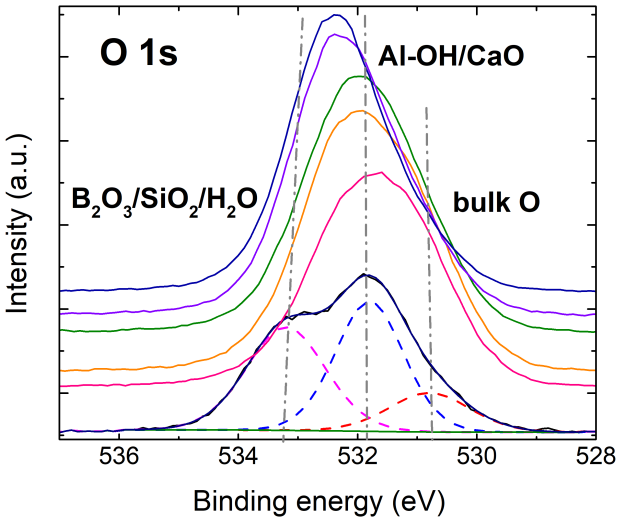

Figure 5.11: Comparison of calibrated high-resolution O 1s peaks of the samples.

Besides, the analysis of the high-resolution Ca 2p and B 1s peaks was carried out. According to the [255] the Ca 2p peak has clearly spaced spin-orbit components: Ca $2p_{3/2}$ and Ca $2p_{1/2}$ split is

about 3.5 eV. In the case of reference and annealed samples, the Ca 2p had also double-split shape with the split distance of about 3.5 eV. (Ca 2p spectra are not shown here).

As for the B 1s peaks, for all samples the position of B 1s peak was about 192.4±0.2 eV is attributed to B_2O_3 [258]. According to the [259] the B 1s peak at 192.4 eV corresponds to B^{+3} homogeneously surrounded by oxygen tetrahedral. Moreover, the elemental boron at 188 eV was not observed in any of the measured B 1s peaks. The obtained B 1s spectra are symmetric and could be fitted by a single chemical environment centred at 193.5 eV, which is attributed to B_2O_3 [260]. (B 1s spectra are not shown here).

Altogether, from the correlative analysis of annealed glass ceramics by Raman and XPS analysis it can be concluded that the replacement of corundum with anorthite and, probably, diffusion of the glass close to the top layer of the samples.

5.3. Etching treatment

In the next step, the *as-fired* samples were porosified in a 3 $molL^{-1}$ KOH solution and the SEM micrographs of the porosified LTCC samples are shown in Figure 5.12. The corresponding SEM images of the substrates in the *as-fired* state are illustrated in Figure 5.3. As shown in Figure 5.12 the surface of the GC840 sample after etching treatment is strongly corroded. However, by increasing the firing peak temperature of the *as-fired* LTCC, the resulting surface after etching becomes smoother and the etching seems to be more controllable. On the other hand, by increasing the firing temperature the penetration depth of the etching solutions declines from roughly 5 μm for GC840 to less than 0.5 μm for GC940. Moreover, the weight loss percentage for all samples was quite low (less than 1%) and was even decreasing when increasing the peak firing temperature. This could be attributed to the increased degree of densification due to the penetration of the melted glass into the gaps between the grains for the LTCC samples fired at higher peak temperatures which in turn makes the LTCC more etch resistant. These results show that although the higher peak temperature is favourable for the fabrication of very smooth surfaces for the LTCC substrates in the *as-fired* state (see Figure 5.3), to obtain a high degree of porosification, a very high peak temperature is not beneficial.

Additionally, the samples were studied by TEM technique and the corresponding TEM images are shown in Figure 5.13. The pores for the GC940 appear to be the largest which could be due to the highest amount of anorthite phase which is expected to be crystallized for this sample compared to others fired at lower temperatures. Also, for the samples fired at lower temperatures, *i.e.* GC840 and GC890 where the *as-fired* sample was not well densified (see Figure 5.3), some of the observed pores are due to the inherent porosity of the substrate in the *as-fired* state, not introduced by the etching process.

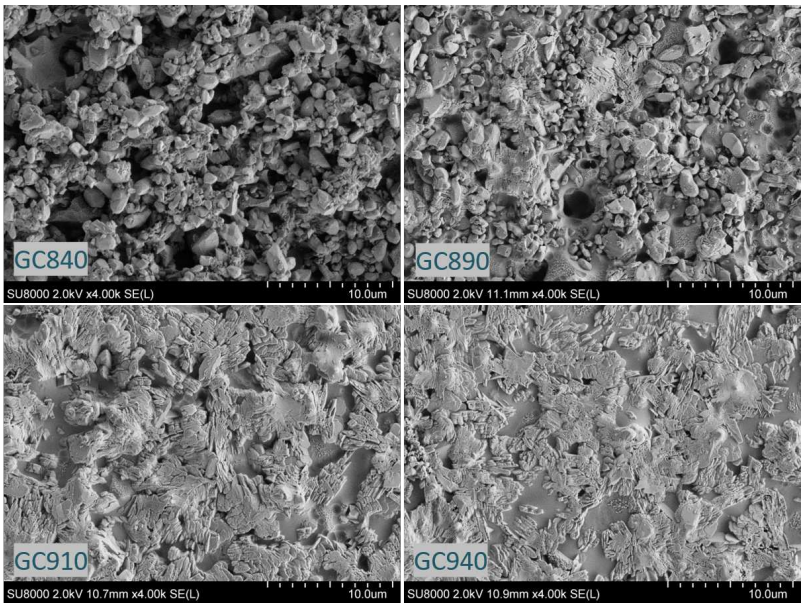

Figure 5.12: SEM images of the different *as-fired* GC LTCC substrates etched for 2 h in 3 mol L^{-1} KOH solution at 75 °C.

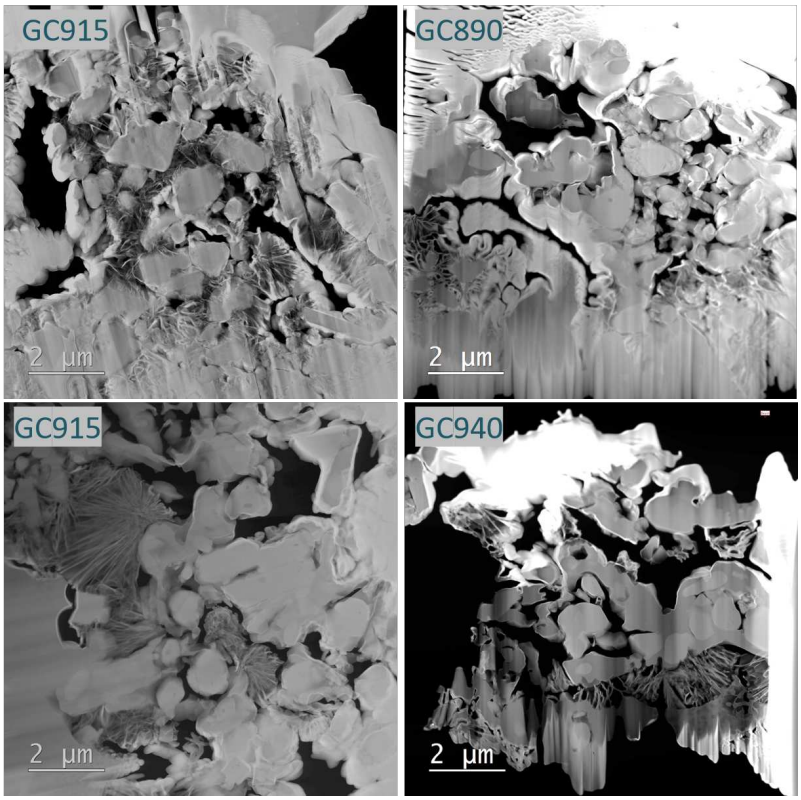

Figure 5.13: Overview of GC LTCC substrates etched in 3 mol L^{-1} KOH solution at 90 °C for 6 hours for the substrates fired at different peak temperatures.

Similar to the etching treatment of GC LTCC fired in industrial environment which were studied in Section 4.1. , for all samples after the etching treatment highly porous silica structures were observed. These structures are generated from the laminar needle-like structures of thermodynamically unstable grown plagioclase feldspars which are typically found in the GC LTCC in the *as-fired* state. They are known to be formed because of the Al and Si ordering in anorthite at temperatures above 1100 K. Salje *et al.* have studied the formation of these needle-like structures in details [261]. The formation of needle-like twin structures in the *as-fired* state of GC LTCC was also observed in the TEM investigations of Steinhäußer *et al.* [79]. They referred these structures which are surrounding the alumina grains and are consisting of Si, Al, Ca, and O, to the anorthic. However, no TEM investigations were carried out by them on the etched samples. The highly porous structures observed in Figure 5.13, however, consisting of only Si and O, which means that they are formed by the depletion of Ca and Al from the anorthic anorthite due to the etching treatment.

Chapter 6.

DETERMINATION OF FLEXURAL STRENGTH OF LTCC SUBSTRATES BY BALL ON THREE BALLS METHOD

The primary aim of this chapter is to introduce an unconventional but straightforward approach for determining the flexural strength of the LTCC substrates. The method is a biaxial bending test called Ball On Three Balls test (B3B) which was discussed in detail in Chapter 2. The B3B test requires very little effort in sample preparation in comparison to the common uniaxial bending tests and is suitable for testing brittle materials, such as LTCC. To implement the test method, a simple mechanical setup was designed. The setup is not only applicable for the LTCC but other ceramic materials and thus can be applied for further research work. Another important aim was to determine whether the setup delivers reliable results and what are its limitations. In this chapter the developed test setup was used for investigation of the influence of etching and firing temperature on the flexural strength. To meet the comparability of all results, it was important to ensure the same conditions for all investigated samples with respect to sintering conditions and etching. Three different commercial LTCC tapes in five batches were studied. One batch for each tape in the *as-fired* state (the same firing conditions), and two extra batches for investigating the impact of etching treatment. Further information on the tapes and the investigated conditions is given later.

6.1. Sample Preparation

The experimental procedure is described in this part regarding the aspects of sample preparation, finding optimal firing and etching conditions, and characterisation methods. The study was limited

to those five batches and 30 samples per batch were required for sufficient statistical analysis. The three types of LTCC tapes investigated in this chapter were GC LTCC, DuPont 951 (DP-951) and DuPont 9k7 (DP 9k7). An overview of the related properties of the examined LTCC tapes is given in Chapter 2.

In the firing process, it was aimed to obtain sintered samples with a defined geometry and good surface quality. A crucial parameter for good surface quality and well sintered LTCC components is the firing profile. The examined profiles were those recommended in literature and manufacturer data sheets for GC LTCC [169] and DP-951 [262], respectively. Since the recommended firing profile for the DP-9k7 [263] requires a very long time (26.5 hours) and challenging to realize by the furnace, this profile was not examined. For GC LTCC, the temperature profile was already reported in previous research [169] and was also discussed in Section 2.1.3.. Nevertheless, typically the profiles were progressively improved by measuring the temperature profile and changing the furnace settings until the measured profile met the manufacturer´s specifications. For a better comparison of profiles and to ensure the formation of anorthite phase the peak temperature for both profiles was set to 900 °C. The corresponding temperature profiles are shown in Figure 6.1. For the convenience, the profiles recommended for CeramTape GC and 951 DuPont are named profile *a-900*, and profile *b-900*, respectively.

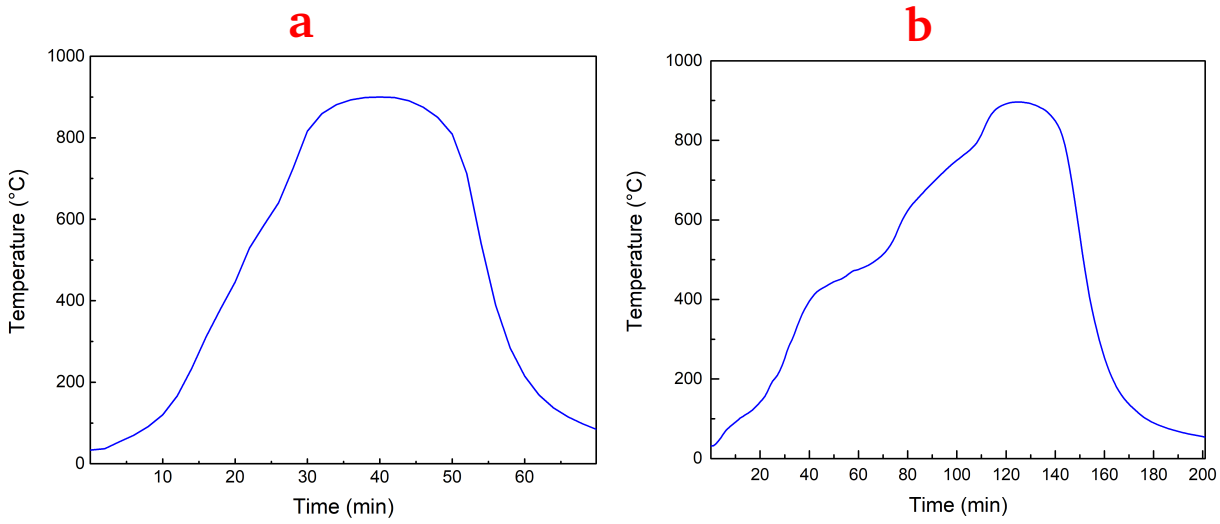

Figure 6.1: The temperature profiles based on manufacturer specifications for **a)** CeramTape GC and **b)** 951 DuPont.

The geometrical properties of the samples are mainly restricted by the designed B3B setup. As the thickness of the single-layer LTCC samples mainly depends on the selected tape, the only variable geometric property was the diameter of the specimen. For the accuracy of the calculations, a diameter of approximately 5 mm was required and data on the shrinkage of the LTCC tapes were gathered. Another requirement was that the samples were circular and not curved or bent heavily. An overview of shrinkage investigation and determination of the circularity of the samples is given in this chapter.

To calculate the cut-out diameter for the final samples, shrinkage analysis was performed for 10 samples of each batch prior to and after the firing process. Weight loss due to sintering was also investigated for these samples. The results are summarised in Table 6.1.

Table 6.1: Shrinkage and weight loss of LTCC tapes fired with profile *b-900*, samples used for B3B tests

LTCC type	x,y shrinkage %	z shrinkage %	Weight loss %
GC	20.50	22.38	16.56
DP-951	14.80	9.22	10.88
DP-9k7	9.68	8.71	12.87

The obtained values are similar to the corresponding references given by manufacturers and literature [169, 262, 263]. These values were used to determine the required cut-out diameter for the final samples for B3B analyses. Hence, the GC LTCC, DP 951, and DP-9k7 were cut to circles with diameters of 6.28, 5.8, and 5.6 mm, respectively. The resulting diameters after firing were in the range of 4.98 to 5.04 mm for all investigated tapes which fulfil the B3B test dimension requirements.

The circular LTCC samples were fired, and their circularity was analysed using a digital microscope and their possible deformation was investigated. Out of 20 investigated samples, only one showed a deviation from the circular geometry. All other fired samples and cut green tapes investigated were nearly perfectly circular and showed less than 2% deviations from circularity. Figure 6.2 shows two examples of the optical microscopy analysis for a perfect and a partially deformed LTCC tape. However, as already discussed the B3B test in Section 2.2.9., this technique is very tolerant against possible errors with respect to the alignment of specimens, the determination of the supporting radius or the measurement of the radius of the specimen. The precision necessary to get measurement uncertainties of less than 1% can easily be reached when testing large specimens with the radius of several millimetres or more. For a support radius of several millimetres and Ra±0.1 mm the error in determining σ_{max} is smaller than 1% [264]. Thus, no further samples were investigated using the digital microscope. The samples used for the determination of flexural strength were examined by eye regarding deformations as heavy deformations were easily visible.

6.2. Morphological characterization of *as-fired* tapes

To determine which temperature profile is suitable for the firing of the samples, the surface morphology was investigated using SEM imaging and roughness measurements. A comparison of the surface micrographs of different tapes fired with profiles *a-900* and *b-900* is given in Figure 6.3. A comparison between the GC fired with *a-900* and *b-900* shows that longer sintering time has a positive effect on the surface morphology. However, it should be noted that peak temperature

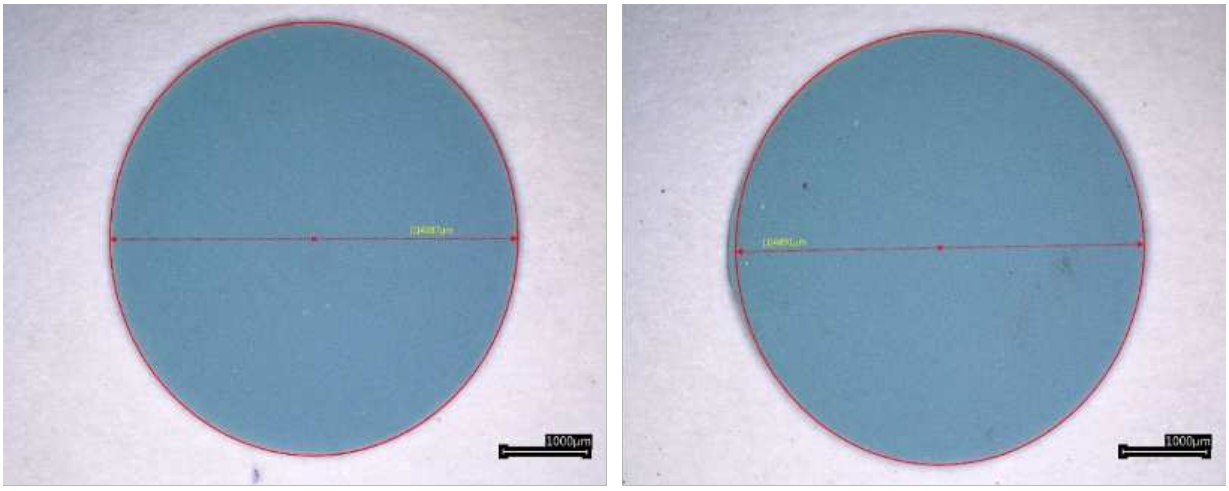

Figure 6.2: Optical microscope images of a perfectly circular (left) and a partially deformed (right) DP-951 LTCC.

seems to have the most significant effect on surface quality as discussed in Chapter 5.

In case of DP-951, it might be concluded from the SEM micrographs that the surface of the sample fired with profile *a-900* is better, but this profile was not considered for further use as the samples were not sintered well as can be seen on the LTCC surface in Figure 6.4. This could be due to the not appropriate burn out of the organic materials with profile *a-900* as this temperature profile is almost three times shorter than that recommended by the manufacturer. Therefore, profile *b-900* was considered for firing DP-951. Similarly, DP-9k7 samples were not properly sintered with profile *a-900*. Thus, the profile *b-900* was selected as a compromise for sintering all three LTCC tapes under the same conditions.

As the selection of the firing profiles based on SEM micrographs was carried out with respect to the commercially fired LTCC substrates, SEM micrographs of the investigated tapes fired by the MSE GmbH company are shown in Figure 6.5. Comparison of these images with Figure 6.3 indicates the best match with the samples fired with profile *b-900*.

Moreover, the roughness measurements were performed on 5 samples for each batch. Measurements on DP 951 and DP-9k7 fired with profile *a-900* were not performed due to the insufficient sintering of the samples. An overview of the roughness values is given in Table 6.2.

Table 6.2: Results of roughness measurements, R_a and R_q values in μm according to EN ISO 25178.

	Profile *a-900*		**Profile *a-950***		**Profile *b-900***	
	R_{ar}	R_q	R_{ar}	R_q	R_{ar}	R_q
GC LTCC	0.549	0.708	0.532	0.696	0.609	0.822
DP-951	-	-	-	-	0.628	0.798
DP-9k7	-	-	-	-	0.855	1.202

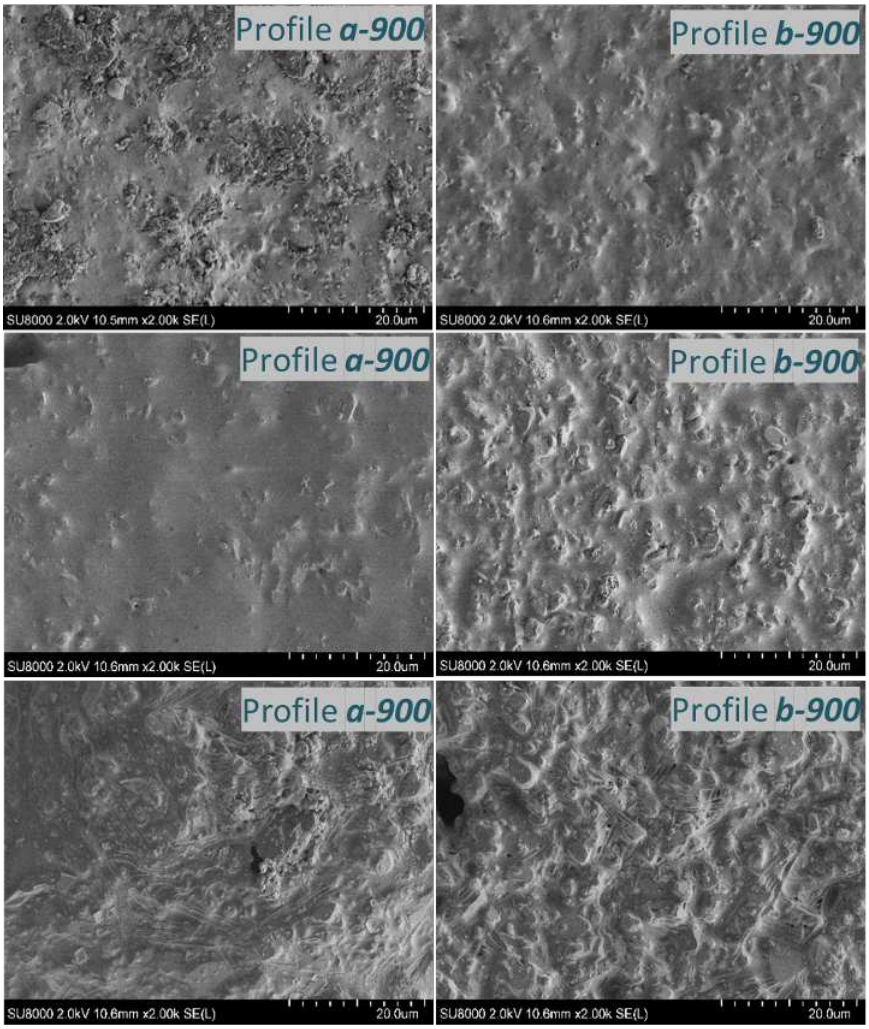

Figure 6.3: SEM surface micrographs of GC LTCC (first row), DP-951 (second row) and DP-9k7 (third row) fired with different temperature profiles.

Figure 6.4: DP-951, green tape and fired with different temperature profiles.

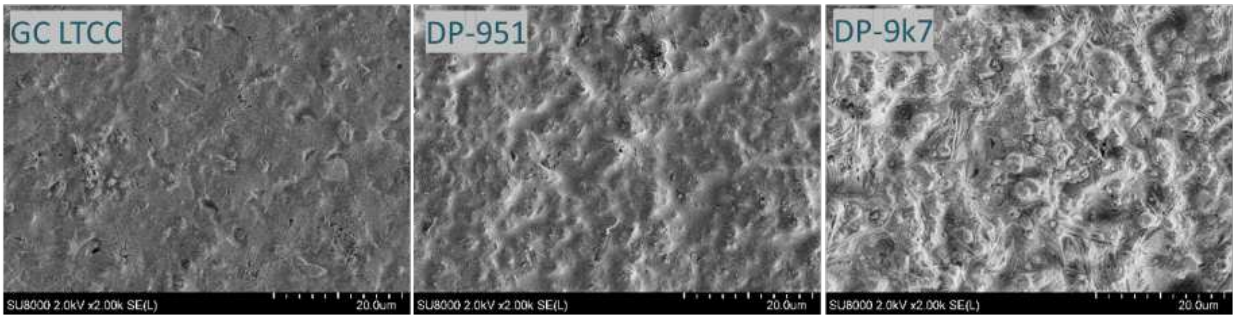

Figure 6.5: SEM micrographs of commercially fired LTCC tapes GC, DP 951, and DP 9k7.

The results of the roughness evaluation are in a good agreement with the SEM micrographs, where *a-950* firing profile (which is almost the same as *a-950* but at a higher peak temperature of 950 °C) resulted in the best surface quality for GC LTCC. Also, based on the roughness parameters for the samples fired with the same profile of *b-900*, which were taken for further analysis, GC LTCC shows the best surface quality, followed by DP-951, whereas the DP-9k7 shows the lowest surface quality. The choice of profile *b-900* for the sintering of the final samples for the determination of flexural strength was based solely on the SEM micrographs and optical images as the samples fired with this profile, due to the longer firing time,are well densified and the surface appears smoother compared to other temperature profiles.

6.3. Wet chemical etching of the *as-fired* samples

The wet chemical etching of the samples was first examined by using two different etching solutions: an acidic solution of 50% H_3PO_4 (P50) and a basic solution of 3 mol L^{-1} NaOH. Those etchants were chosen because they have been investigated well in previous research and therefore, the parameters for an efficient etching were already known. For both etchants, a constant temperature of 90 °C was used while the exposure time was varied. The primary investigations showed that for DP-951, P50 is a very less efficient etching solution compared with 3 mol L^{-1} NaOH. As can be seen in Figure 6.6, at the investigated etching conditions there is almost no etching for DP-951.

Although based on the previous results, P50 at temperatures above 100 °C can etch DP951, such high temperatures are not suitable for the 3 mol L^{-1} NaOH etching solution due to massive bubble formation which distorts the treatment. Therefore, since it was planned to etch both tapes under the same condition, the 3 mol L^{-1} NaOH etching solution was chosen for further investigations. Even this etching solution showed a quite slow rate of dissolution which results in a low degree of porosification which is assumed to hardly affect the flexural strength. Therefore, the samples for B3B test were subjected to a long-term etching (21 hours) and the results are shown in Figure 6.7.

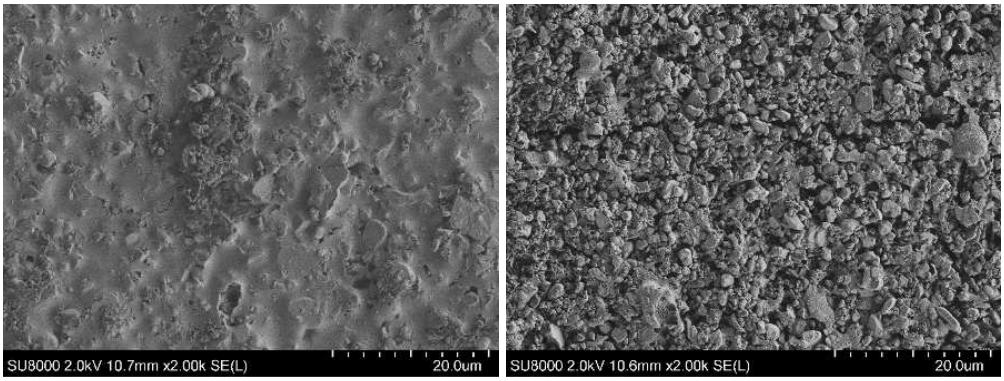

Figure 6.6: SEM micrographs in top view of the DP-951 (left) and GC LTCC etched at 90 °C with P50 solutions for 3 h. The corresponding SEM images of the *as-fired* samples are shown in Figure 6.3.

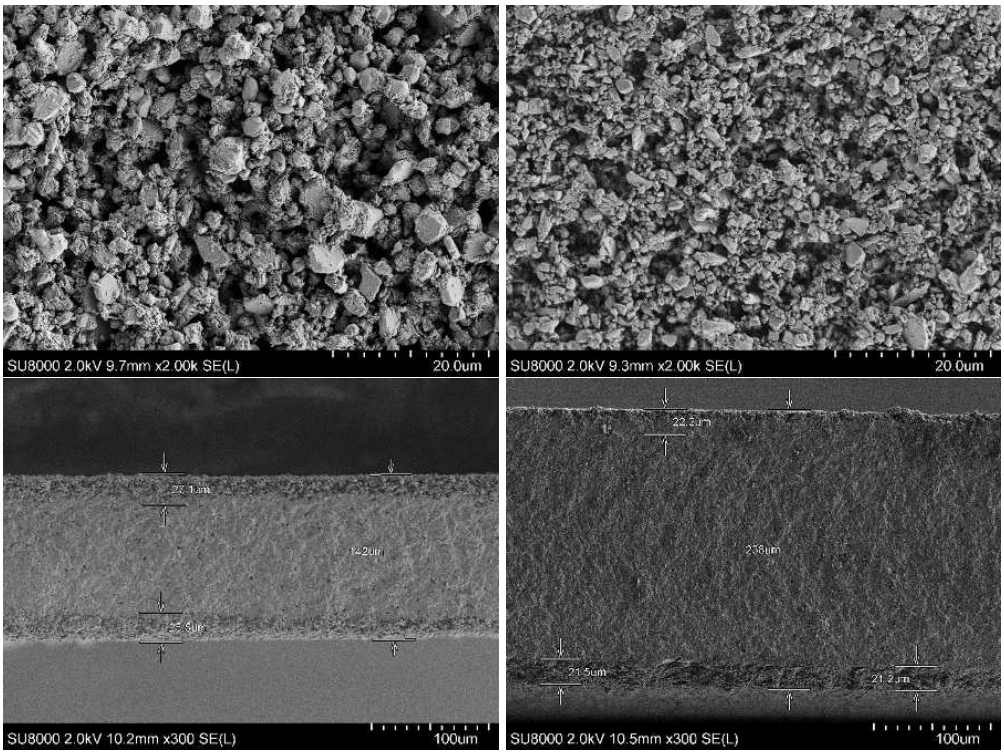

Figure 6.7: SEM micrographs in top view and cross-section of the DP-951 (left) and GC LTCC etched at 90 °C with P50 solutions for 21 h. The corresponding SEM images of the *as-fired* samples are shown in Figure 6.3.

The resulting SEM micrographs show comparable porosification depths for both LTCC tapes after 21 hours of etching. For the GC tape, the dp of approximately 22 μm on both sides roughly amounts 16% of the total tape thickness, while DP-951 sample shows a dp of approximately 26 μm which equals 37% of the total thickness. These amounts of porosification should be enough to expect a change in flexural strength.

For DP-9k7 after etching treatment in either of the etching solutions, the LTCC tape was heavily dissolved and lost its mechanical strength completely. Even samples etched for very short etching

times could not be handled properly as they broke immediately at contact. Etching behaviour of that sort was reported for DP-9k7 in [79]. DP-9k7, which already shows great dielectric properties in the *as-fired* state, consists of lanthanum-borate-glass, that is strongly attacked by the etching solutions. Therefore, controlled porosification of this LTCC type was not possible and thus, this tape was measured only in the *as-fired* state.

6.4. Determination of characteristic flexural strength by the B3B method

After fabrication of desired LTCC samples, the flexural strength for the given LTCC tapes using the B3B setup was characterised. Details on resulting strength values and analysed batches are covered in this Section. As already mentioned, the investigated tapes include 951 and 9k7 from DuPont (DP-951 and DP-9k7), as well as GC LTCC. While all the LTCC systems were investigated in the *as-fired* state, GC LTCC was additionally investigated in the porosified state. All LTCC tapes were fired at a peak temperature of 900 °C. After firing the tapes were etched with NaOH at 90 °C for 21 hours. For each batch, 30 samples were required to perform statistical analysis. Approximately 50 samples were fired for each batch. Deformed samples were sorted out prior to the etching experiments.

All characteristic strength values were calculated as described in Section 2.2.9. . The value of flexural strength for each sample was calculated with a Poisson's ratio of 0.25. The obtained results are depicted in Figure 6.8. The regression according to the Maximum Likelihood is inserted in red. An overview of Weibull-moduli and characteristic flexural strength values are given in Table 6.3. for all investigated batches.

Table 6.3: Weibull-modulus and characteristic flexural strength of investigated LTCC substrates.

Batch	Nr. of samples	Weibull-modulus	characteristic flexural strength *MPa*
GC as-fired	29	9.6	459.6
GC LTCC etched with 3 mol L^{-1}NaOH for 21 h	29	22.9	320.7
DP-951 as-fired	30	12.5	405.7
DP-951 etched with 3 mol L^{-1}NaOH for 21 h	26	14.4	153.6
DP-9k7 fired at 900 °C peak temperature	29	13.9	270.2

The Weibull-moduli for all investigated samples fall in the range of 9.6 to 22.9, which is the typical range for ceramic materials and LTCC according to literature [265]. For example, Bermejo *et al.* reported the value of 9.7 for the Weibull modulus of MKE-100 LTCC (a PbO–glass+Al_2O_3) system from Matsushita [266]. Krautgasser *et al.* on the other hand for the same LTCC system have

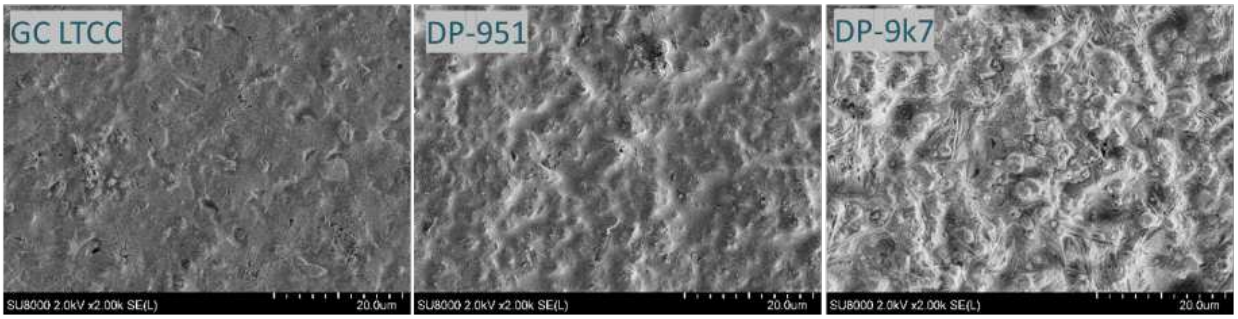

Figure 6.8: Graphical presentation of the results for the flexural strength measurements according to DIN EN 843-5, **a)** GC *as-fired*, **b)** GC etched with 3 mol L^{-1} NaOH at 90 °C for 21h, **c)** DP-951 *as-fired*, **d)** DP-951 etched with 3mol L^{-1} NaOH at 90 °C for 21h, **e)** DP-9k7 *as-fired*.

reported the values in the range of 17 and 25 [267].

The relatively low value of 9.60 for batch 1 indicates a wide probability curve of the strength distribution meaning that the defects are not spread evenly across the ceramic material. Further investigations of the fractured samples should be performed to determine whether the fracture was caused by the setup or influenced by large surface defects.

The Weibull-modulus for the second batch 22.9 is by far higher than the values obtained for other batches, *i.e.* in the range of 9.6 and 14.4.

Comparing the resulting flexural strength of GC (fired with *b-900* profile) of 459.6 MPa to 170 MPa given in [268] indicates a much higher flexural strength than expected. A different source specifies the flexural strength of GC to 320 MPa [269], which is still roughly 40% lower than the observed characteristic flexural strength. The reasons for that can be the different sintering parameters or the miscalculation due to the unknown Poisson's ratio of this tape. A comparison between the as fired and etched samples for GC LTCC shows approximately 30% reduction of characteristic flexural strength. As discussed in the etching treatment results, both sided porosification depth amounts to 16% of the sample thickness which is nearly two times lower than the resulting flexural strength. This hints towards the introduction of defects into the material due to wet chemical etching leading to significantly lower strength values. Further fractographic investigations would be required to acquire more information on the effect of etching.

Comparing the characteristics flexural strength of DP-951 to the manufacturer specifications [262], the obtained strength value is approximately 30% higher than specified. The Poisson's ratio of the material is given as 0.25, therefore, the performed calculation should be correct. It seems that the higher peak temperature used in this work (900 °C instead of 850 °C) has a positive effect on the flexural strength of this tape. The value of characteristic flexural strength of the etched samples is approximately 60% lower than for the as fired samples. When taking into account that the porosification depth amounts to 30% of the sample thickness a trend is observable. A given

relative both sided porosification depth seems to result in double the reduction of flexural strength.

Similarly, for DP-9k7 the resulting characteristic flexural strength is approximately 20% higher than specified by the manufacturer. However, it must be considered that the LTCC tape used for the evaluation has a significantly different composition than the other investigated tapes. Thus, additional experiments are required to verify the effect of sintering conditions on the flexural strength.

Chapter 7.

POROSIFIED LTCC SUBSTRATES FOR GREEN ENERGY PRODUCTION

The growing signs of climate change and the associated demand for new energy sources pose a challenge for societies to utilize alternative energy sources. As already discussed in Chapter 1., a promising technology that meets these requirements is represented by fuel cells (FCs) which are efficient power generation devices even for small scale and transport applications [120, 122]. Although FCs are very attractive by their low or no gas emissions, they require hydrogen as a fuel. Hydrogen as one of the most plentiful elements in the cosmos is the cleanest chemical fuel and thus considered as the fuel of choice for our future energy needs [123]. However, hydrogen can ignite or explode in contact with air and should thus be handled with substantial safety precautions [120]. Furthermore, the very small molecular size of hydrogen makes its storage and transportation very difficult. The storage of hydrogen in liquid form is also ruled out since a lot of energy must be applied for the compression, which seems uneconomical for the desired electricity production with the help of FCs.

In-situ release of hydrogen from a stable hydrogen carrier allows for on-demand hydrogen production for FCs, which solves the problems related to storage and transport of large quantities of hydrogen [121]. In this regard, methanol (MeOH) as the simplest alcohol is a great choice that has the advantages of having a high ratio of hydrogen to carbon, and relatively mild reforming temperature as no C-C bond breakage is required [118]. Also, MeOH is biodegradable and is available as a liquid under atmospheric conditions, which makes it interesting as a hydrogen carrier for technical applications, since it makes transportation and storage much easier. Besides, MeOH is a basic chemical that is produced synthetically every year on a million-ton scale. Compared to methane, which is mainly obtained from natural gas, the production of MeOH is, therefore, more dependent on demand than on resource-based extraction. Biotechnical or renewable processes can also be used to produce methanol [120]. In this chapter, the applicability of porous LTCC for being

used as catalyst support for hydrogen production from MeOH is investigated in detail.

In this chapter, the applicability of porous LTCC for being used as catalyst support for hydrogen production from MeOH is investigated in detail.

7.1. Sample Preparation

Ferro L8 LTCC, owing to its well-investigated porosification behaviour, was examined as a support material for palladium (Pd) catalysts. Two different etching conditions were examined for the Ferro L8 samples. Sample 1 was etched only with P50 solution for 6 h and Sample 2 was etched for 3.5 h with P50 followed by 3 mol L^{-1} NaOH for 4.5 h. Cross-sectional SEM images of the fracture planes of both samples are shown in Figure 7.1. As expected from the nonselective etching of LTCC in the two-step dissolution, larger pore openings are formed for Sample 2 which is beneficial for the subsequent impregnation as the solution can better penetrate the porous layer.

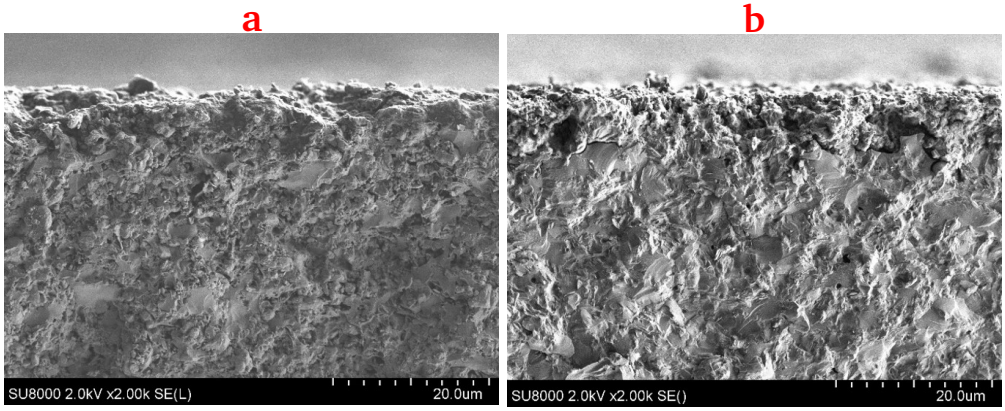

Figure 7.1: Cross-sectional SEM micrographs of Ferro L8 LTCC substrates etched with **a)** P50 (Sample 1) and **b)** P50 followed by 3 mol L^{-1} NaOH (Sample 2).

For the fabrication of metallic catalyst on the porosified LTCC substrates, wet impregnation was employed which is a quite simple and straightforward nanofabrication method. This method consists of contacting a solid support with the precursor solution. The desired species are adsorbed from the liquid phase onto the surface of the support. Low loading can be achieved by adsorption of the precursor ions onto surface groups of the support (ion adsorption) or through the exchange of ions (ion exchange), after which excess precursor is removed. When a higher loading is required, the support is directly dried and the washing step is skipped so that all precursor ends up on the support. The type of product depends on the nature of both the liquid phase and the solid surface, and the reaction conditions [138]. Here, Pd catalysts supported on porosified LTCC substrates were prepared with respect to [270] by using Platinum(II) acetate as Pd precursor. After constant

stirring of the Pd precursor containing LTCC substrates for 2 h at 140 °C in a three-necked flask, the sample was taken from the remaining concentrated solution and then transferred to a beaker and stored in the drying oven at 120 °C for 48 h.

Figure 7.2 shows impregnated Pd nanoparticles in the porous layer of the substrates. As can be seen in the micrographs and also discussed before, due to the more severe etching and bigger gaps and opening at Sample 2, penetration of the precursor into the pores was more facilitated and more Pd is deposited in the pores. Next, the activity of both impregnated catalysts for hydrogen production from MeOH was investigated.

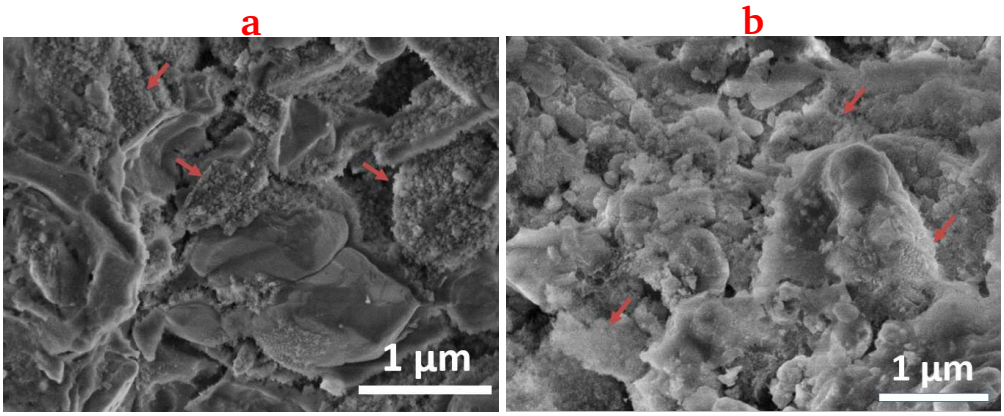

Figure 7.2: Cross-sectional SEM micrographs of Pd-impregnated Ferro L8 LTCC substrates initially etched with a) P50 and b) P50 followed by 3 mol L^{-1} NaOH. Arrows indicate the impregnated Pd catalyst.

Both samples were initially square, thus had to be crushed into smaller pieces to be fitted into the capillary prepared with glass wool and placed in the measurement setup. The reactor was flushed with Ar (12 mL Ar/min) before starting the operation to check the screw connections for tightness. As soon as N_2 and O_2 could no longer be detected, the measurement was started.

7.2. Blank test

The blank test was carried out to make sure about the inertness of the thermometer and the glass wool as well as the leakproofness of the setup. The reactor was initially purged with Ar (12 mL/min) until no longer N_2 and O_2 were detected. The mixture was then heated to 50 °C. When the temperature became constant, the Ar stream was then passed through the bubbler and the gas stream was loaded with H_2O and MeOH. Besides, the temperature ramp was adjusted (see Figure 7.3). Illustration of the processes before the start of the temperature ramp is omitted since only temperature settings and the composition of the atmosphere before flushing with Ar were recorded.

Slight oscillations in the temperature curve up to a reaction time of up to almost 3 h or a corre-

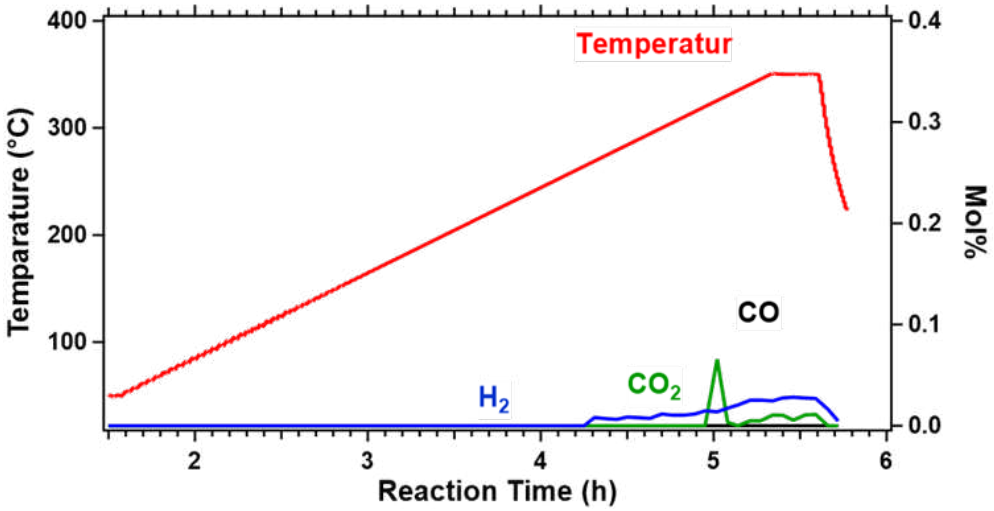

Figure 7.3: Recording the temperature ramp and the chemical activity for the blank LTCC sample. The curves for temperature (red), O_2 (yellow), H_2 (blue), CO_2 (green), CO (black) are shown. The reaction time is plotted on the ordinate, the temperature (left) and the molar fraction of the reaction mixture (right) on the abscissa.

sponding temperature of 155 °C were observed. This oscillation process was a consequence of the oversizing of the thermostat and the low sensitivity of the PID controller in the low-temperature regime. From temperatures of 265 °C and above a poor conversion of the starting materials to H_2 was noticeable, and before that no MeOH and water conversion was observed. The amount of CO remained below the detection limit of the device (approximately 10 ppm). Likewise, no oxygen could be detected, which allowed the conclusion that the setup was sealed and thus the measurement of the composition was not subject to any influence by air. Also, a peak is observed for the CO_2 curve at a temperature of 325 °C (reaction time of 5 h and 1 min) to about 0.066 mol%. However, this peak could be considered as an artefact. Above, there is a slight formation of CO_2, which is much lower than the detected amount at 325 °C, but anyhow indicates the conversion of educts to CO_2. The trend of the CO_2 followed the trend of the H_2 and increased with increasing temperature (up to a maximum value of 0.0111 mol% after a reaction time of 5 h 36 min), but dropped immediately after the onset of the cool-down phase in the reaction mixture after 5 h 36 min. It is remarkable that the amount of CO_2 was consistently below the amount of H_2.

7.3. Reduction at different temperatures (porosified LTCC)

Sample 1

As already discussed, to remove carbon residues from the sample surface at the beginning of each measurement, the sample was oxidised under an oxygen atmosphere. Afterwards, the sample was reduced under H_2 atmosphere. To prevent exploding, the reactor was flushed with Ar between the oxidation and reduction steps and simultaneously cooled down to the desired reduction tempera-

ture. To find the best condition for this reduction step, individual measurements were carried out at four different reduction temperatures of 150, 200, 250, and 300 °C. This allows investigating the effects of different temperatures on the possible formation of Pd alloys with components of the LTCC support and also the associated catalytic activity.

For the reduction temperature of 150 °C (Figure 7.4a), the formation of H_2 was first detected at 170 °C (after a reaction time of 3 h 24 min) and after that, the H_2 amount was progressively increased. The formation of CO and CO_2 was not detected at the start of H_2 formation. CO could only be detected at a temperature of 267 °C and above. No CO_2 formation was found except for one measuring point at 328 °C. However, this peak could be assessed as an artefact. When the constant temperature of 350 °C was reached, the curves of H_2 and CO showed a rather constant catalytic activity. With the onset of the cooldown in the reaction mixture, a rapid and almost linear decrease in reactivity in the reaction mixture was observed. Shortly before the catalytic activity dropped rapidly, the H_2:CO ratio was 0.3401:0.2069. This corresponds to a ratio of 1.644:1. The observed ratio thus clearly deviates by about 18% from the 2:1 ratio which is expected for the MeOH decomposition [271, 272].

For the reduction temperature of 200 °C (Figure 7.4b) H_2 was detected at 162 °C (from a reaction time of 3h and 41min). At temperatures above 256 °C, CO could be recorded with a very similar trend as H_2, and CO_2 was only detected after 6 hours of reaction. However, the amount of around 0.004 mol% CO_2 recorded was far below the amounts of H_2 and CO. When the setpoint temperature of 350 °C was reached, the curves were not flattened. Shortly before the catalytic activity dropped rapidly, the H_2:CO ratio was 0.5565:0.3579. This corresponds to a ratio of 1.555:1, which differs significantly by about 22% from the ratio 2:1 that we would have expected for the MeOH decomposition.

For the measurement at a reduction temperature of 250 °C (Figure 7.4c), a behaviour like that of the previous measurement at 200 °C was observed. H_2 could be detected above 164 °C corresponding to a reaction time of 3 h 25 min. CO was detected at first at 266 °C. Above 333 $degree$C, CO_2 appeared continuously. With a maximum of 0.0046 mol%, the amount of CO_2 formed was again much lower than the portions of CO and H_2. As soon as the cool-down phase started, a rapid and almost linear decrease in reactivity was detected. Shortly before the catalytic activity dropped rapidly, the ratio H_2:CO was 0.5334:0.2947. This corresponds to a value of 1.810:1 which deviates about 9.5% from the ratio 2:1 that is expected for the MeOH decomposition.

For the measurement at a reduction temperature of 300 °C (Figure 7.4d) typical behaviour was observed that was already known from the previous measurements. H_2 was formed at temperatures above 159 °C (after a reaction time of 3h 43min). CO could be detected continuously above 263 °C, and CO_2 was only continuously detected above 304 °C. When the constant temperature of 350 °C was reached, there was a plateau in the H_2 portion of the reaction mixture. Similar to the other measurements the CO curve was consistently below the H_2 curve. Shortly before the catalytic activity dropped rapidly, the ratio H_2:CO was 0.5873:0.3177. This corresponds to a ratio of 1.849:1,

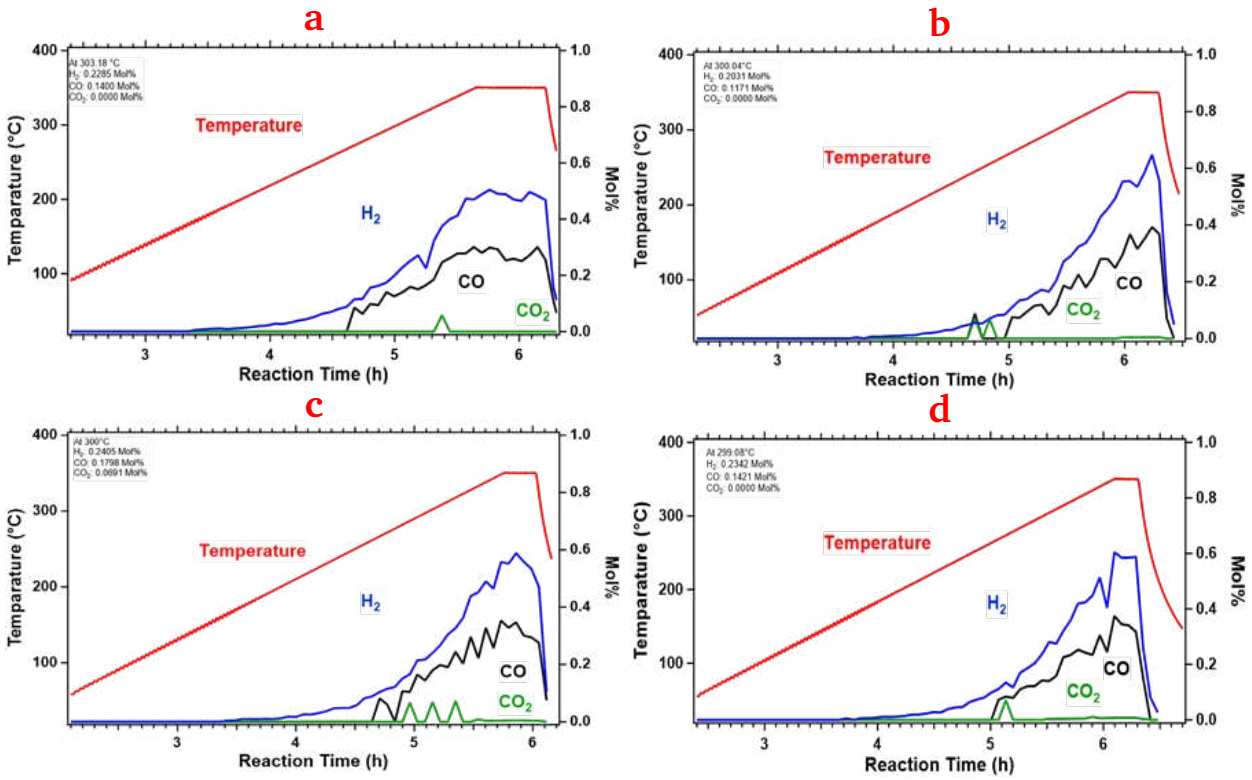

Figure 7.4: Recording of the temperature ramp for sample 1 at reduction temperatures of **a)** 150, **b)** 200, **c)** 250, and **d)** 300 °C. The curves for temperature (red), O2 (yellow), H_2 (blue), CO_2 (green), CO (black) are shown. At the ordinate, the reaction time is applied, at the abscesses the temperature (left) and the proportion of the reaction mixture (right).

which deviates from the ratio 2:1 by about 8% that is expected for the MeOH decomposition.

Sample 2

Similar to Sample 1, four different reduction temperatures were examined for Sample 2 and the influence of reductive pretreatment on alloy formation and the associated catalytic activity were investigated

In Figure 7.5a, the entire recording of the measurement is shown for sample 1 at a reduction temperature of 150 °C. The reduction at 150 °C is presented as an example for all further measurements. This figure shows oxidation at 300 °C for 30 min under an oxygen atmosphere. Then, the temperature was cooled down to 150 °C. The H_2 concentration in the reactor was increased and the temperature further cooled down. The temperature ramp starts from a reaction time of 2h 18min and is shown separately again in Figure 7.5b. Also, for a better presentation of the formed products, for all other experiments, only the temperature ramp of the overall temperature program is shown.

The start of the reaction could be noticed from a temperature of about 164 °C (reaction time of 3 h 36 min). From this temperature, H_2 was detected. CO could only be detected from the temperature

of 245 °C. From this temperature, the amounts of H_2 and CO increased very steeply. Also, CO_2 was detected above a temperature of 311 °C. The amount of CO_2 is far lower than the portion of CO and H_2. At 300 °C, 0.4239 mol% of H_2, and 0.2299 mol% of CO were detected, while no CO_2 could be detected at this temperature. When the constant temperature of 350 °C was reached, the curves reached their maximum, and the reactivity dropped very rapidly once the reaction mixture was cooled. Shortly before the cool-down phase started, the amounts of H_2, CO, CO_2 and were 0.8081, 0.4243, and 0.0108 mol%, respectively. This corresponds to the H_2:CO ratio of 1.905:1 and thus approximately the stoichiometric ratio 2:1, which suggests that mainly MeOH decomposition took place on the catalyst surface (see Equation 1.8 in Chapter 1.).

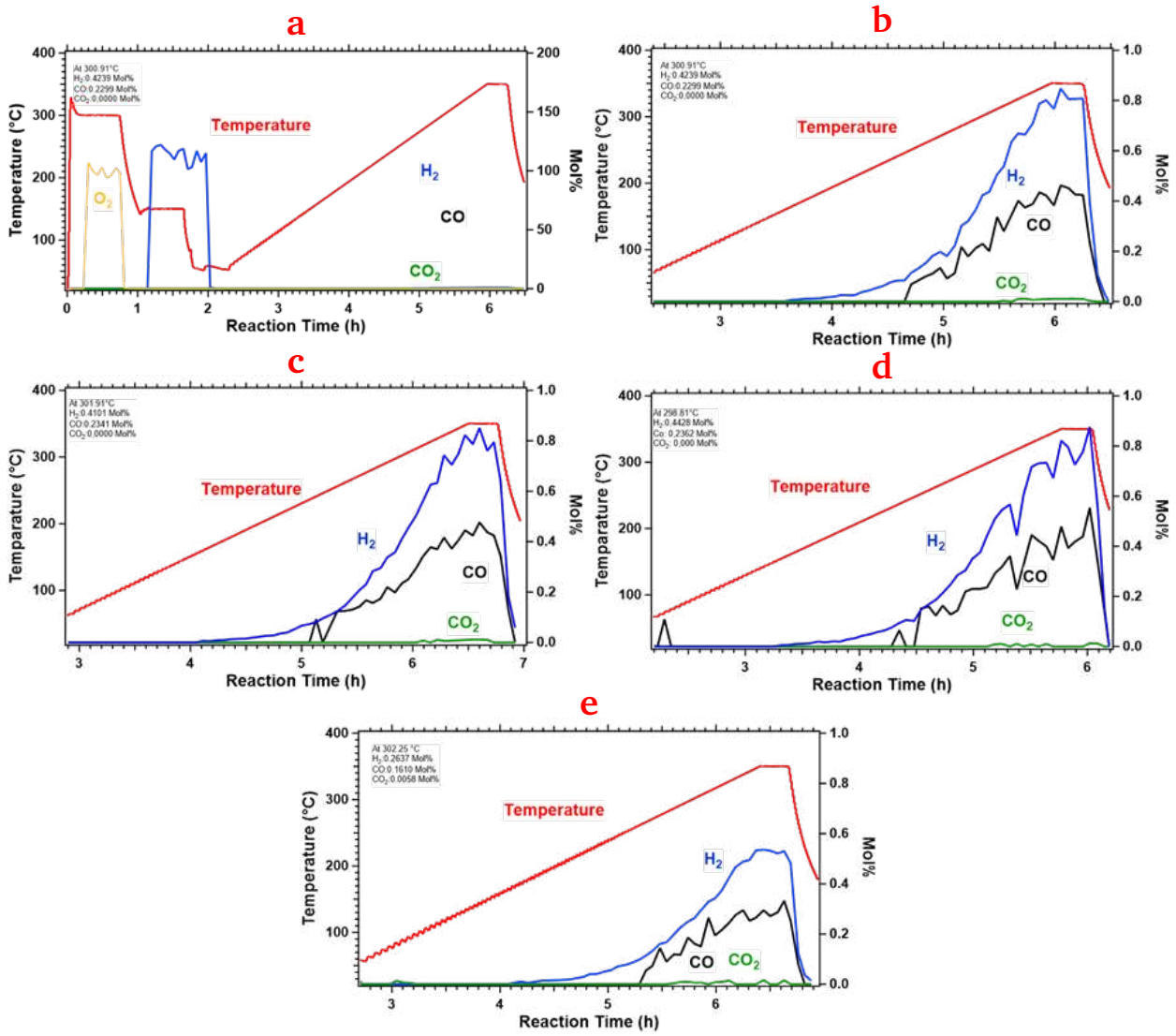

Figure 7.5: a) The overall temperature program for sample 1 at a reduction temperature of 150 °C. **b-e)** Recording of the temperature ramp for sample 1 at reduction temperatures of 150, 200, 250, and 300 °C. The curves for temperature (red), O2 (yellow), H_2 (blue), CO_2 (green), CO (black) are shown. At the ordinate, the reaction time is applied, at the abscesses the temperature (left) and the proportion of the reaction mixture (right).

For the measurement at a reduction temperature of 200 °C (Figure 7.5c), a very similar course of the curves was observed as for the previous measurement at a reduction temperature of 150 °C. The detection of the reaction products for H_2 started at a temperature of about 155 °C (reaction time of 4 h 3min). CO could be detected above a temperature of 241 °C, and CO_2 was recorded after reaching a temperature of 316 °C. Also, similarly, the increase in CO amount occurred very quickly from a temperature of 245 °C. The CO amount remained constantly below the amount of H_2, but the curves showed quite the same trends, and the amount of CO_2 in the reaction mixture was much lower than for CO and H_2. At 301 °C, the amounts of the reaction mixture were read out and 0.4101 mol% of H_2 and 0.2341 mol% of CO were detected. No detectable amount could be identified for CO_2. Thus, it can be assumed that primarily MeOH decomposition took place on the catalyst surface. When the temperature reached its plateau at 350 °C, the curve flattened as before. However, the curves show several jumps and no linear behaviour or constant conversion could be identified. The reactivity dropped very rapidly once the reaction mixture was cooled. The H_2:CO ratio was 0.7947:0.4243 shortly before the catalytic activity dropped. This corresponds to a ratio of 1.873:1 and thus approximately 6% below the stoichiometric ratio 2:1, which is expected for the MeOH decomposition reaction.

For the measurement at a reduction temperature of 250 °C (Figure 7.5d), a similar course of the curves was found as in the two previous measurements. H_2 was again the first product to emerge from 154 °C (reaction time of 3h 18min). CO showed a peak at 237 °C but fell below the detection limit at the next measurement point, but then it could be detected continuously from the temperature of 247 °C. From this temperature, the slope of the curves increased rapidly. CO_2 was only detected at temperatures above 303 °C. The slope of the H_2 curve was steeper here too. The amount of CO_2 formed was again much lower than the amount of CO and H_2. As soon as the cooldown started, a very rapid, almost linear drop in the reaction rates could be detected. The H_2:CO ratio was 0.8759:0.5539 shortly before the catalytic activity decreased. This corresponds to a ratio of 1.581:1. The ratio was with about 21% lower than the proportion that would be expected for MeOH decomposition.

For the measurement at a reduction temperature of 300 °C (Figure 7.5e), the typical trend that had already observed in the previous measurements was detected again. H_2 was formed at above 175 °C (after a reaction time of 4h 12 min). CO was only formed at above 261 °C (from a reaction time of 5h 17min) and was continuously detected from this point on. From this temperature, both curves increased very quickly. CO_2 was only detected at above 280 °C (from a reaction time of 5 h and 33 min). When the constant temperature of 350 °C was reached, a plateau in the H_2 portion of the reaction mixture was observed. The course of the CO curve, however, was characterized by jumps. Again, the amount of CO was consistently below the H_2 amount. The slope of the H_2 curve was almost exponential. Both reaction rates dropped rapidly as soon as the cooldown started. Shortly before the catalytic activity dropped rapidly, the H_2:CO ratio was 0.5301:0.3224 which corresponds to a ratio of 1.644:1. This ratio thus deviated from the ratio 2:1 by about 18% which can be expected for MeOH decomposition.

7.4. Comparison of results

In order to make a good comparison, for both samples, the amounts of produced H_2 and CO were read out at almost the same temperatures of about 300 °C and the results are summarized in Table 7.1. The exact temperature of 300 °C could not always be selected since the composition of the reaction mixture was recorded by the gas chromatograph every four minutes. However, temperatures between 298 and 303 °C were selected to compare the composition.

Table 7.1 shows the compositions of the reaction mixture at different reduction temperatures for both samples, where the optimal values are highlighted in green. For Sample 1, the highest turnover for H_2 is observed for measuring after a reduction at 250 °C. However, this is the same for the highest conversion of CO which is an undesirable product for FCs as it acts as a catalyst poison. Conversions at reduction temperatures of 150, 200 and 250 °C were in a very similar range. However, a significant difference was found at a reduction temperature of 300 °C. At this reduction temperature, conversion of H_2 fell to about 0.2637 mol% and that of CO also decreased to 0.1610 mol%. These were below the previously observed conversions of over 0.400 mol% for H_2 and about 0.2300 mol% for CO. The reduction temperature of 300 °C in the pre-treatment phase can therefore not be assessed as optimal.

Table 7.1: Comparison of the conversions at *ca.* 300 °C in the individual measurements for Sample 1 and Sample 2 and for various previous reduction temperatures. The optimal sales are underlined.

		150 °C	200 °C	250 °C	300 °C
Sample 1	**H_2** *mol%*	0.2285	0.2031	**0.2405**	0.2342
	CO *mol%*	0.1400	0.1171	0.1798	0.1421
Sample 2	**H_2** *mol%*	0.4239	0.4101	**0.4428**	0.2637
	CO *mol%*	0.2299	0.2341	0.2362	0.1610

Similarly, for Sample 2, a reduction at a temperature of 250 °C leads to the highest sale of H_2. As with Sample 1, this reduction temperature also resulted in the highest conversion of CO for the entire measurement series. In contrast to Sample 1, there was no significant difference when applying different reduction temperatures. The values for the sales of H_2 were between 0.2285 mol% (150 °C) and 0.2405 mol% (250 °C).

Moreover, the H_2:CO ratios for both samples correspond to the 2:1 ratio which is expected from MeOH decomposition. Therefore, it can be assumed that mainly MeOH decomposition took place on the catalyst surface. For example, for the reduction temperature of 250 °C the amounts of the reaction mixture for Sample 1 at 299°C, were 0.4428 mol% for H_2 and 0.2362 mol% for CO, while for Sample 2 at 300°C, the values were 0.2405 mol% and 0.1798 mol% for H_2 and CO, respectively. No detectable amount could be identified for CO_2 by using either of samples.

Therefore, it can be concluded that both samples primarily catalysed MeOH decomposition, rather than methanol steam reforming (MSR). However, the catalytic activity (higher H_2 and CO amounts) of Sample 2 which was initially etched in two steps at acidic and alkaline condition was better than Sample 1 which was only etched at the acidic condition. This can be attributed to the increased surface roughness and porosity of Sample 2.

7.5. Long-term activity measurement

After investigating the activity of both samples in H_2 production reactions at different reduction temperatures, their catalytic behaviour was investigated over a longer period under constant reaction conditions, and the obtained results are plotted in Figure 7.6. No temperature ramp was run, but a constant temperature control for the desired period was carried out immediately after the reduction at 300 °C.

For Sample 1 (see Figure 7.6a), at the beginning the conversion of H_2 was 0.3342 mol%,CO_2 and at the end of the long-term measurement, it dropped to a 0.2803 mol%. This corresponds to a relative decrease of around 16%. For Sample 2 (see Figure 7.6b), while the conversion of H_2 was 0.2284 mol% at the beginning, it fell to a 0.1753 mol% at the end of the process. This corresponds to a relative decrease of around 23%.

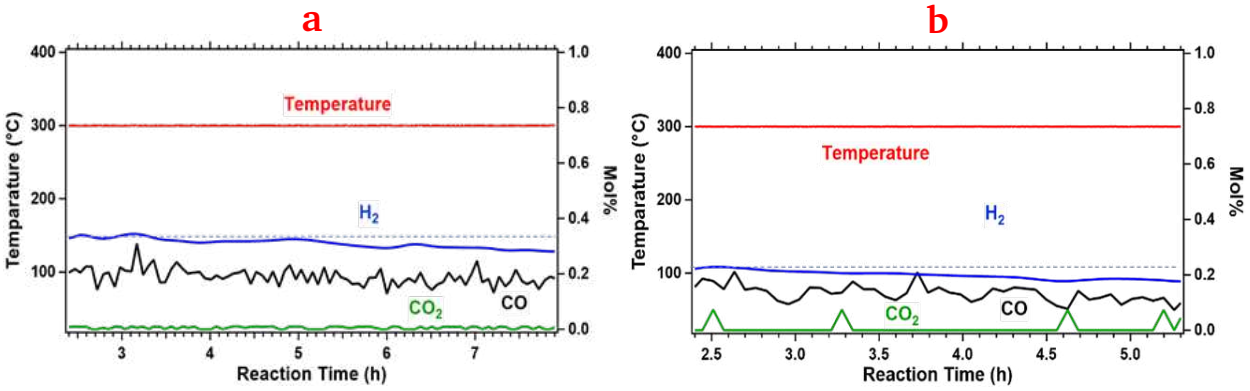

Figure 7.6: Recording the temperature curve for Sample 1 (a) and Sample 2 (b), at a constant temperature of 300 °C. The curves for temperature (red), H_2 (blue), CO_2 (green), CO (black) are shown. The reaction time is plotted on the ordinate, the temperature (left) and the proportion of the reaction mixture (right) on the abscissa.

From the decrease in the production of H_2 and CO over the entire measuring period, which is observed for both samples, it can be concluded that there was a decrease in the catalytic activity over the reaction period. This is a known phenomenon in the decomposition of MeOH on Pd. A possible reason for that lies in the fact that at high temperatures MeOH decomposition also leads to the formation of elemental carbon. It can also be attributed to the product (CO) poisoning. The deposits on the surface of the catalyst and thus blocks the catalytic activity [273].

Chapter 8.

CONCLUSIONS AND OUTLOOK

The porosification of commercially available LTCC substrates, *i.e.* Ferro L8 and GC LTCC due to the wet chemical etching treatment with different solutions was investigated in this dissertation. The method is very straightforward to monitor and the degree of the porosification can be controlled with key etching parameters, such as the bath temperature, etchant concentration, pH, and the duration of the etching treatment. By using the porosification process, LTCC fabrication procedure does not need to be altered since the porosification is generated in the *as-fired* state of commercially available LTCC samples, before final metallization. Furthermore, the advantage of the proposed method is the generation of a surface quality for the etched LTCC which features a bearing plane suitable for further metallization, being an essential pre-requirement for the reliable operation of compact devices or modules for high-frequency applications.

The porosification of LTCC tapes with orthophosphoric acid solution, a standard and commonly used solution for the wet chemical etching process, was comprehensively studied. When applying this solution for the treatment of 180 μm Ferro L8 LTCC, the etching process was so fast that even after 5 min etching more than 40% of the whole LTCC thickness was porosified. Further investigations proved the selective dissolution of celsian phase, which is surrounding corundum grains, thereby a very deep porosification up to the whole substrate thickness could be realized. Kinetic studies were conducted through gravimetric investigations and analyses of porosification depth which showed a higher reaction rate for the less concentrated etchant solution and a dominating reaction-controlled dissolution mechanism.

Moreover, the stiffness behavior of the substrates subjected to this wet-chemical etching process was investigated for substrates with two different thicknesses. The result showed that for the applications where high mechanical strength of LTCC is demanded, the desired mechanical properties are secured when choosing thicker substrates. Also, the mechanical strength of the porosified LTCC substrates was investigated over a large temperature range up to 550 °C indicating a constant storage modulus within the measurement accuracy. This demonstrates that the proposed method

does not limit the application of porosified LTCC at least up to this temperature level. Besides, a straightforward correlation, independent of the etching conditions, between the mechanical properties and the relative porosification depth is presented. This very practical relationship can help to optimize in a straightforward approach the suitable depth of porosification to achieve the desired substrate stiffness. Also, a systematic investigation of the impact of phosphoric acid concentration on the porosification of GC LTCC was carried out by employing etching solutions with the concentrations in the range of 0.5 to 85 wt%. Considering the porosification degree and the surface quality, a concentration of 10 wt% was found to be most efficient.

Moreover, the applicability of alkaline etching solutions for the wet chemical etching of LTCC substrates was examined by employing strong basic solutions of KOH and NaOH at bath temperatures lower than 100 °C. It was found that similar to the etching with orthophosphoric acid, also the feldspar phase is etched faster and more effectively in contrast to the corundum phase. But, when etching with the strong bases the glassy phase of the LTCC is also partially dissolved. However, this concurrent and competitive dissolution of the LTCC components assists in avoiding the sharp and emerged edges around the corundum grains which were observed in previous works. Bath temperature was found to be the most influential parameter since treatment of the sample in contact with the KOH solutions at room temperature, even for a long period of time would not result in an appropriate etching. An explicit porosification of the LTCC requires the temperatures more than 70 °C. Furthermore, the porosification of Ferro L8 with NaOH under well-defined etching condition provided the opportunity for thickness modification through the overall dissolution of the LTCC surface.

As both highly alkaline and highly acidic solutions were examined for the porosification of LTCC substrates and totally different behaviour were observed, for better understanding of the etching mechanism the impact of etchant pH on the porosification behaviour was also studied. Thus, the impact of the solution pH on the porosification behaviour and the potential of PBS as a novel approach for porosification of GC LTCC were comprehensively studied. Based on the obtained results, a pH in the acidic region is most favourable for the etching process. By increasing the acidity of the etchant, superior porosification results can be obtained. Treatment in the acidic condition results in a higher degree of porosity by selective etching of the anorthite phase surrounding corundum grains. In contrast, due to the very slow rate of dissolution in the neutral range, and formation of crystals on the LTCC's surface-near region at highly alkaline condition, neither of these conditions is desirable. PBS showed its best etching performance in the highly acidic regime, *i.e.* pH=1.2 at a relatively low concentration, *i.e.* 0.2 mol L^{-1}.

Comparison of orthophosphoric acid with PBS revealed that the latter is a milder etching solution which, despite the high etching rate, offers better control of the etching process and keeps the surface more intact than the corresponding orthophosphoric solution. The measured reductions in effective relative permittivity of the whole LTCC are with 10%, and 10.8% comparable independent whether a PBS1.2 or a P1 etching solution was applied. Whereas the relative permittivity of the

etched layer treated by PBS1.2 and P1 was calculated to be 6.18 and 5.87, respectively. These values show 18% and 22% reduction in comparison to the initial value for the *as-fired* LTCC. Finally, it is concluded that the buffered etching mixtures can be considered as a promising alternative to pure orthophosphoric etchants in future device fabrication process, due to a smooth LTCC surface topography.

The high surface quality of the porosified LTCC achieved in this work should allow for a high-quality metal deposition, which is essential for the reliable operation of high performance, high-frequency devices. Therefore, in future studies, high-quality metallic structures serving, *e.g.* as antenna elements should be realized on the porosified substrates. The high-frequency behaviour of modified LTCCs could be then investigated at frequencies up to 100 GHz, so that the microstructural changes can be directly correlated with the decrease in permittivity as well as the loss tangent.

Furthermore, the phase development and changes in the crystalline composition of GC LTCC during the sintering process were investigated by employing *in-situ* XRD analysis. From room temperature up to 825 °C no changes in the crystalline composition was measured. From 850 °C the crystalized of wollastonite was traced. By further rising the temperature to above 875 °C crystallization of anorthite phase from the glass phase could be observed. A further temperature increase to 925°C additional anorthite phase was detected while simultaneously the wollastonite fraction decreased. Beyond 925 °C, except for the slight increase in intensity of the newly formed anorthite peaks together with the decrease in the intensity of the corundum phase, no perceptible change in the diffractograms is observed. Anorthite crystallization thus, occurs as a result of two solid phase-boundary reactions involving (i) alumina dissolution and a reduction of the amount of residual glass phase, and (ii) alumina and wollastonite dissolution, without a further substantial reduction of the residual glass mass fraction. According to the obtained results, temperatures between 875 and 925 °C were found to be most suitable for the firing of GC LTCC. Also, the XPS and Raman analyses of LTCC substrates subjected to different firing profiles with varied peak temperature revealed the replacement of corundum with anorthite and, diffusion of the glass close to the surface of the samples. Finally, the *as-fired* samples were subjected to a wet chemical porosification process with an aqueous KOH solution.

Moreover, a B3B test setup was developed and used for the determination of the flexural strength of three different LTCC tapes, *i.e.* GC LTCC, DP951, and DP9k7. Regarding the construction and applicability of the B3B setup, it can be reported that the setup is suitable for the evaluation of flexural strength of the LTCC and other ceramic materials. The fracture behaviour of the samples indicates that the applied calculations are correct as the samples broke into two or three pieces starting from the centre. However, further fracture analysis of the examined specimen should be carried out to determine whether the fracture was indeed initiated in the centre of the specimen.

Finally, for the first time the porosified LTCC was successfully examined in catalytic reactions for clean energy production. Pd nanoparticles were impregnated on the porosified LTCC and the catalyst was used for hydrogen production from methanol and promising results, were obtained.

The developed catalysts primarily catalysed MeOH decomposition, rather than MSR. CO_2, the product which is primarily expected from the MSR process only occurred at high temperatures above 300 °C. The portions were barely noticeable and were mostly around 0.01 mol% which is practically negligible. The lack of CO_2 formation and selectivity is attributed to the insufficient formation of alloys. Because it is known that Pd alone only catalyses the decomposition of MeOH, and its alloys are active for MSR process. Therefore, the formation of bimetallic nanoparticles such as Pd-Zn on the LTCC substrates could be a solution to this problem. In future work, further studies are necessary to improve the activity, selectivity, and long-term activity of the catalyst. For example, specific surface area and porosity of the catalysts prior to and after the catalytic reaction should be measured. Also, detailed study should be performed on the impact of key parameters of the catalytic process such as structure, size, and stability of nanoparticles, as well as support-metal interactions.

REFERENCES

[1] X. Wang and A. Stelzer, "A 79-GHz LTCC patch array antenna using a laminated waveguide-based vertical parallel feed," *IEEE Antennas and Wireless Propagation Letters*, vol. 12, pp. 987–990, 2013.

[2] K.-C. Lin, C.-F. Chang, M.-C. Wu, and S.-J. Chung, "Dual-bandpass filters with serial configuration using LTCC technology," *IEEE transactions on Microwave Theory and Techniques*, vol. 54, no. 6, pp. 2321–2328, 2006.

[3] H. Ren, S. Jiang, M. Dang, T. Xie, H. Tang, H. Peng, H. Lin, and L. Luo, "Investigating on sintering mechanism and adjustable dielectric properties of BLMT glass/$Li_2Zn_3Ti_4O_{12}$ composites for LTCC applications," *Journal of Alloys and Compounds*, vol. 740, pp. 1188–1196, 2018.

[4] Y. Imanaka, *Multilayered low temperature cofired ceramics (LTCC) technology*. Springer Science & Business Media, 2005.

[5] K. Rida, *Packaging of Microwave Integrated Circuits in LTCC Technology*. PhD thesis, Electromagnetism Télécom Bretagne Université de Bretagne Occidentale, 2013.

[6] J. Zheng, C. Xing, Y. Yang, S. Li, H. Wu, and Z. Wang, "Structure, infrared reflectivity spectra and microwave dielectric properties of a low-firing microwave dielectric ceramic Pr_2Zr_3 $(MoO_4)_9$," *Journal of Alloys and Compounds*, vol. 826, p. 153893, 2020.

[7] Y. Zheng and W. Sheng, "Compact lumped-element LTCC bandpass filter for low-loss VHF-band applications," *IEEE Microwave and Wireless Components Letters*, vol. 27, no. 12, pp. 1074–1076, 2017.

[8] T. Rabe, M. Gemeinert, and W. A. Schiller, "Development of Advanced Low Temperature Co-Fired Ceramics (LTCC)," in *Euro Ceramics VIII*, vol. 264 of *Key Engineering Materials*, pp. 1181–1184, Trans Tech Publications Ltd, 7 2004.

[9] H. Bartsch, J. Pezoldt, F. M. M. Sanchez, J. J. J. Rios, J. M. M. Delgado, J. Breiling, and J. Müller, "LTCC as substrate-enabling semiconductor and packaging integration," in *2019*

22nd European Microelectronics and Packaging Conference & Exhibition (EMPC), pp. 1–4, IEEE, 2019.

[10] D. Belavic, M. Hrovat, G. Dolanc, M. S. Zarnik, J. Holc, and K. Makarovic, "Design of LTCC-based Ceramic Structure for Chemical Microreactor.," *Radioengineering*, vol. 21, no. 1, 2012.

[11] B. Jiang, J. Haber, A. Renken, P. Muralt, L. Kiwi-Minsker, and T. Maeder, "Fine structuration of low-temperature co-fired ceramic (LTCC) microreactors," *Lab on a Chip*, vol. 15, no. 2, pp. 563–574, 2015.

[12] M. Rauscher and A. Roosen, "Influence of Low-Temperature Co-Fired Ceramics Green Tape Characteristics on Shrinkage Behavior," *International Journal of Applied Ceramic Technology*, vol. 4, no. 5, pp. 387–397, 2007.

[13] W. H. Zachariasen, "THE ATOMIC ARRANGEMENT IN GLASS," *Journal of the American Chemical Society*, vol. 54, no. 10, pp. 3841–3851, 1932.

[14] D. Hülsenberg, A. Harnisch, and A. Bismarck, *Microstructuring of glasses*, vol. 87. Springer, 2008.

[15] G. M. Fasching, *Werkstoffe für die Elektrotechnik: Mikrophysik, Struktur, Eigenschaften*. Springer-Verlag, 2005.

[16] M. Mu, W. Zhang, F. C. Lee, and Y. Su, "Laminated low temperature co-fired ceramic ferrite materials and the applications for high current POL converters," in *2013 IEEE Energy Conversion Congress and Exposition*, pp. 621–627, IEEE, 2013.

[17] H.-J. Bargel and G. Schulze, *Werkstoffkunde*. Springer-Verlag, 2008.

[18] L. Golonka, K.-J. Wolter, A. Dziedzic, J. Kita, and L. Rebenklau, "Embedded passive components for MCM," in *24th International Spring Seminar on Electronics Technology. Concurrent Engineering in Electronic Packaging. ISSE 2001. Conference Proceedings (Cat. No. 01EX492)*, pp. 73–77, IEEE, 2001.

[19] T. Miyagi, Y. Iseki, K. Higuchi, Y. Shizuki, T. Hanawa, E. Takagi, M. Saito, K. Yoshihara, and M. Konno, "MCM-D/L using copper/photosensitive-BCB multilayer for upper microwave band systems," in *1996 Proceedings 46th Electronic Components and Technology Conference*, pp. 149–153, IEEE, 1996.

[20] S.-F. Gong, J. Strandberg, H. Thiede, H. Hentzell, H. Hesselbom, and W. Karner, "Investigation of high-speed pulse transmission in MCM-D," *IEEE transactions on components, hybrids, and manufacturing technology*, vol. 16, no. 7, pp. 735–742, 1993.

[21] J. J. Licari and L. R. Enlow, *Hybrid microcircuit technology handbook: materials, processes, design, testing and production*. Elsevier, 1998.

[22] L. Ren, X. Luo, and H. Zhou, “The tape casting process for manufacturing low-temperature co-fired ceramic green sheets: A review,” *Journal of the American Ceramic Society*, vol. 101, no. 9, pp. 3874–3889, 2018.

[23] https://www.apitech.com/products/microelectronic-solutions/low-temperature-co-fired-ceramic-ltcc/ "Acccessed: 30 September 2020".

[24] H. T. Sawhill, R. H. Jensen, and K. R. Mikeska, “Dimensional control in low-temperature cofired ceramic multilayers,” *Ceramic Transactions, 15 pp.*, vol. 611, 1990.

[25] S. H. Knickerbocker, A. H. Kumar, and L. W. Herron, “Cordierite glass-ceramics for multilayer ceramic packaging,” *American Ceramic Society Bulletin*, vol. 72, no. 1, pp. 90–95, 1993.

[26] Q. Zhang, X. Luo, W. Li, H. Zhuang, and D. Yan, “Tape casting of AlN/glass composites for LTCC substrate,” *Journal of materials science*, vol. 38, no. 8, pp. 1781–1785, 2003.

[27] R. Karmazin, O. Dernovsek, N. Ilkov, W. Wersing, A. Roosen, and M. Hagymasi, “New LTCC-hexaferrites by using reaction bonded glass ceramics,” *Journal of the European Ceramic Society*, vol. 25, no. 12, pp. 2029–2032, 2005.

[28] S. Kemethmüller, M. Hagymasi, A. Stiegelschmitt, and A. Roosen, “Viscous flow as the driving force for the densification of low-temperature co-fired ceramics,” *Journal of the American Ceramic Society*, vol. 90, no. 1, pp. 64–70, 2007.

[29] H. Jantunen, R. Rautioaho, A. Uusimäki, and S. Leppävuori, “Compositions of $MgTiO_3$–$CaTiO_3$ ceramic with two borosilicate glasses for LTCC technology,” *Journal of the European Ceramic Society*, vol. 20, no. 14, pp. 2331 – 2336, 2000.

[30] J.-S. Park, Y. Kim, H. Shin, J.-H. Moon, and W. Lim, “Calcium Zinc Borosilicate Glass with High Thermal Expansion Coefficient for LTCC Applications,” *Journal of the American Ceramic Society*, vol. 91, no. 11, pp. 3630–3633, 2008.

[31] R. Müller, R. Meszaros, B. Peplinski, S. Reinsch, M. Eberstein, W. A. Schiller, and J. Deubener, “Dissolution of alumina, sintering, and crystallization in glass ceramic composites for LTCC,” *Journal of the American Ceramic Society*, vol. 92, no. 8, pp. 1703–1708, 2009.

[32] L. Ren, X. Luo, Y. Xia, Y. Hu, and H. Zhou, “Fabrication of a high-performance film based borosilicate glass/Al_2O_3 ceramics for LTCC application,” *Journal of the European Ceramic Society*, vol. 37, no. 6, pp. 2415–2421, 2017.

[33] T. Rabe, W. A. Schiller, T. Hochheimer, C. Modes, and A. Kipka, “Zero Shrinkage of LTCC by Self-Constrained Sintering,” *International Journal of Applied Ceramic Technology*, vol. 2, no. 5, pp. 374–382, 2005.

[34] J. Zhou, “Towards rational design of low-temperature co-fired ceramic (LTCC) materials,” *Journal of Advanced Ceramics*, vol. 1, no. 2, pp. 89–99, 2012.

[35] M. Bengisu, "Structure and Properties of Conventional Ceramics," in *Engineering Ceramics*, pp. 447–466, Springer, 2001.

[36] D. Bahat, "Compositional study and properties characterisation of alkaline earth feldspar glasses and glass-ceramics," *Journal of Materials Science*, vol. 4, no. 10, pp. 855–860, 1969.

[37] Y.-P. Fu, C.-C. Chang, C.-H. Lin, and T.-S. Chin, "Solid-state synthesis of ceramics in the BaO–SrO–Al_2O_3–SiO_2 system," *Ceramics international*, vol. 30, no. 1, pp. 41–45, 2004.

[38] J. Kim, S. Hwang, W. Sung, and H. Kim, "Effect of anorthite and diopside on dielectric properties of Al_2O_3/glass composite based on high strength of LTCC substrate," *Journal of materials science*, vol. 43, no. 12, pp. 4009–4015, 2008.

[39] M. M. Krzmanc, M. Valant, and D. Suvorov, "A structural and dielectric characterization of NaxCa1- xAl_2- xSi^{2+} xO_8 (x= 0 and 1) ceramics," *Journal of the European Ceramic Society*, vol. 25, no. 12, pp. 2835–2838, 2005.

[40] C.-L. Lo, J.-G. Duh, B.-S. Chiou, and W.-H. Lee, "Low-temperature sintering and microwave dielectric properties of anorthite-based glass-ceramics," *Journal of the American Ceramic Society*, vol. 85, no. 9, pp. 2230–2235, 2002.

[41] S. Rentsch, *Bestimmung von Materialkennwerten zur Realisierung von Hoch-und Höchstfrequenzkomponenten in LTCC*. Ilmenau, 2011.

[42] D. Hülsenberg, *Keramik: Wie ein alter Werkstoff hochmodern wird*. Springer-Verlag, 2014.

[43] M. Okrusch and S. Matthes, *Mineralogie: eine Einführung in die spezielle Mineralogie, Petrologie und Lagerstättenkunde*. Springer-Verlag, 2013.

[44] M. Eberstein, T. Rabe, and W. A. Schiller, "Influences of the glass phase on densification, microstructure, and properties of low-temperature co-fired ceramics," *International journal of applied ceramic technology*, vol. 3, no. 6, pp. 428–436, 2006.

[45] M. Zawrah and E. Hamzawy, "Effect of cristobalite formation on sinterability, microstructure and properties of glass/ceramic composites," *Ceramics international*, vol. 28, no. 2, pp. 123–130, 2002.

[46] J.-H. Jean, Y.-C. Fang, S. X. Dai, D. L. Wilcox, *et al.*, "Effects of alumina on devitrification kinetics and mechanism of K2O–CaO–SrO–BaO–B2O3–SiO2 glass," *Japanese journal of applied physics*, vol. 42, no. 7R, p. 4438, 2003.

[47] K. Makarovič, A. Meden, M. Hrovat, J. Holc, A. Benčan, A. Dakskobler, and M. Kosec, "The effect of processing conditions on the properties of LTCC material," *Journal of the American Ceramic Society*, vol. 95, no. 2, pp. 760–767, 2012.

[48] Y. J. Seo, J. H. Jung, Y. S. Cho, J. C. Kim, and N. K. Kang, "Influences of particle size of alumina filler in an LTCC system," *Journal of the American Ceramic Society*, vol. 90, no. 2, pp. 649–652, 2007.

[49] C. D. Kumar, T. Sowmya, E. Sunny, N. Raghu, N. Venkataramani, and A. R. Kulkarni, "Influence of Nature of Filler on Densification of Anorthite-Based Crystallizable Glass+ Ceramic System for Low Temperature Cofired Ceramics Application," *Journal of the American Ceramic Society*, vol. 92, no. 3, pp. 595–600, 2009.

[50] M. Gemeinert, *Über LTCC-Werkstoffe aus dem Stoffsystem CaO-La_2O_3-Al_2O_3-B_2O_3*. PhD thesis, Bundesanstalt für Materialforschung und -prüfung, 2009.

[51] D. Thomas, P. Abhilash, and M. T. Sebastian, "Casting and characterization of $LiMgPO_4$ glass free LTCC tape for microwave applications," *Journal of the European Ceramic Society*, vol. 33, no. 1, pp. 87–93, 2013.

[52] R. Mistler, "The principles of tape casting and tape casting applications," in *Ceramic Processing*, pp. 147–173, Springer, 1995.

[53] J. Raynaud, V. Pateloup, M. Bernard, D. Gourdonnaud, D. Passerieux, D. Cros, V. Madrangeas, and T. Chartier, "Hybridization of additive manufacturing processes to build ceramic/metal parts: Example of LTCC," *Journal of the European Ceramic Society*, vol. 40, no. 3, pp. 759 – 767, 2020.

[54] J. Bertinet, E. Leleux, J. Cazenave, J. Ganne, M. Pate, R. Lebourgeois, E. Mueller, and F. Bechtold, "Filtering capacitors embedded in LTCC substrates for RF and microwave applications," *Microwave journal*, vol. 50, no. 11, p. 72, 2007.

[55] https://www.mst.com/msegmbh/products_services/substrates/ltcc/index.html "Acccessed: 30 September 2020".

[56] H. Jantunen, "A NOVEL LOW TEMPERATURE CO- FIRING CERAMIC (LTCC) MATERIAL FOR TELECOMMUNICATION DEVICES," 2001.

[57] V. Sunappan, A. Periannan, C. K. Meng, and W. C. Khuen, "Process issues and characterization of LTCC substrates," in *2004 Proceedings. 54th Electronic Components and Technology Conference (IEEE Cat. No. 04CH37546)*, vol. 2, pp. 1933–1937, IEEE, 2004.

[58] R. M. A. Lee, *Fabrication of 3D microwave and millimetre-wave components in LTCC technology*. University of Leeds, 2014.

[59] Y. Fournier, "3D structuration techniques of LTCC for microsystems applications," tech. rep., EPFL, 2010.

[60] T. Bartnitzek, T. Thelemann, S. Apel, and K.-H. Suphan, "Advantages and limitations of ceramic packaging technologies in harsh applications," in *International Symposium on Microelectronics*, vol. 2016, pp. 581–585, International Microelectronics Assembly and Packaging Society, 2016.

[61] J. Kita, A. Dziedzic, L. J. Golonka, and T. Zawada, "Laser treatment of LTCC for 3D structures and elements fabrication," *Microelectronics International*, 2002.

[62] T. Thelemann, H. Thust, and M. Hintz, "Using LTCC for microsystems," *Microelectronics International*, 2002.

[63] K. A. Peterson, K. D. Patel, C. K. Ho, S. B. Rohde, C. D. Nordquist, C. A. Walker, B. D. Wroblewski, and M. Okandan, "Novel Microsystem Applications with New Techniques in Low-Temperature Co-Fired Ceramics," *International Journal of Applied Ceramic Technology*, vol. 2, no. 5, pp. 345–363, 2005.

[64] https://www.microhybrid.de/produkte/elektronische-mikrosysteme/ltcc-mehrlagenkeramik.html "Acccessed: 25 May 2019".

[65] F. Bechtold, "A comprehensive overview on today's ceramic substrate technologies," in *2009 European Microelectronics and Packaging Conference*, pp. 1–12, 2009.

[66] M. Ko and S. Lyoo, "Novel Double-Layer Structure LTCC Substrate with Enhanced Flexural and Adhesions Strengths," *International Journal of Applied Ceramic Technology*, vol. 8, no. 1, pp. 180–186, 2011.

[67] S. Qian, F. Liu, M. Ma, G. Chen, Z. Liu, and Y. Li, "Mechanical strength enhancement of low temperature co-fired multilayer ceramic substrates by introducing residual stress," *Ceramics International*, vol. 45, no. 8, pp. 10982–10990, 2019.

[68] F. Steinhäußer, A. Talai, R. Weigel, A. Koelpin, A. Bittner, and U. Schmid, "Permittivity reduction and surface modification by porosification of LTCC," *Ceramics International*, vol. 42, no. 7, pp. 8925 – 8931, 2016.

[69] W. T. Sethi, M. Ashraf, S. Alshebeili, M. R. Al-Shareef, and H. M. Behairy, "Design of dual polarized hybrid LTCC antenna for UWB RFID applications," in *2016 5th International Conference on Electronic Devices, Systems and Applications (ICEDSA)*, pp. 1–4, 2016.

[70] A. Bittner, H. Seidel, and U. Schmid, "Permittivity of modified polyimide layers on LTCC," *Microelectronic Engineering*, vol. 88, no. 9, pp. 2977 – 2980, 2011.

[71] A. Sarikaya and F. Dogan, "Effect of various pore formers on the microstructural development of tape-cast porous ceramics," *Ceramics International*, vol. 39, no. 1, pp. 403 – 413, 2013.

[72] B. Synkiewicz, "Reduction of dielectric constant of LTCC substrates by introduction of controlled porosity," *Microelectronics International*, 2016.

[73] A. Bittner and U. Schmid, "The porosification of fired LTCC substrates by applying a wet chemical etching procedure," *Journal of the European Ceramic Society*, vol. 29, no. 1, pp. 99 – 104, 2009.

[74] J. Schelling, "Soil genesis, soil classification and soil survey," *Geoderma*, vol. 4, no. 3, pp. 165–193, 1970.

[75] F. Steinhäußer, A. Talai, G. Göltl, A. Steiger-Thirsfeld, A. Bittner, R. Weigel, A. Koelpin, and U. Schmid, "Concentration and temperature dependent selectivity of the LTCC porosification process with phosphoric acid," *Ceramics International*, vol. 43, no. 1, pp. 714–721, 2017.

[76] F. Steinhäußer, A. Talai, A. Steiger-Thirsfeld, A. Koelpin, R. Weigel, A. Bittner, and U. Schmid, "Graphical based characterisation and modelling of material gradients in porosified LTCC," *Journal of the European Ceramic Society*, vol. 34, no. 11, pp. 2833 – 2838, 2014. Modelling and Simulation meet Innovation in Ceramics Technology.

[77] B. Zhang, H. Gulan, T. Zwick, Y. Li, U. Oderfält, F. Carlsson, and H. Zirath, "Integration of a 140 GHz packaged LTCC grid array antenna with an InP detector," *IEEE Transactions on Components, Packaging and Manufacturing Technology*, vol. 5, no. 8, pp. 1060–1068, 2015.

[78] A. Hajian, D. Müftüoglu, T. Konegger, M. Schneider, and U. Schmid, "On the porosification of LTCC substrates with sodium hydroxide," *Composites Part B: Engineering*, vol. 157, pp. 14–23, 2019.

[79] F. Steinhäußer, K. Hradil, S. Schwarz, W. Artner, M. Stöger-Pollach, A. Steiger-Thirsfeld, A. Bittner, and U. Schmid, "Wet chemical porosification of LTCC in phosphoric acid: Anorthite forming tapes," *Journal of the European Ceramic Society*, vol. 35, no. 15, pp. 4181–4188, 2015.

[80] U. Ullah, N. Mahyuddin, Z. Arifin, M. Z. Abdullah, and A. Marzuki, "Antenna in LTCC technologies: a review and the current state of the art," *IEEE Antennas and Propagation Magazine*, vol. 57, no. 2, pp. 241–260, 2015.

[81] A. Talai, A. Kölpin, A. Bittner, F. Steinhäußer, and U. Schmid, "Porösizierte Glaskeramik-Substrate für die Radarsensorik," in *Automobil-Sensorik 2*, pp. 55–75, Springer, 2018.

[82] F. Steinhäußer, A. Talai, G. Sandulache, R. Weigel, A. Koelpin, W. Hansal, A. Bittner, and U. Schmid, "Pulse plated silver metallization on porosified LTCC substrates for high frequency applications," *Microelectronics Reliability*, vol. 60, pp. 93–100, 2016.

[83] A. Bittner and U. Schmid, "Permittivity of LTCC substrates porousified with a wet chemical etching process," *Procedia Engineering*, vol. 5, pp. 327–330, 2010.

[84] L. M. Anovitz and D. R. Cole, "Characterization and Analysis of Porosity and Pore Structures," *Reviews in Mineralogy and Geochemistry*, vol. 80, pp. 61–164, 01 2015.

[85] R. Haul, "S. J. Gregg, K. S. W. Sing: Adsorption, Surface Area and Porosity. 2. Auflage, Academic Press, London 1982. 303 Seiten," *Berichte der Bunsengesellschaft für physikalische Chemie*, vol. 86, no. 10, pp. 957–957, 1982.

[86] B. Nie, X. Liu, L. Yang, J. Meng, and X. Li, "Pore structure characterization of different rank coals using gas adsorption and scanning electron microscopy," *Fuel*, vol. 158, pp. 908 – 917, 2015.

[87] M. Ruike, T. Kasu, N. Setoyama, T. Suzuki, and K. Kaneko, "Inaccessible Pore Characterization of Less-Crystalline Microporous Solids," *The Journal of Physical Chemistry*, vol. 98, no. 38, pp. 9594–9600, 1994.

[88] Zdravkov, B. and J. Čermák and M. Šefara and J. Janků , "Pore classification in the characterization of porous materials: A perspective," *Open Chemistry*, vol. 5, no. 2, pp. 385–395, 2007.

[89] J. Rouquerol, D. Avnir, C. Fairbridge, D. Everett, J. Haynes, N. Pernicone, J. Ramsay, K. Sing, and K. Unger, "Recommendations for the characterization of porous solids (Technical Report)," *Pure and Applied Chemistry*, vol. 66, no. 8, pp. 1739–1758, 1994.

[90] H. Giesche, "Mercury Porosimetry: A General (Practical) Overview," *Particle & Particle Systems Characterization*, vol. 23, no. 1, pp. 9–19, 2006.

[91] H. K. Toenshoff and B. Denkena, *Basics of cutting and abrasive processes*. Springer, 2013.

[92] E. ISO, "4287–Geometrical Product Specifications (GPS)–Surface Texture: Profile Method–Terms, Definitions and Surface Texture Parameters," *International Organization for Standardization: Geneva, Switzerland*, 1997.

[93] S. Jung, "Oberflächenbeurteilung-Rauheitsmessung," 2012.

[94] D. Brune, R. Hellborg, H. J. Whitlow, and O. Hunderi, *Surface characterization: A user's sourcebook*. John Wiley & Sons, 2008.

[95] F. Crundwell, "The dissolution and leaching of minerals: Mechanisms, myths and misunderstandings," *Hydrometallurgy*, vol. 139, pp. 132 – 148, 2013.

[96] F. Crundwell, "The mechanism of dissolution of minerals in acidic and alkaline solutions: Part I — A new theory of non-oxidation dissolution," *Hydrometallurgy*, vol. 149, pp. 252 – 264, 2014.

[97] M. Bengisu, *Engineering ceramics*. Springer Science & Business Media, 2013.

[98] W. B. White, "Theory of corrosion of glass and ceramics," *Corrosion of glass, ceramics and ceramic superconductors*, no. 2, pp. 2–28, 1992.

[99] G. S. Frankel, J. D. Vienna, J. Lian, J. R. Scully, S. Gin, J. V. Ryan, J. Wang, S. H. Kim, W. Windl, and J. Du, "A comparative review of the aqueous corrosion of glasses, crystalline ceramics, and metals," *npj Materials Degradation*, vol. 2, no. 1, pp. 1–17, 2018.

[100] H. Scholze, *Glass: nature, structure, and properties*. Springer Science & Business Media, 2012.

[101] B. Terry, "The acid decomposition of silicate minerals part I. Reactivities and modes of dissolution of silicates," *Hydrometallurgy*, vol. 10, no. 2, pp. 135 – 150, 1983.

[102] J. I. Drever, *Surface and Ground Water, Weathering, and Soils: Treatise on Geochemistry, Volume 5*, vol. 5. Elsevier, 2005.

[103] S. L. Brantley, J. D. Kubicki, and A. F. White, *Kinetics of water-rock interaction*, vol. 168. Springer, 2008.

[104] W. A. Deer, R. A. Howie, and J. Zussman, "Rock-forming Minerals: Feldspars, Volume 4A," Geological Society of London, 2001.

[105] S. Gudbrandsson, D. Wolff-Boenisch, S. R. Gislason, and E. H. Oelkers, "Experimental determination of plagioclase dissolution rates as a function of its composition and pH at 22°C," *Geochimica et Cosmochimica Acta*, vol. 139, pp. 154 – 172, 2014.

[106] W. H. Casey, "On the relative dissolution rates of some oxide and orthosilicate minerals," *Journal of Colloid and Interface Science*, vol. 146, no. 2, pp. 586 – 589, 1991.

[107] E. H. Oelkers, J. Schott, and J.-L. Devidal, "The effect of aluminum, pH, and chemical affinity on the rates of aluminosilicate dissolution reactions," *Geochimica et Cosmochimica Acta*, vol. 58, no. 9, pp. 2011 – 2024, 1994.

[108] J.-H. Lee, N. Kidera, G. DeJean, S. Pinel, J. Laskar, and M. M. Tentzeris, "A V-band front-end with 3-D integrated cavity filters/duplexers and antenna in LTCC technologies," *IEEE Transactions on Microwave Theory and Techniques*, vol. 54, no. 7, pp. 2925–2936, 2006.

[109] B. Yuan, J. Mou, W. Yu, and X. Lv, "Five-pole LTCC cavity filter for wireless applications at 34GHz," in *2011 IEEE International Conference on Microwave Technology & Computational Electromagnetics*, pp. 193–195, IEEE, 2011.

[110] J. Xiong, Y. Li, Y. Hong, B. Zhang, T. Cui, Q. Tan, S. Zheng, and T. Liang, "Wireless LTCC-based capacitive pressure sensor for harsh environment," *Sensors and Actuators A: Physical*, vol. 197, pp. 30 – 37, 2013.

[111] Q. Tan, W. Lv, Y. Ji, R. Song, F. Lu, H. Dong, W. Zhang, and J. Xiong, "A LC wireless passive temperature-pressure-humidity (TPH) sensor integrated on LTCC ceramic for harsh monitoring," *Sensors and Actuators B: Chemical*, vol. 270, pp. 433 – 442, 2018.

[112] U. Schmid, G. Krötz, and D. Schmitt-Landsiedel, "A volumetric flow sensor for automotive injection systems," *Journal of Micromechanics and Microengineering*, vol. 18, no. 4, p. 045006, 2008.

[113] L. Manjakkal, K. Zaraska, K. Cvejin, J. Kulawik, and D. Szwagierczak, "Potentiometric RuO2–Ta2O5 pH sensors fabricated using thick film and LTCC technologies," *Talanta*, vol. 147, pp. 233 – 240, 2016.

[114] A. Brandenburg, J. Kita, A. Groß, and R. Moos, "Novel tube-type LTCC transducers with buried heaters and inner interdigitated electrodes as a platform for gas sensing at various high temperatures," *Sensors and Actuators B: Chemical*, vol. 189, pp. 80 – 88, 2013. Selected Papers from the 26th European Conference on Solid-State Transducers.

[115] M. Štekovič and J. Šandera, "Fabrication of electrochemical sensor in Low Temperature Co-fired Ceramics," in *Proceedings of the 2014 37th International Spring Seminar on Electronics Technology*, pp. 81–86, IEEE, 2014.

[116] K. Malecha, E. Remiszewska, and D. G. Pijanowska, "Surface modification of low and high temperature co-fired ceramics for enzymatic microreactor fabrication," *Sensors and Actuators B: Chemical*, vol. 190, pp. 873 – 880, 2014.

[117] S. Solomon, G.-K. Plattner, R. Knutti, and P. Friedlingstein, "Irreversible climate change due to carbon dioxide emissions," *Proceedings of the National Academy of Sciences*, vol. 106, no. 6, pp. 1704–1709, 2009.

[118] M. Dresselhaus and I. Thomas, "Alternative energy technologies," *Nature*, vol. 414, no. 6861, pp. 332–337, 2001.

[119] U. Eberle, M. Felderhoff, and F. Schüth, "Chemical and Physical Solutions for Hydrogen Storage," *Angewandte Chemie International Edition*, vol. 48, no. 36, pp. 6608–6630, 2009.

[120] G. A. Olah, "Beyond Oil and Gas: The Methanol Economy," *Angewandte Chemie International Edition*, vol. 44, no. 18, pp. 2636–2639, 2005.

[121] B. Jiang, T. Maeder, A. J. Santis-Alvarez, D. Poulikakos, and P. Muralt, "A low-temperature co-fired ceramic micro-reactor system for high-efficiency on-site hydrogen production," *Journal of Power Sources*, vol. 273, pp. 1202 – 1217, 2015.

[122] D. Li, X. Li, and J. Gong, "Catalytic Reforming of Oxygenates: State of the Art and Future Prospects," *Chemical Reviews*, vol. 116, no. 19, pp. 11529–11653, 2016.

[123] G. Li, C. Gu, W. Zhu, X. Wang, X. Yuan, Z. Cui, H. Wang, and Z. Gao, "Hydrogen production from methanol decomposition using Cu-Al spinel catalysts," *Journal of Cleaner Production*, vol. 183, pp. 415 – 423, 2018.

[124] Y. C. Sharma, A. Kumar, R. Prasad, and S. N. Upadhyay, "Ethanol steam reforming for hydrogen production: Latest and effective catalyst modification strategies to minimize carbonaceous deactivation," *Renewable and Sustainable Energy Reviews*, vol. 74, pp. 89 – 103, 2017.

[125] G. Prieto, J. Zečević, H. Friedrich, K. P. De Jong, and P. E. De Jongh, "Towards stable catalysts by controlling collective properties of supported metal nanoparticles," *Nature materials*, vol. 12, no. 1, pp. 34–39, 2013.

[126] V. Dal Santo, A. Gallo, A. Naldoni, M. Guidotti, and R. Psaro, "Bimetallic heterogeneous catalysts for hydrogen production," *Catalysis Today*, vol. 197, no. 1, pp. 190 – 205, 2012. Special Issue dedicated to Professor Pio Forzatti on the occasion of his 65th birthday.

[127] R. Trane-Restrup, S. Dahl, and A. D. Jensen, "Steam reforming of ethanol: Effects of support and additives on Ni-based catalysts," *International journal of hydrogen energy*, vol. 38, no. 35, pp. 15105–15118, 2013.

[128] A. Arslan, S. Gunduz, and T. Dogu, "Steam reforming of ethanol with zirconia incorporated mesoporous silicate supported catalysts," *International journal of hydrogen energy*, vol. 39, no. 32, pp. 18264–18272, 2014.

[129] Y. Lykhach, S. M. Kozlov, T. Skála, A. Tovt, V. Stetsovych, N. Tsud, F. Dvořák, V. Johánek, A. Neitzel, J. Mysliveček, *et al.*, "Counting electrons on supported nanoparticles," *Nature materials*, vol. 15, no. 3, pp. 284–288, 2016.

[130] N. Cakiryilmaz, H. Arbag, N. Oktar, G. Dogu, and T. Dogu, "Catalytic performances of Ni and Cu impregnated MCM-41 and Zr-MCM-41 for hydrogen production through steam reforming of acetic acid," *Catalysis Today*, vol. 323, pp. 191–199, 2019.

[131] B. Erdogan, H. Arbag, and N. Yasyerli, "SBA-15 supported mesoporous Ni and Co catalysts with high coke resistance for dry reforming of methane," *International Journal of Hydrogen Energy*, vol. 43, no. 3, pp. 1396–1405, 2018.

[132] J. Xin, H. Cui, Z. Cheng, and Z. Zhou, "Bimetallic Ni-Co/SBA-15 catalysts prepared by urea co-precipitation for dry reforming of methane," *Applied Catalysis A: General*, vol. 554, pp. 95–104, 2018.

[133] A. Taguchi and F. Schüth, "Ordered mesoporous materials in catalysis," *Microporous and mesoporous materials*, vol. 77, no. 1, pp. 1–45, 2005.

[134] A. Galarneau, H. Cambon, F. Di Renzo, R. Ryoo, M. Choi, and F. Fajula, "Microporosity and connections between pores in SBA-15 mesostructured silicas as a function of the temperature of synthesis," *New Journal of Chemistry*, vol. 27, no. 1, pp. 73–79, 2003.

[135] P. Munnik, P. E. de Jongh, and K. P. de Jong, "Recent developments in the synthesis of supported catalysts," *Chemical reviews*, vol. 115, no. 14, pp. 6687–6718, 2015.

[136] V. Murugesan, M. Gray, M. Guo, H. Job, L. Kovarik, A. Devaraj, S. Thevuthasan, and K. K. Ramasamy, "Thermally activated nucleation and growth of cobalt and nickel oxide nanoparticles on porous silica," *Journal of Vacuum Science & Technology A: Vacuum, Surfaces, and Films*, vol. 37, no. 3, p. 031101, 2019.

[137] Y. Han and J. Y. Ying, "Generalized fluorocarbon-surfactant-mediated synthesis of nanoparticles with various mesoporous structures," *Angewandte Chemie*, vol. 117, no. 2, pp. 292–296, 2005.

[138] C. Rameshan, H. Lorenz, M. Armbrüster, I. Kasatkin, B. Klötzer, T. Götsch, K. Ploner, and S. Penner, "Impregnated and co-precipitated Pd–Ga_2 O_3, Pd–In_2O_3 and Pd–Ga_2O_3–In_2O_3 catalysts: Influence of the microstructure on the CO_2 selectivity in methanol steam reforming," *Catalysis letters*, vol. 148, no. 10, pp. 3062–3071, 2018.

[139] H. Dong, Y.-C. Chen, and C. Feldmann, "Polyol synthesis of nanoparticles: status and options regarding metals, oxides, chalcogenides, and non-metal elements," *Green chemistry*, vol. 17, no. 8, pp. 4107–4132, 2015.

[140] E. Pizzutilo, J. Knossalla, S. Geiger, J.-P. Grote, G. Polymeros, C. Baldizzone, S. Mezzavilla, M. Ledendecker, A. Mingers, S. Cherevko, *et al.*, "The Space Confinement Approach Using Hollow Graphitic Spheres to Unveil Activity and Stability of Pt-Co Nanocatalysts for PEMFC," *Advanced Energy Materials*, vol. 7, no. 20, p. 1700835, 2017.

[141] P. R. Teixeira, M. S. Santos, A. L. G. Silva, S. N. Báo, R. B. Azevedo, M. J. A. Sales, and L. G. Paterno, "Photochemically-assisted synthesis of non-toxic and biocompatible gold nanoparticles," *Colloids and Surfaces B: Biointerfaces*, vol. 148, pp. 317–323, 2016.

[142] N. G. Bastús, J. Comenge, and V. Puntes, "Kinetically controlled seeded growth synthesis of citrate-stabilized gold nanoparticles of up to 200 nm: size focusing versus Ostwald ripening," *Langmuir*, vol. 27, no. 17, pp. 11098–11105, 2011.

[143] P. Kast, M. Friedrich, D. Teschner, F. Girgsdies, T. Lunkenbein, R. N. d'Alnoncourt, M. Behrens, and R. Schlögl, "CO oxidation as a test reaction for strong metal–support interaction in nanostructured Pd/FeOx powder catalysts," *Applied Catalysis A: General*, vol. 502, pp. 8–17, 2015.

[144] X. Du, S. Luo, H. Du, M. Tang, X. Huang, and P. K. Shen, "Monodisperse and self-assembled Pt-Cu nanoparticles as an efficient electrocatalyst for the methanol oxidation reaction," *Journal of Materials Chemistry A*, vol. 4, no. 5, pp. 1579–1585, 2016.

[145] P. F. Siril, L. Ramos, P. Beaunier, P. Archirel, A. Etcheberry, and H. Remita, "Synthesis of ultrathin hexagonal palladium nanosheets," *Chemistry of Materials*, vol. 21, no. 21, pp. 5170–5175, 2009.

[146] X. Huang, S. Tang, X. Mu, Y. Dai, G. Chen, Z. Zhou, F. Ruan, Z. Yang, and N. Zheng, "Freestanding palladium nanosheets with plasmonic and catalytic properties," *Nature nanotechnology*, vol. 6, no. 1, pp. 28–32, 2011.

[147] Z. Fan, X. Huang, C. Tan, and H. Zhang, "Thin metal nanostructures: synthesis, properties and applications," *Chemical Science*, vol. 6, no. 1, pp. 95–111, 2015.

[148] D. P. Debecker, K. Bouchmella, M. Stoyanova, U. Rodemerck, E. M. Gaigneaux, and P. H. Mutin, "A non-hydrolytic sol–gel route to highly active MoO_3–SiO_2–Al_2O_3 metathesis catalysts," *Catalysis Science & Technology*, vol. 2, no. 6, pp. 1157–1164, 2012.

[149] D. P. Debecker, M. Stoyanova, U. Rodemerck, P. Eloy, A. Léonard, B.-L. Su, and E. M. Gaigneaux, "Thermal Spreading As an Alternative for the Wet Impregnation Method: Advantages and Downsides in the Preparation of MoO_3/SiO_2- Al_2O_3 Metathesis Catalysts," *The Journal of Physical Chemistry C*, vol. 114, no. 43, pp. 18664–18673, 2010.

[150] N. Köpfle, T. Götsch, M. Grünbacher, E. A. Carbonio, M. Hävecker, A. Knop-Gericke, L. Schlicker, A. Doran, D. Kober, A. Gurlo, *et al.*, "Zirconium-Assisted Activation of Palladium To Boost Syngas Production by Methane Dry Reforming," *Angewandte Chemie International Edition*, vol. 57, no. 44, pp. 14613–14618, 2018.

[151] B. Zhang, Y. Niu, J. Xu, X. Pan, C.-M. Chen, W. Shi, M.-G. Willinger, R. Schlögl, and D. S. Su, "Tuning the surface structure of supported PtNi x bimetallic electrocatalysts for the methanol electro-oxidation reaction," *Chemical Communications*, vol. 52, no. 20, pp. 3927–3930, 2016.

[152] S. Rudi, D. Teschner, V. Beermann, W. Hetaba, L. Gan, C. Cui, M. Gliech, R. Schlögl, and P. Strasser, "pH-Induced versus Oxygen-Induced Surface Enrichment and Segregation Effects in Pt–Ni Alloy Nanoparticle Fuel Cell Catalysts," *ACS Catalysis*, vol. 7, no. 9, pp. 6376–6384, 2017.

[153] V. Papaefthimiou, T. Dintzer, M. Lebedeva, D. Teschner, M. Hävecker, A. Knop-Gericke, R. Schlögl, V. Pierron-Bohnes, E. Savinova, and S. Zafeiratos, "Probing metal–support interaction in reactive environments: an in situ study of PtCo bimetallic nanoparticles supported on TiO_2," *The Journal of Physical Chemistry C*, vol. 116, no. 27, pp. 14342–14349, 2012.

[154] W. Nawrot and K. Malecha, "Biomaterial Embedding Process for Ceramic–Polymer Microfluidic Sensors," *Sensors*, vol. 20, no. 6, p. 1745, 2020.

[155] P. Bembnowicz, M. Małodobra, W. Kubicki, P. Szczepańska, A. Górecka-Drzazga, J. Dziuban, A. Jonkisz, A. Karpiewska, T. Dobosz, and L. Golonka, "Preliminary studies on LTCC based PCR microreactor," *Sensors and Actuators B: Chemical*, vol. 150, no. 2, pp. 715–721, 2010.

[156] W. Nawrot, M. Fiedot-Toboła, and K. Malecha, "PDMS—LTCC lab on chip for photocatalytic effect analysis," in *2017 21st European Microelectronics and Packaging Conference (EMPC) & Exhibition*, pp. 1–5, IEEE, 2017.

[157] P. L. Suryawanshi, S. P. Gumfekar, B. A. Bhanvase, S. H. Sonawane, and M. S. Pimplapure, "A review on microreactors: Reactor fabrication, design, and cutting-edge applications," *Chemical Engineering Science*, vol. 189, pp. 431–448, 2018.

[158] M. Berenguel-Alonso, I. Ortiz-Gómez, B. Fernández, P. Couceiro, J. Alonso-Chamarro, L. Capitán-Vallvey, A. Salinas-Castillo, and M. Puyol, "An LTCC monolithic microreactor for the synthesis of carbon dots with photoluminescence imaging of the reaction progress," *Sensors and Actuators B: Chemical*, vol. 296, p. 126613, 2019.

[159] R. Knitter, D. Göhring, P. Risthaus, and J. Hausselt, "Microfabrication of ceramic microreactors," *Microsystem Technologies*, vol. 7, no. 3, pp. 85–90, 2001.

[160] F. Meschke, G. Riebler, V. Hessel, J. Schürer, and T. Baier, "Hermetic gas-tight ceramic microreactors," *Chemical Engineering & Technology: Industrial Chemistry-Plant Equipment-Process Engineering-Biotechnology*, vol. 28, no. 4, pp. 465–473, 2005.

[161] E. Kjeang, N. Djilali, and D. Sinton, "Microfluidic fuel cells: A review," *Journal of Power Sources*, vol. 186, no. 2, pp. 353–369, 2009.

[162] J. Hereijgers, T. Breugelmans, and W. De Malsche, "Chromatography as an inspiration for microreactors," *Journal of Chemical Technology & Biotechnology*, vol. 90, no. 12, pp. 2122–2131, 2015.

[163] K. S. Elvira, X. C. I. Solvas, R. C. Wootton, and A. J. Demello, "The past, present and potential for microfluidic reactor technology in chemical synthesis," *Nature chemistry*, vol. 5, no. 11, p. 905, 2013.

[164] Frank Steinhäußer, *Porosizieren von LTCC-Substraten mit Phosphorsäure für Hochfrequenzanwendungen*. PhD thesis, TU Wien, 2015.

[165] R. M. German, P. Suri, and S. J. Park, "liquid phase sintering," *Journal of materials science*, vol. 44, no. 1, pp. 1–39, 2009.

[166] M. R. Gongora-Rubio, P. Espinoza-Vallejos, L. Sola-Laguna, and J. Santiago-Aviles, "Overview of low temperature co-fired ceramics tape technology for meso-system technology (MsST)," *Sensors and Actuators A: Physical*, vol. 89, no. 3, pp. 222–241, 2001.

[167] W. Smetana, B. Balluch, G. Stangl, S. Lüftl, and S. Seidler, "Processing procedures for the realization of fine structured channel arrays and bridging elements by LTCC-Technology," *Microelectronics Reliability*, vol. 49, no. 6, pp. 592 – 599, 2009. IMAPS-CPMT Poland 2008.

[168] M. Unger, W. Smetana, and W. Ehrenzweig, "Mechanical characteristics of LTCC (Low Temperature Cofired Ceramics)-tapes for mechanical application," in *2007 30th International Spring Seminar on Electronics Technology (ISSE)*, pp. 59–64, IEEE, 2007.

[169] M. Franz, I. Atassi, A. Maric, B. Balluch, M. Weilguni, W. Smetana, C. Kluge, and G. Radosavljevic, "Material characteristics of the LTCC base material CeramTape GC," in *2012 35th International Spring Seminar on Electronics Technology*, pp. 276–281, IEEE, 2012.

[170] M. Brunella, A. Serafini, and M. Tanzi, "Characterization of 2D polymeric biomaterial structures or surfaces," in *Characterization of Polymeric Biomaterials*, pp. 3–19, Elsevier, 2017.

[171] Y. Wang and V. Petrova, *Scanning Electron Microscopy*, ch. 6, pp. 103–126. John Wiley and Sons, Ltd, 2012.

[172] C. Scheu and W. D. Kaplan, "Introduction to Scanning Electron Microscopy," *In-Situ Electron Microscopy: Applications in Physics, Chemistry and Materials Science. Wiley-VCH, Weinheim, Germany*, pp. 1–37, 2012.

[173] G. R. Holdren Jr and P. M. Speyer, "Reaction rate-surface area relationships during the early stages of weathering. II. Data on eight additional feldspars," *Geochimica et Cosmochimica Acta*, vol. 51, no. 9, pp. 2311–2318, 1987.

[174] F. Marinello, P. Bariani, E. Savio, A. Horsewell, and L. De Chiffre, "Critical factors in SEM 3D stereo microscopy," *Measurement Science and Technology*, vol. 19, no. 6, p. 065705, 2008.

[175] W. Drzazga, J. Paluszynski, and W. Slowko, "Three-dimensional characterization of microstructures in a SEM," *Measurement Science and Technology*, vol. 17, no. 1, p. 28, 2005.

[176] J. S. Villarrubia, A. Vladár, and M. T. Postek, "Scanning electron microscope dimensional metrology using a model-based library," *Surface and Interface Analysis: An International Journal devoted to the development and application of techniques for the analysis of surfaces, interfaces and thin films*, vol. 37, no. 11, pp. 951–958, 2005.

[177] D. Stokes, F. Morrissey, and B. Lich, "A new approach to studying biological and soft materials using focused ion beam scanning electron microscopy (FIB SEM)," in *Journal of Physics: Conference Series*, vol. 26, p. 50, IOP Publishing, 2006.

[178] M. Alicona, "Mex manual for mex 5.0. 1 en 01.02. 2008," *Alicona Imaging GmbH*, 2008.

[179] Support Application in X Ray Micro-Analysis. Saint Laurent Du Var,France, 2002.

[180] Scandium Solution Height Software. Olympus Soft Imaging Solutions GmbH, Munster, Germany, 2017.

[181] L. Carli, "3D-SEM metrology for coordinate measurements at the nanometer scale," 2010.

[182] D. Scharstein and R. Szeliski, "A taxonomy and evaluation of dense two-frame stereo correspondence algorithms," *International journal of computer vision*, vol. 47, no. 1-3, pp. 7–42, 2002.

[183] C. Azevedo and E. Marques, "Three-dimensional analysis of fracture, corrosion and wear surfaces," *Engineering Failure Analysis*, vol. 17, no. 1, pp. 286–300, 2010.

[184] C. Clarkson, N. Solano, R. Bustin, A. Bustin, G. Chalmers, L. He, Y. Melnichenko, A. Radliński, and T. Blach, "Pore structure characterization of North American shale gas reservoirs using USANS/SANS, gas adsorption, and mercury intrusion," *Fuel*, vol. 103, pp. 606 – 616, 2013.

[185] M. Schmitt, C. P. Fernandes, J. A. da Cunha Neto, F. G. Wolf, and V. S. dos Santos, "Characterization of pore systems in seal rocks using Nitrogen Gas Adsorption combined with Mercury Injection Capillary Pressure techniques," *Marine and Petroleum Geology*, vol. 39, no. 1, pp. 138 – 149, 2013.

[186] Y. Zhao, S. Liu, D. Elsworth, Y. Jiang, and J. Zhu, "Pore Structure Characterization of Coal by Synchrotron Small-Angle X-ray Scattering and Transmission Electron Microscopy," *Energy & Fuels*, vol. 28, no. 6, pp. 3704–3711, 2014.

[187] L. A. Harris and C. S. Yust, "Transmission electron microscope observations of porosity in coal," *Fuel*, vol. 55, no. 3, pp. 233–236, 1976.

[188] J.-L. Faulon, J. P. Mathews, G. A. Carlson, and P. G. Hatcher, "Correlation between micro-porosity and fractal dimension of bituminous coal based on computer-generated models," *Energy & fuels*, vol. 8, no. 2, pp. 408–414, 1994.

[189] E. Cuerda-Correa, M. Díaz-Díez, A. Macías-García, and J. Gañán-Gómez, "Determination of the fractal dimension of activated carbons: Two alternative methods," *Applied surface science*, vol. 252, no. 17, pp. 6102–6105, 2006.

[190] A. W. Adamson and A. P. Gast, *Physical chemistry of surfaces*, vol. 150. Interscience publishers New York, 1967.

[191] S. Lowell and J. Shields, "Influence of contact angle on hysteresis in mercury porosimetry," *Journal of Colloid and Interface Science*, vol. 80, no. 1, pp. 192–196, 1981.

[192] Z. Liu and D. Winslow, "Sub-distributions of pore size: A new approach to correlate pore structure with permeability," *Cement and Concrete Research*, vol. 25, no. 4, pp. 769 – 778, 1995.

[193] S. P. Rigby, R. S. Fletcher, and S. N. Riley, "Characterisation of porous solids using integrated nitrogen sorption and mercury porosimetry," *Chemical Engineering Science*, vol. 59, no. 1, pp. 41–51, 2004.

[194] V. Saxena, I. Shukla, and L. M. Pandey, "Chapter 8 - Hydroxyapatite: an inorganic ceramic for biomedical applications," in *Materials for Biomedical Engineering* (A.-M. Holban and A. M. Grumezescu, eds.), pp. 205 – 249, Elsevier, 2019.

[195] M. Birkholz, *Thin film analysis by X-ray scattering, chapter 1 Principles of X-ray Diffraction*. John Wiley & Sons, 2006.

[196] S. J. Hill, *Inductively coupled plasma spectrometry and its applications*, vol. 8. John Wiley & Sons, 2008.

[197] D. A. Skoog and J. J. Leary, *Instrumentelle Analytik: Grundlagen-Geräte-Anwendungen*. Springer-Verlag, 2013.

[198] A. Limbeck, M. Bonta, and W. Nischkauer, "Improvements in the direct analysis of advanced materials using ICP-based measurement techniques," *Journal of Analytical Atomic Spectrometry*, vol. 32, no. 2, pp. 212–232, 2017.

[199] http://www.rohs-cmet.in/content/icp-oes; "Acccessed: 25 May 2019".

[200] A. A. Ammann, "plasma mass spectrometry (ICP MS): a versatile tool," *Journal of mass spectrometry*, vol. 42, no. 4, pp. 419–427, 2007.

[201] R. E. Russo, X. Mao, H. Liu, J. Gonzalez, and S. S. Mao, "Laser ablation in analytical chemistry—a review," *Talanta*, vol. 57, no. 3, pp. 425–451, 2002.

[202] A. Limbeck, P. Galler, M. Bonta, G. Bauer, W. Nischkauer, and F. Vanhaecke, "Recent advances in quantitative LA-ICP-MS analysis: challenges and solutions in the life sciences and environmental chemistry," *Analytical and bioanalytical chemistry*, vol. 407, no. 22, pp. 6593–6617, 2015.

[203] S. Smetaczeck, "Development of ICP-based methods for laterally resolved stoichiometry determination of $Li_{7-3x}Al_xLa_3Zr_2O_{12}$ garnets," Diplomarbeit, TU Wien, 2016.

[204] N. Egeland, "Raman spectroscopy applied to enhanced oil recovery research," Master's thesis, University of Stavanger, Norway, 2015.

[205] A. Marcelli, A. Cricenti, W. M. Kwiatek, and C. Petibois, "Biological applications of synchrotron radiation infrared spectromicroscopy," *Biotechnology Advances*, vol. 30, no. 6, pp. 1390 – 1404, 2012. Special issue on ACB 2011.

[206] M. El-Desawy, *Characterization and application of aromatic self-assembled monolayers*. PhD thesis, Bielefeld University, Germany, 2007.

[207] M. Burrell, "Chemical Analysis, Electron Spectroscopy," in *Encyclopedia of Materials: Science and Technology* (K. J. Buschow, R. W. Cahn, M. C. Flemings, B. Ilschner, E. J. Kramer, S. Mahajan, and P. Veyssière, eds.), pp. 1142 – 1149, Oxford: Elsevier, 2001.

[208] https://www.tec-science.com/material-science/material-testing/bending-flexural-test/; "Acccessed: 25 May 2019".

[209] J. Hodgkinson, "7 - Flexure," in *Mechanical Testing of Advanced Fibre Composites* (J. Hodgkinson, ed.), Woodhead Publishing Series in Composites Science and Engineering, pp. 124 – 142, Woodhead Publishing, 2000.

[210] M. T. Sebastian and H. Jantunen, "Low loss dielectric materials for LTCC applications: a review," *International Materials Reviews*, vol. 53, no. 2, pp. 57–90, 2008.

[211] E. DIN, "843-1, Hochleistungskeramik-Mechanische Eigenschaft monolithischer Keramik bei Raumtemperatur-Teil 1: Bestimmung der Biegefestigkeit," 2008.

[212] D. Munz and T. Fett, *Ceramics: mechanical properties, failure behaviour, materials selection*, vol. 36. Springer Science & Business Media, 1999.

[213] K. Jlassi, M. M. Chehimi, and S. Thomas, *Clay-polymer nanocomposites*. Elsevier, 2017.

[214] R. Bermejo, "Mechanical properties of low temperature co-fired ceramics: testing methodologies for strength characterization," *J. Microelectron. Electron. Compon. Mater*, vol. 42, no. 4, pp. 254–259, 2012.

[215] A. Börger, P. Supancic, and R. Danzer, "The ball on three balls test for strength testing of brittle discs: stress distribution in the disc," *Journal of the European Ceramic Society*, vol. 22, no. 9, pp. 1425 – 1436, 2002.

[216] M. Dios, I. Kraleva, Z. González, P. Alvaredo, B. Ferrari, E. Gordo, and R. Bermejo, "Mechanical characterization of Ti (C, N)-based cermets fabricated through different colloidal processing routes," *Journal of Alloys and Compounds*, vol. 732, pp. 806–817, 2018.

[217] A. A. Porporati, T. Miyatake, K. Schilcher, W. Zhu, and G. Pezzotti, "Ball-on-ring test in ceramic materials revisited by means of fluorescence piezospectroscopy," *Journal of the European Ceramic Society*, vol. 31, no. 12, pp. 2031 – 2036, 2011.

[218] W. Harrer, R. Danzer, P. Supancic, and T. Lube, "The ball on three balls test: strength testing of specimens of different sizes and geometries," in *Proc. 10th Eur. Ceram. Soc. Conf.,(ed. JG Heinrich and C. Aneziris)*, pp. 1271–1275, 2007.

[219] https://www.bohler-edelstahl.com/en/products/k110/; "Acccessed: 30 September 2019".

[220] https://www.kugelpompel.at; "Acccessed: 30 September 2019".

[221] https://https://d2zo35mdb530wx.cloudfront.net/_legacy/UCPthyssenkruppBAMXAustria/assets.files/download/baustahl_datenblatt_tk_3505.pdf; "Acccessed: 30 September 2019".

[222] A. Hajian, S. Smetaczek, C. Zellner, M. Stöger-Pollach, T. Konegger, A. Limbeck, and U. Schmid, "Tailored and deep porosification of LTCC substrates with phosphoric acid," *Journal of the European Ceramic Society*, vol. 39, no. 10, pp. 3112 – 3119, 2019.

[223] A. Hajian, M. Brehl, T. Koch, C. Zellner, S. Schwarz, T. Konegger, D. de Ligny, and U. Schmid, "Wet-chemical porosification of LTCC substrates: Dissolution mechanism and mechanical properties," *Microporous and Mesoporous Materials*, vol. 288, p. 109593, 2019.

[224] R. C. Pullar, S. J. Penn, X. Wang, I. M. Reaney, and N. M. Alford, "Dielectric loss caused by oxygen vacancies in titania ceramics," *Journal of the European ceramic society*, vol. 29, no. 3, pp. 419–424, 2009.

[225] J. Varghese, P. Ramachandran, M. Sobocinski, T. Vahera, and H. Jantunen, "ULTCC glass composites based on rutile and Anatase with cofiring at 400° C for high frequency applications," *ACS sustainable chemistry & engineering*, vol. 7, no. 4, pp. 4274–4283, 2019.

[226] B. Lafuente, R. T. Downs, H. Yang, and N. Stone, "The power of databases: the RRUFF project," in *Highlights in mineralogical crystallography*, pp. 1–29, Walter de Gruyter GmbH, 2016.

[227] L. Li, C. A. Peters, and M. A. Celia, "Effects of mineral spatial distribution on reaction rates in porous media," *Water resources research*, vol. 43, no. 1, 2007.

[228] R. A. Berner, "Rate control of mineral dissolution under earth surface conditions," *American Journal of Science*, vol. 278, no. 9, pp. 1235–1252, 1978.

[229] G. Jordan and W. Rammensee, "Dissolution rates and activation energy for dissolution of brucite (001) : A new method based on the microtopography of crystal surfaces," *Geochimica et Cosmochimica Acta*, vol. 60, no. 24, pp. 5055 – 5062, 1996.

[230] A. C. Lasaga, "Chemical kinetics of water-rock interactions," *Journal of Geophysical Research: Solid Earth*, vol. 89, no. B6, pp. 4009–4025, 1984.

[231] G. Gardner and G. Nancollas, "Kinetics of crystal growth and dissolution of calcium and magnesium fluorides," *Journal of dental research*, vol. 55, no. 3, pp. 342–352, 1976.

[232] S. Hamzat and G. Nancollas, "Kinetics of dissolution of magnesium fluoride in aqueous solution," *Langmuir*, vol. 1, no. 5, pp. 573–576, 1985.

[233] R. Rice, "Use of normalized porosity in models for the porosity dependence of mechanical properties," *Journal of materials science*, vol. 40, no. 4, pp. 983–989, 2005.

[234] https://www.ferro.com/products/product-category/electronic-materials/ltcc-material-systems/low-temperature-co-fired-_ltcc_--materials/l8-ltcc-material-systems-for-low-mid-frequency-applications; "Acccessed: 30 September 2020".

[235] D. Jurków and L. Golonka, "Low-pressure, thermo-compressive lamination," *Journal of the European Ceramic Society*, vol. 32, no. 10, pp. 2431–2441, 2012.

[236] J.-B. Ollagnier, O. Guillon, and J. Rödel, "Effect of anisotropic microstructure on the viscous properties of an LTCC material," *Journal of the American Ceramic Society*, vol. 90, no. 12, pp. 3846–3851, 2007.

[237] M. Hrovat, K. Kielbasinski, K. Makarovič, D. Belavič, and M. Jakubowska, "The characterisation of lead-free thick-film resistors on different low temperature Co-fired ceramics substrates," *Materials Research Bulletin*, vol. 47, no. 12, pp. 4131–4136, 2012.

[238] P. Koutsoukos, Z. Amjad, M. Tomson, and G. Nancollas, "Crystallization of calcium phosphates. A constant composition study," *Journal of the American Chemical Society*, vol. 102, no. 5, pp. 1553–1557, 1980.

[239] W. T. Wofford and E. F. Gloyna, "Solubility of potassium hydroxide and potassium phosphate in supercritical water," *Journal of Chemical and Engineering Data*, vol. 40, no. 4, pp. 968–973, 1995.

[240] K. Hüttner, "Über die Einwirkung der Phosphorsäure auf Kieselsäure und Silikatgläser," *Zeitschrift für anorganische Chemie*, vol. 59, no. 1, pp. 216–224, 1908.

[241] G. Zuo, Y. Wan, and Y. Zhang, "Preparation and characterization of a novel laminated magnetic hydroxyapatite for application on gene delivery," *Materials Letters*, vol. 68, pp. 225–227, 2012.

[242] P. Mokoena, I. Nagpure, V. Kumar, R. Kroon, E. Olivier, J. Neethling, H. Swart, and O. Ntwaeaborwa, "Enhanced UVB emission and analysis of chemical states of Ca5 (PO4) 3OH: Gd3+, Pr3+ phosphor prepared by co-precipitation," *Journal of Physics and Chemistry of Solids*, vol. 75, no. 8, pp. 998–1003, 2014.

[243] A. Hajian, M. Stöger-Pollach, M. Schneider, D. Müftüoglu, F. K. Crunwell, and U. Schmid, "Porosification behaviour of LTCC substrates with potassium hydroxide," *Journal of the European Ceramic Society*, vol. 38, no. 5, pp. 2369–2377, 2018.

[244] J. Machorro, J. Olvera, A. Larios, H. Hernández-Hernández, M. Alcantara-Garduño, and G. Orozco, "Electrodialysis of phosphates in industrial-grade phosphoric acid," *International Scholarly Research Notices*, vol. 2013, 2013.

[245] A. Shaltout, R. Seoudi, E. El-Ashkar, and K. Eid, "Developed Method for Spectroscopic Studies of Viscous Samples," *Analytical letters*, vol. 41, no. 17, pp. 3034–3048, 2008.

[246] W. J. Symes Jr, G. R. Prinzbach, J. J. Maloney, J. E. Henry, O. W. Brown, S. Sridharan, Y.-S. Her, S. Wang, G. E. Graddy Jr, G. E. Sakoske, *et al.*, "Mid-K LTCC compositions and devices," Feb. 13 2018. US Patent 9,892,853.

[247] J. Henry, O. Brown, E. Graddy, E. Stadnicar, and B. Gardner, "New Ferro L8 LTCC system ready for high reliability electronic packaging applications," *Additional Papers and Presentations*, vol. 2011, no. CICMT, pp. 000119–000126, 2011.

[248] R. E. Benner, J. R. Mitchell, and R. W. Grow, "Raman scattering as a diagnostic technique for cathode characterization," *IEEE Transactions on Electron Devices*, vol. 34, no. 8, pp. 1842–1847, 1987.

[249] A. S. Jbara, Z. Othaman, and M. Saeed, "Structural, morphological and optical investigations of θ-Al_2O_3 ultrafine powder," *Journal of Alloys and Compounds*, vol. 718, pp. 1 – 6, 2017.

[250] P. Richet, P. Gillet, A. Pierre, M. A. Bouhifd, I. Daniel, and G. Fiquet, "Raman spectroscopy, x-ray diffraction, and phase relationship determinations with a versatile heating cell for measurements up to 3600 K (or 2700 K in air)," *Journal of Applied Physics*, vol. 74, no. 9, pp. 5451–5456, 1993.

[251] G. Berthomé, E. N'Dah, Y. Wouters, and A. Galerie, "Temperature dependence of metastable alumina formation during thermal oxidation of FeCrAl foils," *Materials and Corrosion*, vol. 56, no. 6, pp. 389–392, 2005.

[252] V. Simon, M. Todea, A. Takács, M. Neumann, and S. Simon, "XPS study on silica–bismuthate glasses and glass ceramics," *Solid state communications*, vol. 141, no. 1, pp. 42–47, 2007.

[253] Y. Tanizawa and T. Suzuki, "Effects of silicate ions on the formation and transformation of calcium phosphates in neutral aqueous solutions," *Journal of the Chemical Society, Faraday Transactions*, vol. 91, no. 19, pp. 3499–3503, 1995.

[254] J. T. Kloprogge, L. V. Duong, B. J. Wood, and R. L. Frost, "XPS study of the major minerals in bauxite: gibbsite, bayerite and (pseudo-) boehmite," *Journal of colloid and interface Science*, vol. 296, no. 2, pp. 572–576, 2006.

[255] E. Korin, N. Froumin, and S. Cohen, "Surface analysis of nanocomplexes by X-ray photoelectron spectroscopy (XPS)," *Acs Biomaterials Science & Engineering*, vol. 3, no. 6, pp. 882–889, 2017.

[256] D. J. Joyner and D. M. Hercules, "Chemical bonding and electronic structure of B2O3, H3BO3, and BN: An ESCA, Auger, SIMS, and SXS study," *The Journal of Chemical Physics*, vol. 72, no. 2, pp. 1095–1108, 1980.

[257] A. V. Naumkin, A. Kraut-Vass, S. W. Gaarenstroom, and C. J. Powell, "NIST standard reference database 20, version 4.1," *The National Institute of Standards and Technology NIST*, pp. 1–49, 2012.

[258] A. Burke, C. Brown, W. Bowling, J. Glaub, D. Kapsch, C. Love, R. Whitaker, and W. Moddeman, "Ignition mechanism of the titanium–boron pyrotechnic mixture," *Surface and Interface Analysis*, vol. 11, no. 6-7, pp. 353–358, 1988.

[259] A. K. Rumaiz, C. Jaye, J. Woicik, W. Wang, D. Fischer, J. Jordan-Sweet, and C. Chien, "Boron migration due to annealing in CoFeB/MgO/CoFeB interfaces: A combined hard x-ray

photoelectron spectroscopy and x-ray absorption studies," *Applied Physics Letters*, vol. 99, no. 22, p. 222502, 2011.

[260] C. Zhou, Y. Tang, W. Wang, S. Zhou, L. Zhao, H. Li, and H. Diao, "Preparation of p+-layers using water vapour as oxidant in BBr3 diffusion for silicon solar cells," *Journal of Physics D: Applied Physics*, vol. 46, no. 28, p. 285102, 2013.

[261] E. K. Salje, A. Buckley, G. Van Tendeloo, Y. Ishibashi, and G. L. Nord, "Needle twins and right-angled twins in minerals; comparison between experiment and theory," *American Mineralogist*, vol. 83, no. 7-8, pp. 811–822, 1998.

[262] https://https://www.dupont.com/products/greentape-951-ltcc-material-system.html; "Acccessed: 25 May 2019".

[263] https://www.dupont.com/products/green-tape-9k7-ltcc-material-system.html; "Acccessed: 25 May 2019".

[264] A. Börger, P. Supancic, and R. Danzer, "The ball on three balls test for strength testing of brittle discs: Part II: analysis of possible errors in the strength determination," *Journal of the European Ceramic Society*, vol. 24, no. 10, pp. 2917 – 2928, 2004.

[265] http://www.keramverband.de/brevier_engl/5/3/3/5_3_3_4.htm; "Acccessed: 25 May 2019".

[266] R. Bermejo, P. Supancic, I. Kraleva, R. Morrell, and R. Danzer, "Strength reliability of 3D low temperature co-fired multilayer ceramics under biaxial loading," *Journal of the European Ceramic Society*, vol. 31, no. 5, pp. 745 – 753, 2011.

[267] C. Krautgasser, R. Danzer, P. Supancic, and R. Bermejo, "Influence of temperature and humidity on the strength of low temperature co-fired ceramics," *Journal of the European Ceramic Society*, vol. 35, no. 6, pp. 1823–1830, 2015.

[268] http://http://www.matweb.com/search/datasheet.aspx?matguid=c00994cd9e48429f92782ab0c2fd94e5&ckck=1; "Acccessed: 25 May 2019".

[269] M. Weilguni, W. Smetana, G. Radosavljevic, J. Nicolics, W. Goebl, and A. Hofmann, "Low temperature co-fired ceramics processing parameters governing the performance of miniaturized force sensors," *Additional Papers and Presentations*, vol. 2012, no. CICMT, pp. 000411–000416, 2012.

[270] H. Lorenz, Q. Zhao, S. Turner, O. I. Lebedev, G. Van Tendeloo, B. Klötzer, C. Rameshan, K. Pfaller, J. Konzett, and S. Penner, "Origin of different deactivation of Pd/SnO_2 and Pd/GeO_2 catalysts in methanol dehydrogenation and reforming: A comparative study," *Applied Catalysis A: General*, vol. 381, no. 1, pp. 242 – 252, 2010.

[271] M. Borasio, O. Rodríguez de la Fuente, G. Rupprechter, and H.-J. Freund, "In situ studies of methanol decomposition and oxidation on Pd (111) by PM-IRAS and XPS spectroscopy," *The Journal of Physical Chemistry B*, vol. 109, no. 38, pp. 17791–17794, 2005.

[272] J. Y. Damte, S.-l. Lyu, E. G. Leggesse, and J. C. Jiang, "Methanol decomposition reactions over a boron-doped graphene supported Ru–Pt catalyst," *Physical Chemistry Chemical Physics*, vol. 20, no. 14, pp. 9355–9363, 2018.

[273] S. Hokenek and J. N. Kuhn, "Methanol decomposition over palladium particles supported on silica: Role of particle size and co-feeding carbon dioxide on the catalytic properties," *ACS Catalysis*, vol. 2, no. 6, pp. 1013–1019, 2012.

List of Figures

1.1 Comparison of **a)** amorphous and **b)** crystalline silicate networks. Si: silicon, Al: aluminum, Ca: calcium, Na: sodium, BO: bridging oxygen, NBO: non-bridging oxygen, IB: ionic bond[17]. 3

1.2 Different types of LTCC—composition, raw materials, and sintering mechanisms [8, 33]. 7

1.3 Tape casting process for the ceramic slurry [22, 53]. 7

1.4 **a)** A typical LTCC packaging process [54] **b)** Cross-section of an LTCC module [55]. 8

1.5 A typical LTCC firing profile. 9

1.6 An LTCC-based radiation sensor of a satellite [64]. 10

1.7 Schematic cross-section of different pore geometries. 16

1.8 The transition from waviness to roughness with decreasing wavelength [93]. 17

1.9 Unfiltered and filtered profiles [93]. 17

1.10 Comparison of the uptake of ions by the dissolution of crystalline albite, and albite composition glass [98]. 20

1.11 A corroded glass surface with ion-depleted leached layer, overlying precipitate or gel layer which ultimately recrystallizes on the surface [98]. 21

1.12 The structure of the charge interface, showing the changes in potential due to the space-charge layer, the so-called Helmholtz layer and the Gouy–Chapman layer [96]. 22

1.13 A model fo dissolution of silicate [103]. 23

1.14 The pH-dependency of reaction rate for quartz dissolution [96]. 23

1.15 Classification of feldspars [104]. 24

1.16 The effect of pH of the solution on the dissolution rate of anorthite [105]. 25

2.1 **a)** Photograph and **b)** schematic view of the etching setup with atmospheric pressure and 570 mL load capacity. (1: capped beaker, 2: temperature sensor, 3: sample holder, 4: sample clamp, 5: safety corner, 6: holder cross, 7: holder foot, 8: LTCC sample, 9: magnetic stirring bar, 10: hotplate) [164]. 34

2.2 **a)** The setup with the fixture inside the beaker, **b)** and **c)** front- and side-view of the sample holder and clamps loaded with samples, respectively. 35

2.3 Model of viscous flow sintering; glass phase melts and wets the alumina grains [166]. 36

2.4 **a)** Belt furnace used for firing the LTCC specimens, **b)** temperature and belt speed control unit, and **c)** air flow control and general control units. 37

2.5 View on the setup to measure the temperature profile at large (on the left) and in detail on fixation of the thermocouple to the belt (on the right). A sheet of A-tape and an alumina substrate were placed on top after the image was taken. 39

2.6 The firing profiles for GC LTCC with two different peak temperatures of 890 °C and 940 °C. To estimate the temperature repeatability, a mean value of three measurement cycles is given, whereas error bars indicate the deviations between the measurement cycles. 39

2.7 **a)** Schematic representation of the reactor setup. **b)** Flow diagram of the entire apparatus. The gas supply was controlled via the Mass Flow Controller (MFC). Solid lines show the pipeline while dashed lines represent the data transfer. 40

2.8 An overview of the measurement setup. 41

2.9 Representation of the measurement procedure. The curves for temperature (red) and the gases O_2 (yellow), H_2 (blue), CO_2 (green), CO (black) are shown. Also, the areas of oxidation step (highlighted in purple), reduction step (highlighted in blue) and temperature ramp (highlighted in red) are shown. The reaction time is plotted on the ordinate, the temperature (left), and the mole fraction of the reaction mixture (right) on the abscissa. 42

2.10 Existing signals in SEM analysis, upon those the backscattered electrons, secondary electrons, and characteristic X-rays are commonly used. Modified from [107, 172]. 43

2.11 **a)** Illustration of projection distance parameter for Stereo Creator reconstruction. **b)** An ideal (left) and a non-ideal (right) eucentric tilting [178]. 46

2.12 **a)** Configurations for stereo pair imaging in SEM. **b)** Adjustment in the SEM to obtain stereo images in the eucentric point. Top images show the error introduced by tilting the sample on the wrong plane, while bottom images show tilting on the eucentric plane [183]. 46

2.13 Hysteresis loop in pore-size distribution obtained from mercury porosimetry [192]. 49

2.14 Schematic representation of an ink-bottle pore at different states; **a)** empty pore, **b)** pore fully intruded with mercury and **c)** mercury partially trapped after the experiment (adapted from [90]). 49

2.15 **a)** Schematic of an ICP-OES setup [199], **b)** Schematic set-up of an ICP-MS [200]. . 53

2.16 Schematic of a laser ablation system, using ICP-OES or ICP-MS for detection (adapted from [201]). 54

2.17 Energy-level diagram for the three different forms of scattering. 55

2.18 Mean free path of electrons in solids as a function of their energy [206]. 56

2.19 Energy level diagram [206]. 57

2.20 **a)** Schematic of three-point bending test setup [208], **b)** the corresponding shear force and bending moment diagrams [209]. 59

2.21 **a)** Schematic representation of a B3B setup and **b)** FE simulation of the ball on three balls test assembly [215, 216]. 61

2.22 Stress distribution in a disc during typical loading conditions in a B3B test modelled with FE analysis. Dark areas indicate regions with high tensile stress, whereas the point marked with *I* represents the region of highest compressive stress [215]. . . . 62

2.23 **a)** Schematic of the test plate with grid and test numbers, **b)** Optical image of area 4 (applied force of 3.9 N), a small imprint is visible in the area marked with the red circle, **c)** Optical image of area 15 (applied force of 10N), where a larger imprint is visible. 65

2.24 **a)** 3D rendering of a quarter cut of the B3B setup, **b)** actual setup. Note that the block has a different geometry as only the thickness is important to keep the guide in place, under the setup is a positioning stage used to centre the setup to the machine punch. 66

2.25 Dial gauge mounted to a precision measuring table. 70

3.1 Mass removal of Ferro L8 as a function of time at varying bath temperatures, due to the etching with **a)** P50, and **c)** P85, and two representative cross-sectional SEM micrographs of Ferro L8 LTCC etched at 90 °C for 120 min with **b)** P50, and **d)** P85. 73

3.2 **a)** Top-view and **b)** corresponding cross-sectional SEM micrographs of Ferro L8 LTCC substrates etched with P50 at different etching times and bath temperatures. An SEM micrograph of an as-fired Ferro L8 LTCC is shown for comparison (**c**). Red arrows represent the depth of porosification. 74

3.3 Elemental distribution in an area of 100 μm × 100 μm for the *as-fired* and P50 etched Ferro L8. The colour represents the measured signal intensities in counts per second (cps) according to the scale bars. For the reason of comparison, the same scaling was used for all three samples. 76

3.4 **a)** X-ray diffraction diagrams for Ferro L8 as green tape, *as-fired*, and etched with a P50 etching solution. The intensity levels are shifted for comparison reasons. **b)** SEM micrograph of Ferro L8 etched with P50. Positions 1 and 2 represent alumina grains and glass matrix, respectively. 77

3.5 Raman spectra normalised to the maximum of the band in the Q-range, for *as-fired* LTCC and substrates etched with P50 at T_b=90 °C. Each spectrum is an average of 180 individual measurements. The reference spectra which were obtained from the RRUFF Database are shown at the bottom of the plot. The peak at 404 cm^{-1} which is marked with an arrow was used for estimation of etching depth. 78

3.6 Raman spectra normalized to the maximum of the band in the Q-range, for the *as-fired* LTCC and substrates etched with P50 for different times at T_b=90 °C. All spectra were normalized to their overall area. The red spectrum is related to the estimated maximum depth of porosification, d_p. The values given next to the spectra represent the depth at which the spectrum is acquired. 79

3.7 TEM lamella of a dense, *as-fired* Ferro L8 with three representative locations and the corresponding SAED patterns. 80

3.8 **a)** Cross-sectional view on the microstructure of surface-near porosified Ferro L8, and **b)** HAADF-STEM image **c)** and **d)** the corresponding EDX line profiles across a partially porosified section of the Ferro L8 LTCC etched with P50 for 30 min at T_b= 90 °C. For visualization purposes of the very low amount of Ba and Ti, these elements are plotted separately in **d**. 81

3.9 TEM images of a porosified LTCC substrate with three labelled locations for SAED analyses. At position 1, amorphous glass can be observed, whereas positions 2 and 3 represent crystalline corundum and celsian phase, respectively. 82

3.10 Pore opening diameter distribution and cumulative pore volume of samples in the etched (top) and the *as-fired* state (bottom). As seen from these results, apparent porosity larger than 10 μm can be primarily traced to the intrusion of interstitial space between aligned samples and hence, are disregarded during the interpretation of results. 83

3.11 Comparison of dissolution rates when etching Ferro L8 with P50 and P85 etching solutions at different bath temperatures. 84

3.12 Porosification depth d_p and corresponding Arrhenius diagrams when etching Ferro L8 with P50 (**a** and **c**), and P85 (**b** and **d**) solutions at different etching times. The E_a values determined from the linearly fitted lines and the R-square values for the linear fitting are given in 3.1. 85

3.13 Room temperature storage modulus of Ferro L8 substrates with two different thickness values of 180 and 520 μm etched with P50 at 75 °C for different etching times. The results for 180 μm thick LTCC etched at 90 °C are shown for comparison. . . . 87

3.14 The temperature-dependent storage modulus of Ferro L8 substrates with two different thicknesses of **a)** 180, and **b)** 520 μm, etched with P50 at 75 °C for different etching times. 88

3.15 **a)** Storage modulus of Ferro L8 substrates with two different thicknesses of 180 and 520 μm etched with P50 at T_b=75 °C for different etching times indicating results that are independent of the etching conditions. The results for 180 μm thick LTCC etched at T_b=90 °C are shown for comparison. **b)** The relation between storage modulus and the relative depth of porosification can be adequately described by an exponential fit function, assuming a porosity of 20% within the etched layer based on mercury intrusion porosimetry results. 89

3.16 SEM micrographs in top view of GC LTCC in the *as-fired* state as well as etched with 0.2 mol L^{-1} PBS with different pH values for 60 min at 90 °C. 90

3.17 Surface (**a**) and cross-section (**b**) of the GC LTCC etched with 0.2 mol L^{-1} PBS13.2 for 240 min at 90 °C. 91

3.18 Mass removal and porosification depth of GC LTCC substrates etched with PBS of different pH values. Due to the exceptionally high etching rates in the highly acidic region, etching times longer than 60 min were avoided. 92

3.19 SEM micrographs in the top view of the GC LTCC **a)** in the *as-fired* state, and etched at 90 °C with 0.2 mol L^{-1} solutions of **b)** Na_3PO_4 for 240 min, **c)** Na_2HPO_4 for 240 min, and **d)** NaH_2PO_4 for 60 min. 93

3.20 Cross-sectional SEM micrographs of the GC LTCC etched with 0.2 mol L^{-1} solutions of **a)** HCl for 1 h and **b)** NaOH for 4 h at 90 °C; **c)** the corresponding X-ray diffractograms. The peaks indexed by star sign are related to the new crystals formed on the surface of GC LTCC due to NaOH treatment. 94

3.21 **a)** X-ray diffractograms of GC LTCC etched with PBS at different pH-values compared to the *as-fired* LTCC; **b)** For better illustration of the small peaks observed after etching with PBS13.2, which are marked, the corresponding diffractograms are compared separately to the *as-fired* state in b. Stars label the new peaks formed after the etching treatment. 95

3.22 SEM micrographs in the top (**a**) and the cross-sectional (**b**) view of the GC LTCC etched with PBS1.2 at T_b= 90 °C for 120 min. 96

3.23 EDX line profile (along the indicated arrow), and elemental mapping (inside the indicated rectangle) for Al, Si, and Ca as key elements of the GC LTCC tape etched with PBS1.2. 96

3.24 TEM images of a porosified GC LTCC with three labelled locations for SAED analyses. 97

3.25 **a)** and **b)** Mass removal of GC tape as a function of time at varying bath temperatures, due to the etching with 0.2 mol L^{-1} PBS1.2, and **c)** dissolution rates as a function of bath temperatures, of the graphs given in b). For T_b= 90 °C only the first regime up to t=1 h is considered. 98

3.26 Porosification depth d_p (**a**) and corresponding Arrhenius diagrams (**b**) when etching GC with 0.2 mol L^{-1} PBS1.2 at different etching times and bath temperatures. . . . 99

3.27 SEM micrographs in cross-sectional and top view (insets) of GC LTCC etched with H_3PO_4 at different concentrations for 60 min at T_b = 90 °C. 100

3.28 Mass removal and d_p values for GC LTCC etched by orthophosphoric acid-based etching solutions with different concentrations. 101

3.29 Concentration-dependent kinematic viscosity of orthophosphoric acid at room temperature [245]. 102

3.30 Cumulative pore volume, pore opening diameter and relative pore volume for GC LTCC etched under different etching conditions. 103

3.31 SEM micrographs in top and cross-sectional view of GC LTCC etched with P1 at 90 °C and PBS1.2 at 90 °C and 75 °C, respectively. Insets in the second row represent lower magnification SEM images of corresponding cross-sections. 104

3.32 Effective relative permittivity of GC LTCC samples etched with PBS1.2 (left) and P1 (right) etchants at 90 °C, in dependence of etching times and corresponding d_p values. The red triangle represents the measured permittivity for the *as-fired* GC LTCC.105

4.1 SEM micrographs in top view of GC LTCC for **a)** *as-fired* state, and etched for 2 h with 3 mol L^{-1} KOH at **b)** 25 °C, **c)** 55 °C, **d)** 70 °C, **e)** 80 °C, and **f)** 90 °C. 109

4.2 SEM micrographs in top view of GC LTCC etched with 3 mol L^{-1} KOH at 80 °C for **a)** 60 min, **b)** 220 min, **c)** 330 min, and **d)** 930 min. 110

4.3 Stereo-SEM images of GC LTCC substrates **a)** *as-fired*, and **b)** etched with 3 mol L^{-1} KOH at 75 °C, and **c)** etched with P85 at 100 °C to illustrate LTCC surface modifications due to etching. 110

4.4 X-ray diffractograms of powdered GC LTCC before and after treatment with 3 mol L^{-1} KOH at 90 °C (an: anorthite, c: corundum). The intensity levels are shifted for comparison reasons. 111

4.5 EDX line profile across an unmodified, *as-fired* area of the GC LTCC etched in 3 mol L^{-1} KOH solution at 90 °C for 4 hours. 112

4.6 EDX line profile across an etched region indicating three different phases: pure Alumina at position 1, pure Silica at position 2 and Ca-rich aluminosilicate at position 3. The color used for each position is in correspondence with the chemical which is dominantly found in that position. Thus, position 1 is Al-enriched, while positions 2 and 3. are enriched in Si, and Ca, respectively. 113

4.7 TEM lamella of a KOH-etched GC LTCC with three representative locations labelled and the corresponding SAED analyses. At position 1 pure silica shows a nanocrystalline microstructure, close to an amorphous phase, whereas positions 2 and 3 feature pure alumina and Ca-rich aluminosilicate with a single-crystalline morphology.114

4.8 SEM micrograph in top view of the GC LTCC etched with 3M KOH (left) and the magnified SEM micrograph of the indicated rectangle (right). Arrows indicate the foam-like silica structures developed due to the etching process. 115

4.9 Bright-field TEM images of the GC LTCC etched with orthophosphoric acid (left) and KOH (right) etching solutions. White areas in the TEM image are indicating the pores.116

4.10 SEM micrograph in top view of the Ferro L8 LTCC surface in the *as-fired* state. . . . 117

4.11 SEM micrographs in top view of the Ferro L8 LTCC substrate surface etched with 1 mol L−1 NaOH at 75 °C for different etching times. 118

4.12 SEM micrographs in top view of the Ferro L8 surface etched for 4 h with 3 mol L^{-1} (left column) and 6 mol L^{-1} NaOH (right column) at different bath temperatures. . 119

4.13 Decrease in thickness of Ferro L8 as a function of etching time t due to treatment with NaOH etching solution at various bath temperatures and different concentrations.120

4.14 Roughness values for Ferro L8 LTCC substrates etched with NaOH at different times and etchant temperatures for varying NaOH concentrations. 120

4.15 **a)** Pore opening diameter distribution and cumulative pore volume of etched (top) and *as-fired* (bottom) samples, showing the bias caused by interstitial intrusion between specimens at pore opening diameters above 10 μm. **b)** Cross-sectional SEM image of the Ferro L8 LTCC etched with 3 mol L^{-1} NaOH solution at 90 °C for 6 h. 122

4.16 Mass removal of Ferro L8 LTCC due to etching with different NaOH concentrations as a function of etching times at varying bath temperatures 123

4.17 Comparison of dissolution rates when etching Ferro L8 with different etchants (left), and magnified plot of the data points in the area indicated by a rectangle (right). . 124

4.18 Porosification depths, d_p, values of Ferro L8 etched at various bath temperatures and different NaOH concentrations. The inserted straight lines serve as guide to the eyes 125

4.19 Cross-sectional SEM image of the Ferro L8 LTCC in the *as-fired* state, and etched with 6 mol L^{-1} NaOH solution at 90 °C for different etching times. 126

4.20 Porosification and partial substrate dissolution, represented by d_p' versus time for Ferro L8 etched with various bath temperatures and different NaOH concentrations. The inserted straight lines serve as guide to the eyes 127

4.21 Porosification depths, d_p, of the etchant versus the decrease in thickness as a function of etching temperature for various NaOH concentrations. Inserted lines serve as guides to the eye. 127

4.22 Schematic representation for pure surface porosification at different etching times (upper row) and porosification with partial substrate dissolution at different etching times (lower row). 127

4.23 Logarithm of d_p versus reciprocal bath temperature when etching Ferro L8 with NaOH solutions of various concentrations for different treatment times. 128

4.24 Logarithm of d_p' (Porosification + partial dissolution of the substrate) versus reciprocal bath temperature when etching Ferro L8 with NaOH solutions of various concentrations for different treatment times. 129

4.25 Predicted response for mass removal, porosification depth, and decrease in thickness of Ferro L8 LTCC substrates due to the etching with NaOH solutions according to the polynomial model. 131

5.1 Temperature program for XRD measurements while in-situ sintering the GC LTCC substrate. 133

5.2 *In situ* X-ray diffractograms of a GC LTCC subjected to different temperatures between **a)** 25 and 825 °C, and **b)** 850 and 1000 °C. The intensity levels are shifted for comparison reasons. 134

5.3 SEM micrographs of the GC LTCC green tapes, as well as substrates sintered at different peak temperatures. 135

5.4 X-ray diffractograms of GC LTCC green tapes fired with profiles of different peak temperatures. The intensity levels are shifted for comparison reasons. 136

5.5 **a)** Overview of the GC LTCC green tape in the dark field (top left), and bright field (top right) modes. The bright-field image is clockwise rotated for 90°. **b)** EDX mapping results for the indicated area (O is excluded), **c)** SAED analyses of three locations labelled in the bright field image. 137

5.6 Normalised Raman scattering spectra for GC green tape, and GC790 to GC940 samples. 138

5.7 Normalised Raman spectra of the different GC samples. The maxima of the sample peaks were attributed to the reference peaks from RRUFF database. Blue arrows - anorthite, red arrows - corundum, black arrows - CaO (B_2O_3) matrix, green arrows - wollastonite. 139

5.8 Normalised Raman spectra of GC840 and GC890 samples. 140

5.9 Comparison of calibrated high-resolution Al 2p peaks of the samples. 142

5.10 Comparison of calibrated high-resolution Si 2p peaks of the samples. 142

5.11 Comparison of calibrated high-resolution O 1s peaks of the samples. 143

5.12 SEM images of the different *as-fired* GC LTCC substrates etched for 2 h in 3 mol L^{-1} KOH solution at 75 °C. 145

5.13 Overview of GC LTCC substrates etched in 3 mol L^{-1} KOH solution at 90 °C for 6 hours for the substrates fired at different peak temperatures. 145

6.1 The temperature profiles based on manufacturer specifications for **a)** CeramTape GC and **b)** 951 DuPont. 148

6.2 Optical microscope images of a perfectly circular (left) and a partially deformed (right) DP-951 LTCC. 150

6.3 SEM surface micrographs of GC LTCC (first row), DP-951 (second row) and DP-9k7 (third row) fired with different temperature profiles. 151

6.4 DP-951, green tape and fired with different temperature profiles. 151

6.5 SEM micrographs of commercially fired LTCC tapes GC, DP 951, and DP 9k7. . . . 152

6.6 SEM micrographs in top view of the DP-951 (left) and GC LTCC etched at 90 °C with P50 solutions for 3 h. The corresponding SEM images of the *as-fired* samples are shown in Figure 6.3. 153

6.7 SEM micrographs in top view and cross-section of the DP-951 (left) and GC LTCC etched at 90 °C with P50 solutions for 21 h. The corresponding SEM images of the *as-fired* samples are shown in Figure 6.3. 153

6.8 Graphical presentation of the results for the flexural strength measurements according to DIN EN 843-5, **a)** GC *as-fired*, **b)** GC etched with 3 mol L^{-1} NaOH at 90 °C for 21h, **c)** DP-951 *as-fired*, **d)** DP-951 etched with 3mol L^{-1} NaOH at 90 °C for 21h, **e)** DP-9k7 *as-fired*. 155

7.1 Cross-sectional SEM micrographs of Ferro L8 LTCC substrates etched with **a)** P50 (Sample 1) and **b)** P50 followed by 3 mol L^{-1} NaOH (Sample 2). 158

7.2 Cross-sectional SEM micrographs of Pd-impregnated Ferro L8 LTCC substrates initially etched with a) P50 and b) P50 followed by 3 mol L^{-1} NaOH. Arrows indicate the impregnated Pd catalyst. 159

7.3 Recording the temperature ramp and the chemical activity for the blank LTCC sample. The curves for temperature (red), O_2 (yellow), H_2 (blue), CO_2 (green), CO (black) are shown. The reaction time is plotted on the ordinate, the temperature (left) and the molar fraction of the reaction mixture (right) on the abscissa. 160

7.4 Recording of the temperature ramp for sample 1 at reduction temperatures of **a)** 150, **b)** 200, **c)** 250, and **d)** 300 °C. The curves for temperature (red), O2 (yellow), H_2 (blue), CO_2 (green), CO (black) are shown. At the ordinate, the reaction time is applied, at the abscesses the temperature (left) and the proportion of the reaction mixture (right). 162

7.5 **a)** The overall temperature program for sample 1 at a reduction temperature of 150 °C. **b-e)** Recording of the temperature ramp for sample 1 at reduction temperatures of 150, 200, 250, and 300 °C. The curves for temperature (red), O2 (yellow), H_2 (blue), CO_2 (green), CO (black) are shown. At the ordinate, the reaction time is applied, at the abscesses the temperature (left) and the proportion of the reaction mixture (right). 163

7.6 Recording the temperature curve for Sample 1 (a) and Sample 2 (b), at a constant temperature of 300 °C. The curves for temperature (red), H_2 (blue), CO_2 (green), CO (black) are shown. The reaction time is plotted on the ordinate, the temperature (left) and the proportion of the reaction mixture (right) on the abscissa. 166

List of Tables

1.1 The commonly used conductors with LTCC and HTCC materials [4]. 4

1.2 Some advantages of LTCC over other commonly used substrate technologies [23]. . 5

1.3 Technical characteristics of LTCC, HTCC, and PCB substrates [65]. Typical values are listed. 10

1.4 Properties and compositions of some commercially available LTCC systems before and after sintering [50]. 12

1.5 Some commonly used roughness parameters and their definitions [94]. 18

2.1 Technical information and properties of the tapes used in this work. 32

2.2 Orthophosphoric acid etching solutions with different concentrations. 32

2.3 PBS buffer ranges, and the required amount of each component for preparing 500 mL of 0.2 mol L^{-1} solution. 33

2.4 Solutions prepared from individual PBS components without pH adjustment. 33

2.5 Airflow parameters during firing 37

2.6 Parameters of the LA-ICP-MS experiments. 55

2.7 Constants evaluated for three different Poisson´s ratios [215]. 62

2.8 Evaluated range of parameters for the factor f [215, 218]. 63

3.1 Activation energies from the Arrhenius diagrams in Figure 3.12. 86

3.2 Activation energies from the Arrhenius diagrams in Figure 3.26. 99

3.3 The d_p and porosities of the GC LTCC substrates treated for 30 min at different etching conditions. Pore openings larger than 5 μm are excluded. 104

4.1 Roughness parameters for *as-fired* and etched GC LTCC. 111

4.2 Activation energies from the Arrhenius diagrams of Figure 4.23. 128

4.3 Activation energies from the Arrhenius diagrams of Figure 4.24. 129

5.1 The relative atomic concentration of chemical elements on the surface of the samples calculated from high-resolution XPS spectra. 141

5.2 Chemical bond concentration determined from deconvoluted Al 2p peaks of the samples. 141

5.3 Chemical bond concentration determined from deconvoluted Si 2p peaks of the samples. 142

5.4 Chemical bond concentration determined from deconvoluted O 1s peaks of the samples. 143

6.1 Shrinkage and weight loss of LTCC tapes fired with profile *b-900*, samples used for B3B tests 149

6.2 Results of roughness measurements, R_a and R_q values in μm according to EN ISO 25178. 150

6.3 Weibull-modulus and characteristic flexural strength of investigated LTCC substrates. 154

7.1 Comparison of the conversions at *ca.* 300 °C in the individual measurements for Sample 1 and Sample 2 and for various previous reduction temperatures. The optimal sales are underlined. 165

Nomenclature

Abbreviations

μR	Microreactor
3D	Three-Dimensional
B3B	Ball-on-Three-Balls
BO	Bridging Oxygen
CAD	Computer Aided Design
cps	Counts Per Second
DBFIB	Dual-Beam Focused Ion Beam
DEM	Digital Elevation Model
DI	Deionized
DMA	Dynamic-Mechanical Analysis
DOE	Design of experiments
DP951	Dupont 951 Tape
DP9k7	Dupont 9k7 Tape
EDX	Energy-Dispersive X-ray Spectroscopy
EELS	Electron Energy Loss Spectroscopy
FC	Fuel Cell
FE(M)	Finite Element (Method)
Ferro L8	L8 LTCC Tape
GBC	Glass Bonded Ceramics

GC LTCC	CeramTape GC
GCC	Glass-Ceramic Composites
GC	Glass-Ceramics
GPS	Global Positioning Systems
HTCC	High Temperature Co-Fired Ceramic
IB	Ionic Bond
ICP-MS	Inductively Coupled Plasma Mass Spectrometry
ICP-OES	Inductively Coupled Plasma Optical Emission Spectroscopy
ICP	Inductively Coupled Plasma
IoT	Internet of Things
ISAS	Institute of Sensor and Actuator Systems
LA-ICP-MS	Laser Ablation Inductively Coupled Plasma Mass Spectrometry
LA	Laser Ablation
LOC	Lab-on-a-Chip
LTCC	Low Temperature Co-Fired Ceramic
MCM-C	Ceramic Multi-Chip Module
MCM-D	Deposited Multi-Chip Module
MCM-L	Laminated Multi-Chip Module
MCM	Multi-Chip Module
MEMS	Micro-Electro-Mechanical Systems
MeOH	Methanol
MFC	Mass Flow Controller
MSA (Model)	Minimum Solid Area (Model)
MSE	Micro Systems Engineering GmbH
MSR	Methanol Steam Reforming
NBO	Non-Bridging Oxygen

NP	Nanoparticle
PBS	Phosphate Buffer Solution
PCB	Printed Circuit Board
PS	Polystyrene
PTFE	Polyterafluorethylene
RDS	Rate-Determining Step
RF	Radio Frequency
RH	Relative Humidity
RT	Room Temperature
SAED	Selected Area Electron Diffraction
SEM	Scanning Electron Microscopy
SR	Steam Reforming
STEM	Scanning Transmission Electron Microscopy
TEM	Transmission Electron Microscopy
TPH (sensor)	Temperature-Pressure-Humidity(sensor)
XPS	X-ray Photoelectron Spectroscopy
XRD	X-ray Diffraction

Chemical Formulas

$(Ca, Na)Al(Si, Al)_3O_8$	Labradorite
$[A^-]$	Concentration of Conjugated Base
$[HA]$	Concentration of Acid
$[PBS]$	Concentration of Phosphate Buffer Solution
Ag	Silver
Al_2O_3	Alumina, Corundum
AlN	Aluminium Nitride
Au	Gold

$Ba[Al_2Si_2O_8]$	Celsian
$Ca[Al_2Si_2O_8]$	Anorthite
$Ca_3[Si_3O_9]$	Wollastonite
CH_3OH	Methanol
CO	Carbon Monoxide
CO_2	Carbon Dioxide
$GaAs$	Gallium Arsenide
$H2$	Hydrogen
H_2O	Hydrogen Oxide (Water)
H_3PO_4	(Ortho)phosphoric Acid
HCl	Hydrochloric Acid
KOH	Potassium Hydroxide
$Mg_2Al_3[AlSi_5O_{18}]$	Cordierite
Mo	Molybdenum
Na_2HPO_4	Disodium Phosphate
$Na_3PO_4.12H_2O$	Trisodium Phosphatedodecahydrate
NaH_2PO_4	Monosodium Phosphate
$NaOH$	Sodium Hydroxide
Pd	Palladium
PS	Polystyrene
TiO_2	Titanium Dioxide
W	
ZnO	Zinc Oxide

Physical Symbols

ν	Poisson's Ratio
σ	Flexural Strength

ε_r	Relative Permittivity
C	Capacitance
CTE	Coefficient of Thermal Expansion
d_p	Porosification Depth
E	Young's Modulus
E'	Storage Modulus
E_a	Activation Energy
E_b	Binding Energy
F_s	Shear Force
m	Weibull-Modulus
N	Number of Evaluated Samples
P	Total Porosity
P_d	Projection Distance
P_{fi}	Probability Value
pK_a	Negative Log of Acid Dissociation Constant
R	Disc Radius
R_a	Support Radius
R_b	Ball Radius
R_q	Quadratic Mean Roughness
R_{ar}	Arithmetic Average Roughness
t	Etching Time
T_b	Bath Temperature
$tan\delta$	Dissipation Factor or Loss Tangent

List of Publications

Journal papers as first author:

1. **A. Hajian**, T. Konegger, K. Bielecki, B. Mieller, T. Rabe, S. Schwarz, C. Zellner, U. Schmid (**2020**), "Wet chemical porosification with phosphate buffer solutions for permittivity reduction of LTCC substrates" submitted to *Journal of Alloys and Compounds*, Under review.

2. **A. Hajian**, D. Müftüoglu, T. Konegger, M. Schneider, U. Schmid (**2019**) "On the porosification of LTCC substrates with sodium hydroxide" *Composites Part B: Engineering*, 157, 14-23.

3. **A. Hajian**, M. Brehl, T. Koch, C. Zellner, S. Schwarz, T. Konegger, D. de Ligny, U. Schmid (**2019**) "Wet-chemical porosification of LTCC substrates: Dissolution mechanism and mechanical properties" *Microporous and Mesoporous Material*, 288, 109593-109602.

4. **A. Hajian**, S. Smetaczek, C. Zellner, M. Stöger-Pollach, T. Konegger, A. Limbeck, U. Schmid (**2019**) "Tailored and deep porosification of LTCC substrates with phosphoric acid" *Journal of the European Ceramic Society*, 39, 3112-3119.

5. **A. Hajian**, M. Stöger-Pollach, M. Schneider, D. Müftüoglu, F.K. Crunwell, U. Schmid (**2018**) "Porosification Behaviour of LTCC Substrates with Potassium Hydroxide" *Journal of the European Ceramic Society*, 38, 2369-2377.

6. **A. Hajian**, J. Ghodsi, A. Afraz, O. Yurchenko, G. Urban (**2016**) "Nanomolar detection of methylparaben by a cost-effective hemoglobin-based biosensor" *Materials Science and Engineering: C*, 69, 122-127.

7. **A. Hajian**, A.A. Rafati, O. Yurchenko, G. Urban, A. Afraz, M. Najafi, A. Bagheri (**2015**) "Nanostructured flower like Pt-Ru for ethanol oxidation and determination" *Journal of the Electrochemical Society*, 162(1), B41-B46.

8. **A. Hajian**, A.A. Rafati, A. Afraz, M. Najafi (**2014**) "Electrosynthesis of polythiophene nanowires and their application for sensing of chlorpromazine" *Journal of The Electrochemical Society*, 161 (9), B196-B200.

9. **A. Hajian**, A.A. Rafati, A. Afraz, M. Najafi (**2014**) "Electrosynthesis of high-density polythiophene nanotube arrays and their application for sensing of riboflavin" *Journal of Molecular Liquids*, 199, 150-155.

10. **A. Hajian**, S. Azizian (**2012**) "On the adsorption of some phenolic compounds from aqueous solutions onto activated carbon cloth: Equilibrium and kinetic studies" *Journal of Dispersion and Technology*, 33, 1629-1634.

Journal papers as co-author:

1. F. Fazlali, P. Hashemi, S. Khoshfetrat, R. Halabian, B. Baradaran, M. Johari-Ahar, P. Karami, **A. Hajian**, H. Bagheri, "Electrochemiluminescent biosensor for ultrasensitive detection of lymphoma cancer in early stage using CD20 markers as B cell-specific antigens" submitted to *Bioelectrochemistry*, Under review.

2. A. Ghoorchian, A. Afkhami, T. Madrakian, R. Rameshan, C. Rameshan, **A. Hajian**, (**2020**) "Absorbance-based spectroelectrochemical sensor for determination of ampyra based on electrochemical preconcentration" Sensors and Actuators B: Chemical, 275, 180-189.

3. F. Fazlali, **A. Hajian**, A. Afkhami, H. Bagheri, (**2020**)"A superficial approach for fabricating unique ternary AgI@TiO_2/Zr-MOF composites: An excellent interfacial with improved photocatalytic light-responsive under visible light" *Journal of Photochemistry and Photobiology A: Chemistry*, 400 (1), 112717.

4. A. Khanmohammadi, A. Aghaei, E. Vahedi, A. Qazvini, M. Ghanei, A. Afkhami, **A. Hajian**, H. Bagheri, (**2020**) "Electrochemical biosensors for the detection of lung cancer biomarkers: A review" *Talanta*, 206(1),120251-120266.

5. I. Lau, **A. Hajian**, F. Michler, G. Gold, F. Lurz, U. Schmid, K. Helmreich, R. Weigel, A. Koeplin, (**2019**) "Influence of the PCB manufacturing process on the measurement error of planar relative permittivity sensors up to 100 GHz" *IEEE Transactions on Microwave Theory and Techniques*, 67 (7), 2793-2804.

6. A. Aghaie, A. Khanmohammadi, **A. Hajian**, U. Schmid, H. Bagheri, (**2019**) "Nonenzymatic electrochemical determination of paraoxon ethyl in water and fruits by graphene-based NiFe bimetallic phosphosulfide nanocomposite as a superior sensing layer" *Food Analytical Methods*, 12 (7), 1545-1555.

7. E. Mahmoudi, **A. Hajian**, M. Rezaei, A. Afkhami, A. Amine, H. Bagheri (**2019**) "A novel platform based on graphene nanoribbons/protein capped Au-Cu bimetallic nanoclusters: Application to the sensitive electrochemical determination of bisphenol A" *Microchemical Journal*, 145, 242-251.

8. M.S. Shahrivar, N. Karimian, H. Fakhri, **A. Hajian**, A. Afkhami, H. Bagheri (**2019**) "Design and application of a non-enzymatic sensor based on Metal-Organic Frameworks for the simultaneous determination of carbofuran and carbaryl in fruits and vegetables" *Electroanalysis*, 31, 1-12.

9. M. Sajadpour, H. Siampour, S. Abbasian, M. Amiri, R. Rameshan, C. Rameshan, **A. Hajian**, H. Bagheri, A. Moshaii (**2019**) "A non-enzymatic glucose sensor based on the hybrid thin films of Cu on acetanilide/ITO" *Journal of The Electrochemical Society*, 166 (13) B1116-B1125.

10. A. Afkhami, H. Fakhri, **A. Hajian**, E. Mahmoudi, H. Bagheri, (**2019**) "High-performance electrochemical enzyme sensor for the organophosphate pesticides detection using modified metal-organic framework sensing platform" *Bioelectrochemistry*, 107348.

11. N. Karimian, H. Fakhri, S. Amidi, **A. Hajian**, F. Arduini, H. Bagheri (**2019**) "A novel sensing layer based on metal-organic framework UiO-66 modified with TiO_2-graphene oxide: application to rapid, sensitive and simultaneous determination of paraoxon and chlorpyrifos" *New Journal of Chemistry*, 43, 2600-2609.

12. N. Pajooheshpour, M. Rezaei, **A. Hajian**, A. Afkhami, M. Sillanpää, F. Arduini, H. Bagheri (**2018**) "Protein templated Au-Pt nanoclusters-graphene nanoribbons as a high performance sensing layer for the electrochemical determination of diazinon" *Sensors and Actuators B: Chemical*, 275, 180-189.

13. T. Rahmani, **A. Hajian**, A. Afkhami, H. Bagheri, (**2018**) "A novel and high performance enzymeless sensing layer for electrochemical detection of methyl parathion based on BSA templated Au-Ag bimetallic nanoclusters" *New Journal of Chemistry*, 42, 7213-7222.

14. T. Rahmani, H. Bagheri, M. Behbahani, **A. Hajian**, A. Afkhami, (**2018**) "Modified 3D graphene-Au as a novel sensing layer for direct and sensitive electrochemical determination of carbaryl pesticide in fruit, vegetable, and water samples" *Food Analytical Methods*, 11, 3005-3014.

15. S. Najari, H. Bagheri, Z.M. Khoshhesab, **A. Hajian**, A. Afkhami, (**2018**) "Electrochemical sensor based on gold nanoparticle-multiwall carbon nanotube nanocomposite for the sensitive determination of docetaxel as an anticancer drug" *Ionics*, 89, 1–11.

16. H. Bagheri, **A. Hajian**, M. Rezaei, A. Shirzadmehr (**2017**) "Composite of Cu metal nanoparticles-multiwall carbon nanotubes-reduced graphene oxide as a novel and high performance platform of the electrochemical sensor for simultaneous determination of nitrite and nitrate" *Journal of Hazardous Materials*, 324, 762-772.

17. H. Bagheri, A. Afkhami, H. Khoshsafar, **A. Hajian**, A. Shahriyari (**2017**) "Protein capped Cu nanoclusters-SWCNT nanocomposite as a novel candidate of high performance platform for organophosphates enzymeless biosensor" *Biosensors and Bioelectronics*, 89, 829–836.

18. H. Salehzadeh, D. Nematollahi, **A. Hajian**, (**2017**) "1,2,4-Triazole-3-thiol-protected silver-nanoparticles as a platform for ECE electrochemical reaction" *Electrochemistry Communications*, 82, 56–60.

19. H. Bagheri, N. Pajooheshpour, B. Jamali, S. Amidi, **A. Hajian**, H. Khoshsafar (**2017**) "A novel electrochemical platform for sensitive and simultaneous determination of dopamine, uric acid and ascorbic acid based on Fe_3O_4-SnO_2-Gr ternary nanocomposite" *Microchemical Journal*, 131, 120-129.

20. A. Afraz, **A. Hajian**, Z. Niknam, E. Mosayebi, A. Yusefi, M. Sillanpää (**2017**) "Amine-functionalized magnetic-silica core-shell nanoparticles for removal of Hg^{2+} from aqueous solution" *Journal of Dispersion and Technology*, 38, 750-756.

21. H. Zeinali, H. Bagheri, Z.M. Khoshhesab, H. Khoshsafar, **A. Hajian** (**2017**) "Nanomolar simultaneous determination of tryptophan and melatonin at a new ionic liquid carbon paste electrode modified with reduced graphene oxide/SnO_2-Co_3O_4@rGO nanocomposite" *Materials Science and Engineering: C*, 71, 386-394.

22. H. Bagheri, E. Ranjbari, M. Amiri-Aref, **A. Hajian**, Y. H. Ardakani, Salimeh Amidi (**2016**) "Modified fractal iron oxide magnetic nanostructure: A novel and high performance platform for redox protein immobilization, direct electrochemistry and bioelectrocatalysis application" *Biosensors and Bioelectronics*, 85, 814-821.

23. J. Ghodsi, **A. Hajian**, A.A. Rafati, Y. Shoja, O. Yurchenko, G. Urban (**2016**) "Electrostatically immobilized hemoglobin on silica-coated magnetic nanoparticles for simultaneous determination of dopamine, uric acid, and folic acid" *Journal of the Electrochemical Society*, 163 (13), B609-B616.

24. H. Khoshsafar, H. Bagheri, M. Rezaei, A. Shirzadmehr, **A. Hajian**, Z. Sepehri (**2016**) "Magnetic carbon paste electrode modified with a high performance composite based on molecularly imprinted carbon nanotubes for sensitive determination of levofloxacin" *Journal of the Electrochemical Society*, 163(8): B422-B427.

25. E. Mosayebi, A. Azizian, **A. Hajian** (**2015**) "Synthesis of nanostructured and microstructured ZnO and $Zn(OH)_2$ on activated carbon cloths by hydrothermal and microwave-assisted chemical bath deposition methods" *Superlattices and microstructures*, 81, 226-232.

26. A. Afraz, A.A. Rafati, **A. Hajian**, M. Khoshnoud (**2014**) "Electrodeposition of Pt nanoparticles on new porous graphitic carbon nanostructures prepared from biomass for fuel cell and methanol sensing application" *Electrocatalysis*, 6, 220-228.

27. A.A Rafati, A. Afraz, **A. Hajian**, P. Assari (**2014**) "Simultaneous determination of ascorbic acid, dopamine, and uric acid using a carbon paste electrode modified with multiwalled carbon nanotubes, ionic liquid, and palladium nanoparticles" *Microchimica Acta*, 181, 1999-2008.

28. A. Afraz, A.A Rafati, **A. Hajian** (**2013**) "Analytical sensing of hydrogen peroxide on Ag nanoparticles-multiwalled carbon nanotube-modified glassy carbon electrode" *Journal of Solid State Electrochemistry*, 17, 2017-2025.

29. A. Bagheri, A.A. Rafati, A. Adel Tajani, A. Afraz Borujeni, **A. Hajian** (**2013**) "Prediction of the surface tension, surface concentration and the relative Gibbs adsorption isotherm of non-ideal binary liquid mixtures" *Journal of Solution Chemistry*, 42, 2071-2086.

30. A.A. Rafati, A. Afraz Borujeni, M. Najafi, **A. Hajian** (**2012**) "Synthesis and characterization of supported silica nano hollow spheres with CdS quantum dots" *Journal of Molecular Liquids*, 174, 124-128.

Conference Presentations:

Presenting author is underlined

1. **A. Hajian**, C. Zellner, S. Schwarz, T. Konegger, M. Schneider, U. Schmid "Towards Tailored Porosification of LTCC Substrates: Study of the Etching Process" 16th European Ceramic Society Conference, ECerS XVI, 2019, Turin, Italy. (Talk)

2. **A. Hajian**, M. Schneider, D. Müftüoglu, H. Homolka, U. Schmid "Morphology and porosification behavior of LTCC substrates: Impact of sintering temperature" Ceramic Interconnect and Ceramic Microsystems Technologies (CICMT) 2019, Shanghai, China. (Talk)

3. U. Schmid, **A. Hajian**, A. Bittner "Wet chemical Etching as an Effective Technique for the Local Permittivity Reduction of LTCC Substrates" Ceramic Interconnect and Ceramic Microsystems Technologies (CICMT) 2019, Shanghai, China. (Invited talk)

4. **A. Hajian**, M. Schneider, D. Müftüoglu, U. Schmid "Investigating the effect of etching parameters on the porosification of LTCC with sodium hydroxide" Electroceramics XVI, 2018, Hasselt, Belgium. (Poster)

5. M. Brehl, M. Rita Cicconi, A. Veber, **A. Hajian**, U. Schmid, D. De Ligny, "Structural Investigation of Glasses in the BaO-B_2O_3-SiO_2 System with Coupled Raman/Brillouin Spectroscopy" Physics of Non-Crystalline Solids & European Society of Glass conference 2018, Saint Malo, France. (Talk)

6. **A. Hajian**, J. Ghodsi, A. Afraz, A.A. Rafati, Y. Shoja, O. Yurchenko, G. Urban "Development of a Novel Biosensor for Nanomolar Detection of Methylparaben" 29th Eurosensors Conference 2015 Freiburg, Germany. (Poster)